Department of Electronic and Electrical Engineering

Development of New Technology for the Accurate Determination of the Density of High Value Fluids

Craig McGregor Hutchison

Ph.D.

2003

Acknowledgments

This work was undertaken as part of the Postgraduate Training Partnership (PTP) between the National Engineering Laboratory (NEL) and University of Strathclyde. The PTP scheme is a joint initiative of the UK's Department of Trade and Industry (DTI) and the Engineering and Physical Sciences Research Council (ESPRC), and is financially assisted by the DTI. I gratefully acknowledge grant support from both NEL and ESPRC.

I would like to thank both of my supervisors, Mr Jim Watson of the National Engineering Laboratory and Dr Brian Stimpson of University of Strathclyde for their invaluable assistance throughout the project.

I would also like to thank my colleagues Mr Denis Ferguson, Mr Robert Anderson and Mr Graeme Ryan of the National Engineering Laboratory for their assistance throughout the project. Their outstanding skills in all areas of engineering and science were vital to the success of this project.

Abstract

The development and validation of new technology for the accurate and traceable metering of high value fluids is presented here. The focus of this doctoral submission is on the determination of fluid density by the measurement of relative permittivity.

A prototype cell, comprising a re-entrant cavity resonator, for the precise determination of the relative permittivity of gases and hydrocarbon liquids over a wide range of both pressures and temperatures has been developed for this work. Accuracies of measurement of relative permittivity with the re-entrant cavity resonator technique of better than 1 ppm may be achieved.

Reference quality relative permittivity measurements were performed and expressions developed for ethylene which are specific to industrial metering applications ($0 \leq t \leq 30^{0}\mathrm{C}$ and $5 \leq p \leq 10\mathrm{MPa}$). The uncertainty in values of density calculated from the mapping relationship is approximately 0.03 % in density at a 95 % confidence level.

The laboratory facility used to perform the fluid mapping or characterisation was based around a high-performance RF network analyser as the principle measuring instrument. However, an on-line instrument must be simple to operate, relatively compact, robust and considerably less expensive; particularly if it is to be widely deployed. The aimed accuracy in the measurement of relative permittivity of the on-line instrument was 5 ppm; a factor of five lower than the laboratory instrument.

For the on-line instrument, the re-entrant cavity resonator was incorporated into a feedback oscillator circuit as the frequency determining element. The accuracy of measurement of relative permittivity of the on-line instrument was 2.5 ppm; a factor of two greater than the aimed accuracy. This accuracy of frequency measurement is only achievable over a relatively narrow range of operating conditions, which is ultimately a

limiting factor in the applicability of the on-line instrument for high precision relative permittivity measurements in the field.

Contents

Page Number

List of Figures

Page Number

List of Tables

Page Number

List of Graphs

List of Plots

Page Number

1. Introduction

The accurate determination of both mass and volumetric flow rates is dependent upon a knowledge of the density of the fluid at the metering conditions. The most widely implemented method for fiscal, custodial transfer and sales related mass flow metering is the use of a volumetric flow metering device together with an on-line densitometer. The uncertainty in mass flow measurement is dependent equally on the uncertainty in volumetric flow rate and in density.

The flow meter may require a knowledge of the fluid density to establish the volumetric flow rate at metering conditions. The calculation of volumetric flow rate, however, may also require a knowledge of the density since it is often necessary to reduce the measurement of volume throughput to standard conditions. It can therefore be seen that density measurement, volumetric and mass flow measurement are of equal importance. To establish the energy flow rate it is also necessary to know the heating value of the fluid at some specified reference conditions.

The density of fluids and fluid mixtures at metering conditions are currently determined either directly using an on-line densitometer or indirectly using an appropriate equation of state.

All commercial densitometers, however, operate on an oscillatory principal and as such are dependent on other fluid properties. Added hydrodynamic mass, or boundary layer effects, are dependent upon the viscosity; and secondary flow effects upon the speed of sound in the fluid at metering conditions. Studies have shown that the magnitude of such effects on earlier versions of commercial densitometers can amount to several percent in density. Refinements to the design of densitometers can help reduce the magnitude of such corrections but not eliminate them entirely. Corrections to the indicated density require a knowledge of both the viscosity and the speed of sound in the fluid at the conditions of measurement.

In addition many commercial densitometers, particularly those used in offshore applications, operate under high pressure and high temperature conditions but checks and calibrations are carried out at, or close to, ambient conditions. This can be a further significant source of error in density measurement. Ideally calibration should be undertaken at metering pressures and temperatures with samples of either the actual working gases or with gas mixtures of similar physical properties.

The principal factors which influence the performance of an on-line densitometer are:-

- installation effects on the operation of the densitometer;
- the influence of viscosity and speed of sound, particularly at 'near' critical conditions, on the operation of the densitometer; and
- single-point calibration of the densitometer.

As a result of the difficulties in the use, and calibration, of commercial on-line densitometers many gas producers and distributors have opted to determine the density of the gas flows indirectly by gas chromatography. Density, in this instance, is derived from an equation of state and a knowledge of the temperature, pressure and composition of the fluid.

In principle, the gas chromatographic technique for the determination of density should be as effective as that using full calibrated and traceable densitometers. This assumes that a valid equation of state is employed for the gas mixture and that measurements of temperature, pressure and composition are made to a sufficiently high standard.

The principal factors which influence the determination of density by this indirect method are:-

- the suitability of the equation of state for use with the gas mixture;

- installation effects on the gas chromatograph;
- errors in the calibration and use of the gas chromatograph; and
- the magnitude of the uncertainties in the measured temperature, pressure and composition of the gas.

The method of gas chromatography to determine the density of gas flows is costly and is only affordable when the number of metering stations is small.

As a direct consequence of the above, transporters and distributors of natural gas are investing in new and more cost effective methods for determining mass and energy flow rates and are, therefore, seriously considering the replacement of all their on-line densitometers with alternative technology. Since the number of metering stations in this instance is large the alternative technology must have a low unit cost.

Similarly, producers of high value products, such as petrochemical refineries, have indicated that they are giving serious consideration to replacing their on-line densitometers with alternative technology. The change in this instance is mainly driven by economic considerations. While they are fully satisfied with the performance and traceability of their volumetric metering facilities (usually orifice plates and turbine meters) their density metering capabilities are poor and lack proper traceability. Errors in density metering, typically around 0.25%, are the largest source of error in their custodial transfer and sales metering calculations. The accuracy of metering currently provided by on-line densitometers is therefore no longer deemed adequate for their purposes and metering improvements are necessary to help maintain the efficient and viable operation of their customer base. The factors which have influenced this decision include the errors resulting from poor calibration, installation effects, speed of sound and viscosity corrections and the high cost of maintaining and calibrating such instruments.

There therefore exists a need for new, accurate and traceable methods for the on-line determination of fluid density. It is unlikely that this objective can be achieved through

the direct measurement of density and indirect methods would appear to offer the best opportunity for advancement. The choice of alternative measurement parameters is dependent upon a number of factors:-

- the metering conditions (liquid phase, supercritical gas phase or gas phase operation);
- the sensitivity of the parameters to density for the specific fluid system; and
- the feasibility of making laboratory measurements of the property to *map* or *characterise* its behaviour in terms of density and temperature dependence.

The alternative parameters being considered by gas distributors and producers of high-value products are *speed of sound* and *relative permittivity*. Determination of one, or both, of these independent parameters can yield the density and, possibly also, in the case of the gas distributors, the heating value of the gas at metering conditions. Both parameters can, with careful design of equipment, be measured with a high degree of precision in an on-line situation, however it is the determination of fluid density by the measurement of relative permittivity that is the focus of the thesis presented here.

The density and temperature dependence of the relative permittivity of non-polar fluids, such as natural gases, and high value fluids, such as ethylene, can be accurately described by the Clausius-Mossotti relation; a well known theoretical relationship between relative permittivity and density.

In order to determine the density of a fluid from a precise measurement of relative permittivity it is necessary to have an established relationship, such as the Clausius-Mossotti relation, between the relative permittivity, temperature and density of the fluid. This fluid *mapping* or *characterisation* can be established from a series of reference quality relative permittivity and density measurements in the laboratory. Regression of these measurements then yields an expression for the density of the fluid in terms of relative permittivity and temperature.

Measurement techniques for relative permittivity have been refined in recent years and it is now possible, using the latest technology, to make precise measurements in the relevant pressure and temperature range in the laboratory and in on-line situations to within an uncertainty of a few parts per million using relatively simple and robust instrumentation. The National Engineering Laboratory, who are at the forefront of developments in this field, have developed a prototype cell[1], comprising a re-entrant cavity resonator, for the precise determination of the relative permittivity of gases and hydrocarbon liquids over a wide range of both pressures and temperatures. This choice of experimental method is reviewed in Chapter 3: Choice of Experimental Technique.

Precise measurements of relative permittivity coupled with the known theoretical relationship with density therefore opens up an alternative indirect route to determining the density of gases and liquids both in the laboratory and in on-line situations.

1.1 Objectives of the Work

The programme of work which forms the object of this doctoral submission centres around the development and validation of the above technology for the accurate and traceable metering of high value fluids.

The prototype permittivity cell, developed by NEL, comprises a re-entrant cavity resonator operating at RF frequencies. For low loss dielectric fluids, like natural gas and ethylene, the relative permittivity can be derived solely from measurements of the resonant frequency of the cavity through the relation:-

$$\varepsilon_r(t,p) = \left(\frac{f_0(t)}{f_{\varepsilon_r}(t,p)} \right)^2 , \qquad (1.1)$$

where ε_r is the relative permittivity of the fluid at temperature t and absolute pressure p;

$f_0(t)$ is the resonant frequency of the cavity under vacuum conditions, $\varepsilon_r = 1$ at temperature t; and

$f_{\varepsilon_r}(t,p)$ is the resonant frequency of the fluid filled cavity at the conditions of measurement.

The relationship between permittivity and resonant frequency given by equation (1.1) applies to better than 1 part per million provided:-

- the cavity has a high electrical quality factor at resonance, $Q > 1000$; and
- the dimensions of the dielectric filled cavity are the same as those of the evacuated cavity at the same temperature of measurement.

Excluding temperature effects, which may be easily quantified, the dimensional stability of the cavity is influenced by:-

- the dilation of the dielectric filled cavity with applied pressure; and
- the effective dilation of the dielectric filled cavity due to a change in the penetration depth of the electromagnetic field into the metal surfaces of the cavity.

In order to maintain the level of precision of expression (1.1) it is therefore necessary to correct for the effects of the above influences.

One of the objectives of the present work was therefore to investigate the dimensional stability of the re-entrant cavity resonator both in terms of the applied physical pressure of the contained dielectric fluid and the spatial distribution of the electromagnetic field between evacuated and filled conditions.

Two arrangements of the permittivity cell are possible:-

- a laboratory version with high-quality electrical instrumentation suitable for precise measurements on fluids and for mapping relative permittivity as a function of both density and temperature; and
- a robust, yet precise, on-line version with built-in electronics and low-cost instrumentation suitable for the precise measurements on fluids as a function of both density and temperature.

It was an objective of the present work to develop and commission the laboratory facility for making precise measurements of the relative permittivity of high value fluids over an industrially relevant range of temperatures and pressures.

A further objective was to employ the laboratory facility in the mapping of the relative permittivity of an industrially important fluid as a function of temperature and density over the relevant range of temperatures and pressures. The fluid chosen for characterisation was ethylene.

Ethylene, as the simplest form of unsaturated hydrocarbons, is one of the most important materials used in chemical industries. It is used mainly as a chemical intermediate in the production of polymer plastics and other industrial chemicals such as ethanol and ethylene oxide. However, due to its relatively simple molecular structure, it is also the subject of considerable research in the development of theories on molecular interaction.

It was also an objective of the present work to obtain, from regression of the laboratory mapping measurements, expressions for the density of ethylene in terms of relative permittivity and temperature. The expressions are intended to represent the laboratory measurements to within the experimental uncertainty over the full range of industrial operating conditions.

The new technology also has applications to impure fluids. Like pure industrial fluids the need for accurate density data of corresponding impure fluids is important for custodial transfer agreements. The compositions of such fluid mixtures are so variable however that it is very difficult to obtain sufficiently comprehensive experimental data for many applications.

Although this topic is not covered in the work presented here it can be shown that given an approximate composition of a fluid mixture it is possible to determine its density from a single measurement of the relative permittivity. The implications of this would be of considerable benefit to the chemical and petrochemical industries, and as a result this topic is considered as a recommendation for further work.

The laboratory facility would be based around a high-performance RF network analyser as the principle measuring instrument. This methodology is, however, completely inappropriate as the basis of an on-line measurement instrument. An on-line instrument must be simple to operate, relatively compact, robust and considerably less expensive; particularly if it is to be widely deployed.

Consequently another objective of the work was to develop a robust, on-line instrument, with low-cost electronics for making precise measurements of the relative permittivity of high value fluids over an industrially relevant range of temperatures and pressures.

To summarise, the principal objectives of this doctoral submission are:-

- to develop a prototype laboratory facility for the accurate metering of the density of high-value fluids and fluid mixtures based on the measurement of relative permittivity;

- to develop a prototype on-line instrument for the accurate metering of the density of high-value fluids and fluid mixtures based on the measurement of relative permittivity; and
- to provide the underpinning traceability framework for the application and development of the latest advances in technology.

References

1. Watson, J.T.R. *Methods for the Precise Measurement of the Relative Permittivity of Natural Gases.* Flow Centre Report No. 095/97 produced for Ruhrgas AG; National Engineering Laboratory, East Kilbride, Glasgow, January 1998.

2. Dielectric Theory

An overview is presented here of the macroscopic and microscopic properties of dielectric materials.

The object of this chapter is to provide a general summary on dielectric theory of materials and, more importantly, to explain the development of the Clausius-Mossotti relation, which determines the relationship between the relative permittivity and density of non-polar gases.

2.1 Introduction

Every material has a unique set of electrical characteristics that are dependent on its dielectric properties. Properties of these materials are of interest to scientists and engineers whose concerns may vary from those requiring a knowledge of the dependence of dielectric loss on frequency and temperature in order to find a material whose loss is negligible over a certain frequency range, to those who may use these dielectric properties to form a relation between dielectric phenomena and chemical composition and behaviour. Petrochemical refineries, who produce high value products such as ethylene, require accurate measurements on density for fiscal metering purposes. The known relationship between relative permittivity and density therefore provides an indirect route to determining the density of gases and liquids.

The electrical properties of dielectric materials are usually described in terms of the relative permittivity. For most materials this quantity is independent of the strength of the electric field for all normal laboratory conditions, but in the case of alternating fields depends on the frequency. It also depends on parameters such as temperature and pressure which define the physical state of the material.

2.2 Macroscopic Properties of Dielectrics

It was in 1837 that Faraday first noticed that when an insulating material was inserted between the two metal plates of a capacitor, across which a constant voltage was applied, the capacitance increased. Such a material is classified as a dielectric if it has the ability to store energy when subjected to an external electric field. In order to describe the dielectric properties of such materials Faraday introduced the term *specific inductive capacity* which was defined as the ratio of the capacitance of a capacitor filled with the insulating material to that of the empty capacitor. The specific inductive capacity is also known as the *dielectric constant* or *relative permittivity.*

In order to relate the relative permittivity of a material to its intrinsic properties it is necessary to consider what happens to a dielectric when it is subjected to an electric field.

Dielectrics are *non-metal* substances which may be regarded from the standpoint of electromagnetic theory as continuous media which becomes polarised through the interaction of an electric field. Dielectric materials are invariably insulators and therefore contain no free charges. Each electron in the material is bound to a particular atom by the electrostatic attraction between the negative electronic charge and the positive charge on the nucleus. In the absence of any external electric field, the electrons are distributed symmetrically around the nucleus. When an electric field is applied, the electrons and the nucleus are displaced relative to one another until the internal forces of attraction balance those due to the electric field. The electrons are displaced in a direction opposite to that of the field while the nucleus is displaced in the same direction as the field. Each atom therefore acquires an electric dipole moment which is in the same direction as the applied electric field. The action of an electric field in inducing a dipole moment in each atom of the dielectric is termed polarisation. Figure (2.1) illustrates the polarisation of an atom by an electric field:-

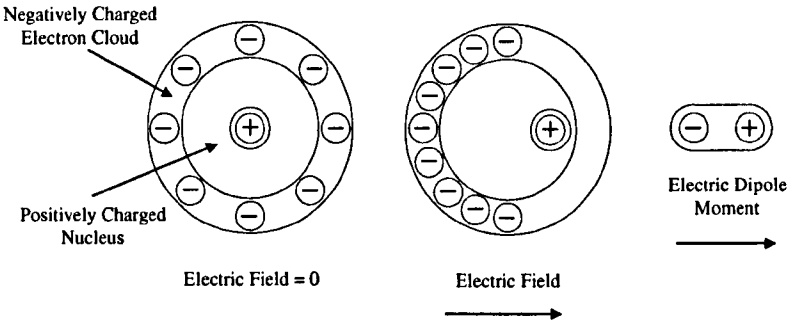

Figure 2.1 Polarisation of an atom in an electric field.

The polarisation of a material is defined as the electric dipole moment per unit volume and is proportional to the electric field, $\underline{E}$, for all ordinary field strengths:-

$$\underline{P} = \varepsilon_0 \chi \underline{E}, \tag{2.1}$$

where χ is the electric susceptibility or polarisability of the material; and

ε_0 is the permittivity of free space.

The electric susceptibility is a measure of the material's polarisability and is characteristic for any given material. The relative permittivity is defined by the electric susceptibility as, $\varepsilon_r = 1 + \chi$. In general ε_r depends on temperature, frequency and, to a lesser extent, pressure.

Faraday's experiment of inserting a dielectric between the parallel plates of a capacitor, held at a constant voltage, is illustrated in figure (2.2) below:-

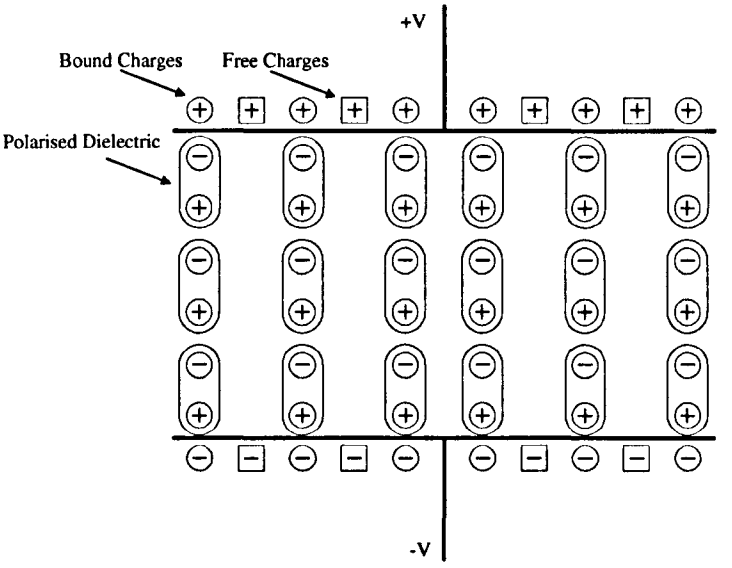

Figure 2.2 Schematic representation of dielectric polarisation.

The polarised dielectric can be visualised as a chain of dipoles which form under the action of the electric field and bind free charges of the opposite polarity at the plates of the capacitor. These bound charges are effectively cancelled out due to the charges at either end of the dipole chain. A dielectric material therefore allows more charge onto the plates of the capacitor and hence increases the storage capacity of a capacitor by neutralising charges at the capacitor plates.

The atomic dipoles are parallel and therefore the resultant moment for an element of volume dv is $\underline{P}dv$, where $\underline{P}$ is the polarisation of the material. The potential of such an element a distance r away is[1]:-

$$dV = \frac{1}{4\pi\varepsilon_0}(\underline{P}dv).grad\left(1/r\right), \tag{2.2}$$

where the differentiation is with respect to the co-ordinates of the volume element containing the dipoles. The potential due to a finite volume of dielectric is then:-

$$V = \int \frac{1}{4\pi\varepsilon_0}\left(\underline{P}.grad\left(1/r\right)\right) dv\,, \tag{2.3}$$

however, since $div\left(\underline{P}/r\right) = 1/r\, div\underline{P} + \underline{P}.grad\left(1/r\right)$, equation (2.3) becomes:-

$$V = \int \frac{1}{4\pi\varepsilon_0} div\left(\underline{P}/r\right) dv - \int \frac{1}{4\pi\varepsilon_0}\frac{1}{r} div\,\underline{P}\, dv\,,$$

$$= \int \frac{1}{4\pi\varepsilon_0}\frac{1}{r}\underline{P}.\underline{dS} - \int \frac{1}{4\pi\varepsilon_0}\frac{1}{r} div\,\underline{P}\, dv\,, \tag{2.4}$$

where the volume integral has been transformed to a surface integral using Gauss' theorem of divergence.

The two terms in equation (2.4) show that the resultant potential can be attributed to an apparent surface charge of density $P\cos\theta$, where θ is the angle $\underline{P}$ makes with the normal to the surface of the dielectric, and an apparent volume distribution whose charge density is $-div\underline{P}$. The apparent volume distribution of charge density occurs only if the material is anisotropic or if the applied electric field varies within the material, since the relative displacement of the positive and negative charges will change from one region of the material to another causing a non-uniform polarisation. The surface charge density is present when there is an applied electric field and vanishes if the field is removed. These apparent charges are called polarisation charges and may be represented by the bound charges on the plates of the capacitor in figure (2.2).

Gauss' theorem states that the integral $\int \underline{E}.\underline{dS}$ of the normal component of $\underline{E}$ over any closed surface is equal to the total charge within the surface, divided by ε_0. However if the surface is within a dielectric the total charge must include both the apparent surface

charge density, ρ, and the apparent volume charge density, $-divP$. The volume charge density is thus $\rho - (div\underline{P})$, so that Gauss' law now becomes:-

$$\int \underline{E}.\underline{dS} = \int div\,\underline{E}\; dv = \frac{1}{\varepsilon_0}\int (\rho - div\,\underline{P})\, dv \text{, and re-arranging gives:-}$$

$$\int div(\varepsilon_0 \underline{E} + \underline{P})\, dv = \int \rho\, dv,$$

where $(\varepsilon_0 \underline{E} + \underline{P})$ is defined as the electric displacement or electric flux density, and is given the symbol $\underline{D}$, such that:-

$$\int \underline{D}.\underline{ds} = \int div\underline{D}\; dv = \int \rho\, dv,$$

and, since the volume integrals must be equal over any chosen arbitrary volume, we have:-

$$div\underline{D} = \rho, \qquad (2.5)$$

which is the differential form of Gauss' theorem for dielectrics.

In an isotropic dielectric, $\underline{P}$ is parallel to $\underline{E}$, and hence also $\underline{D}$. Therefore, using equation (2.1), we can define the electric displacement as $\underline{D} = \varepsilon_0(1+\chi)\underline{E}$, and substituting $\varepsilon_r = (1+\chi)$, gives:-

$$\underline{D} = \varepsilon_0 \varepsilon_r \underline{E}, \qquad (2.6)$$

where ε_r is the relative permittivity of the dielectric.

The electric displacement $\underline{D}$ may be considered as the true (or total) charge density on the plates of the capacitor and is therefore the sum of the bound and free charge densities in figure (2.2).

The capacity of a dielectric filled parallel plate capacitor can now be calculated using the expression derived in equation (2.6) for the electric flux density. Using Gauss' law, with the chosen surface enclosing the positive plate of the capacitor and passing through the dielectric material, the following relation can be obtained:-

$$\int \underline{D}.\underline{dS} = q, \tag{2.7}$$

where q is the total charge on the capacitor plate.

The electric flux density for this simple geometry can be considered constant over the surface of the plate and normal to it, therefore equation (2.7) may be written as:-

$$A\underline{D} = A\varepsilon_r\varepsilon_0\underline{E} = q, \tag{2.8}$$

where A is the area of the plate, and equation (2.6) has been substituted for $\underline{D}$.

The definition of capacity is $C = {}^{q}/_{V} = {}^{q}/_{\underline{E}d}$, where V is the potential across the plates and d is their separation. Therefore, by rearranging equation (2.8) for the electric field within the dielectric, the expression for the capacitance now becomes:-

$$C = {}^{A\varepsilon_r\varepsilon_0}/_{d}, \tag{2.9}$$

Thus the presence of the dielectric has increased the capacitance of the capacitor by the factor ε_r, which is the result found by Faraday.

The most straight forward measurement of the relative permittivity of a dielectric material is the comparison of a capacitance value with and without a dielectric material present.

2.3 Microscopic Properties of Dielectrics

In section 2.2 a dielectric material was considered as a continuous medium which, under the action of an electric field, becomes polarised. The polarisability of any given material was characterised by the term electric susceptibility, which was related to the relative permittivity of the dielectric by the equation $\varepsilon_r = 1 + \chi$, where the relative permittivity was taken as an experimentally determined quantity. However the idea of considering the dielectric material as a continuous medium is inappropriate for modern atomic theory, by which any material is regarded as being constructed of atoms or molecules.

Each atom consists of a heavy, positively charged nucleus surrounded by a negatively charged electron cloud. The atom is electrically neutral with equal amounts of positive and negative charge. The same is true when atoms join together, either by transferring or sharing charges, to form a molecule. The distribution of charge in an atom is symmetrical and therefore no atom posses a permanent electric dipole moment. This however is not true of molecules, which may be considered as either polar, possessing a permanent electric dipole moment, or non-polar, which do not.

Homonuclear diatomic molecules such as H_2, N_2 or O_2 have a symmetrical charge distribution and are therefore non-polar, but asymmetrical molecules such as KCl and HCl are polar, since there is a net transfer of charge from one atom to another. A simple picture of the KCl molecule is that of two ions, K^+ and Cl^-, with the electric dipole

moment equal to the product of the electronic charge and the intermolecular distance. The measured dipole moments are generally smaller than those suggested by this simple model due to the fact that the charge tends to reside more in between the two atoms rather than around them. For covalently bonded molecules most of the charge resides between the two nuclei and therefore the electric dipole moments are far less than the product of the electronic charge and the internuclear distance.

For more complicated triatomic molecules, such as CO_2 and H_2O, it is the symmetry of the molecules that determines as to whether or not the molecule is polar or non-polar. For example CO_2 has no electric dipole moment and therefore must be symmetrical, O - C - O, whereas H_2O has a large dipole moment indicating that it is asymmetrical. Thus the absence or presence of an electric dipole moment can give important information about the structure of a molecule and its chemical bonding. Furthermore, it is obvious that by considering the dielectric material from an atomic theory standpoint there will be more than one polarisation effect when the dielectric is subjected to an electric field.

A dielectric material may have several polarisation effects, or mechanisms, that contribute to it's overall relative permittivity. The simplest mechanism occurs when an electric field acts on an individual atom, see figure (1.1), displacing the nucleus with respect to the electrons that surround it resulting in an induced electric dipole moment. This is called *electronic polarisation* and is operative in all dielectric materials. In a material composed of heteronuclear polar molecules, such as KCl or H_2O, each molecule has a permanent electric dipole moment. In the absence of an electric field each molecule is randomly orientated and the material has no net polarisation. The action of applying an electric field to such a material has two effects. The first effect is that the electric field tends to rotate the molecules to align with the field resulting in the material acquiring a net electric dipole moment, this is called *orientational polarisation.* The second effect is that the electric field will tend to stretch the bonds between the ions which increases the electric dipole moment. The displacement of these charged atoms, or groups of charged atoms, with respect to one another is called *atomic polarisation.*

All these mechanisms yield a polarisation which is proportional to the electric field acting on the charged particles. Electronic and atomic polarisation are temperature independent but orientational polarisation is dependent on the extent to which the applied electric field can align the molecules against the disordering effects of thermal motion, therefore making it temperature dependent. When more than one polarisation mechanism is in operation each will give a contribution to ε_r. If any of these cease to be operative it will be detected as a decrease in ε_r. This is most noticeable in the case of polar liquids which have high values of ε_r due to the orientational polarisation. When the material becomes solid ε_r drops dramatically due to the fact that the dipoles can no longer rotate in the solid state.

2.3.1 Relative Permittivity of Non-Polar Gases

When a uniform electric field is applied to a non-polar gas, the only polarisation effect that occurs is that due to electronic polarisation. No translational force acts on the molecule as a whole, since it is electrically neutral, and the centre of mass remains fixed. The electrons and nucleus are, however, subjected to forces of opposite sign, and they will therefore be displaced in the opposite directions until the internal forces of attraction balance those due to the external electric field. The molecule thereby acquires an induced electric dipole moment when the field is applied. The forces exerted on the charged constituents of the molecule are parallel to the field, and proportional to it, as are the induced electric dipole moments. Since the electrons are much lighter than the nucleus, their displacement is greater, as the position of the centre of mass is unchanged.

The induced electric dipole moment is related to the electric field by the following expression:-

$$\underline{p} = \alpha \underline{E}, \tag{2.10}$$

where $\underline{p}$ is the induced electric dipole moment;

$\underline{E}$ is the field acting on the molecule; and

α is a constant known as the microscopic polarisability.

The term α is also known as the molecular or atomic polarisability, depending on whether molecules or atoms respectively are being discussed, and is value is typical for each different type.

The aims of dielectric theory are:-

- to obtain a relationship between the relative permittivity, which is a macroscopic quantity, and the microscopic dipole moment, or molecular polarisability, of a molecule or atom; and

- to be able to make a theoretical calculation of the polarisability of particular molecules or atoms, in order to understand the phenomenon of polarisation and it's dependence on frequency, temperature and applied electric field strength.

The first task can be achieved fairly reasonably, but the second requires the use of quantum mechanics, and therefore has only been solved for the simplest of atoms[3].

The electric field, $\underline{E}$, in equation (2.10) is called the local field, since it is the actual field acting on each molecule. This is not necessarily the same as the external electric field, $\underline{E_0}$, applied, for example, by maintaining a voltage difference between two plates of a capacitor, since each molecule is subjected also to the electric fields of neighbouring molecules which, like it, have acquired dipole moments under the influence of the

electric field. The local field is equal to the vector sum of the external field and the fields due to the neighbouring molecules.

The general relation between the electric displacement, $\underline{D}$, the external electric field, $\underline{E_0}$, the polarisation, $\underline{P}$, and the relative permittivity is:-

$$\underline{D} = \varepsilon_0 \underline{E_0} + \underline{P} = \varepsilon_r \varepsilon_0 \underline{E_0}, \tag{2.11}$$

where equation (2.6) has been substituted for $\underline{D}$.

Here $\underline{P}$ is the induced electric dipole moment per unit volume, or polarisation, and is therefore related to the local field $\underline{E}$ by the expression:-

$$\underline{P} = n\alpha \underline{E}, \tag{2.12}$$

where n is the number of molecules per unit volume.

The polarisation can also be defined in terms of relative permittivity by rearranging equation (2.11) to give:-

$$\underline{P} = \varepsilon_0 \underline{E_0}(\varepsilon_r - 1). \tag{2.13}$$

Equations (2.12) and (2.13) are two alternative expressions for polarisation, thus providing the link between the macroscopically measured relative permittivity and the molecular polarisability. In order to obtain a relationship between these two parameters the relationship between the local electric field and the external electric field must be known.

This relationship was first developed by Lorentz[1] who suggested that the volume of gas around a particular molecule should be divided into two parts and the contribution of each be considered separately. A schematic of the Lorentz model is shown in figure (2.3) below, where the dielectric is subjected to an external electric field by inserting it between the plates of a parallel capacitor held at constant potential:-

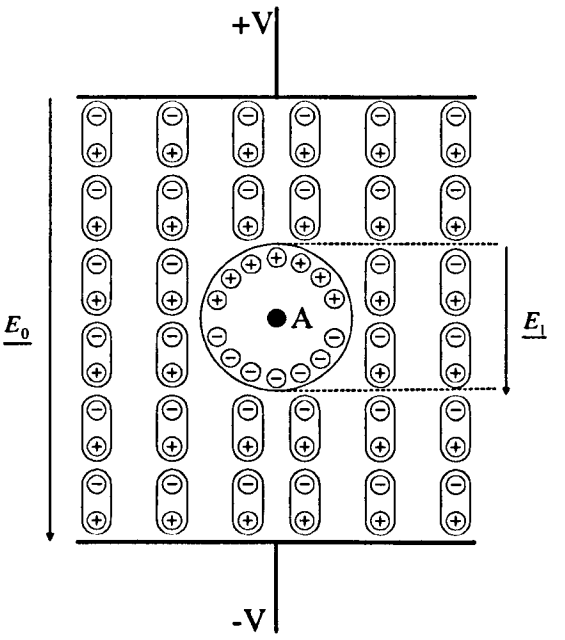

Figure 2.3 Lorentz model for determination of local electric field.

The reference molecule, A, is surrounded by an imaginary sphere whose size is so large that when considering the local field acting on A at the centre of the sphere, the effect of the molecules in the region outside the sphere may be evaluated by regarding the region outside as a continuum. If the molecules inside the sphere are removed while the polarisation outside remains *frozen*, the field acting on A will occur from two sources. The first is from the external electric field, $\underline{E_0}$, and the second is from the free ends of the dipole chains that line the walls of the sphere, $\underline{E_1}$. There are, however, molecules inside the sphere, and their contribution to the local field must also be included and is

represented as $\underline{E_2}$. The local field is then expressed as the summation of each component of electric field acting on the molecule:-

$$\underline{E} = \underline{E_0} + \underline{E_1} + \underline{E_2}. \tag{2.14}$$

The surface charges that line the walls of the sphere are similar to those described in section 2.2, and thus have a charge density of $P\cos\theta$, where θ is the angle $\underline{P}$ makes with the normal to the spherical surface. It can be shown[2] that by integrating over the spherical surface the contribution to the local field made by these surface charges is:-

$$\underline{E_1} = \frac{P}{3\varepsilon_0}. \tag{2.15}$$

The contribution to the local field from the molecules inside the sphere is difficult to calculate, since it requires an accurate knowledge of how the molecules are arranged and their polarisation. However, Lorentz showed that the additional individual field effects of the molecules within the sphere on the molecule A mutually cancel, so that:-

$$\underline{E_2} = 0. \tag{2.16}$$

This is a reasonable approximation when the molecules are arranged either in a highly symmetrical array or in complete disorder, like a gas where the molecules are moving randomly, independently of one another.

The local field is now given by:-

$$\underline{E} = \underline{E_0} + \frac{\underline{P}}{3\varepsilon_0}, \tag{2.17}$$

where equations (2.15) and (2.16) have been substituted for $\underline{E_1}$ and $\underline{E_2}$, respectively.

The expression for the local electric field, given by equation (2.17), can be substituted into the expression for the polarisation, given by equation (2.12), so that:-

$$\underline{P} = n\alpha\left(\underline{E_0} + \frac{\underline{P}}{3\varepsilon_0}\right). \tag{2.18}$$

Elimination of $\underline{P}$ using equation (2.13) gives:-

$$\frac{(\varepsilon_r - 1)}{(\varepsilon_r + 2)} = \frac{n\alpha}{3\varepsilon_0}. \tag{2.19}$$

This equation was first derived by Clausius and Mossotti[2] and is known by their names. It shows the relationship between the macroscopic relative permittivity and the microscopic polarisability of the dielectric. The number density of molecules, n, is given by:-

$$n = \frac{\rho N}{M} \tag{2.20}$$

where ρ is the density;

N is Avogadro's number; and

M is molecular weight.

Substitution of equation (2.20) into equation (2.19) gives:-

$$\frac{(\varepsilon_r - 1)}{(\varepsilon_r + 2)}\frac{M}{\rho} = \frac{N\alpha}{3\varepsilon_0}, \tag{2.21}$$

where $\frac{N\alpha}{3\varepsilon_0}$ is called the molar dielectric polarisability.

The Clausius-Mossotti equation, expressed in the form of equation (2.21), determines the relationship between the relative permittivity and density of the gas. Measurements on gases and liquids[4], however, have shown that the use of the Clausius-Mossotti equation in this form cannot completely describe the relation between relative permittivity and the density of non-polar fluids, since it may not always be possible to neglect the contribution to the local electric field from $\underline{E_2}$. It is therefore necessary to use a virial series expansion equation of the simple Clausius-Mossotti equation to accurately describe the relation of relative permittivity to the density of non-polar fluids:-

$$\frac{(\varepsilon_r - 1)}{(\varepsilon_r + 2)} V_m = A_{\varepsilon_r} + \frac{B_{\varepsilon_r}(T)}{V_m} + \frac{C_{\varepsilon_r}(T)}{V_m^2} + \ldots, \tag{2.22}$$

where A_{ε_r}, B_{ε_r}, C_{ε_r} are termed the dielectric virial coefficients; and

V_m is the molar volume, $V_m = \frac{M}{\rho}$.

At very low densities, or gases up to moderate pressures, the molar volume $V_m \to \infty$, and therefore equation (2.22) becomes $A_\varepsilon = \frac{N\alpha}{3\varepsilon_0}$, and is thus equal to equation (2.21). The first dielectric virial coefficient, A_{ε_r}, therefore represents the isolated molecule contribution to the total polarisation. The second dielectric virial coefficient, B_{ε_r}, represents the excess contribution to total polarisation due to the interaction of molecular pairs, which is not described by the Lorentz field. Likewise the third dielectric virial coefficient, C_{ε_r}, represents the interaction of molecular triplets. When the coefficients

B_ε and C_{ε_r} are included, the relative permittivity of the fluid now becomes temperature, as well as density, dependent.

Since measurements of A_{ε_r} gives values for molecular polarizabilities, and B_{ε_r} and C_{ε_r} yield information on molecular interactions it can be seen that measurements of the dielectric constant, combined with density data, also provide useful information for the development of theories on molecular interactions and molecular polarisability.

To determine the density of a fluid from a precise measurement of relative permittivity it is necessary to have an established relationship, such as equation (2.22), between the relative permittivity, temperature and density of the fluid. This fluid *mapping* or *characterisation* can be established from a series of accurate relative permittivity and density measurements in the laboratory. Regression of these measurements then yields the coefficients A_ε, B_ε and C_{ε_r} in equation (2.22). These parameters need only be established once for each fluid system.

The theory in this section holds not only for non-polar gases, but for all gases, since the application of an electric field will always cause a distortion of the molecule and thus induce a dipole moment. In the case of polar gases, however, there is an additional effect arising from the presence of the permanent dipole moments. In the absence of an applied electric field these point in random directions and there is no net polarisation of the gas. When a field is applied, there is a small excess in the number of dipoles pointing with the field over those pointing against the field, and so there is a contribution to the net polarisation. The excess number is determined by the Boltzmann distribution, since a dipole pointing with the field has a slightly lower energy than one pointing against the field, and so is slightly more favoured in the distribution. For polar fluids the temperature dependence of A_ε has to be included in equation (2.22), since the orientational polarisation is a temperature dependent quantity.

2.4 Time-Dependent Electric Fields

The dielectric theory introduced thus far has been developed by assuming that the electric field applied to the dielectric material is static, resulting in real quantities such as relative permittivity and polarisability being used to describe the properties of dielectric material. The theory also holds for time dependent electric fields, however, the relative permittivity and polarisability now become complex quantities due to the fact that the dielectric material now exhibits an energy loss.

When a static electric field is applied to a dielectric the material becomes polarised. The displacement of charges associated with this polarisation will usually show some inertia. Thus if a constant electric field is suddenly applied to a dielectric material the resultant polarisation will not occur immediately, but will approach its static state gradually. Therefore, when a time dependent electric field is applied to a dielectric material there may occur a phase difference between the applied electric field, $\underline{E}$, and the resultant electric displacement, $\underline{D}$, due to the fact the dipoles require a finite time to become polarised.

If the dielectric material is subjected to a periodic electric field[5]:-

$$\underline{E} = \underline{E}_0 \cos(\omega t), \tag{2.23}$$

where $\underline{E}_0$ is the amplitude of electric field; and

$\frac{\omega}{2\pi}$ is the frequency;

there must be, after a sufficient length of time, a resultant periodic electric displacement field:-

$$\underline{D} = \underline{D_0}\cos(\omega t - \delta), \tag{2.24}$$

where $\underline{D_0}$ is the amplitude of the displacement field; and

δ is the phase difference between $\underline{E}$ and $\underline{D}$.

Equation (2.24) may be expressed as:-

$$\underline{D} = \underline{D_1}\cos\omega t + \underline{D_2}\sin\omega t,$$

$$\text{where } \underline{D_1} = \underline{D_0}\cos\delta \text{ and } \underline{D_2} = \underline{D_0}\sin\delta. \tag{2.25}$$

For most dielectrics $\underline{D_0}$ is proportional to $\underline{E_0}$, (equation (2.6)), but the ratio $\underline{D_0}/\underline{E_0}$ is normally frequency dependent. Therefore two frequency dependent relative permittivities can be introduced as:-

$$\varepsilon_r' = \frac{\underline{D_1}}{\varepsilon_0 \underline{E_0}} \quad \text{and} \quad \varepsilon_r'' = \frac{\underline{D_2}}{\varepsilon_0 \underline{E_0}}, \tag{2.26}$$

which can be linked by using equations (2.25) and (2.26) to give:-

$$\tan\delta = \frac{\varepsilon_r''}{\varepsilon_r'}. \tag{2.27}$$

The quantity ε'' is proportional to energy loss in dielectrics, and equation (2.27) is known as the loss tangent.

The energy loss in a dielectric material that is subjected to a time dependent electric field may be determined by again considering the case where a dielectric material is inserted between the plates of a capacitor.

If a capacitor in vacuum is connected to a sinusoidal voltage source:-

$$V = V_0 e^{j\omega t}, \tag{2.28}$$

the current through the capacitor is:-

$$I_C = \frac{dq}{dt} = j\omega C_0 V = I_0 e^{j(\omega t + \pi/2)}, \tag{2.29}$$

where q is the charge stored in the capacitor; and

C_0 is the capacitance of the capacitor in vacuum;

which leads the voltage source by 90°. However for a capacitor containing a dielectric there may appear, in addition to the charging current, a loss current component which is in phase with the applied voltage:-

$$I_L = GV, \tag{2.30}$$

where G is the conductance of the dielectric.

The total current through the capacitor is given by:-

$$I = I_C + I_L = (j\omega C + G)V, \tag{2.31}$$

where C is now the capacitance of the dielectric filled capacitor.

The phase relationships between these currents are illustrated in figure (2.4) below:-

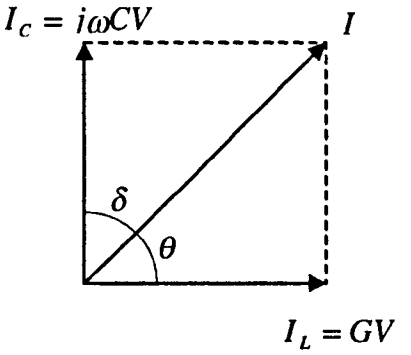

Figure 2.4 Total current through capacitor with dielectric loss.

The total current through the capacitor is inclined by a *power factor angle* $\theta < 90°$ against the applied voltage V, and by a loss angle δ, against the $+j$ axis.

The dielectric filled capacitor may be represented by a number of equivalent circuits, the simplest of which, however, consists of an ideal capacitor in parallel with a resistor, as illustrated in figure (2.5) below:-

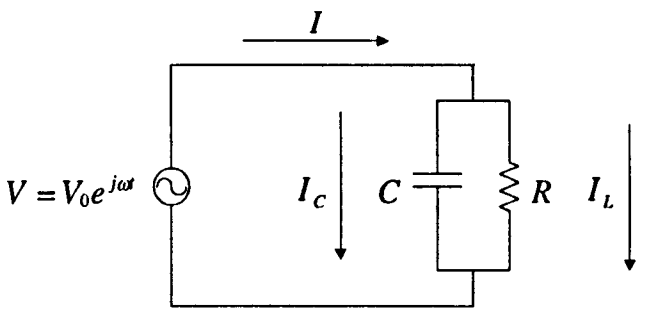

Figure 2.5 Equivalent circuit of dielectric material subjected to a time varying electric field.

It is not possible to conclude, however, that the electrical behaviour of a dielectric material corresponds to such a circuit, since the frequency response of this circuit, which can be expressed by the ratio of loss current to charging current or the loss tangent,:-

$$\tan\delta = \frac{I_L}{I_C} = \frac{1}{\omega RC}, \tag{2.32}$$

may not agree with that observed because the conductance term need not only be due to a migration of charge carriers, but may represent any energy consuming process. In a more general way, this is a direct consequence of the fact that the circuit elements R and C are not constant but depend upon the frequency and temperature in so far as the parameters ε_r' and ε_r'' are themselves dependent on the same variables. Thus making it difficult to use any one circuit to explain the electrical behaviour of a dielectric material.

It has therefore become customary to refer to the existence of a loss current in addition to a charging current by the introduction of a *complex relative permittivity* which may be expressed as:-

$$\varepsilon_r = \varepsilon_r' - j\varepsilon_r''. \tag{2.33}$$

By inserting the complex relative permittivity into equation (2.31) for the loss current through a capacitor, the total current through the capacitor can now be written as:-

$$I = \left(j\omega\varepsilon_r' + \omega\varepsilon_r'' \right) C_0 V, \tag{2.34}$$

where $C_0\varepsilon_r$ has been substituted for C.

The loss tangent now becomes, $\tan\delta = \frac{\varepsilon_r''}{\varepsilon_r'}$, which is the same as that derived in equation (2.27).

The product $\omega\varepsilon_r''\varepsilon_0$ is equivalent to a dielectric conductivity and sums over all the dissipative effects in the material such as electronic and ionic conductivity, space charge polarisation or frequency dependent loss such as that due to the friction generated by the orientation of dipoles.

The real component of the relative permittivity, ε_r', is a measure of how much energy from an external electric field is stored per period in a dielectric material. ε_r' is greater than one for most solids, liquids and gases. The imaginary component of the relative permittivity, ε_r'', is called the loss-factor, and is a measure of the dissipation per period for an external electric field. ε_r'' is always greater than zero and is usually much smaller than ε_r'. For gases ε_r'' is extremely small and as a result it is not necessary to include it in the Clausius-Mossotti equation, given by equation (2.22).

2.5 The Frequency Dependence of the Relative Permittivity

Maxwell's equations for electromagnetic waves show that the velocity in a dielectric medium is equal to $(\mu_r\mu_0\varepsilon_r\varepsilon_0)^{-\frac{1}{2}}$ where μ_r and μ_0 are the relative and free space magnetic permeabilities, respectively. In free space the velocity is $(\mu_0\varepsilon_0)^{-\frac{1}{2}}$. If the medium is non-magnetic then $\mu_r = 1$, and the ratio of the velocity of the electromagnetic waves in free space to the velocity in the medium is equal to $\varepsilon_r^{\frac{1}{2}}$. However this ratio also defines the refractive index, n, of the medium and experiment should confirm the

relation $n = \sqrt{\varepsilon_r}$. Measurements show, however, that in general, with the exception of simple non-polar gases, this relation does not seem to be valid since ε_r is found to be much greater than n^2. The reason for this is due to the fact that the refractive index is determined at optical frequencies, of the order of 10^{15}Hz, whereas the relative permittivity is usually measured at much lower frequencies. If the relative permittivity is measured as a function of frequency it is usually found to decrease, not gradually, but in a series of sharp drops at certain frequencies, until it approaches n^2, as illustrated in figure (2.6) below:-

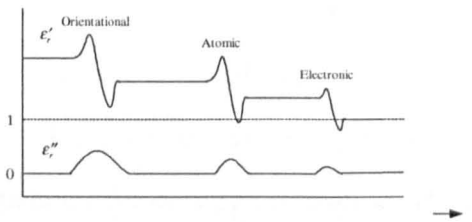

Figure 2.6 Variation of relative permittivity with frequency.

Associated with each drop in ε_r' there is a finite energy dissipation or dielectric loss ε_r''. These rapid changes in relative permittivity suggest that for each of the frequencies at which they occur, one of the polarisation mechanisms ceases to be operational due to the fact that the polarisation can no longer orientate at the same frequency as the applied electric field, thus the mechanism no longer makes any contribution to the relative permittivity. The limiting frequencies of the three mechanisms are related to the inertia of the respective entities. Typically, electronic polarisation exists up to about 10^{16} Hz, atomic polarisation up to about 10^{13} Hz while orientational polarisation may exist anywhere in the region from 10^2 Hz to 10^{10} Hz, dependent on the fluid and temperature.

There are two different causes that can give rise to the behaviour exhibited in figure (2.6), these are namely resonance absorption and dipole relaxation.

Resonance absorption is explained by imagining that any induced dipole consists of a positive and a negative charge, the simplest case being that of the nucleus and electron charge around it, which are bound together by elastic restoring forces. If the nucleus is considered as stationary the electrons are free to oscillate and will have a natural frequency of oscillation ω_0. The application of an alternating electric field sets such electrons into forced oscillation which can follow the field up until ω_0, beyond which the inertia of the electrons becomes dominant and the oscillations cease. This system is analogous to the mechanical problem of a driven simple harmonic oscillator.

If the dielectric material is subjected to an oscillating electric field $\underline{E} = \underline{E_0} e^{-j\omega t}$ [1] each electron in the atom, or molecule, is displaced a distance $\underline{x}$ by the field, and the restoring force is $\omega_0^2 \underline{x}$. In addition there will be a damping coefficient γ since there will always be some mechanism for energy dissipation. Hence the equation of motion is:-

$$m\frac{d^2\underline{x}}{dt^2} + \gamma\frac{d\underline{x}}{dt} + \omega_0^2\underline{x} = -e\underline{E_0}e^{-j\omega t}, \tag{2.35}$$

where m is the mass of the electron; and
$-e$ is the charge of the electron.

The solution of equation (2.35) (neglecting transient effects) is:-

$$\underline{x} = \frac{-e\underline{E}}{m\{(\omega_0^2 - \omega^2) - j\gamma\omega\}}. \tag{2.36}$$

The instantaneous electric dipole moment due to the displacement of the electron is $\underline{p} = -e\underline{x}$, and if there are n molecules per unit volume, the polarisation $\underline{P}$ is:-

$$\underline{P} = n\underline{p} = \frac{ne^2\underline{E}}{m}\frac{1}{\left(\omega_0{}^2 - \omega^2\right) - j\gamma\omega}. \tag{2.37}$$

For dense substances a correction for the differences between the local field and the external field may be applied in the same way as section 2.3, giving:-

$$\frac{\varepsilon_r - 1}{\varepsilon_r + 2} = \frac{n^2 - 1}{n^2 + 2} = \frac{ne^2}{3m\varepsilon_0}\frac{1}{\left(\omega_0{}^2 - \omega^2\right) - j\gamma\omega}, \tag{2.38}$$

where equations (2.12) and (2.21) have been used.

Due to the tendency to treat the electrical and optical frequency range as two separate fields of interest, the Clausius-Mossotti equation, equation (2.21), was formulated independently for the optical frequency range by Lorentz and also by Lorenz[2] , with the relative permittivity replaced by the square of the refractive index, as shown in equation (2.38). Equation (2.38) shows that both ε_r and n must be regarded as complex. If the real and imaginary parts are separated the resulting expressions may be plotted as a function of frequency, illustrated in figure (2.7) below:-

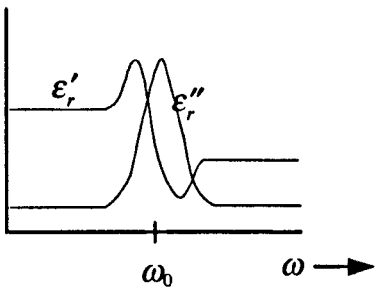

Figure 2.7 Resonance absorption.

Figure (2.7) shows that the real part of the relative permittivity, ε_r' , which is associated with the energy storage of the dielectric, has a high value at frequencies below ω_0 but

drops to a lower value above ω_0. The drop in energy storage can be seen to correspond to an increase in the energy loss of the dielectric, ε_r''. This type of resonance interaction could account for the decrease in relative permittivity shown in figure (2.6) where absorption of energy from the alternating electric field into the dielectric has taken place.

A change in relative permittivity with frequency implies that the refractive index is also frequency dependent. Thus the refractive index will behave similarly to the relative permittivity as a function of frequency. In the optical region, variation of the refractive index with frequency has been known for a long time, and is called dispersion. In general the refractive index increases with frequency, and this is called *normal dispersion.* The reverse case, where the refractive index decreases with increasing frequency, occurs only in the vicinity of an absorption line and is called *anomalous dispersion.*

At a sufficiently high frequency the only polarisation mechanism which remains is the electronic polarisation which usually has a resonance at about 10^{16} Hz. Therefore for all optical materials the relative permittivity and refractive index drop to a low value in the ultraviolet and there is a strong absorption, however the materials become transparent again as the X-ray region is approached.

The other effect which may give rise to a frequency dependent relative permittivity is called dipole relaxation, and occurs for polar molecules only. The relative permittivity for a polar dielectric will decrease if the orientation of the permanent dipoles is inhibited in some way. Again if an alternating electric field is applied the dipoles must be able to orientate themselves quickly enough to follow the field in order to make a full contribution to the polarisation. If this orientation takes a finite time τ, then the dipoles will not be able to follow a field whose angular frequency is such that $\omega\tau > 1$. In the region where $\omega\tau \approx 1$, the relative permittivity will decrease and absorption of energy will take place from the alternating electric field into the dielectric. The rate of energy

transfer, or decay of polarisation, is of the form $e^{-t/\tau}$, where τ is the characteristic relaxation time, and is proportional to the instantaneous value of polarisation. An expression for the polarisation of the dielectric may be obtained, which again may be shown to be complex, resulting in a complex relative permittivity. When the real and imaginary parts of the relative permittivity are plotted as a function of frequency a similar result to that shown in figure (2.7) is obtained, and ε_r' is shown to decrease rapidly in the region where $\omega\tau \approx 1$, while ε_r'' increases to a maximum in this region.

For non-polar gases and vapours, the relative permittivities are constant for all frequencies up to about 10^{16} Hz, the start of the infrared spectrum.

References

1. Bleaney, B.I. and Bleaney, B. *Electricity and Magnetism;* Clarendon Press, Oxford, 1959.
2. Von Hippel, A (Editor) *Dielectric Materials and Applications;* The Technonlgy Press of M.I.T., John Wiley and sons, Inc., New York, Chapman and Hall, Ltd. London, 1954.
3. Rosenberg, H. M. *The Solid State*; Oxford University Press Inc., New York, 3rd edition, 1995.
4. Scaife, B.K.P. *Complex Permittivity - Theory and Measurement;* The English Universities Press Ltd., London, 1971.
5. Frohlich, H. *Theory of Dielectrics: Dielectric Constant and Dielectric Loss;* Clarendon Press. Oxford, 2nd edition, 1958.

3. Choice of Experimental Technique

An overview is presented here of some of the most common and well established measurement techniques that are used to measure the relative permittivity of materials over the entire frequency spectrum.

The object of this chapter is to provide a general review of the measurement techniques with a view to explaining the choice of experimental technique that was adjudged to be most appropriate for the determination of the relative permittivity of fluids over an industrially relevant range of temperatures and pressures.

3.1 Measurement Techniques

Since the relative permittivity of a dielectric is a function of frequency, a complete determination of the property would involve characterisation over the entire spectrum from zero frequency up to and beyond optical frequencies. No single method of measurement covers this enormous range and as a result there exists a large number of different techniques; each having a specific range of frequencies for which they are most appropriate. Ideally the ranges of frequencies should overlap, enabling a complete coverage of the spectrum to be obtained. This ideal has almost been accomplished and work in recent years has concentrated on improving the established techniques of measurement, particularly in terms of accuracy and reproducibility[1].

Accordingly, the object of this section is to provide a general review of the well established and proven techniques rather than describe all the measurement techniques and variations thereof that are suitable for measurement over the entire frequency spectrum.

Dielectric measurement techniques may be subdivided into two general categories :-

- the frequency region where the dielectric under study may be considered as a lumped parameter component; and
- the region where the wavelength of the electric field is of comparable magnitude to the physical dimensions of the dielectric under study and, as a consequence, the dielectric ceases to behave as a lumped circuit component and is referred to as a *distributed parameter system.*

The transition from lumped to distributed parameter behaviour normally takes place within the range 200 to 600 MHz. Thus from this frequency upwards into the microwave and optical frequency regions the dielectric under study behaves as a distributed parameter system.

Dielectrics as lumped parameter systems have been explained in Chapter 2 by way of example of an equivalent parallel lumped component circuit where the characterisation of the sample under study is accomplished through capacitive measurements. However, over the distributed parameter frequency region dielectric measurement techniques are based on the relationship between the complex values of the propagation factor of the electromagnetic wave, the relative permittivity and the index of refraction.

In the case of a transverse electromagnetic wave (TEM wave) propagating in the x direction in a dielectric continuum of complex relative permittivity, ε_r, the electric, $\underline{E}$, and magnetic, $\underline{H}$, field vectors may be expressed as:-

$$\underline{E} = \underline{E_0} e^{j\omega t - \gamma x}, \text{ and} \tag{3.1}$$

$$\underline{H} = \underline{H_0} e^{j\omega t - \gamma x}, \tag{3.2}$$

where ω is the angular frequency;

t is the time;

x is the direction of propagation; and

γ is the complex propagation factor.

The complex propagation factor, γ, may be expressed as:-

$$\gamma = j\omega(\varepsilon_r \mu_r)^{1/2} = \alpha + j\beta, \tag{3.3}$$

where μ_r is the relative magnetic permeability of the dielectric material;

α is the attenuation factor of the electromagnetic wave; and

β is the phase constant of the electromagnetic wave.

In the case of isotropic non-magnetic dielectric materials $\mu_r = 1$.

The electromagnetic wave amplitude oscillates with a periodicity λ and may be illustrated as being enclosed between exponential envelopes determined by the attenuation constant α; as shown in figure (3.1a) below:-

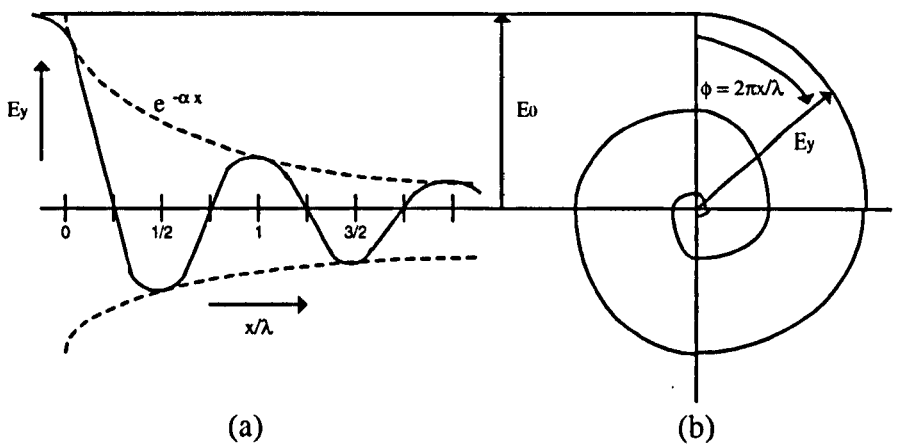

Figure 3.1 Electromagnetic wave in space.

Alternatively, in polar co-ordinates, the electromagnetic wave may be illustrated as a radius vector which, rotating clockwise with distance travelled, describes a logarithmic spiral; as shown in figure (3.1b) above, where the parameter x is replaced by the phase angle ϕ according to the relation $x/\lambda = \phi/2\pi$.

In vacuum $\alpha = 0$ and the propagation factor of equation (3.3) may be written as:-

$$\gamma_0 = j\omega(\varepsilon_0\mu_0)^{1/2} = j\beta_0, \tag{3.4}$$

where ε_0 is the permittivity of free space;

μ_0 is the permeability of free space.

If λ_0 is the wavelength in free space and λ is that in the dielectric medium, then the corresponding phase constants are $\beta_0 = 2\pi/\lambda_0$ and $\beta = 2\pi/\lambda$. Accordingly, the refractive index is:-

$$n = \lambda_0/\lambda = \beta/\beta_0. \tag{3.5}$$

For a non-magnetic loss-free dielectric medium the above simplifies to the well known Maxwell relation:-

$$n^2 = \varepsilon_r. \tag{3.6}$$

The refractive index is, of course, also complex and may be represented as:-

$$[n(1-jk)]^2, \tag{3.7}$$

where k is absorption index (attenuation per period) and is given by

$$k = \alpha\lambda/2\pi = \alpha/\beta.$$

From the foregoing equations, it can be shown that the real and imaginary values of the complex relative permittivity may be expressed as:-

$$\varepsilon_r' = \frac{\beta^2}{\beta_0^2} - \frac{\alpha^2}{\beta_0^2}$$

$$= n^2.\left(1 - \frac{\alpha^2}{\beta^2}\right), \tag{3.8}$$

and

$$\varepsilon_r'' = 2\alpha\frac{\beta}{\beta_0^2}$$

$$= n^2\frac{2\alpha}{\beta}. \tag{3.9}$$

When dielectric measurements on materials are performed with a waveguide, the electromagnetic waves may propagate in the TE or TM mode and the complex relative permittivity of the dielectric material is then proportional to the square of the ratio of the complex propagation factor of the electromagnetic wave in the dielectric material to that in vacuum, which can be expressed by:-

$$\varepsilon_r = \left(\frac{\gamma}{\gamma_0}\right)^2 + \left(\frac{\lambda_0}{\lambda_c}\right)^2, \tag{3.10}$$

where λ_c is the cut-off wavelength for the cross section of the waveguide for the propagation mode in question.

For TEM waves $\lambda_c = \infty$ and equation (3.10) reduces to $\varepsilon_r = \left(\gamma/\gamma_0\right)^2$. In terms of the more general expression, (3.10), the real and imaginary parts of the complex relative permittivity are given by:-

$$\varepsilon_r' = \lambda_0^2\left(\frac{\beta^2 - \alpha^2}{(2\pi)^2} + \frac{1}{\lambda^2}\right), \tag{3.11}$$

and

$$\varepsilon_r'' = \left(\frac{\lambda_0}{\pi}\right)^2 \cdot \left(\frac{\alpha\beta}{2}\right). \tag{3.12}$$

The dissipation factor of the dielectric material is equal to the tangent of the phase angle, δ, between the electric field vector, $\underline{E}$, and the resulting dielectric displacement vector, $\underline{D}$, or the ratio of the energy dissipated to 2π times that reversibly stored in the same dielectric volume per one half period of oscillation. The latter ratio, as shown in Chapter 2, is equivalent to $\varepsilon_r''/\varepsilon_r'$, or more conveniently at microwave frequencies:-

$$\tan\delta = 1/Q, \tag{3.13}$$

where Q is the electrical quality factor of the waveguide.

From the foregoing considerations, it is apparent that relative permittivity measurement techniques fall into one of two categories, according to whether the dielectric under study behaves as a lumped parameter component or as part of a distributed parameter system at the frequency of measurement. The various measurement techniques that encompass the frequency spectrum are illustrated schematically in figure (3.2)[1] below:-

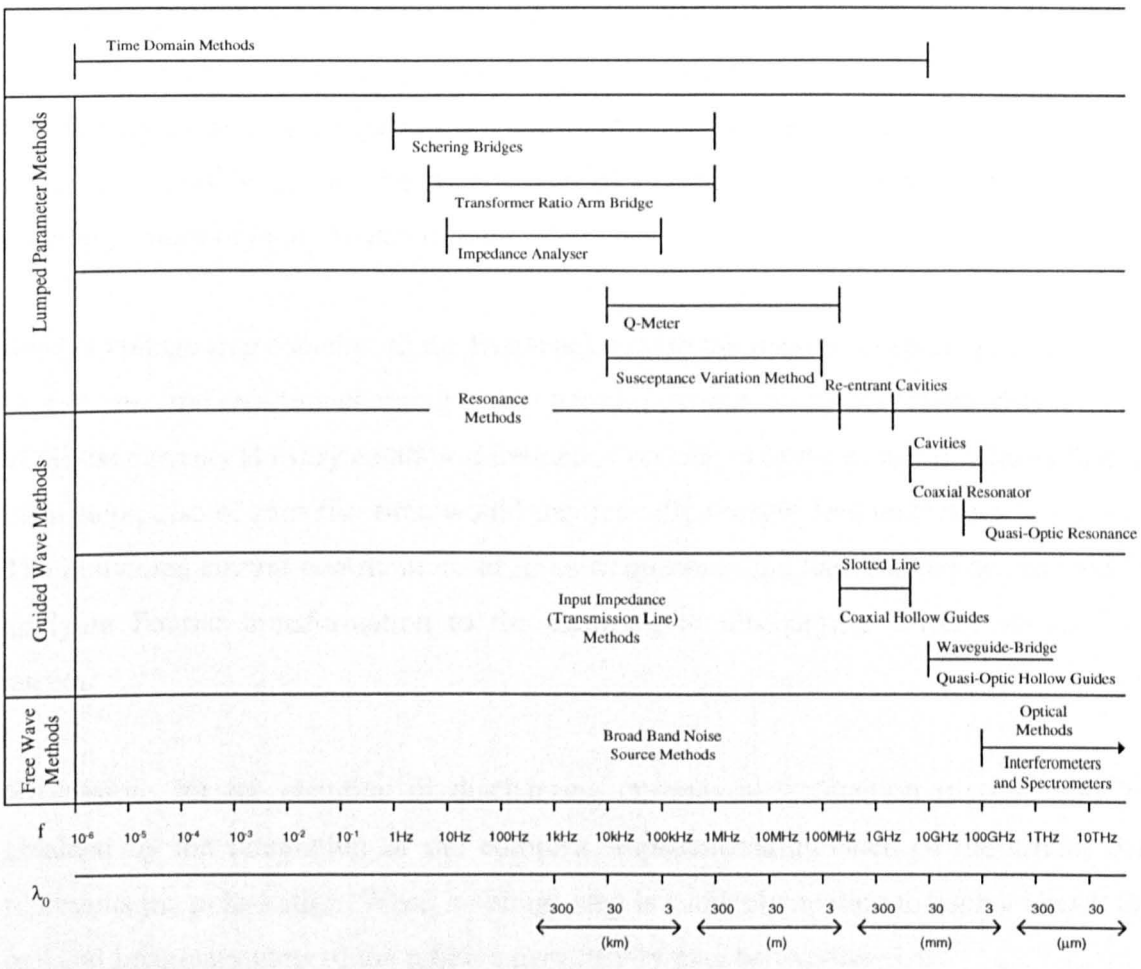

Figure 3.2 Measurement techniques over various frequency ranges.

More detailed descriptions of the various measuring techniques are given in the classic texts by Von Hippel[2], Scaife[3], Bartnikas[1] and de Vos[4]. Other useful summaries and

reviews are given by Frolich[5] and Bussey[6]. The object of this section, however, is to provide a general review of the well established techniques with a view to explaining the choice of experimental technique.

3.1.2 Measurements at Low Frequencies

Very low frequency measurements can reveal important information on the interfacial polarisation behaviour and provides a means for identifying the mobility and type of the conduction ions. The measurement technique is performed by applying a voltage step across the dielectric under study and subsequently observing the shape of the charging or discharging current as a function of time. The instantaneous value of the charging or discharging current defines the polarisation of the dielectric from which the complex relative permittivity may be determined.

Since a voltage step contains all the frequencies up to the maximum value determined by its rise time, the resulting charging or discharging current necessarily represents the sum of all the currents at every excitation frequency contained in the pulse. It follows that an ideal step pulse of zero rise time would theoretically contain frequencies up to infinity. The individual current contributions at these frequencies can therefore be determined by applying Fourier transformation to the charging or discharging current versus time curves.

Expressions for the charging or discharging currents as a function of time may be obtained by the integration of the complex impedance/admittance of the circuit that represents the polarisation. When a voltage step is suddenly applied to such a circuit the real and imaginary parts of the relative permittivity may be expressed as:-

$$\varepsilon_r'(\omega) = \int_0^{t_2} \phi(t)\cos\omega t\,dt + \frac{C_{t_2}}{C_0}, \text{ and} \qquad (3.14)$$

$$\varepsilon_r''(\omega) = \int_0^{t_2} \phi(t) \sin \omega t \, dt + \frac{G}{\omega C_0}, \tag{3.15}$$

where $\phi(t)$ is a current decay function describing the current flowing due to the voltage step applied at $t = 0$;

C_{t_2} is the capacitance at the upper frequency limit;

C_0 is the capacitance in vacuum; and

G is the conductance of the dielectric material.

It is evident that if the function $\phi(t)$ is sufficiently well characterised, the real and imaginary parts of the relative permittivity may be determined as a function of frequency.

Numerical methods are normally used to obtain the function $\phi(t)$ by integration of a large number of current-time measurements. This method necessarily restricts the upper and lower frequency limits, since the integrals of expressions (3.14) and (3.15) must be truncated to finite values of t. The lowest frequency limit is fixed by elapsed time of the measurement and the accuracy of the current measurement. The highest frequency limit is imposed by the rise time current measuring device and the smallest time interval between current measurement points.

The errors in the numerical method are primarily introduced because of the finite time interval of integration and also the uncertainty in the current rise/decay function $\phi(t)$.

3.1.3 Measurements at Intermediate Frequencies

Dielectric measurements in the intermediate frequency range from about 1 Hz to 1 MHz are commonly performed using $R-C$ (Resistance-Capacitance) bridge measurement techniques.

The Schering bridge is extensively used to perform dielectric measurements in this region since it can cover the entire specified frequency range without serious impairment of accuracy. In practice a substitution method of measurement, as illustrated in figure (3.3), is employed because of its greater accuracy.

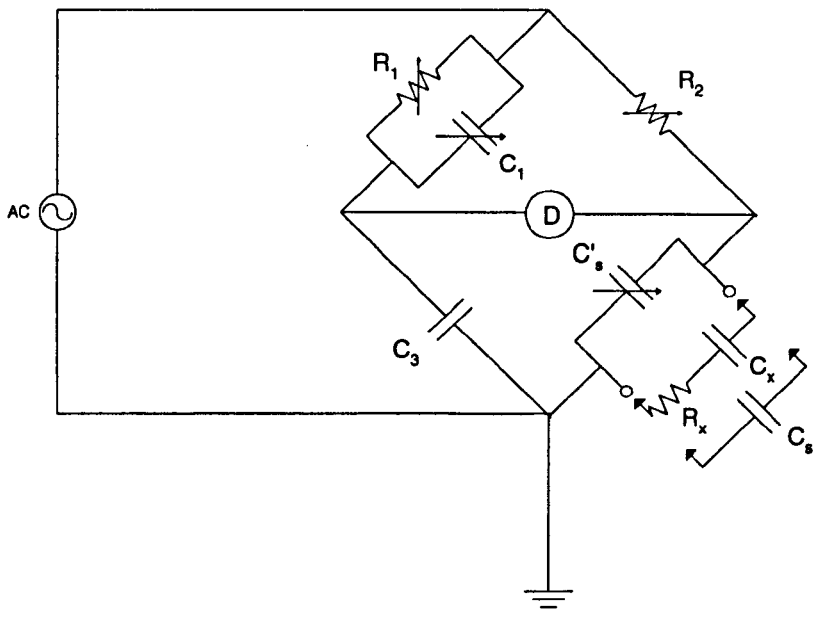

Figure 3.3 Schering bridge for substitution measurements.

When dealing with $R-C$ bridges, it is necessary to take into account various stray effects between the R and C elements themselves as well as those between the elements and ground. The stray capacitances between the elements themselves and ground give rise to shunting effects between the different bridge arms and ground, which introduce unpredictable errors into the measurement.

There are essentially two methods for reducing or eliminating the stray capacitance effects in $R-C$ bridges. One approach involves the use of shields by surrounding the bridge arms in metallic containers that are either grounded directly or maintained at a constant potential. The screening modifies the value of the element itself: with a

capacitor the effect is merely to alter the effective capacitance for which corrections may be taken into account in calibration. With a resistor the effect is to add a small parallel capacitance to the element which results in the element having a frequency dependent complex impedance. The other approach is to employ a *Wagner earth* connection in the bridge circuit to completely eliminate the effect of stray capacitance formed between the detector and ground. The Wagner's earth technique consists of two auxiliary bridge arms, of variable impedance. By repeatedly balancing the bridge with and without the Wagner earth connection in place, the potential across the detector is nullified and the stray capacitance effects between the bridge arms and ground are eliminated. A disadvantage of this method is that the successive balances are time consuming and tedious.

As illustrated in figure (3.3), with a standard capacitor, C_s, in the circuit a bridge balance is obtained by manipulating R_1 and C_1 with C_s' set to a value C_{s1}'. Subsequently C_s is replaced with the dielectric specimen and only C_s' is varied to obtain a balance at a value C_{s2}'. Obviously, since no changes have been effected in the impedances of the other arms, the capacitance in the measurement arm must be equal for the two respective balance steps; that is:-

$$C_s + C_{s1}' = C_x + C_{s2}', \tag{3.16}$$

from which the specimen capacitance is easily determined. Thus the stray capacitive coupling effects and uncertainties in component value are cancelled out since the difference between the capacitance of the specimen and standard capacitor is determined solely in terms of the change in the value of the standard capacitor.

For more accurate measurements of this type a three-terminal capacitor design is frequently used. The guard ring eliminates fringing effects at the edges of the electrodes

and also largely eliminates the dependence of the unknown capacitance of the leads which connect the test capacitor to the bridge.

From the nature of the balance equations of the Schering bridge, it can be perceived that the balance condition is determined by expressions that are ratios, differences or products of resistances and capacitances. It has been recognised for some time that precise measurements may be performed using a transformer arrangement that effectively constitutes an inductively coupled voltage divider, whose ratio is more accurately determined and stable than any possible combination of resistors and capacitors. Indeed ratio accuracies of a few parts per million may be possible[1].

Cole and Gross[7] where one of the first to utilise this technique for dielectric measurements and their basic circuit is illustrated in figure (3.4) below:-

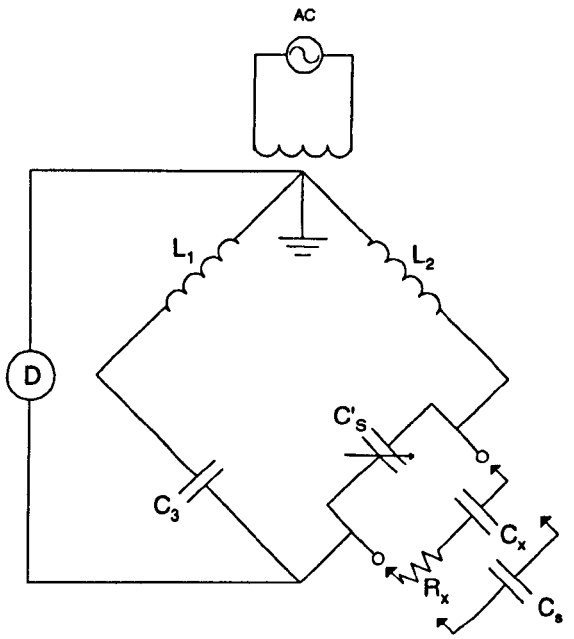

Figure 3.4 Transformer ratio arm bridge.

The $R-C$ arms 1 and 2 of the Schering bridge have been replaced with two inductive ratio arms which have very nearly unity coupling.

With the junction of the ratio arms grounded any impedance placed across one arm appears across the other due to the nearly unity coupling between the two inductive arms, L_1 and L_2. Hence the balance of the bridge is not affected, thereby disposing of the use of guard circuits and their balancing requirements.

Because of their precision and accuracy, bridge-type measurements have been used more extensively than impedance analyser-type measurements. Due to the fact that bridges require long balancing times and a relatively large number of precision-adjustable components, the use of impedance analysers were primarily used in cases where lower accuracy and shorter measurement time were of prime importance. However the situation has changed significantly with the advancement of computers and digital technology.

An alternating current (AC) circuit-impedance analyser may be employed to measure the absolute value of impedance of the simple electric circuit represented by the capacitive reactance of the test capacitor at the particular test frequency in parallel with an equivalent resistance or conductance representing insulator resistance and dielectric loss. Knowledge of the operating frequency, between 10 Hz and 100 kHz, in this instance, enables the specimen capacitance to be determined. The errors introduced due to the effects of residual resistance and inductive reactance associated with the connecting leads must be taken into account when undertaking measurements of high accuracy. Most modern impedance analysers have features which enable residual impedance to be measured and compensated for automatically by measuring in the open-circuit condition in the case of capacitance determination.

The performance of commercial impedance analysers of the highest specification is typically 0.05% absolute uncertainty although their ability to detect small changes, their

resolution, will in some cases be much better. Hence the change in impedance/capacitance which could be reliably detected with this type of instrument is potentially of the order 0.005%, or 50 ppm, provided the frequency stability of the instruments internal source is of a sufficiently high standard.

3.1.4 Measurements in the Upper and High Frequency Range

For dielectric measurements above 1 MHz bridge techniques are generally not used because of the errors introduced by residual impedances. When measurements are carried out within the range of 100 kHz to 200 MHz, resonant techniques are commonly employed.

The various resonant circuits used for dielectric measurements comprise and inductor and a standard capacitor, which together form a closed circuit. At these frequencies micrometer electrodes are required to avoid the errors arising from residual impedances. The micrometer electrode system eliminates the errors caused by series inductance and resistance of the connecting leads and the measuring capacitor at high frequencies by maintaining the inductance and resistance constant regardless of whether the dielectric sample is in the circuit or not. An example of this type of circuit is the Q-meter (resonant rise) circuit, illustrated in figure (3.5) below:-

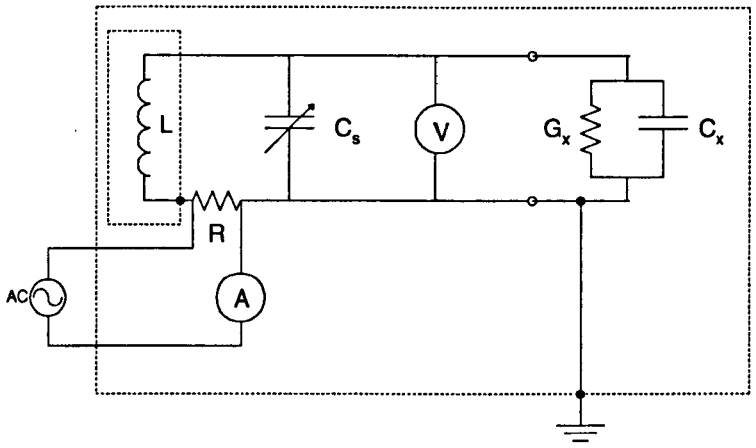

Figure 3.5 Q-Meter (resonant rise) circuit.

The Q-meter may be tuned to resonance either by the adjustment of C_s or the frequency of the generator. In order to attain resonance in the particular frequency range of interest, a number of inductive coils, L, of varying inductance, or, variable standard capacitors, C_s, may be used. The electrical quality factor, Q, of the circuit is defined by the ratio of the peak voltage V_0 across the generator to the peak voltage across the inductor, V_L, such that at resonance:-

$$\frac{V_0}{V_L} \approx \left(1+\omega^2 L^2/R^2\right)^{1/2},$$

$$\approx (1+Q), \tag{3.17}$$

where ω is the frequency of the generator;

L is the inductance of the inductor;

R is the resistance of the resistor; and where $\omega L/R$ has been substituted with Q.

Thus for large electrical quality factors $V_0/V_L \approx Q$. With the dielectric specimen connected to the Q-meter the circuit is tuned to resonance and the values C_s' and V_L' noted and Q' determined. The specimen is then removed and the circuit is re-tuned, and the new values C_s and V_L noted. The capacitance of the dielectric material is given by the difference between the capacitance values of the variable standard:-

$$C_x = C_s' - C_s, \tag{3.18}$$

and the dissipation factor may be expressed as:-

$$\tan\delta = \frac{1}{Q_x}, \tag{3.19}$$

where $\frac{1}{Q_x} = \frac{C_s'}{C_x}.\left[\frac{1}{Q} - \frac{1}{Q'}\right]$.

The accuracy of the Q-meter method for capacitance and dissipation factor is typically 0.1% and 2% respectively[1].

An alternative technique to the Q-meter method is that of the susceptance variation method. This method, originally developed by Hartshorn and Ward[8], makes use of the fact that the shape, in particular the width, of the resonance curve of a resonant circuit is a measure of the dissipation factor of the circuit and dielectric loss of the material under study. The simplified Hartshorn and Ward circuit is illustrated in figure (3.6) below:-

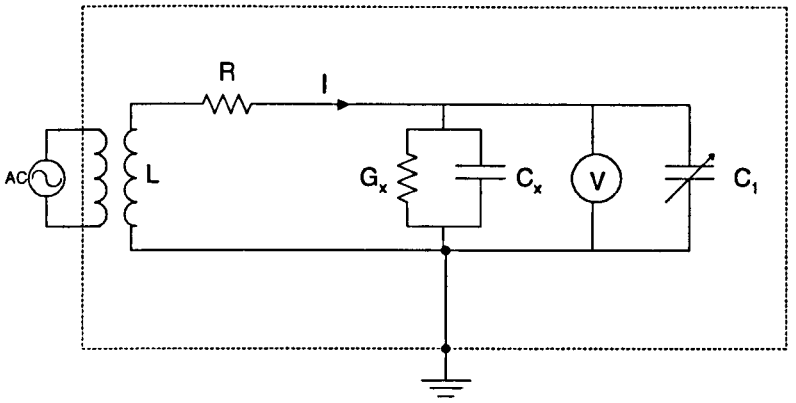

Figure 3.6 Simplified Hartshorn and Ward circuit.

The generator is loosely coupled to the measurement circuit so that the frequency of the generator is unaffected by the measurement circuit. However present designs do not use this approach, and the generator input is directly connected across the measuring circuit in series with a variable capacitor. By variation of the generator frequency or the capacitance around the resonance value, two resonance curves may be defined, as illustrated in figure (3.7) below, one for the tuned circuit on its own and one for the circuit including the dielectric material.

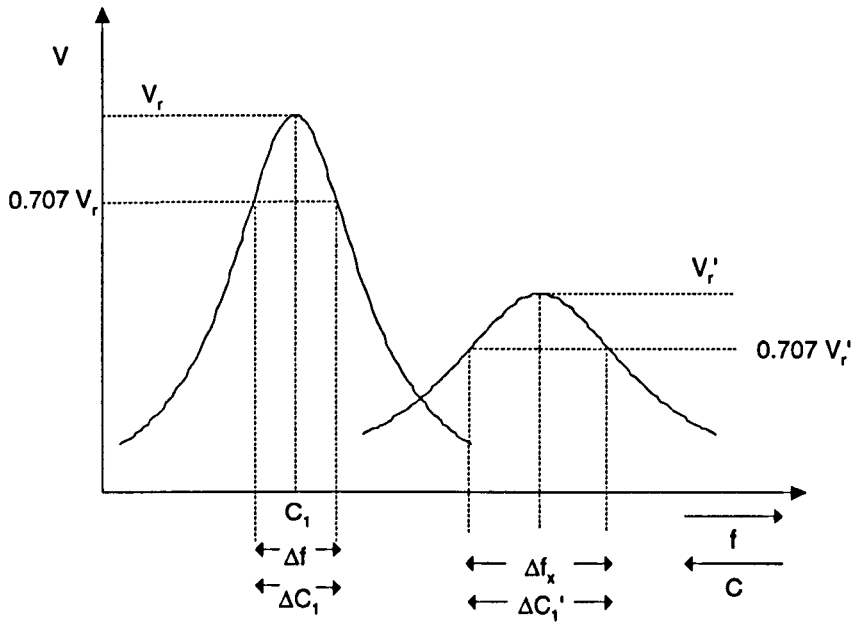

Figure 3.7 Resonance curve of Hartshorn and Ward circuit.

From the measurements illustrated in figure (3.7) both capacity and dissipation factor can be determined.

In the capacitance variation measurement procedure with this circuit, the first step with the dielectric sample disconnected consists of tuning the circuit to resonance with capacitor C_1 and noting the corresponding voltage V_r. The circuit is then detuned on both sides of resonance with C_1 (an additional vernier capacitor may be used for these small capacitance changes) until the voltmeter indicates the half power points, $\frac{V_r}{\sqrt{2}}$, and the two readings of the variable capacitor, C_{1_1} and C_{1_2} are noted. The same procedure is then repeated with the dielectric sample connected in the circuit, and the corresponding values of C_1', C_{1_1}', C_{1_2}' and V_r' are noted. The capacitance of the dielectric material is given by the difference between the capacitance values of the variable standard at resonance:-

$$C_x = C_1 - C_1^{'}, \tag{3.20}$$

and the dissipation factor may be expressed as:-

$$\tan\delta = \frac{\Delta C_1 - \Delta C_1^{'}}{2.C_x}, \tag{3.21}$$

where ΔC_1 is the difference in half power capacitance values with the dielectric sample disconnected; and

$\Delta C_1^{'}$ is the difference in half power capacitance values with the dielectric sample connected.

The frequency variation method uses the same circuit as above and results in similar expression for capacitance and dissipation factor.

The accuracy of the susceptance variation is generally equal to that of the Q-meter method[2].

As the frequency of measurement increases, the inductance must necessarily decrease as the square of frequency, since the capacitance in the circuit is approximately constant. Indeed, at frequencies in excess of 100 MHz, the inductance coils may consist of a single loop of wire or a portion thereof. Below a limiting value the dissipation factor of the total inductance of the circuit increases rapidly to a value that renders the circuit useless for measurement purposes. This situation can be avoided up to 500 MHz and possibly a several GHz by using a re-entrant cavity.

Works, Dakin and Boggs[9] developed a re-entrant cavity for solid dielectric measurements at 500 MHz. The micrometer electrode system is placed along the axis of a cylindrical cavity, thus producing a line shorted at both ends. The resonant frequency

is dependent on the geometry of the cavity and the loading capacitance of the micrometer electrode system. Such cavities are generally designed to have low dissipation, or high Q values. Coupling into and out of the cavity is achieved by two antennae. The use of a re-entrant cavity is the first step in the transition from a lumped to a distributed parameter system. The inductance and part of the tuning capacitance are distributed, whereas the measuring capacitance is lumped. The measuring technique is identical to that of Hartshorn and Ward.

3.1.5 Measurements in the High Frequency Range

The methods described in the previous section give rise to errors which steadily increase with increasing frequency. Corrections for these frequencies may be made, but even so a limiting frequency is eventually reached where errors arise due to the spatial variation of the electromagnetic field intensity and the dielectric material must be considered as part of a distributed parameter system. Depending upon the frequency range of interest, the dielectric material may be contained within a coaxial line, an open or closed resonator, in a waveguide, or in a free space path.

The most common technique for characterising dielectric materials in the frequency range from 300 MHz to 5 GHz involves the transmission line approach. Present day measurements are essentially based on the shorted coaxial line method by Roberts and Von Hippel[1]. This method of measurement is illustrated with a hollow transmission line in figure (3.8) below:-

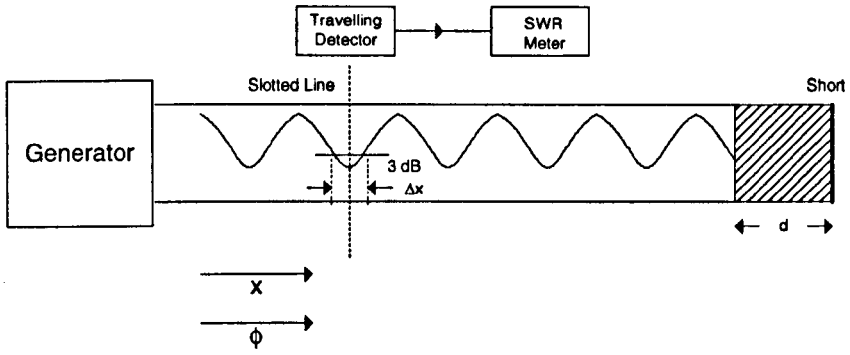

Figure 3.8 Standing wave pattern within slotted line shortened transmission line.

In this measuring system the dielectric sample under study is contained at the end of the shortened transmission line. Electromagnetic waves of a particular frequency are radiated into the transmission line and reflections caused by the impedance mismatch between the dielectric sample and the line result in a standing wave pattern being set up in the line. The standing wave pattern is measured by a movable probe detector mounted on a slotted line along the axis of the transmission line. The real and imaginary parts of the relative permittivity are determined in terms of the ratio of the electric field strength in the node and antinode and the distance of the first node from the surface boundary of the dielectric sample.

The impedance of the terminating short circuit is transformed through the dielectric material and is given by[2]:-

$$Z = \left(\frac{j\omega\mu_0}{\gamma} \right) \tanh(\gamma d), \tag{3.22}$$

where γ is the complex propagation factor of the electromagnetic wave in the dielectric material, which is defined in expression (3.10).

The complex propagation factor, γ, may be obtained if the input impedance, Z, of the transmission line is measured; subsequently the complex relative permittivity, ε_r, may be determined from expression (3.10). The impedance at the sample face, for a lossless line, is measured by the probe as:-

$$Z_{meas} = f\mu_0\lambda_g\left(\frac{1-jS\tan\phi}{S-j\tan\phi}\right), \tag{3.23}$$

where λ_g is the wavelength in the line;

ϕ is the phase distance from an electric field node; and

S is voltage standing wave ratio (VSWR).

The VSWR, S, is determined, as illustrated in figure (3.8), in terms of the width of the nodes, Δx, at the 3 dB points and may be expressed as:-

$$S = \frac{\lambda_g}{\pi\Delta x}. \tag{3.24}$$

Therefore, in the measurement procedures, after the VSWR, S, and phase distance, ϕ, parameters are determined, the input impedance, Z, may be equated from which the complex propagation factor of the electromagnetic wave in the dielectric material, γ, and in turn the complex relative permittivity, ε_r, may be deduced.

The accuracy of shortened coaxial line method can be within $\pm 1\%$ for relative permittivity and $\pm 200\mu m$ for dielectric loss[1].

For measurements above 5 GHz resonant cavity methods are generally used. Essentially a resonator may be viewed as a transmission line which is shorted at both of its ends, with the separation between the ends being an arbitrary multiple of half wavelengths.

Upon insertion of a dielectric material into the resonator the resonator wavelength changes; therefore the frequency or dimensional shift necessary to re-establish resonance is a measure of the dielectric properties of the material. As a result of the high values of Q which are intrinsic with well designed cavity resonators, the resonant cavity is particularly suited for the measurement of low loss dielectrics. From the above consideration, it is apparent that any individual resonator will be a relatively narrow band device, with the measurement frequency range dependent upon the resonator geometry, the dielectric properties of the material, and its location within the resonator.

Possibly the most commonly used cavity resonator to perform dielectric measurements in this frequency range is the rectangular cavity type[10]. The cavity as used in the perturbation technique is illustrated in figure (3.9) below:-

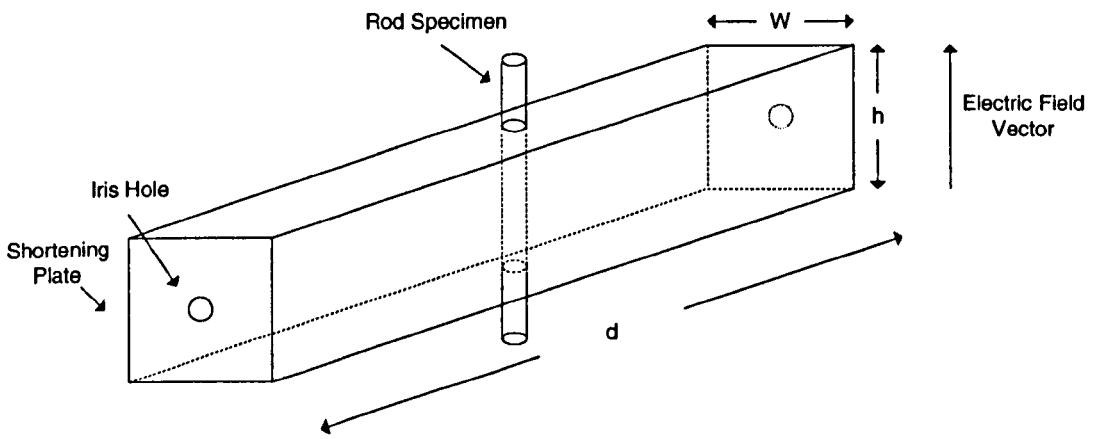

Figure 3.9 Rectangular cavity resonator.

The resonant frequency of the empty closed cavity is determined by the geometry of the cavity as well as the odd number, N, of half-waves along the cavity, and may be expressed as:-

$$f_0 = 15\left[\left(\frac{1}{w}\right)^2 + \left(\frac{N}{d}\right)^2\right]^{1/2}, \tag{3.25}$$

where w and d are the width and length of the cavity.

From above it can be seen that the as the frequency is increased the size of the cavity must necessarily decrease. The size of the iris holes in the transmitting and detecting ends of the waveguide are generally optimised. A cavity with a high Q and minimal loading effects requires a small iris, whereas a higher signal-to-noise ratio of the output power signal would be achieved with a larger iris opening.

The quality factor, Q_0, of the empty resonant cavity may be expressed as:-

$$Q_0 = \frac{f_0}{\Delta f_0}, \tag{3.26}$$

where f_0 is the central resonant frequency of the resonant curve; and

Δf_0 is the half-power bandwidth of the resonant curve at the 3 dB points.

Similarly, the quality factor, Q_{ε_r}, of the dielectric filled cavity may be expressed as:-

$$Q_{\varepsilon_r} = \frac{f_{\varepsilon_r}}{\Delta f_{\varepsilon_r}}. \tag{3.27}$$

The relative permittivity and the dissipation factor of the dielectric material are calculated in terms of Q_0, Q_{ε_r}, f_0 and f_{ε_r}:-

$$\varepsilon_r = \left(\frac{V_C\left(f_0 - f_{\varepsilon_r}\right)}{2.V_{\varepsilon_r}.f_{\varepsilon_r}} \right) + 1, \tag{3.28}$$

and

$$\tan\delta = \frac{\left[\frac{V_C}{4.V_S}\cdot\left(\frac{1}{Q_{\varepsilon_r}}-\frac{1}{Q_0}\right)\right]}{\left[\left(\frac{V_C\left(f_0-f_{\varepsilon_r}\right)}{2.V_S\cdot f_{\varepsilon_r}}\right)+1\right]}, \tag{3.29}$$

where V_0 is the volume of the empty cavity; and

V_S is the volume of the dielectric material.

In the case where the dielectric material under study completely fills the resonator the relative permittivity and the dissipation factor of the dielectric material are given by[11]:-

$$\varepsilon_r = \left(\frac{f_0}{f_{\varepsilon_r}}\right)^2, \tag{3.30}$$

and

$$\tan\delta = \frac{1}{Q_{\varepsilon_r}} - \frac{1}{Q_0} \tag{3.31}$$

Waveguides and resonant cavities of the type described above become impractical at very high frequencies, where the wavelengths fall in the millimetre range, due to excessively high attenuation losses. Also, the physical size of the apparatus become overly small and impractical for most applications. In this range of frequencies optical

methods employing free travelling waves become most efficient for dielectric measurement purposes.

In the millimeter wavelength region, the free-space waveguide-bridge method is quite commonly used for dielectric measurements. The measurement procedure involves the insertion of the dielectric material between two waveguide transmitter/detectors in one arm of a balanced bridge. The resultant phase shift and insertion loss of the bridge circuit are measured by means of a precision phase shifter and attenuator positioned in the other arms. With the condition that the material is rotated in the plane of incidence so that the incidence angle is set equal to Brewster's angle reflections between the material and the waveguide transmitter/detectors can be virtually eliminated. Under such circumstances, the relative permittivity and the dissipation factor of the dielectric material are given by:-

$$\varepsilon_r = 1 + 2\left(\frac{\Delta\phi}{d_s}\right)\cos\theta + \left(\frac{\Delta\phi}{d_s}\right)^2, \tag{3.32}$$

and

$$\tan\delta = \frac{\lambda \ln\left(\eta\left(\varepsilon_r - \sin^2\theta\right)^{1/2}\right)}{\varepsilon_r \pi d_s}, \tag{3.33}$$

where d_s is the thickness of the dielectric material;

$\Delta\phi$ is the phase shift in the same units as d_s;

λ is the wavelength in the same units as d_s;

θ is the angle of incidence (Brewster's angle); and

η is the voltage transmission coefficient.

The waveguide-bridge technique yields satisfactory results up to nearly 100 GHz.

Above 50 GHz quasi-optical and optical methods become superior to all other techniques.

Quasi-optical measurement techniques have included the use of optical cavity resonators. Optical resonators are similar to other resonators, in that the length of the resonator represents a large number of wavelengths and the dielectric material, which is in the form of a sheet, assumes only a fraction of the overall length. The tuning of the resonator may be accomplished by variation of the geometry or excitation frequency.

One type of optical resonator is the confocal resonator, which is based on the classical Fabry-Pérot interferometer. The confocal resonator is illustrated in figure (3.10) below:-

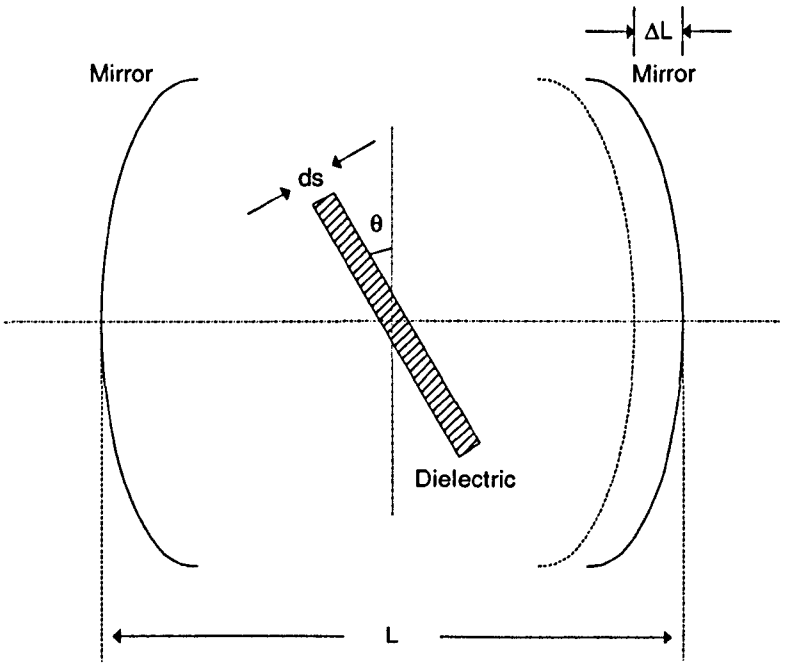

Figure 3.10 Confocal optical resonator.

The resonant frequency is perturbed by the insertion of the dielectric material into the cavity and the resonant frequency is again restored by moving one of the mirrors inward by a distance ΔL. The dielectric material is inserted at an angle to eliminate standing wave effects by allowing the reflected waves from the air/dielectric interface to escape the resonator. This procedure is unsuitable for dissipation factor measurements as the power escaping from the resonator lowers the Q of the resonator and subsequently obscures the change in Q produced by the perturbation.

As resonance is restored by moving one of the mirrors inward by a distance ΔL following insertion of the dielectric material, the real value of the refractive index may be expressed as:-

$$n' = \left(\frac{\varepsilon_r'}{\varepsilon_0}\right)^{1/2},$$

$$= 1 + \frac{\Delta L}{d_s}, \tag{3.34}$$

where d_s is the thickness of the dielectric material (note expression (3.34) has been approximated for a *thick* dielectric material).

The confocal optical resonator has been used successfully up to approximately 350 GHz[1].

Dielectric measurements at frequencies above 70 GHz are generally achieved with true free space optical techniques, which permit the use of larger dielectric specimens and have less dimensional restrictions. In fact, between 300 to 3000 GHz optical methods become compulsory. Since the infrared wavelength region extends from approximately $1\,mm$ to $100\,\mu m$, infrared sources and detectors must be employed.

A conventional method for dielectric measurements in this frequency range is through the use of a Michelson interferometer. One example of this technique, as developed by Breeden and Shepard[1] is illustrated in figure (3.11) below:-

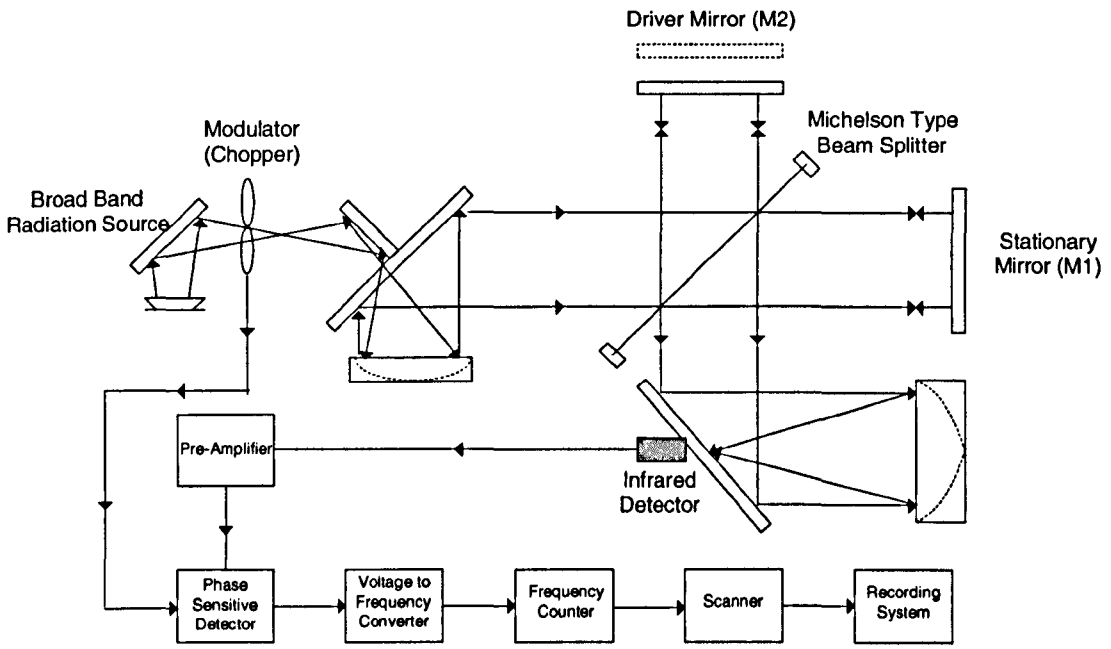

Figure 3.11 Spectrometer arrangement with Michelson beam splitter.

Bremsstrahlung emission of the vapour discharge is commonly used as the broad band radiation source. Since the radiated power is of a very low level, efficient optical systems and sensitive detectors are required.

In this interferometer the radiation from the broad band source is divided into two paths of variable length and recombined at an infrared detector whose output can be recorded as a function of differential length in the two paths. The modulated radiation from the source is separated at the beam splitter and reflected from the mirrors M1 and M2 to the detector. Since the position of M1 is held fixed, the path length of the radiated beam to this mirror is also constant. In contrast, the mirror M2 is moved at a constant speed

starting from a reference length point, L_0, that corresponds to a zero path difference with respect to the radiation of the path of M1. Thus the transmitted radiation power is recorded as a function of the path difference in L from the reference point L_0. A plot of the power versus L is termed an *interferogram*; the power spectrum of the incoming radiation is therefore given by the Fourier transform of the interferogram.

In the measurement procedure, the zero path difference point of the mirror M2 is established by observing the position of M2 corresponding to the maximum detected power. The dielectric material under test is then inserted into the beam path of M1 which results in a path length change in L or phase shift which is determined by adjusting the mirror M2 to yield the new maximum power position. The phase shift due to the insertion of the dielectric material into the beam path has been shown to be[1]:-

$$\phi_s = \left(\beta_0 - \beta_{\epsilon_r}\right)d_s - \phi, \tag{3.35}$$

where β_0 and β_{ϵ_r} are the phase constants expressed in equation (3.5);

d_s is the thickness of the dielectric material; and

ϕ is the phase angle of the system.

The phase shift introduced into the beam path of mirror M2 by moving it by an amount equal to ΔL is given by:-

$$\beta_0 \Delta L, \tag{3.36}$$

so that the value ΔL for maximum detected power is defined by equating expressions (3.35) and (3.36) and whereby it follows that the refractive index may be expressed as:-

$$n = 1 + \frac{\Delta L}{d_s} - \frac{\phi}{\beta_0 d_s}, \tag{3.37}$$

For a relatively thick dielectric material, the term $\frac{\phi}{\beta_0 d_s}$ tends to zero and since $\varepsilon_r \approx n^2$, the relative permittivity is shown to be:-

$$\varepsilon_r \approx \left(1+\frac{\Delta L}{d_s}\right)^2 . \tag{3.38}$$

Experimentally the power distribution spectrum is recorded as a function of path length. The power distribution spectra with and without the dielectric material inserted are recorded graphically, and the displacement between the two maxima of the respective spectra is equal to ΔL.

3.2 Choice of Experimental Technique

The factors considered in selecting the most appropriate experimental technique for making precise measurements of the relative permittivity of high value fluids over an industrially relevant range of temperatures and pressures were as follows:-

- The precision of the measurement technique.
- The suitability of the measurement technique for use with fluids above ambient pressure.
- The suitability of the measuring technique for use both in the laboratory and for on-line measurements.
- Manufacturing considerations.
- Practical considerations including robustness, ease of assembly and operation.
- Cost and availability of the associated instrumentation.
- Further development costs.

Of the numerous relative permittivity measurement techniques only two were considered to be suitable for the application under consideration here. The two techniques selected by NEL were:-

- the transformer ratio arm bridge with a concentric-cylinder capacitor arrangement; and
- the re-entrant cavity resonator with a swept-frequency generator or as part of feedback oscillator arrangement.

The transformer ratio arm bridge technique comprises two identical cylindrical capacitors, one maintained under vacuum while the other is filled with the dielectric fluid under study. The four-arm AC bridge circuit is employed with the capacitors forming two arms of the circuit.

Besides the properties of the capacitors (or cells), the method relies heavily upon the ratio transformer component which is difficult and costly to manufacture. This component is also found in precision resistance-comparator bridges such as are used in thermometry. Commercial transformer ratio equipment is available with resolutions down to 1 part in 10^8.

The concentric-cylinder three-terminal capacitor, as developed by the National Bureau of Standards (NBS)[11], was considered to be the most appropriate for the trasformer-ratio technique. This type of capacitor comprises three concentric cylinders (electrodes) electrically isolated from each other, and separated by some 3 and 4 mm respectively. The solid inner cylinder is electrically grounded and fastened to a metal block which encloses the entire capacitor and acts as an electrical shield. The diameter of the inner post is stepped in such a manner that the two outer-cylinders can be mounted coaxially on the same. Electrical insulators are fixed to the stepped surfaces of the central post and isolate all three cylinders from each other. Electrical connection to the middle cylinder is formed by a lead passing down through a hole in the central cylinder then out through a

radial hole to the inner surface of the cylinder. The designs are such that no solid insulation appears in the annular gap between the middle and outer cylinders. The surfaces of such capacitors are plated with gold to reduce losses arising from oxide films on their surfaces.

Manufacturing difficulties exist with the concentric-cylinder capacitor through the requirement for four electrical insulators. Materials previously used by NBS, such as high-density poly-propelene, would not be suitable for use with natural gas mixtures, and an alternative readily-machined material, with known physical properties such as quartz, would be required. The influence of temperature on the capacitance of the measurement cell would be minimised through the use of Invar for all metal parts. The residual effects of temperature on the cell capacitance would be calculable, provided an insulating material with known thermal expansion coefficient is used for its fabrication.

Though the overall geometry of the cell is relatively simple, it comprises a significant number of components and there was some doubt as to whether a sufficiently reliable theoretical model could be developed to account for the dilation of the cell with pressure. The influence of pressure on the cell capacitance would probably have to be established through calibration with a gas of known electrical characteristics, such as helium.

A practical disadvantage of capacitive type cells is that, due to the presence of the electrical insulators, there is a poor thermal path between the containment vessel and the inner electrodes.

Properly implemented, the transformer ratio technique with a suitable concentric-cylinder capacitor arrangement, could yield extremely high precision in the laboratory environment being similar to what has been, and is still used, in capacitance standards work. However, it was believed to be completely inappropriate as the basis of an on-line measuring instrument.

Re-entrant cavity resonators have been used for the accurate measurement of the complex relative permittivity of solid insulators. More recently, they have been developed for accurate measurement of the relative permittivity of fluids and fluid mixtures[12, 13]. They are also widely used in the communications industry (e.g. TV transmitters) as bandpass filters.

Resonators reported in the literature are self-contained pressure vessels which can be filled with the pressurised test fluid. They are fabricated using only metal parts, a gold O-ring seal and glass-insulated feed-through electrical connections. Externally, the resonator is of cylindrical form. Internally, the dielectric fluid under test fills a volume consisting of two separate toroidal sections. The first of these has a relatively large annular gap, of some 20 mm, which at RF frequencies behaves as an inductor, and the second, with a 1 mm annular gap, which behaves as a capacitor. The inductive section is provided with two antenna: one of which acts as a transmitter and couples an external RF source to the cavity; the second, acts as a receiver and couples the magnetic component of the internal field out of the cavity to an external detection system.

Re-entrant cavity resonators have particular advantages over other designs in that they have only two resonant modes, each well separated in frequency, and that the principal, or first frequency, mode is both stable and non-degenerate.

Detailed theoretical models have been developed for such re-entrant cavities and are applicable for use with dielectric fluids having both high relative permittivites and high loss factors. Provided the Q of the re-entrant cavity is sufficiently high, and the dimensions of the dielectric filled cavity are the same as those of the evacuated cavity at the same temperature of measurement, the relative permittivity of the dielectric fluid can be derived to a precision of better than 1 ppm solely from measurements of the resonance frequencies.

The Q factor of the re-entrant cavity would be optimised geometrically and enhanced by electroplating the inner surfaces of the resonator with a high-conductivity material.

The dimensional stability of the cavity is influenced by the dilation of the cavity with temperature; the dilation of the dielectric filled cavity with applied pressure; and the effective dilation of the dielectric filled cavity due to a change in the penetration depth of the electromagnetic field into the metal surfaces of the cavity.

The effects of temperature on the dimensional stability of the re-entrant cavity would be quantified by characterising the vacuum resonant frequency of the cavity over the range of temperatures under consideration. The small number of components and simple geometry allows the effects of pressure to be simulated and accounted for through the use of finite element analysis together with the above-mentioned theoretical model. Similarly, the effective dilation of the cavity due to a change in penetration depth can be accounted for with the theoretical model.

An advantage of the re-entrant cavity is that it is relatively simple to manufacture and assemble.

The re-entrant cavity resonator can act as a passive transmission element and be driven through resonance with a swept-frequency generator, or it can act as the frequency determining element of a feedback oscillator circuit arrangement.

The availability of relatively low-cost, synthesised-frequency, sources is advantageous for laboratory measurements with the re-entrant cavity, but would be difficult to exploit as the basis of an on-line instrument.

An on-line instrument must be simple to operate, relatively compact, robust and considerably less expensive; particularly if it is to be widely deployed. In order to satisfy the above criterion, the re-entrant cavity resonator would be incorporated into a feedback

oscillator circuit as the frequency determining element. The on-line instrument would be maintained in continuous oscillation very close to its natural resonant frequency with relatively in-expensive modular electronic components and measured with a frequency counter.

An intercomparison between the transformer ratio arm bridge with a concentric-cylinder capacitor arrangement; and the re-entrant cavity resonator with a swept-frequency generator or as part of feedback oscillator arrangement; is given in table (3.1) below:-

Issue	Technique	Strengths	Weaknesses
Laboratory Instrument			
1. Uncertainty and Precision of Measurement	Concentric-Cylinder Capacitor (CCC)	Proven accuracy of 1 ppm at 25 ^{0}C and 0.1 MPa. Associated electrical circuits provide very high resolution (0.05 ppm). Systematic error resulting from gaseous adsorption less than re-entrant cavity technique.	Dimensional stability of cell difficult to maintain. Large systematic errors could result. Uncertainty of measurements at other conditions more difficult to establish. Difficult to account for the dilation of the cell with pressure. Calibration of cell with known fluid may be necessary to establish effect of pressure dilation.
	Re-entrant Cavity Resonator (RCR)	The effect of pressure on the dilation of the cell can be adequately modelled. No calibration of the cell required. Reliable and traceable values for the uncertainty of measurement can be established at all conditions from measurement of frequency.	Potential accuracy of 1 ppm at 25 ^{0}C and 0.1 MPa. Possible systematic error in the measurement of permittivity at ambient pressure resulting from the effects of gaseous adsorption.
2. Mechanical issues to be resolved.	CCC	-	Four spacers made of quartz or other suitable insulating material to be fabricated. Metal surfaces require to be electroplated with gold and/or silver. Specialised pressure vessel electrical feed-throughs would need to be developed if it is necessary for the screens of the three coaxial cables to be isolated from the wall of the vessel.
	RCR	-	Metal surfaces require to be electroplated with gold and/or silver.
3. Instrumentation issues to be	CCC	-	Consideration needs to be

resolved.			given to the screening and guarding requirements of external wiring and instrumentation. Possibility of some of the key components of the external circuit (standard capacitors, transformer ratio, etc.) may require separate temperature stabilisation.
	RCR	-	-
4. Fabrication	CCC	-	Manufacturing costs of cell and electrical feed-throughs would be approximately £4000 - £6000. Machining of insulating spacers, pressure vessel and electroplating of surfaces will be an additional cost.
	RCR	Only four basic components required for the basic measurement cell. Manufacturing costs of cell and electrical feed-throughs less than for CCC.	Machining of pressure vessel and electroplating of surfaces will be an additional cost.
5. Assembly	CCC	-	More complicated than RCR method. More components to be assembled and aligned in a stable configuration. Internal electrical connections to be made to electrodes.
	RCR	Relatively simple apart from the electrical feed-throughs. However, these components are common to both the CCC and RCR technique.	-
6. Calibration Requirements	CCC	-	Most likely that the instrument will have to be calibrated at pressure with a fluid of known physical properties.
	RCR	None, provided a specific measurement procedure is followed. However, pre-calibration of the vacuum resonant frequency as a function of temperature leads to a more effective	-

		measurement procedure.	
7. Development Costs	CCC	-	Possibly twice as great as that for than re-entrant cavity technique.
	RCR	Relatively low since based on established technology and instrumentation. Feed-through technology well established.	
8. Practical Considerations	CCC	-	Poor heat path to internal components of measurement cell. Will take longer for all components to reach a uniform temperature. Less robust than RCR. Test fluid is less able to flow freely through the device. Possibility that condensate droplets and particles build up in inner annulii.
	RCR	Robust. Good heat path to internal components. The test fluid is able to flow freely through the device and the shape enables condensate droplets and solid particulates to be dislodged.	-
9. Ease of Use	CCC	-	Instrumentation possibly more difficult to use than for re-entrant cavity technique. Components of the external circuit may have to be temperature controlled.
	RCR	-	-
On-Line Instrument			
Overall	CCC	Direct-reading three-terminal capacitance meter is commercially available with required accuracy and resolution.	Cost of capacitance meter ranges between £10000 and £17000, depending upon specification. Much less robust than re-entrant cavity resonator. Less easy to assemble and maintain.

	RCR	Measurements could possibly be made using a good quality frequency counter costing some £2500. Good quality UHF amplifiers are available commercially at low cost for use in the feedback oscillator.	Special driving circuit to be developed for the re-entrant cavity to operate as part of a feedback oscillator circuit. Cost of development and testing of the driving circuit very expensive.

Table 3.1 Intercomparison between transformer ratio arm bridge with a concentric-cylinder capacitor arrangement; and the re-entrant cavity resonator with a swept-frequency generator or as part of feedback oscillator arrangement.

Were the precision of measurements at ambient conditions the sole consideration then one of the more traditional techniques of measurement, particularly the transformer ratio arm with a concentric-cylinder capacitor technique, would be the best choice. However, particular concerns were given to the dimensional stability of the above technique at elevated temperatures and pressures. Calculations made by NEL show that dimensional changes, displacement distortion, misalignment of the cells of the order of 1μm (fractionally greater than the wavelength of red light) could produce changes to the cell constant, and introduce significant errors in the measurement of relative permittivity.

For this reason, and other factors listed in table (3.1), it was decided by NEL that the re-entrant technique was the most appropriate experimental technique for making precise laboratory measurements of the relative permittivity of high value fluids over an industrially relevant range of temperatures and pressures. For similar reasons the re-entrant cavity technique was also chosen for on-line use. The ability to validate directly the operation of the on-line instrument with the laboratory instrumentation was also an important factor in choosing the re-entrant cavity technique for on-line use.

References

1. Bartnikas, R (Editor) *Engineering Dielectrics Volume II B Electrical Properties of Solid Insulating Materials: Measurement Techniques*; ASTM Special Technical Publication 926, 1916 Race Street, Philadelphia, Pa. 19103, 1987.
2. Von Hippel, A (Editor) *Dielectric Materials and Applications*; The Technology Press of M.I.T., John Wiley and sons, Inc., New York, Chapman and Hall , Ltd., London, 1954.
3. Scaife, B.K.P. *Complex Permittivity - Theory and Measurement;* The English Universities Press Ltd., London, 1971.
4. de Vos, F. C. *The Experimental Determination of Dielectric Properties at Frequencies Between 50 c/s and 5000 Mc/s*; PhD Thesis, University of Leiden, Excelsior, 1958.
5. Frohlich, H. *Theory of Dielectrics: Dielectric Constant and Dielectric Loss;* Clarendon Press. Oxford, 2nd edition, 1958.
6. Bussey, H. E. *Measurement of RF Properties of Materials – A Survey*; Proceedings of the IEEE, Vol. 55, No. 6, June 1967.
7. Cole, R. H. and Gross, P. M. Review of Scientific Instruments, Vol. 20, pp 252, 1949.
8. Hartshorn, L. and Ward W. H., *The Measurement of Permittivity and Power Factor of Dielectrics at Frequencies from 10^4 to 10^8 cps*; Journal of IEEE (London), Vol. 79, pp 597-609, November 1936.
9. Works, C. N., Dakin, T. W. and Boggs, F. W., *A Resonant-Cavity Method for Measuring Dielectric Properties at Ultra-High Frequencies*; Proceedings of the IRE, pp 245, April 1945.
10. American Society for Testing and Materials, *Test Method D2520 Standard Test Methods for Complex Permittivity (Dielectric Constant) of Solid Electrical Insulating Materials at Microwave Frequencies and Temperatures to 1650^0C.*

11. Watson, J.T.R. *Methods for the Precise Measurement of the Relative Permittivity of Natural Gases.* Flow Centre Report No. 095/97 produced for Ruhrgas AG; National Engineering Laboratory, East Kilbride, Glasgow, January 1998.
12. Goodwin, A.R.H., Mehl, J.B. and Moldover, M.R. *Reentrant radio-frequency resonator for automated phase-equilibria and dielectric measurements in fluids;* Rev. Sci. Instruments, 1996, 67(12), 4294-4303.
13. Hamelin, J., Mehl, J. B. and Moldover, M. R., *Resonators for accurate dielectric measurements in conducting liquids,* National Institute of Standards and Technology, Physical and Chemical Properties Division, Gaithersburg, Maryland 20899, Review of Scientific Instruments, 69 (1), 255-260, 1998.

4. Theory of Operation: Re-entrant Cavity Resonator

This chapter describes the theory of operation of the re-entrant cavity resonator as applied to the measurement of the relative permittivity of gases and hydrocarbon liquids over a wide range of both pressures and temperatures.

4.1 Introduction

The accuracy of measurement of relative permittivity with the re-entrant cavity resonator technique is better than 1 ppm provided that the cavity has a sufficiently high electrical quality factor and the dimensions of the evacuated cavity are the same as those of the filled cavity at the same temperature and pressure of measurement. The dimensions of the cavity are effected by changes in temperature, pressure and penetration depth of the electromagnetic field within the cavity.

In order to quantify and correct for the effects of changes in pressure and penetration depth of the electromagnetic field a mathematical model of the cavity was developed around an established theoretical model of the same. The theoretical model establishes accurate relationships between the dielectric constant of the fluid, the geometry of the cavity, the resonance frequency and the quality factor, and allows the effects of change in pressure and penetration depth to be accounted for.

The chapter also includes details on the uncertainties involved in the measurement of the relative permittivity with the re-entrant cavity resonator technique.

4.2 Parallel LCR Circuit Approximation

It can be seen from figure (4.1), below, that, externally, the resonator is of cylindrical form and comprises of two metal parts. The outer, lower, part of the resonator is a hollow metal cylinder closed at the bottom. The inner, upper, part of the resonator serves

as the lid to the cavity and has a cylindrical neck expanding into a bulbous extension that nearly fills the middle of the cavity. Internally, the fluid under test fills a volume consisting of two separate toroidal sections. The first of these has a relatively large annular gap, of some 20 mm, which at radio frequencies behaves as an inductor, and the second, with a 2 mm annular gap, behaves as a capacitor. Re-entrant resonators with effectively separate electric and magnetic fields can be considered as a lumped-element circuit, therefore, in a first approximation, the re-entrant cavity functions as a parallel LCR network.

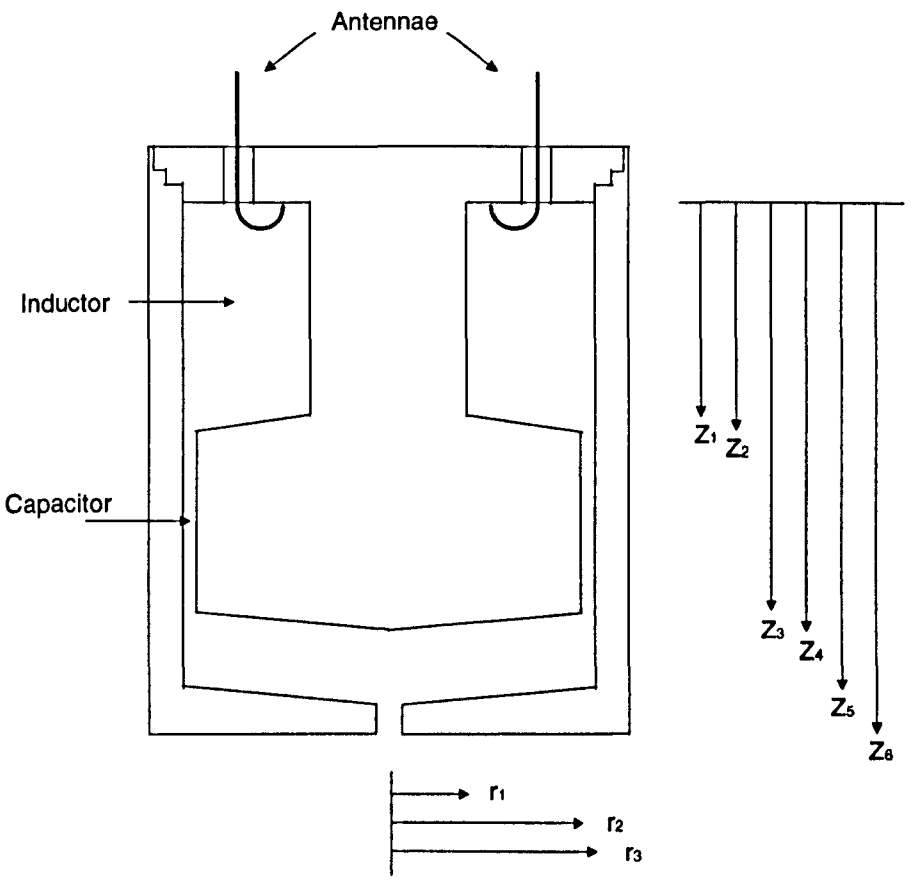

Figure 4.1. Re-entrant cavity resonator. Approximate dimensions in mm are; r1=10.98, r2=27.22, r3=29.22, z1=30.775, z2=32.775, z3=58.35, z4=61.34, z5=69.875, z6=75.94.

The re-entrant resonator, considered as a lumped-electrical *LCR* parallel circuit, consists of a capacitor shunted across an inductor with resistance. Figure (4.2)(a), below, illustrates such a system, with a capacitor, C, in parallel with an inductor, L, which is in series with a resistance, R_s. The series resistance, R_s, of the circuit may be considered as the surface resistance of the resonator due to the finite conductivity of the internal metal surface of the resonator. The series resistance can be replaced by an equivalent parallel resistance, R_p, as illustrated in figure (4.2)(b), below:-

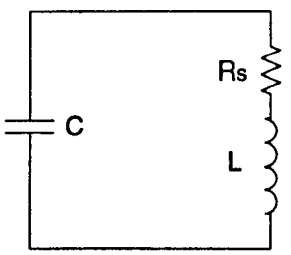

Figure 4.2(a).

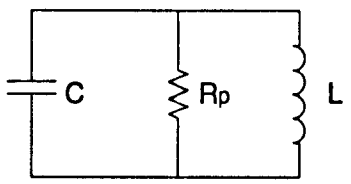

Figure 4.2(b).

Figures 4.2(a) and 4.2(b). Parallel resonant circuit.

The resonant frequency of the LCR parallel circuit can be obtained by considering the admittance operator[3] of the circuit in figure (4.2)(a):-

$$Y = j\omega C + \frac{1}{R_S + j\omega L} = j\omega C + \frac{R_S - j\omega L}{R_S{}^2 + \omega^2 L^2}, \qquad (4.1)$$

Resonance can be defined as the point at which the network has a unity power factor[2], that is the energy absorbed by the inductor is equal to the energy released by the capacitor every quarter-cycle, which occurs when the admittance is real. Equating the imaginary terms of equation (4.1) to zero, results in an expression for the resonant angular frequency:-

$$\omega = \left(\frac{1}{LC}\right)^{1/2}\left(1-\frac{R_S{}^2C}{L}\right)^{1/2} = \left(\frac{1}{LC}\right)^{1/2}\left(1-\frac{1}{Q^2}\right)^{1/2}, \tag{4.2}$$

where Q is the quality factor of the circuit and can be expressed as $Q = \frac{\omega L}{R_S}$ or as $Q = \frac{f}{\Delta f}$, where $f = \frac{\omega}{2\pi}$ and Δf is the half-power bandwidth of the resonant curve at the 3 dB points.

Provided Q is of a sufficient magnitude then the second term in equation (4.2) can be neglected, giving the expression for resonant angular frequency as:-

$$\omega = \left(\frac{1}{LC}\right)^{1/2}. \tag{4.3}$$

The admittance at this point is:-

$$Y = \frac{R_S}{\left(R_S{}^2 + \omega^2 L^2\right)} = \frac{R_S C}{L} = \frac{1}{Q^2 R_S}. \tag{4.4}$$

The reciprocal of the admittance at resonance is called the 'parallel resistance' and is equal to the equivalent parallel resistance, R_p, in figure (4.2)(b).

Figure (4.1) shows that the capacitance of the resonator is mainly determined by the annular gap in the middle of the cavity whereas the inductance is mainly determined by the toroidal section to the top of the cavity. The capacitance of the capacitive section when filled with a fluid equals $C = \varepsilon_r C_0$, where $\varepsilon_r \equiv \frac{\varepsilon}{\varepsilon_0}$ is the relative electric permittivity of the fluid in the cavity and C_0 is the capacitance of the section under vacuum conditions, ($C_0 \approx 27$ pF). Once the cavity is filled with a dielectric fluid the

capacitance of the section increases by an amount determined by the value of the relative permittivity of the fluid. Due to the relative magnetic permeability, $\mu_r \equiv \frac{\mu}{\mu_0}$, of all gases being negligibly different from unity, the inductance does not change significantly when a gas fills the cavity, ($L_0 \approx 7$ nH) .

For a cavity under vacuum conditions equation (4.3) may be expressed as:-

$$2\pi . f_0 = \frac{1}{\sqrt{L_0 C_0}},$$

where f_0 is the resonant frequency of the cavity under vacuum conditions; and

C_0 is the capacitance of the capacitive section under vacuum conditions,

and for a gas filled cavity as:-

$$2\pi . f_{\varepsilon_r} = \frac{1}{\sqrt{L_0 \varepsilon_r C_0}},$$

where f_{ε_r} is the resonant frequency of the cavity under fluid filled conditions; and

ε_r is the relative permittivity of the fluid within the cavity.

From this it can be seen that the resonant frequency of the gas filled cavity is related to that of the evacuated cavity by the equation:-

$$f_{\varepsilon_r} = \frac{f_0}{\sqrt{\varepsilon_r}}, \tag{4.5}$$

and that the relative permittivity may be easily obtained, by rearranging equation (4.5), from the ratio of the two frequencies:-

$$\varepsilon_r = \left(\frac{f_0}{f_{\varepsilon_r}}\right)^2. \tag{4.6}$$

It is important to note that equations (4.5) and (4.6) are only true if the cavity has a quality factor at resonance in excess of 1000 and the dimensions of the filled cavity are the same as those of the evacuated cavity (See section 4.5).

Electromagnetic energy is magnetically coupled into and out of the cavity by two coupling loops, as illustrated in figure (4.3), below. The first acts as a transmitter and couples and external RF source into the cavity. As the current flows in the antenna loop the resulting magnetic flux of the same generates axially symmetric current sheets flowing down through the neck which generate a purely azimuthal magnetic field. This magnetic field then threads the second antenna loop which acts as a receiver coupling the magnetic component of this internal field to an external detection system. The degree of coupling can be controlled by rotating the coupling loops, maximum coupling occurring when the plane of the loop is normal to the magnetic field. It is, however, advantageous to minimise the coupling between the cavity and the external measurement circuitry to reduce the effects of loading.

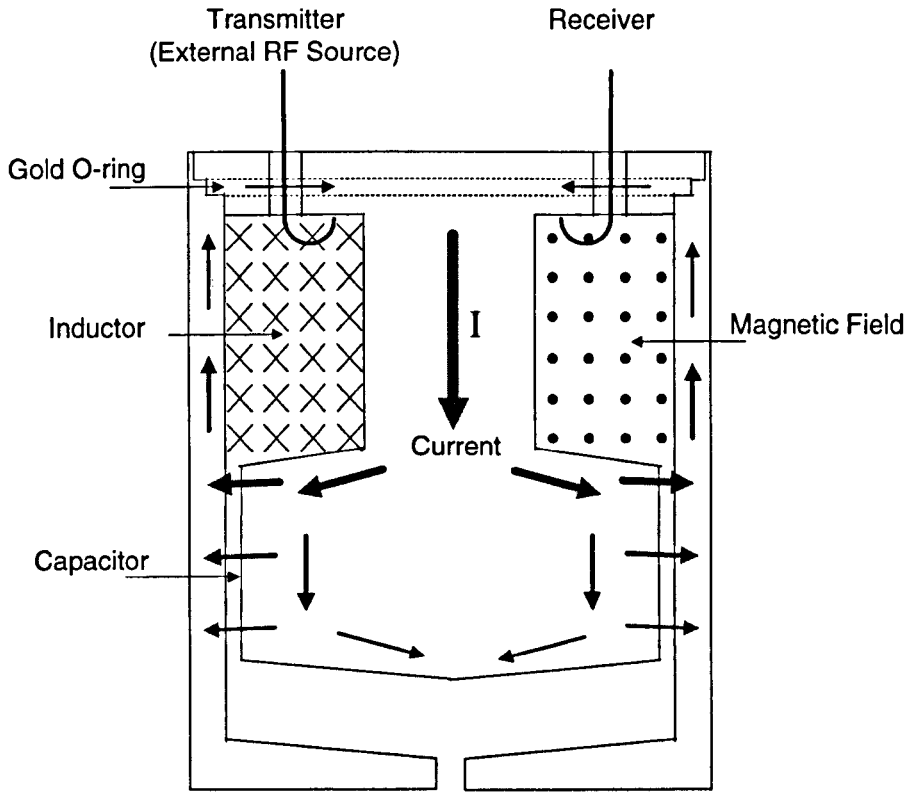

Figure 4.3 Re-entrant cavity resonator. Electromagnetic coupling and surface current flow.

In free oscillations of the cavity at RF frequencies, current flows from one face of the capacitor to the other. The current flows through the neck into the bulbous extension, across the capacitor, through the upper portion of the outer cylinder, through the gold O-ring and finally through the lid, as illustrated in figure (4.3). For the case where the capacitor is being charged by the current flowing down the neck into the bulbous extension, the conduction current density is at it's greatest in the neck, however as the capacitive section is approached the conduction current density decreases rapidly owing to the rapid increase of the displacement current density across the capacitive section. The conduction current density finally decays to zero as it flows down through to the bottom of the bulbous extension.

Due to the skin effect the conduction current is confined to flow in a thin boundary layer at the surface of the metal. The thickness of the layer δ is given by:-

$$\delta = \frac{1}{\sqrt{\pi \mu' \sigma(t) f}}, \tag{4.7}$$

where $\sigma(t)$ and μ' are the electrical conductivity at temperature ,t, and magnetic permeability of the metal carrying the current; and

f is the resonant frequency of the cavity.

Therefore, the surface resistance, R_s, which is directly proportional to δ (see equation (4.10)), is dependent on the operating frequency.

4.3 Mode Degeneracy

Resonators in general have many different modes of resonance, that is to say, if the frequency of excitation energy into the cavity is swept, the response of the cavity would show many resonance peaks separated in frequency over the swept range.

For example, NEL have developed a spherical cavity resonator for the measurement of relative permittivity operating at the lower end of the microwave spectrum, 1 to 6 GHz[3]. A measurement of the relative permittivity of a test fluid at set conditions can be obtained from the radius and resonant frequencies of the cavity when filled with the test fluid. By using a network analyser to excite the cavity and observing the position of one, or more, resonance curves the relative permittivity of the dielectric contained in the cavity can be determined. Full mathematical solutions of Maxwell's wave equations have been established for a number of simple cavity geometries including spheres. The resonant frequency of the sphere is a function of both the internal radius, the real part of

the relative permittivity of the material enclosed within the sphere and the mode of the resonant electromagnetic wave. The fundamental theory of the spherical resonator is developed assuming that it possesses an ideal spherical geometry without apertures or intrusions and also is constructed of a material with high electrical conductivity.

Practical considerations determine that not all of the resonance frequencies can be observed in practice. Only a close approximation to the ideal spherical shape can be attained in reality, therefore the imperfections in the geometry of the manufactured sphere will influence which modes can support resonance. The geometry of the essential conducting antenna penetrating the sphere, largely determines which of the modes of resonance can be launched and sustained within the resonant cavity. Any such intrusive coupling has an effect of altering the damping and resonance characteristics of the cavity. Also, the excitation and detection system has an upper frequency limit, therefore, resonant modes out with this limit will not be observed.

The influence of geometric imperfections of the spherical resonator lead to mode degeneracy. In a perfect spherical cavity the alignment of the electromagnetic field at resonance is determined largely by the mode of coupling, the position and alignment of the excitation and detection antennae. For an imperfect geometry, up to three such electromagnetic field distributions will be supported for each mode of resonance, the alignment of each corresponding with the principal axes of the deformed cavity. Each of these split modes exhibit different resonance characteristics, principally: amplitude, half-power bandwidth and central resonance frequency. The frequency spacing of the three resonant frequencies will be dependent largely upon the magnitude of the dimensional imperfections of the sphere. Surface discontinuities, butted faces or joints for example, will have distinct influence upon the quality factor and hence the sustainability of the split modes.

In practice, the observed response curve for an imperfect cavity at conditions close to resonance will be some combination of the three split mode response curves, each with

its own magnitude, half-power bandwidth and central resonant frequency. The potential existence of other than a single resonant mode introduces a significant degree of uncertainty into the frequency determination.

With the introduction of a dielectric into the cavity the resonance characteristics of one or more of the split modes may change and the shape of the observed response curve for the dielectric may differ markedly from that obtained under vacuum conditions. Since it is not possible to establish which of the split mode characteristics may have changed, this introduces an uncertainty into the frequency determination and hence on any measurement of permittivity.

Re-entrant cavity resonators have particular advantages over other resonator designs in that their resonant modes are each well separated in frequency and the fundamental frequency mode is both stable and non-degenerate. The re-entrant cavity utilised in this work has its fundamental resonant mode at around 395 MHz, it's next mode does not occur until above 1.8 GHz.

4.4 Theoretical Model

A detailed theoretical model of the re-entrant cavity has been developed by Goodwin *et al*[4]. The theoretical model develops accurate relationships connecting the dielectric constant of the fluid, the geometry of the cavity, the resonance frequency and the quality factor. The model accounts for the finite wavelength of the electromagnetic field, the electrical conductivity of the conducting surface and coupling to the external electronics. It does not account, however, for the presence of the antennae in the main toroidal section or the presence of apertures in the walls of the cavities.

As previously mentioned, the re-entrant resonator can be regarded in the lowest approximation as an LCR oscillator with it's main capacitance associated with the small annular gap between the bulbous extension and the outer cylinder. There are also

additional contributions to this capacitance from fringing fields and from the large gap at the bottom of the cavity. The capacitor is in parallel with a current path which encloses the annular region at the top of the resonator. The low frequency inductance of this region can be calculated by noting that the magnetic field generated by an arbitrary superposition of axially symmetric current sheets is purely azimuthal and therefore may be expressed as:-

$$H = \frac{I}{2\pi r}, \tag{4.8}$$

where H is the magnetic field; and

I is the sum of all the currents encircling the cross section of the toroid.

The associated inductance of this region is therefore:-

$$L_T = \frac{\mu_0}{2\pi}\left[\frac{z_1 r_2 - z_2 r_1}{r_2 - r_1}\ln\left(\frac{r_2}{r_1}\right) + z_2 \ln\left(\frac{r_3}{r_2}\right) + z_2 - z_1\right], \tag{4.9}$$

$\approx$ 6.2nH (for the selected geometry),

where L_T is the inductance of the toroidal region;

μ_0 is the magnetic permeability of free space; and

z_1, z_2, r_1, r_2, r_3 are dimensions illustrated in figure 4.1.

As mentioned previously, the conduction current is confined to flow in a thin boundary layer at the surface of the metal of thickness δ. Dissipation within this layer can be accounted for by an equivalent series resistance given by the expression:-

$$R_s = \frac{\mu'\delta\omega}{4\pi}\left[\frac{z_1}{r_1}+\frac{z_2}{r_3}+\ln\frac{r_3}{r_1}+\frac{\left(\ln\frac{r_2}{r_1}\left(r_2^2+(z_2-z_1)^2\right)^{\frac{1}{2}}\right)}{r_2}\right], \qquad (4.10)$$

$\approx$ 8.4 mΩ (for the selected geometry and surface finish),

where μ' is the magnetic permeability of the surface metal;

δ is the thickness of the conducting layer (skin-depth); and

z_1, z_2, r_1, r_2, r_3 are dimensions illustrated in figure 4.1.

The wavelength of electromagnetic radiation at the vacuum resonant frequency of the cavity is approximately $\lambda = 750\,\text{mm}$. Thus the resonator dimensions are not sufficiently small that all the finite-size effects can be neglected. Both finite-size and dissipative effects can be included in the theoretical model by considering the resonator as a pair of coupled coaxial waveguides.

Goodwin *et al*[4] considered the inductive and capacitive toroidal sections as coupled coaxial cylindrical waveguides with the dielectric fluid confined to the annular regions $a \le r \le b$, where a and b are the inner and outer radii of the coaxial sections respectively. The surface metal of electrical conductivity σ' and magnetic permeability μ' forms the radial boundaries, which are assumed thick compared with the skin depth δ at frequencies of measurement. The exact equations for a coaxial waveguide with walls of finite conductivity are unnecessary for most applications and it is more useful to use approximations of the exact solutions.

Since the walls of the resonator have finite conductivity the transmission structure cannot be considered ideal. The coaxial waveguide transmission structure must therefore be considered as a transmission line with distributed series resistance in the conductors

in the line and distributed shunt conductance because of leakage through the dielectric of the line. Figure (4.4), below, is a schematic of the distributed parameter line:-

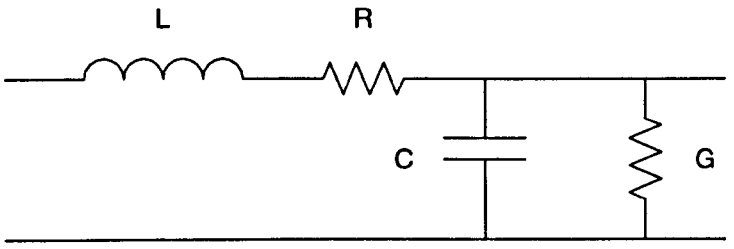

Figure 4.4 Schematic of a distributed parameter transmission line.

where L is the series inductance per unit length;
R is the series resistance per unit length;
C is the shunt capacity per unit length; and
G is the shunt conductance per unit length.

The important parameters are the distributed series impedance and the parallel conductance, which are, respectively:-

$$Z = (1+j)R + j\omega L, \qquad Y = j\omega C. \tag{4.11}$$

The values used in these expressions are:-

$$L = \frac{\mu}{2\pi}\ln\left(\frac{b}{a}\right), \qquad C = \frac{2\pi\varepsilon}{\ln\left(\frac{b}{a}\right)}, \qquad R\frac{1}{2\pi\sigma'\delta}\left(\frac{1}{a}+\frac{1}{b}\right). \tag{4.12}$$

These parameters may be use to determine the propagation constant, $\gamma = \sqrt{ZY}$, and the characteristic impedance, $Z_0 = \sqrt{\frac{Z}{Y}}$, of the line.

A section of waveguide of length l, terminated by an impedance Z_T, can be represented by the T-equivalent circuit illustrated in figure (4.5) below:-

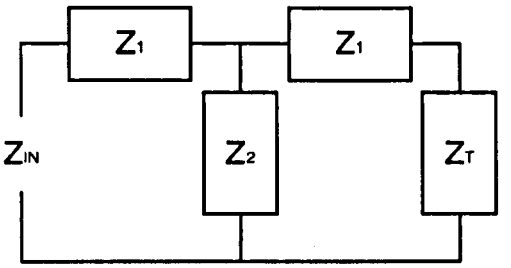

Figure 4.5 T-equivalent circuit of a waveguide section.

where the impedances are:-

$$Z_1 = Z_0 \tanh\left(\gamma \frac{l}{2}\right)$$

$$= \left(\frac{l}{2}\right)\left[j\omega L + (1+j)R\left[1 + \omega^2 LC\frac{l^2}{12} + \ldots\right]\right], \tag{4.13}$$

$$Z_2 = \frac{Z_0}{\sinh(\gamma l)}$$

$$= \frac{1 + \omega^2 LCl^2/6 + \ldots.}{j\omega Cl}. \tag{4.14}$$

The quantity $LC = \mu\varepsilon$ is the inverse of the squared propagation speed of the material within the cavity. The quantities $(\omega l)^2 LC$ are therefore small and series terms beyond those displayed above can be neglected.

The resonator can be modelled as two sections of coaxial waveguide terminated at the lower end by a cylindrical capacitor, as illustrated in figure (4.6), below:-

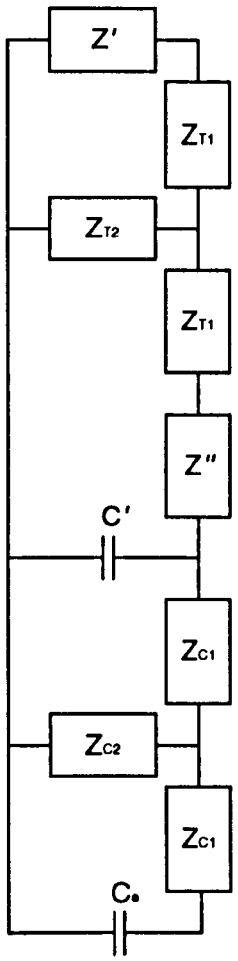

Figure 4.6 Schematic representation of resonator.

The T-equivalent parameters Z_{T1} and Z_{T2} represent the inductive toroidal section and the parameters Z_{C1} and Z_{C2} represent the capacitive toroidal section. The capacitance associated with the fringing fields at the upper ends of the capacitive section is C'. The terminating capacitance C_e is the sum of a similar fringing term C'' and the capacitance C_2 of the cylindrical capacitor at the bottom of the resonator. The impedances Z' and

Z'' are associated with radial current flow in the upper and lower surfaces of the inductive section, respectively.

The T-equivalent impedances of the inductive section are:-

$$Z_{T1} = \frac{1}{2}\left(j\omega L_T + (1+j)R'_T\right)\left(1 + \omega^2 L_T C_T / 12\right), \tag{4.15}$$

$$Z_{T2} = \frac{\left(1 + \omega^2 L_T C_T / 6\right)}{j\omega C_T}, \tag{4.16}$$

where L_T from equation (4.9);

$R' = R.Z_1$ with R from equation (4.12); and

$C_T = {2\pi\varepsilon z_1}\Big/{\ln(r_3/r_1)} \approx 1.7.\varepsilon_r pF$ from equation (4.12).

The T-equivalent impedances of the coaxial capacitive section are:-

$$Z_{C1} \approx {j\omega L_C}\Big/{2}, \tag{4.17}$$

$$Z_{C2} = \left(1 + \omega^2 L_C C_1 / 6\right)\left(j\omega C_1\right) \tag{4.18}$$

where $C_1 = {2\pi\varepsilon\left(z_3 - z_2\right)}\Big/{\ln\left(r_3/r_2\right)} \approx 20.\varepsilon_r pF$ from equation (4.12); and

$L_C = \dfrac{\mu\left(z_3 - z_2\right)}{2\pi}\ln\left(\dfrac{r_3}{r_2}\right) \approx 0.36nH$ from equation (4.12).

The finite-size and dissipation terms have been dropped from equation (4.17) due to the smallness of ωL_c.

The inductive toroidal section is terminated at its upper end by the impedance $Z' = (1+j)R'$, where:-

$$R' = \frac{\mu}{2\pi} \ln\left(\frac{r_3}{r_1}\right). \tag{4.19}$$

The impedance associated with radial current flow at the lower, sloping surface of the inductive toroidal section is given by a similar expression $Z'' = (1+j)R''$ where R″ is given by equation (4.19) with r_3 replaced with r_2.

Shunting susceptances occur at the discontinuities between the two sections of waveguide, these are shown in figure (4.6) by the capacitances C' and C''. Formulas from Marcuwitz[5] have been used to estimate the values of these capacitances, $C' \approx 1.9pF$ and $C' \approx 2.2pF$.

The cylindrical capacitance at the bottom of the resonator, C_2, is given by the expression:-

$$C_2 = {}^{\pi\varepsilon r_2^2}\!/_{z_6 - z_4} \approx 1.7\varepsilon_r pF. \tag{4.20}$$

The resonant frequency can be represented as a complex number, $\omega = 2\pi(f + jg)$, whose imaginary part corresponds to the damping rate, or equivalently, to the half-width of the resonance line shape. Using equation (4.3) the resonance frequency can be approximated to:-

$$4\pi^2(f+jg)^2 \approx \frac{1-(1-j)\omega R_S C_4}{L_T(C_4+C_T/3)+L_C\left[(C_e+C_1^2/3C_4)-C_eC'/C_4\right]}, \tag{4.21}$$

where $C_4 = C_1 + C' + C'' + C_2$.

Equating the real and imaginary parts of the complex expression above gives the resonant frequency, f, and quality factor, Q, of the cavity:-

$$f = \frac{1}{2\pi}\sqrt{\frac{(1-\omega R_S C_4)}{L_T(C_4+C_T/3)+L_C\left[(C_e+C_1^2/3C_4)-C_eC'/C_4\right]}}, \tag{4.22}$$

$$Q = \frac{1-\omega R_S C_4}{\omega R_S C_4\left(1-{}^{1}\!/_{4Q^2}\right)}. \tag{4.23}$$

The re-entrant cavity developed by Goodwin is applicable for use with fluids having both high permittivities and high loss factors. Goodwin reported that the Q-values of their brass and Inconel cavities were 920 and 240, respectively, at vacuum conditions. When used with even very low-loss liquids the Q-values of these cavities will decrease by an order of magnitude or more, depending on the test fluid and the conditions of measurement. However, when used with non-polar fluids, in the range of conditions under consideration here, the Q-value would only decrease $\approx$ 7% at most from the vacuum value. Under vacuum conditions the NEL cavity has a resonant frequency of approximately 400 MHz and a quality factor in excess of 2000.

4.5 Simplified Model

Provided the quality factor of the cavity can be maintained in excess of 1000, Goodwin's complicated theoretical model can be replaced by the following general model for all resonant cavities which is applicable to an absolute precision of better than 1 ppm.

The resonant frequency of a low-loss cavity filled with a low-loss, non-conducting medium such as natural gas is related to that of the evacuated cavity at the same temperature and by the equation:-

$$f_{\varepsilon_r}(t,p) = \frac{f_0(t)}{\sqrt{\mu_r \varepsilon_r(t,p)}}, \tag{4.24}$$

where $f_{\varepsilon_r}(t,p)$ is the resonant frequency of the fluid filled cavity at the conditions of measurement;

$f_0(t)$ is the resonant frequency of the cavity under vacuum conditions, $\varepsilon_r = 1$ at temperature t;

μ_r is the relative magnetic permeability of the fluid at the conditions of measurement (μ_r is negligibly different from unity for all fluids except oxygen, for which $\mu_r = 1.0000019$); and

ε_r is the relative permittivity of the fluid at temperature t and absolute pressure p.

Taking the magnetic permeability to be unity, the relative permittivity of the contained dielectric can be obtained from the ratio of the frequencies at the same temperature of measurement:-

$$\varepsilon_r(t,p) = \left(\frac{f_0(t)}{f_{\varepsilon_r}(t,p)} \right)^2 \tag{4.25}$$

The designs of re-entrant cavities to date are not ideally suited for high-precision measurement of permittivity. The relationship between permittivity and resonant frequency given by equation (4.25) applies to better than 1 part per million provided:-

- the cavity has a high quality factor at resonance, $Q > 1000$; and
- the dimensions of the dielectric filled cavity are the same as those of the evacuated cavity at the same temperature of measurement.

The factors affecting the dimensional stability of the cavity are:-

- the dilation of the dielectric filled cavity with applied pressure, p; and
- the effective dilation of the dielectric filled cavity due to a change in the penetration depth, δ, of the electromagnetic waves inside the cavity.

A more accurate expression for the relative permittivity of the enclosed dielectric is therefore:-

$$\varepsilon_r(t,p) = \left(\frac{f_0(t)}{f_{\varepsilon_r}(t,p)} \right)^2 (1 + C_p)(1 + C_\delta) \tag{4.26}$$

where C_p is the correction factor for dilation due to pressure; and

C_δ is the correction factor for effective dilation due to a change in the penetration depth, δ.

4.6 Quality Factor

The quality factor, Q, is dependent primarily on the electrical conductivity of the inner surfaces of the resonator. At the resonant frequency of the cavity, ≈ 400 MHz, the current is confined to flow in a 'skin' layer of around 6 μm. Since the current is confined to flow in this thin layer, or plate, the cavity has a lower conductivity at higher frequencies due to the effective area of conduction being reduced with increase of frequency. In order to increase the conductivity of the cavity the inner surfaces have been electro-plated with both gold and silver, both of which have higher conductivities than the Beryllium alloy Copper from which the cavity is made. The cavity has been plated with silver to a depth of approximately 8-9 μm with a gold layer of 1-2 μm on top of that. The current now flows in an approximate 10μm layer of high conductivity metal. The silver has a higher conductivity than gold but is more sensitive to contamination therefore the gold acts as a protective layer to the silver.

4.7 Correction for the Dilation Due to Pressure

By housing the re-entrant cavity within a separate pressure vessel the influence of pressure on the dimensions of the cavity have been minimised. The capacitances and inductances in equations (4.22) and (4.23) depend on the resonator dimensions, and hence on temperature and pressure of the fluid contained in the cavity. The capacitance, C_1, the major component of the total capacitance, is most sensitive to pressure owing to the small annular gap, $r_3 - r_2$. Though dimensional change in an internally pressurised cavity can be modelled, it can not be so with sufficient accuracy, therefore calibration would have to be made with a known fluid as a function of temperature and pressure. However, by utilising a separate containment vessel the need for subsequent calibration can be eliminated. Goodwin used measurements on helium to determine the pressure dependence of capacitance, C_1. Goodwin also considered the remaining, less sensitive to dimensional change, capacitances and inductances to be constant in his analysis.

Reliable estimates of the dimensional changes, $\Delta\bar{x}$, in the cavity dimensions, $\bar{x}$, with pressure have been obtained from detailed finite element studies using ANSYS (a finite-element analysis package produced by SAS IP Inc.). (See Chapter 5: Pressure Effect Corrections)

The electrical model of the cavity, developed by Goodwin, enables the resonant frequency and the quality factor to be calculated as a function of the cell dimensions, $\bar{x}$, the relative permittivity of the enclosed media, ε_r, and the electrical conductivity of the internal surface layer, $\sigma(t)$:-

$$f = f\{\bar{x}, \varepsilon_r, \sigma(t)\} \text{ and } Q = \{\bar{x}, \varepsilon_r, \sigma(t)\}$$

Using the ANSYS results for the changes to the individual cavity dimensions with pressure, $\Delta\bar{x}$, the electrical model enables the resultant frequency change and corresponding correction factor, C_p, in equation (4.26) to be established.

By considering only the effects of pressure on the relative permittivity of the dielectric contained within the cavity, equation (4.26) can be written as:-

$$\varepsilon_r(p) = \left(\frac{f_0}{f_0(p)}\right)^2 (1 + C_p) \tag{4.27}$$

When determining the correction factor C_p it has been assumed the cavity is in an evacuated state, $\varepsilon_r = 1$, and at ambient temperature, so that the only dimension changes being considered are those due to pressure. Therefore the frequency $f_0(p)$ in equation (4.27) is the resonant frequency of the evacuated cavity at a specified pressure.

Initial analysis of the results of the electrical model calculations showed that:-

$$C_p \propto p. \tag{4.28}$$

Values of the correction factor C_p,

$$C_p = \frac{1}{\left(f_0 / f_0(p)\right)^2} - 1, \text{ from equation (4.27) with } \varepsilon_r = 1,$$

were calculated by the model as a function pressure, p. The model assumes the physical dimensions of the cavity are those at ambient conditions.

The relationship between C_p and p is illustrated in graph (4.1) below:-

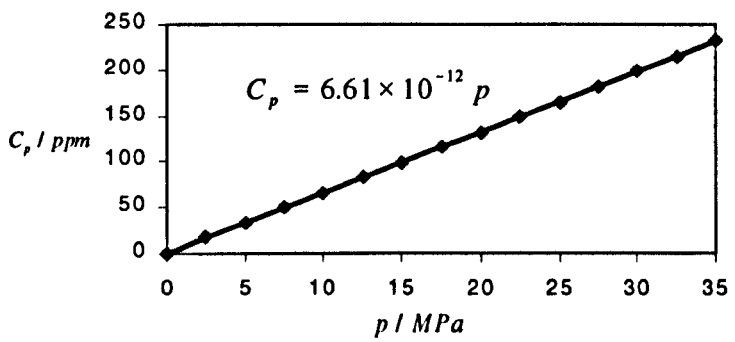

Graph 4.1 Relationship between computed C_p and p.

From graph (4.1) and equation (4.28) it can be seen that for the specific cavity geometry, $\bar{x}$, and the material of construction, the correction factor for the dilation of the cavity due to pressure is:-

$$C_p = A.p\,, \tag{4.29}$$

where A is a constant, such that $A = 6.61\times10^{-12}$ Pa^{-1}; and

p is the absolute pressure of the dielectric medium in Pa.

At an operating pressure of 10 MPa the correction is ≈ 66 ppm. At ambient pressure the correction factor is small but not negligible. It should be noted that the correction factor has a positive sign. As the pressure in the pressure containment vessel is increased the principal dimensional change is a decrease in the length of both the capacitive and inductive sections of the cavity by about 1μm at 10 MPa. The ratio of the internal diameter of the cavity to the diameter of the bulbous extension remains virtually independent of pressure. This finding is in accord with the theoretical expression for the radial dilation of an infinitely long cylinder. This decrease in length of both the capacitive and inductive sections at 10 MPa has an effect of lowering the value of each section by approximately 40 ppm and 26 ppm respectively. Both of these changes increase the resonant frequency by an expected 33 ppm, thus resulting in the obtained correction factor for the dilation of the cavity due to pressure of ≈ 66 ppm at 10 MPa.

The ANSYS study showed that there is a slight tapering at one end of the bulbous extension due to the presence of the thermometer well and is accounted for in the electrical model of the cavity by integrating the capacitance over the sloping region.

The estimated total uncertainty in the factor C_p is $\pm 0.1 C_p$. The latter takes account of the uncertainties in the elastic modulii of the beryllium-copper alloy and the uncertainties introduced by imperfections in the electrical model of the cavity.

Equation (4.27) takes account of all changes in the dimensions of the cavity with applied pressure.

4.8 Correction for the Effective Dilation Due to the Change in Penetration Depth

Equation (4.25) applies only if the spatial distribution of the electric and magnetic fields within the re-entrant cavity are identical in the evacuated and filled conditions. As the relative permittivity of the dielectric contained in the cavity increases from $\varepsilon_r = 1$ the resonant frequency of the cavity decreases in accordance with equation (4.25), however, equation (4.25) does not take account of the change in electromagnetic dimensions, $\Delta\bar{x}'$, associated with this change in frequency. Therefore a correction to equation (4.25) is required to take account of the fact that the physical dimensions, $\bar{x}$, of the cavity differ from its electromagnetic dimensions, $\bar{x}'$.

This important correction results from the penetration of the magnetic field into the metal surfaces bounding the cavity. The effective depth of penetration of the field, or 'skin-depth', was shown previously in equation (4.7) $\left(\delta = \frac{1}{\sqrt{\pi\mu'\sigma(t)f}}\right)$ to be a frequency dependent quantity. Since it can be shown from equation (4.25) that:-

$$f_{\varepsilon_r} \approx \frac{f_0}{\sqrt{\varepsilon_r}} \quad < \quad f_0,$$

at the same temperature t, it follows that the penetration depth in the evacuated cavity, δ_0, will therefore also differ from that in a dielectric filled cavity, δ_{ε_r}, at the same temperature t. Using equation (4.7) it follows that the penetration depth in a dielectric filled cavity is:-

$$\delta_{\varepsilon_r} = \delta_0 \frac{\sqrt{f_0}}{\sqrt{f_{\varepsilon_r}}} \quad > \quad \delta_0,$$

thus the electromagnetic dimensional change, $\Delta\bar{x}'$, between a dielectric filled cavity and an evacuated cavity, at the same temperature, t, is:-

$$\Delta\bar{x}' = \delta_0\left(\frac{\sqrt{f_0}}{\sqrt{f_{\varepsilon_r}}} - 1\right).$$

Some cavity dimensions are increased by this amount and others are decreased by it. For $\varepsilon_r = 1.1$ (e.g. a natural gas at a pressure of 10 MPa) and $\varepsilon_r = 1.6$ (e.g. ethylene at a pressure of 12 MPa) the effective dimensional changes are some 0.12 and 0.52 μm respectively. The most significant dimensional change occurs at the radial gap of the annular capacitor, C_1, which increases by $2.\delta_0\left(\frac{\sqrt{f_0}}{\sqrt{f_{\varepsilon_r}}}\right)$ at temperature t.

Using these electromagnetic dimensional changes, $\Delta\bar{x}'$, the electrical model enables the resultant frequency change and corresponding correction factor, C_δ, in equation (4.26) to be established.

By considering only the effects of penetration depth on the relative permittivity of the dielectric contained within the cavity, equation (4.26) can be written as:-

$$\varepsilon_r(t) = \left(\frac{f_0(t)}{f_{\varepsilon_r}(t)}\right)^2 \left(1 + C_\delta\right) \qquad (4.30)$$

When determining C_δ it has been assumed that the cavity is at ambient pressure, so that the only dimension changes being considered are those due to relative permittivity. Therefore the frequency $f_{\varepsilon_r}(t)$ in equation (4.30) is the resonant frequency of the filled cavity at a specified temperature.

Initial analysis of the results of the electrical model calculations showed that:-

$$C_\delta \propto \delta_0(t)\left(\frac{\sqrt{f_0(t)}}{\sqrt{f_{\varepsilon_r}(t)}}-1\right) \qquad (4.31)$$

However, due to the surface of the cavity being composed of electroplated metals of irregular thickness, the effective electrical conductivity of the surface layers is not readily established and as a consequence the effective penetration depth can not be calculated directly from equation (4.7). The penetration depth can, however, be related to the quality factor, Q, of the cavity, a directly measurable quantity, through equations (4.7) and (4.23). From equation (4.10) it can be shown that:-

$\delta \propto R_s$ where R_s is the surface resistance of the cavity,

and from equation (4.23) it can be shown that:-

$$Q \propto \frac{1}{R_s} \quad \text{so that,}$$

$$\delta \propto \frac{1}{Q}.$$

Thus it follows that equation (4.31) may now be written as:-

$$C_\delta \propto \frac{1}{Q_0(t)}\left(\frac{\sqrt{f_0(t)}}{\sqrt{f_{\varepsilon_r}(t)}}-1\right) \qquad (4.32)$$

where $Q_0(t)$ is the quality factor of the evacuated cavity at temperature t.

Values of the quantity,

$$\frac{C_\delta}{\left(\sqrt{f_0}/\sqrt{f_{\varepsilon_r}}\right)-1}, \qquad \text{where } C_\delta = \frac{\varepsilon_r}{\left(f_0^2/f_{\varepsilon_r}^2\right)} - 1, \text{ from equation (4.26),}$$

were calculated by the model along with Q_0 as a function of electrical conductivity for various relative permittivities.

The model considers the surface of the cavity as a single homogeneous layer of electrical conductivity, σ. The electrical conductivities used in the model ranged from stainless steel $\left(\sigma \approx 0.1 \times 10^7 \Omega^{-1} m^{-1}\right)$ to pure silver $\left(\sigma \approx 4 \times 10^7 \Omega^{-1} m^{-1}\right)$[6]. These values encompass the range of electrical conductivities of the electroplated cavity over its entire working temperature range. The model assumes the physical dimensions of the cavity are those at ambient conditions.

The relative permittivities used in the electrical model ranged up to $\varepsilon_r = 1.6$. These values encompass the range of permittivities of fluids such as natural gas and ethylene at pressures up to 12 MPa and temperatures up to 40°C. The choice of ε_r used in the electrical model is however arbitrary since it has been found that the relationship between C_δ and Q_0 may be considered independent of ε_r.

The relationship between computed C_δ and Q_0 is illustrated in graph (4.2) below:-

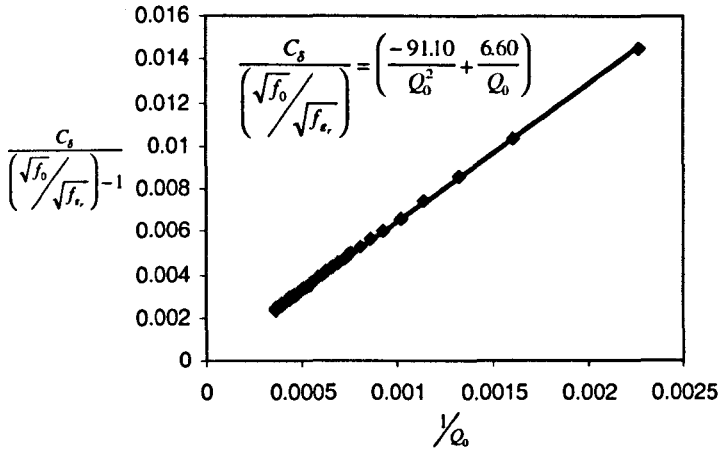

Graph 4.2 Relationship between computed C_δ and Q_0.

From graph (4.2) and equation (4.32) it can be seen that for the specific cavity geometry, $\bar{x}$, the correction factor for the dilation of the cavity due to change in penetration depth is:-

$$C_\delta = \frac{1}{Q_0(t)}\left(B - \frac{C}{Q_0(t)}\right)\left(\frac{\sqrt{f_0(t)}}{\sqrt{f_{\varepsilon_r}(t)}} - 1\right), \tag{4.33}$$

where $Q_0(t)$ is the quality factor of the evacuated cavity at temperature t;

$f_0(t)$ is the resonant frequency of the evacuated cavity at temperature t;

$f_{\varepsilon_r}(t)$ is the resonant frequency of the fluid filled cavity at temperature t; and

B, C are constants, such that $B = 6.60$ and $C = 91.10$.

In equation (4.33) the second order Q_0 coefficient is weakly dependent upon ε_r, however, over the range of permittivities considered, the effect on C_δ has been found to

be negligible. The second order Q_0 coefficient used in equation (4.33) is the median of the coefficients found in the range up to $\varepsilon_r = 1.6$.

The correction factor due to change in penetration depth has been verified by using the electrical model to calculate the resonant frequency of an evacuated cavity whose dimensions have been altered to match those of a filled cavity, $f_{0(\delta_{\varepsilon_r})}$. If this frequency is substituted into equation (4.25) the equation now becomes exact as the spatial distribution of the electric and magnetic fields within the resonator are identical in both the evacuated and filled configurations, and can be expressed as:-

$$\varepsilon_r = \left(\frac{f_{0(\delta_{\varepsilon_r})}}{f_{\varepsilon_r}} \right)^2 \tag{4.34}$$

where $f_{0(\delta_{\varepsilon_r})}$ is the resonant frequency of the evacuated cavity having the dimensions of the filled cavity; and

f_{ε_r} is the resonant frequency of the filled cavity.

Equation (4.34) is therefore equal to equation (4.30) and is confirmed on comparison of results obtained from the electrical model.

For a dielectric filled cavity of $\varepsilon_r = 1.1$, such as natural gas at 10 MPa at ambient temperature and having an electrical conductivity of $(\sigma \approx 2.5 \times 10^7 \Omega^{-1} m^{-1})$, the difference between the predicted resonant frequency from equation (4.25) and the true resonant frequency, obtained from the electrical model is ≈ 36 ppm, resulting in a correction of ≈ 72 ppm for the dilation of the cavity due to change in penetration depth. For a dielectric filled cavity of $\varepsilon_r = 1.6$, such as ethylene at 12 MPa at ambient temperature and having an electrical conductivity of $(\sigma \approx 2.5 \times 10^7 \Omega^{-1} m^{-1})$, the

difference between the predicted resonant frequency from equation (4.25) and the true resonant frequency, obtained from the electrical model is ≈ 186.5 ppm, resulting in a correction of ≈ 373 ppm for the dilation of the cavity due to change in penetration depth.

The estimated total uncertainty in the correction factor C_δ is $\pm 0.05\, C_\delta$. The latter takes account of the uncertainties introduced by imperfections in the electrical model of the cavity.

4.9 The Influence of Temperature

Temperature influences the resonance characteristics of the cavity in two ways. Through:-

- the dilation of the cavity with temperature; and
- the change in the electrical conductivity of the internal surface layer.

The combined effects of temperature can be fully accounted for by undertaking a series of measurements of the resonant frequency of the evacuated cavity over the range of operating temperatures. These measurements can then be represented by an expression of the form:-

$$f_0(t) = f_0(20).\left(1+\sum_{i=1}^{n}\alpha_i.(t-20)^i\right), \tag{4.35}$$

where $f_0(20)$ and α are constants obtained from regression.

If measurements of the quality factor of the evacuated cavity are also obtained over the range of operating temperatures they can be represented by an expression of the form:-

$$Q_0(t) = Q_0(20).\left(1+\sum_{i=1}^{n}\beta_i.(t-20)^i\right), \tag{4.36}$$

where $Q_0(20)$ and β are constants obtained from regression.

Provided no changes are made to the assembled cavity, its electrodes, or to the internal surfaces, constants established for equations (4.35) and (4.36) should remain valid for a prolonged period of time.

4.10 Final Operating Equation

With the correction factors and relationships established in the preceding sections the operating equation, for the permittivity of the enclosed medium, becomes:-

$$\varepsilon_r(t,p) = \left[\frac{f_0(20).\left(1+\sum_{i=1}^{n}\alpha_i.(t-20)^i\right)}{f_{\varepsilon_r}(t,p)}\right]^2.(1+A.p).$$
$$\left[1+\frac{1}{Q_0(20).\left(1+\sum_{i=1}^{n}\beta_i.(t-20)^i\right)}\right]\left[B-\frac{C}{Q_0(20).\left(1+\sum_{i=1}^{n}\beta_i.(t-20)^i\right)}\right]\left[\frac{\sqrt{f_0(t)}}{\sqrt{f_{\varepsilon_r}(t)}}-1\right] \tag{4.37}$$

where $f_0(20)$, $Q_0(20)$, α and β are constants obtained from the regression of the resonance frequency and quality factor measurements in vacuum;

$f_{\varepsilon_r}(t,p)$ is the measured resonance frequency at the conditions of measurement;

p is the absolute pressure in Pa; and

t is the temperature in Celsius.

4.11 Uncertainty in Calculated Permittivity

The main parameters to be determined for a measurement of permittivity using the re-entrant cavity method are:-

- the temperature of the cavity;
- the resonant frequency of the evacuated cavity at temperature t; and
- the resonant frequency of the filled cavity at the conditions of measurement.

The system pressure, p, and the quality factor, Q, of the evacuated cavity at temperature t also enter into the calculation but are required only for low order corrections.

The resonant frequency of the evacuated cavity is obtained from the correlation of vacuum frequency measurements, equation (4.35). The uncertainty, at a 95% confidence level, in this value is:-

$$U_{f_0}^2 = \left(2\sigma_{regression}\right)^2 + \left(\frac{\partial f_0(t)}{\partial t}.U_t\right)^2 \tag{4.38}$$

where $\sigma_{regression}$ is the standard deviation resulting from the regression of the measured $f_0(t)$ values; and

U_t is the estimated uncertainty, at a 95% confidence level, in the measurement of temperature.

The estimated uncertainty in the measurement of temperature is 4 mK.

The uncertainty in the measurement of relative permittivity at the conditions of measurement is given by the expression:-

$$\left(\frac{U_{\varepsilon_r}}{\varepsilon_r}\right)^2 = 4.\left[\left(\frac{U_{f_0}}{f_0}\right)^2 + \left(\frac{U_{f_{\varepsilon_r}}}{f_{\varepsilon_r}}\right)^2\right] + \left[\frac{U_{C_p}}{1+C_p}\right]^2 + \left[\frac{U_{C_\delta}}{1+C_\delta}\right]^2,$$

$$\approx 4.\left[\left(\frac{U_{f_0}}{f_0}\right)^2 + \left(\frac{U_{f_{\varepsilon_r}}}{f_{\varepsilon_r}}\right)^2\right] + \left[0.1\,C_p\right]^2 + \left[0.05\,C_\delta\right]^2 \qquad (4.39)$$

where U_{f_0} is obtained from equation (4.38); and

f_0 is obtained from equation (4.35).

The mean value of the frequency, f_{ε_r}, and the uncertainty in the same, $U_{f_{\varepsilon_r}}$, are obtained from the analysis of a set of up to 16 measurements of resonance frequency made at each measurement condition.

4.12 Influence of Temperature Gradients and Heat Transfer Modes on the Operation of the Re-Entrant Cavity

As previously mentioned the relationship between permittivity and the resonance frequency of the cavity only applies if the spatial distribution of the electric and magnetic fields within the resonator are identical in the evacuated and filled configurations at the same temperature of measurement. Two factors were identified which influenced the dimensions of the cavity these are:-

- the dilation of the filled cavity with applied pressure; and

- the effective dilation of the filled cavity due to a change in the electromagnetic penetration depth.

If the re-entrant cavity were to be operated in a poorly thermostated environment then an additional, but less easily quantifiable, factor also applies. The temperature distribution in the evacuated cavity may differ from that in the fluid filled cavity. In the former case, the temperature of the stem and bulbous extension and the temperature of the enclosing shell are governed largely by the heat flow through the pressure vessel plug. After an adequate period of time the temperature of the stem and bulbous extension will approach that of the pressure vessel plug. The temperature of the shell, however, is also influenced by heat flow through the annulus between it and the inner wall of the pressure vessel.

When this annular gap is evacuated only small amounts of energy can be transferred by radiation from the low emissivity surfaces and the temperature of the shell is likely to be that of the stem and the bulb. However, when the cavity is filled with gas, heat transfer in the outer annulus is mainly by gaseous conduction and convection. If the temperature of the pressure vessel wall is everywhere the same as the pressure vessel plug then the temperature of the stem, bulb and shell will approach some uniform temperature. However, were a vertical temperature gradient to exist in the thermostat then the temperature distribution in the re-entrant cavity would differ from that in the evacuated case though the thermometer in the bulbous extension indicated the same temperature.

Calculations using the electrical model have shown that if the lower half of the shell were some 10 mK lower in temperature from that of the stem and bulb the error in measured permittivity would be 1.5 ppm. Care should therefore be taken to ensure that adequate thermostating is applied. If this is not possible, for example in the field apparatus, then vacuum measurements should be avoided completely. Instead the reference resonance frequency, $f_0(t)$, should be established from measurements on a known fluid such as helium or methane at ambient pressure.

References

1. Bleaney, B.I. and Bleaney, B. *Electricity and Magnetism*; Clarendon Press, Oxford, 1959.
2. Boylestad, R.L. *Introductory Circuit Analysis*; Macmillan Publishing Company, New York, 1990.
3. Watson, J.T.R. *The Relative Permittivity of Oils*; Flow Centre Report No. 251/99 produced for NMSPU; National Engineering Laboratory, East Kilbride, Glasgow, June 1999.
4. Goodwin, A.R.H., Mehl, J.B. and Moldover, M.R. *Reentrant radio-frequency resonator for automated phase-equilibria and dielectric measurements in fluids;* Rev. Sci. Instruments, 1996, 67(12), 4294-4303.
5. Marcuwitz, N. *Waveguide Handbook;* McGraw-Hill, New York, 1951
6. Kaye G.W.C, Laby T.H *Tables of Physical and Chemical Constants;* Longman Group Ltd. 1995.

5. Pressure Effect Corrections

This chapter describes the finite element analysis studies that were carried out on the re-entrant cavity resonator in order to obtain an accurate model of the dimensional stability of the cavity with applied pressure. The chapter gives a brief overview of finite element analysis and describes the criteria that must be satisfied in order to conduct a linear structural analysis. The process of setting up the finite element model in terms of simplification and modelling of the geometry, the element selection and mesh generation and the application of loads to the structure is described.

The results obtained from the analysis are reviewed and the important structural displacements are identified and presented at an operating cavity pressure of 10 MPa. The results are verified to be of the correct order of magnitude by an appropriate hand calculation and are further validated by conducting a separate finite element structural analysis on a cylindrical structure of which the expressions of radial dilation with pressure are known. The results of this validate the finite element analysis. The accuracy of the results is mainly dependent on the uncertainty in the material properties of the cavity, namely the elastic modulus, or Young's modulus, which is known at best to 10%.

The chapter also includes the process of element type selection and mesh density selection. The choice of element type was made by comparing results obtained from an analysis using two different types of element. The mesh density selection was done by carrying out a mesh refinement technique on the selected element.

The chapter's last section summarises the methods used in the assessment of the results obtained from the finite element analysis.

5.1 Introduction to Finite Element Analysis

Finite element analysis[1] is essentially an approximate method for calculating the behaviour of a real structure by performing an algebraic solution of a set of equations describing an idealised model structure with a finite number of variables. The essence of the approach is to use a computer to represent this model structure using a discretised approach, where the geometric shape or internal stress-strain-displacement fields are described by a set of elements bounded by a mesh or grid of lines and surfaces. Each element is assumed to be defined by its boundary geometry, its material properties and basic parameters such as thickness and cross-sectional area. It is also possible to assume allowable displacement shapes for these elements, for example, linear, quadratics, polynomials, trigonometric functions and so on. The individual elements have to be assembled together in such a way as to ensure the displacements and stresses are continuous in some fashion to adjoining elements across the structure, the internal stresses are in equilibrium with each other and the applied loads and the prescribed boundary conditions are satisfied. The behaviour of the complete, idealised structure is determined as the total sum of the behaviour of its elements.

In solving any structural problem, whatever the type of structure, whatever the type of loading (static or dynamic) and whatever the nature of the structure's material, there are only three types of argument that can be used. These three arguments are quite separate and distinct and it is important to understand their simplicity, considering the intricacies of the finite element. The arguments are:-

- Equilibrium:- These arguments relate stress to the applied forces, or often stresses to other stresses whether there are applied forces or not. For example, if a structure is excited dynamically then the inertia forces can be inserted into the equations of equilibrium as if the problem was still static. If

displacements are small then the equations of equilibrium are linear.

- Compatibility:- These relate strains to displacements and are purely geometrical arguments which depend on the definition of strain and the type of deformation and geometry of the particular structure. If the displacements are small then the compatibility equations are also linear.

- Stress-Strain Law:- These constitutive relations are empirical and depend on experimental evidence. They may include thermal effects, and for ferrous materials the relationship may be elasto-plastic with irreversible plasticity. For many structural materials within their useful working range these laws may be taken as linear.

In a structural analysis the variation of stresses and strains in an elastic body can be described by simultaneous differential equations. These equations cannot be solved for complex geometries, however they can be solved for simple shapes such as triangles or quadrilaterals, or any shapes that constitute an element. The main computational stage of a finite element analysis therefore consists of the solution of such a set of simultaneous equations. In a structural analysis these equations relate the displacements and rotations at the nodes to the forces and moments at the nodes.

It is important to note that the simultaneous equations are linear and that the method can only provide solutions directly for linear systems. For structures this generally implies the following limitations:-

- the material must obey Hooke's Law, i.e. the stress-strain curve must be linear for the range of strains considered;
- the load paths must be independent of the magnitude or sign of the loads;
- the displacements must be small; and
- the loads must not vary with displacements.

The basic concept in the finite element method is approximating a real structure by a finite element model made up of an assembly of these elements, i.e. simple shapes joined at common nodes. The actual problem is then solved by invoking the arguments of equilibrium, compatibility at the common nodes for each element, incorporating the appropriate stress-strain law and applying the known restraints and forces.

5.2 Purpose of Analysis

The objective of the finite element analysis was to obtain an accurate model of the dimensional stability of the re-entrant cavity resonator with applied pressure. A theoretical model of the cavity has been developed that enables the resonant frequency and quality factor to be calculated as a function of the cavity dimensions, $\bar{x}$ (see Chapter 4). Therefore, data on the dimensional changes, $\Delta\bar{x}$, of the cavity with pressure enables the corresponding frequency and quality factor changes to be calculated. The dimensional changes of the cavity were obtained using ANSYS (a finite-element analysis package produced by SAS IP Inc.).

A knowledge of the dimensional stability of the cavity with applied pressure allows the resonant frequency of the cavity to be corrected, and thus increases the accuracy of relative permittivity measurement. It should be pointed out that the aim of this analysis is solely to increase the accuracy of relative permittivity measurement and not to investigate the requirement for such a correction in terms of the relationship between relative permittivity and density of the fluid. Making the relative permittivity

measurement as accurate as possible enables the cavity to be used with a wide variety of gaseous and liquid systems.

The use of a separate pressure vessel to house the re-entrant cavity reduces the effects of pressure on the dimensions since there is applied pressure on the inside and the outside of the cavity, as illustrated in figure (5.1) below:-

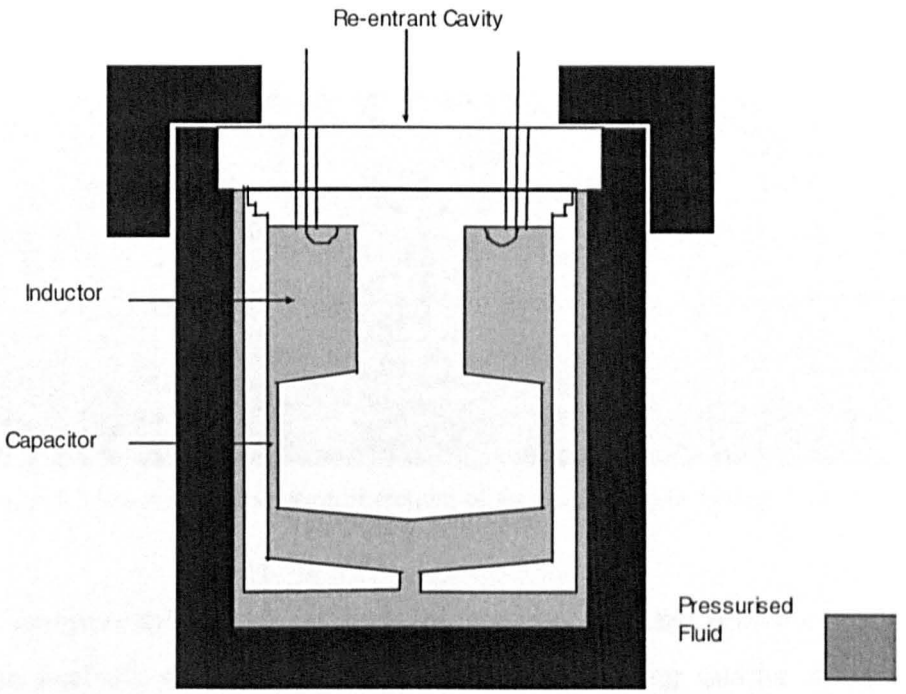

Figure 5.1 Schematic of Re-entrant Cavity and Pressure Vessel Housing.

The resonant frequency is mainly dependent on the values of the capacitive and inductive sections, which are, in turn, dependent on the resonator dimensions and thus the temperature and pressure of the gas contained within the cavity.

5.3 Finite Element Model

The geometrical structure used in the finite element analysis is a simplified version of the actual structure. As shown in figure (5.1), the lid of the resonator is extremely thick

in comparison to other resonator dimensions and is attached to the pressure vessel, therefore it was assumed that the dilation of this part of the cavity would be negligible and could be considered as a point of zero displacement and therefore need not be modelled. The finite element consists of the innershell and outershell of the cavity modelled from the lid of the cavity downwards. In order to simplify the analysis these two sections were modelled separately, maximising the number of elements that could be used and reducing running time of the computer. Both sections are illustrated in figure (5.2) below:-

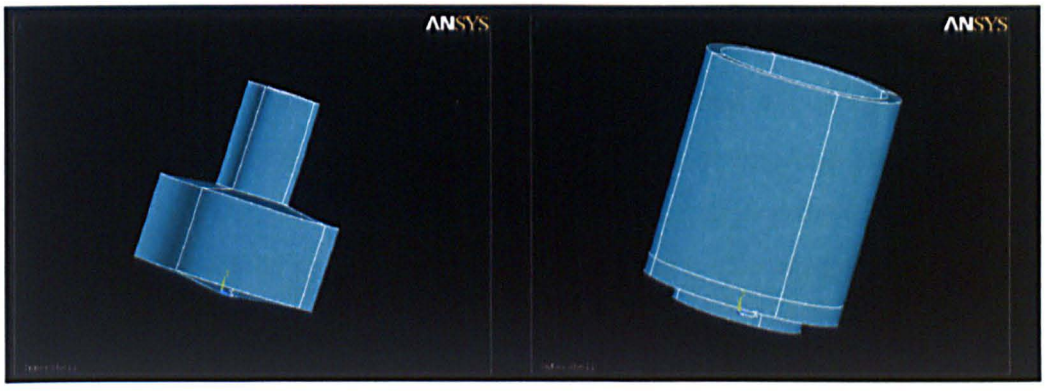

Figure 5.2 Innershell and Outershell sections of the cavity modelled using ANSYS.

Due to the axisymmetric nature of both the structure and the pressure loads on the structure the analysis was simplified further by considering quarter models of the structures illustrated in figure (5.2). This simplification again increases the number of elements that could be used and reduces the running time of the computer.

Due to the steady loading conditions on the structure the type of analysis is defined as a *static structural analysis*. Static analysis is used to determine displacements, stresses, strains and forces in structures caused by loads that do not induce significant inertia effects. As mentioned previously, the variation of stresses and strains in an elastic body can be described by simultaneous differential equations, however these equations are linear and the method can only provide solutions directly for linear systems, i.e. systems

that exhibit small stresses and strains. The type of analysis performed by ANSYS is therefore a *linear static analysis.*

In order to conduct a finite element analysis the structure geometry must first be defined and idealised as a series of discrete finite elements, known as a mesh. Using pre-processor and mesh generation programs which are graphically orientated, ANSYS enables the geometry to be defined and meshed automatically. This interactive method of generating the idealised structure through automatic mesh generation is termed *solid modelling*, where the geometry and boundaries of the mesh are defined by the user, but the actual nodes and elements are generated by the program. The geometry of the structure is described by a volume bounded by line segments which are in turn bounded by keypoints. A knowledge of these keypoints, line segments and areas is enough to completely describe the geometry of the structure. By specifying the number of elements to lie along the boundaries of the geometry or rather, the actual element size, the program can generate a mesh automatically. It is important to note that such an automatic mesh is non-unique since more than one type of mesh can be generated for any structure. A particular mesh will depend on factors such as, ordering of line segment definition, element size and the type of element used.

Since the models of the structure under consideration here are three dimensional, the choice of which type of element used to mesh the structure was naturally a solid 3-D element. The structural analysis was carried out using the SOLID 92 element[2], this element is of tetrahedral form and is ideally suited to model irregular meshes. The element is defined by ten nodes each having three degrees of freedom, translations in the nodal x, y, and z directions.

The density of the mesh used in the finite element method is limited by the maximum number of nodes that the software allows and therefore ultimately limited by the size and type of element used. For structural displacement any inherent finite element approximations arise in the satisfaction of the equilibrium conditions[3], the compatibility

conditions are usually satisfied exactly within the element and if they are also satisfied throughout the structure then the structural displacements will converge towards the true value as the element mesh is refined.

The art of using the finite element method is the choice of correct mesh density required to solve a problem. If the mesh is too course then the inevitable element distortions will result in an unstable solution. Alternatively, if the mesh is too fine then the running time may not justify the accuracy obtained. The process of meshing is therefore repeated until the structural displacements have converged to a suitable level of accuracy with a reasonable running time. It should be pointed out from an engineering point of view that convergence may not be necessary if the user is confident that the finite element model does represent the essential features of the real structure behaviour, therefore it is useful to have an idea of the expected structural displacement when evaluating the performance of the mesh.

Figure (5.3) illustrates meshed sections of the quarter model structures. The figure illustrates the smallest element sizes that were possible with the limitations of the software. The choice of the finest mesh available is justified in that there are negligible differences in running time for this problem by using either a coarse or a fine mesh, therefore it is obvious to chose the mesh which should produce the most accurate results. (See section 5.6 for details on mesh refinement).

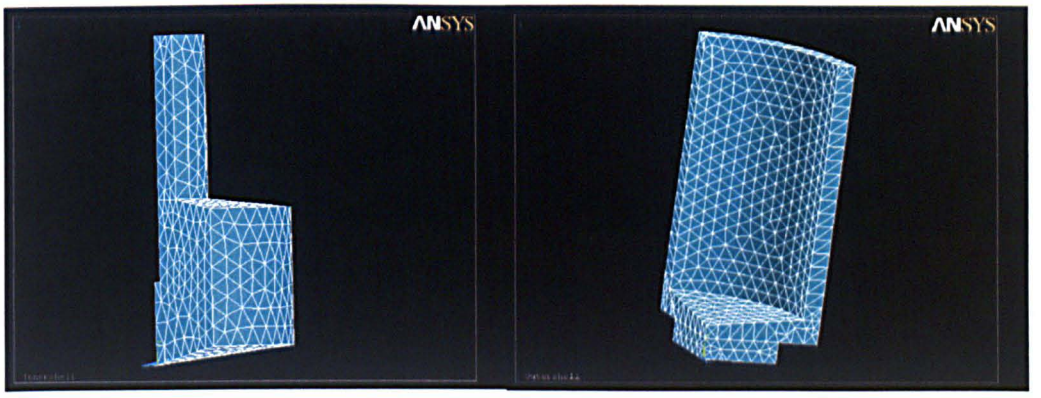

Figure 5.3 Automatic mesh generation of structures using the smallest allowable element size.

Once the structure has been idealised into the mesh of finite elements the loads must be applied to the model. The term loads in ANSYS include boundary conditions and externally or internally applied forcing functions[4]. The loads that need to be considered in this structural analysis are degree of freedom constraints and surface loads. A degree of freedom constraint fixes a degree of freedom to a known value, in a structural analysis examples of these are specified displacements and symmetry boundary conditions. The surface load in this case is obviously the pressure of the gas contained within the structure.

As mentioned previously the innershell and outershell structures have been modelled from the lid of the cavity downwards since it was assumed there would be zero displacement of this part of the cavity with applied pressure. The zero displacement of this section defines the first boundary condition, or degree of freedom constraint. The constraints applied to the structure must represent the actual physical problem and therefore the structure must be constrained somehow in all three degrees of freedom. Figure (5.4) illustrates all loads applied to the structures including degree of freedom constraints, symmetry and pressure.

(a) (b)

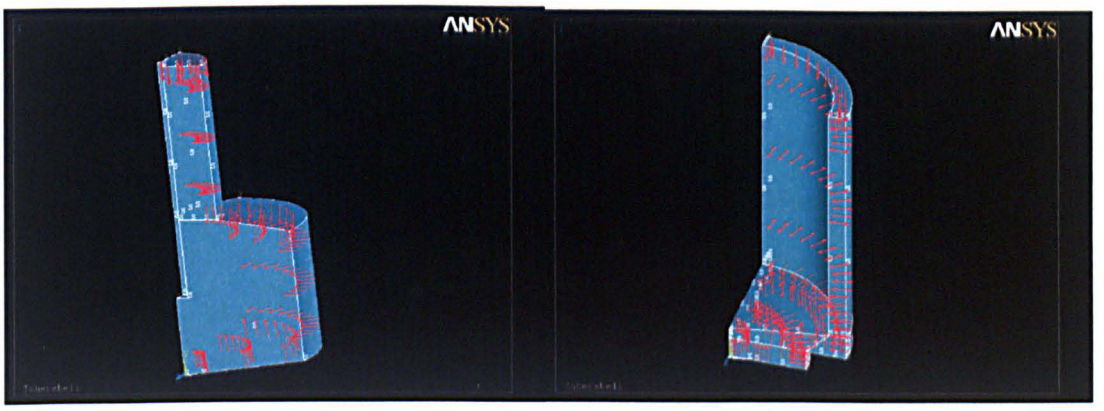

(c) (d)

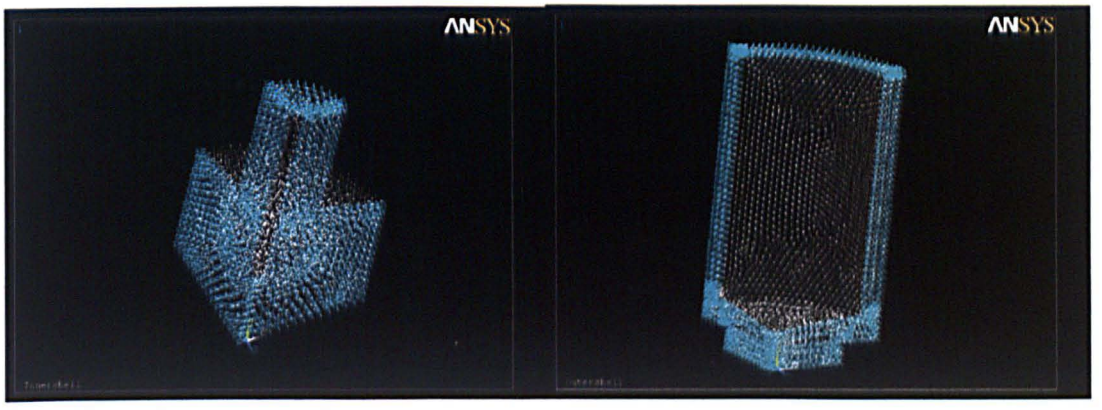

Figure 5.4 Loads applied to innershell and outershell. Figures (a) and (b) illustrate symmetry boundary conditions and pressure loading, (c) and (d) illustrate degree of freedom constrains.

Figure (5.4)(a) shows the planes of symmetry for the innershell structure, the planes lie perpendicular to each other and are marked by the symbol '*S*'. The pressure acting on the innershell is represented by the arrows, the direction of the arrows illustrates that the pressure only acts on the external surfaces of the innershell. Figure (5.4)(b) shows the planes of symmetry for the outershell structure, the planes again lie perpendicular to each other and are marked by the symbol '*S*'. The pressure acting on the outershell is again represented by arrows. The double headed arrows indicate that the pressure acts internally and externally on the outershell. Figures (5.4)(c) and (d) are nodal plots of the structure and both indicate the degree of freedom constraints placed on the innershell and outershell. Figure (5.4)(c) illustrates the innershell and shows the constraints on the

three degrees of freedom, one for each possible displacement direction. The nodes with the blue symbols attached indicate that displacement constraints have been applied to them. The nodes in the y-plane at the top of the stem have been constrained to have no displacement in the y-direction since this is where the lid of the cavity joins the innershell and its dilation has been assumed to be zero. The nodes on the plane of symmetry, $x = 0$, are constrained to have no displacement in the x-direction. Likewise the nodes on the plane of symmetry, $z = 0$, are constrained to have no displacement in the z-direction. These constraints simulate the actual way a cylinder would compress under axisymmetric pressure. Figure (5.4)(d) illustrates the outershell and again using a nodal plot of the structure shows the three degrees of freedom constraints. The constraints placed on the outershell are essentially the same as those of the innershell, the nodes in the y-plane at the top of the structure are constrained to have no displacement in the y-direction in the same manner as those of the innershell and the nodes constrained along the planes of symmetry again simulate the compression of an actual cylinder.

5.4 Interpretation of Results

The basic result of the finite element analysis is the deflection of the structure at the node points. Other results such as stresses and strains are then derived from the displacements. There are many variations that can be used for presenting these results, however graphical displays are often used to convey the results of an analysis. Figure (5.5) illustrates the results obtained from analysis of the innershell and the outershell at a pressure of 10 MPa. The mesh used in these results was constructed using the smallest element size available.

(a) (b)

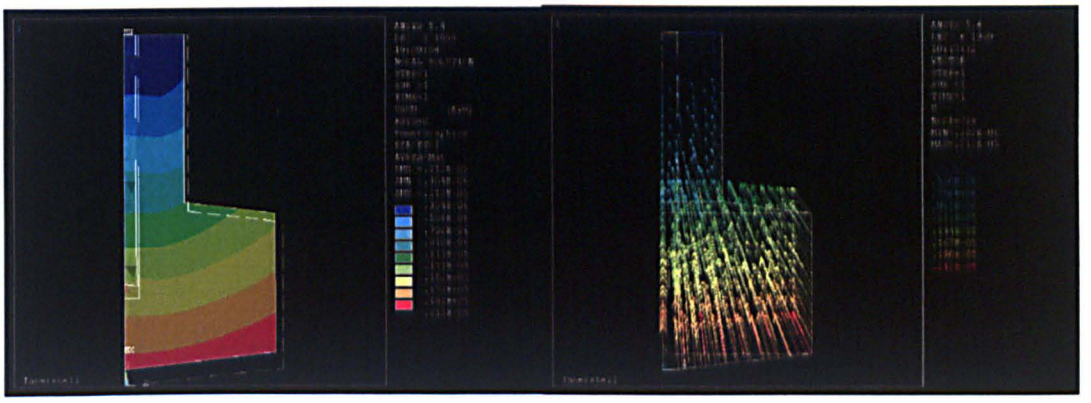

(c) (d)

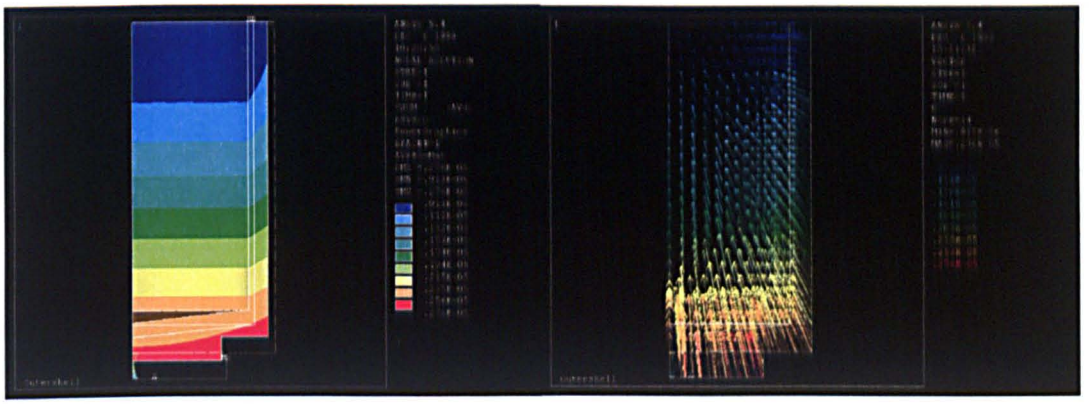

Figure 5.5 Results obtained from analysis of the innershell and the outershell at a pressure of 10 MPa. Figures (a) and (c) show the deformed and undeformed structures of the innershell and outershell respectively as well as the displacement values of the nodes. Figures (b) and (d) are vector plots and they illustrate the direction and magnitude of the nodal displacement.

Figures (5.5)(a) and (b) illustrate the deformed and undeformed structures of the innershell and outershell respectively and also show the displacement values of the nodes. The white outline is the undeformed structure and the coloured section is the deformed structure. The difference between the deformed and undeformed structures has been exaggerated for clarity.

It is obvious to see that the structures have been compressed by the applied pressure. These results are to be expected, even in the case of the outershell which has pressure acting internally and externally, since the pressure on the external surface acts on a larger surface area and therefore exerts a larger force on the external surface than on the internal surface. The coloured sections indicate the actual displacements of the nodes, calculated through a 3-D Pythagorean relationship.

Figures (5.5)(c) and (d) are vector plots of the innershell and outershell respectively and they illustrate the direction and magnitude of the resultant nodal displacement.

As mentioned previously the objective of the finite element analysis was to model the effects of change in cavity dimensions with applied pressure in order to calculate the resultant change in resonant frequency and quality factor of the cavity. Therefore, the important resonator dimensions are the radii and lengths that are used to calculate the capacitance and inductance of the cavity. These dimensions are given in Chapter 4 and illustrated in Figure (5.6) below:-

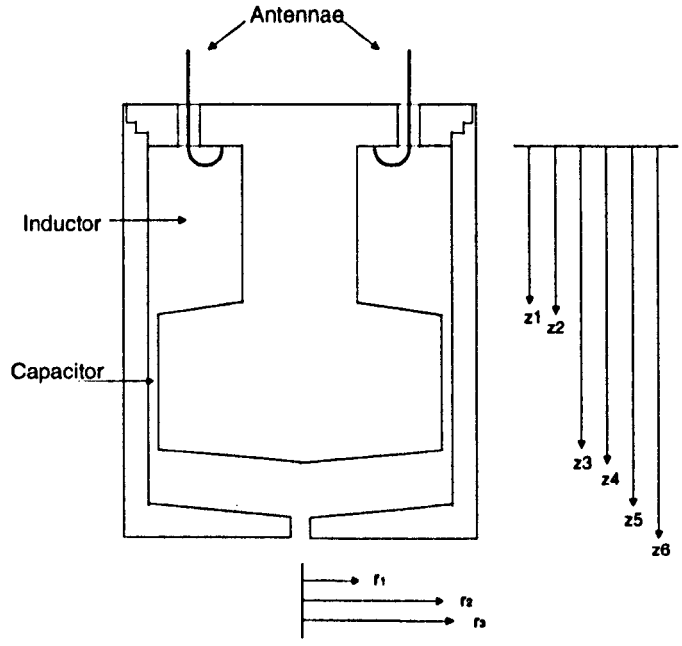

Figure 5.6 Dimensions of cavity. The radii and lengths are used to calculate the capacitance and inductance of the cavity.

The changes in these dimensions with an applied pressure of 10 MPa is shown in table (5.1) below:-

Dimensions	Length in mm	Change in length in m
r_1	10.98	0.425×10^{-6}
r_2	27.22	0.847×10^{-6}
r_3	29.22	0.913×10^{-6}
z_1	30.775	0.103×10^{-5}
z_2	32.775	0.115×10^{-5}
z_3	58.35	0.194×10^{-5}
z_4	61.34	0.201×10^{-5}
z_5	69.875	0.227×10^{-5}
z_6	75.94	0.237×10^{-5}

Table 5.1. Results of finite element model of innershell and outershell at applied pressure of 10 MPa.

Table (5.1) illustrates the results from the finite element model of the innershell and outershell at a maximum operating pressure of 10 MPa. Data for dimensional change at lower pressures were also recorded although not presented here.

5.5 Validation

It is good practice when carrying out a finite element analysis to examine the accuracy of the results obtained, since the finite element analysis is approximate in nature and it may not be possible to determine if the results of an analysis are right or wrong only if they are fit for their purpose. The first step in validating the results from the analysis is to verify that they are sensible i.e. the order of displacement magnitude is correct. This process was carried out by doing a compressibility hand calculation of the cavity[5]:-

$$\frac{\Delta V}{V} = \frac{P}{K}, \tag{5.1}$$

where $\frac{\Delta V}{V}$ is the fractional decrease in volume of body;

P is the applied pressure to the body; and

K is the bulk modulus of the body (taken to be approximately 100 GPa.)

With an applied pressure of 10 MPa the fractional decrease in volume of the body was found to be approximately 10^{-4}. Since $V + \Delta V = (L + \Delta L)^3$, where L is the length of the body, $\frac{\Delta L}{L} = \frac{1}{3}.\frac{\Delta V}{V}$, so $\frac{\Delta L}{L} = 30 \times 10^{-6}$ m, which is commensurate with the dimensional change data presented in table (5.1). This result confirms that the results from the finite element analysis were of the correct magnitude.

A second way of validating the results obtained from a finite element analysis would be to compare them to an analytical expression, however if such an analytical equation was available there would be no point in conducting a finite element analysis to begin with. If, however, there exists an analytical equation that represents a section of the structure being modelled, then such an equation could be used to verify and validate the results. The capacitance section shown in figure (5.1) is the major component of the total capacitance and is most sensitive to pressure owing to the small annular gap, $r_3 - r_2$. The results from the finite element analysis conducted on the innershell and outershell show as the pressure in the containment vessel is increased the principal dimensional change is a decrease in the length of both the capacitive and inductive sections of the cavity. The results also show that the ratio of the internal diameter of the cavity to the diameter of the bulbous extension remains virtually independent of pressure. This finding is in

accord with the theoretical expression for the deformation of an infinitely long thick walled cylinder.

Using the analytical equation for the radial dilation of an infinitely long cylinder[6], the radial displacement, U, of an arbitrary point R in the cylinder is given by:-

$$U = R.\frac{(1-\mu).(a^2 p_i - b^2 p_0)}{E(b^2 - a^2)} + \frac{1}{R}\frac{(1+\mu)a^2 b^2 (p_i - p_0)}{E(b^2 - a^2)} \tag{5.2}$$

where a is the internal diameter;

b is the external diameter;

p_i is the internal pressure;

p_0 is the external pressure;

E is the modulus of elasticity; and

μ is Poisson's ratio.

In the case considered here the same pressure is applied to both the inner and outer surfaces of the cylinder, therefore $p_i = p_0 = p$, and equation (5.2) reduces to:-

$$U = -R\frac{(1-\mu)p}{E}. \tag{5.3}$$

Equation (5.3) shows that the displacement is independent of the diameter of the cylinder and dependent only on pressure and material properties. The displacement of the internal diameter, D, of the outer cylinder is given by:-

$$U_{Outer} = -D\frac{(1-\mu)p}{E}, \tag{5.4}$$

and for the outer diameter, d, of the inner cylinder given by:-

$$U_{Inner} = -d\frac{(1-\mu)p}{E}. \tag{5.5}$$

It can then be shown that the ratio of these two diameters, D and d changes with pressure according to:-

$$\frac{D(p)}{d(p)} = \frac{D(0) - D(0)(1-\mu)p/E}{d(0) - d(0)(1-\mu)p/E} = \frac{D(0)}{d(0)} \tag{5.6}$$

where $D(0)$ is the internal diameter of the outer cylinder at vacuum;

$d(0)$ is the outer diameter of the inner cylinder at vacuum;

$D(p)$ is the internal diameter of the outer cylinder at pressure p; and

$d(p)$ is the outer diameter of the inner cylinder at vacuum.

Equation (5.6) shows that the ratio of the diameters of the cylinders are independent of pressure. This calculation is only true for the specific case of an infinitely long cylinder. In the case under consideration here the cylinders are completely surrounded by fluid and the ends of the cylinders are also subject to longitudinal tensile stress therefore decreasing the length of the cylinders and increasing their diameters.

Using ANSYS a separate finite element model structural analysis was undertaken to model the effects of pressure on the dimensional stability of an 'infinitely' long cylinder in order to verify the results of the analytical expression. The case of an infinitely long cylinder with applied internal and external pressure is not dissimilar to the actual finite element analysis of the cavity. Therefore, by validating the analytical expressions for the cylinder using ANSYS this can also be considered as a verification of the ANSYS

method, since both problems have similar geometry, boundary conditions, symmetry and pressure loadings.

A finite element model of an infinitely long cylinder was constructed using such techniques as described in section 5.3. The results from the analysis for the displacements of the inner and outer radii of the cylinder were found to be in agreement with the analytical expressions of equations (5.4) and (5.5), thus verifying the ANSYS method and results.

The estimated uncertainty in the dimensional changes, $\Delta\bar{x}$, in the cavity dimensions, $\bar{x}$, due to pressure is $\pm 0.1\,\delta\bar{x}$. The main uncertainty in this type of analysis arises from the uncertainty in material properties; namely the modulus of elasticity, or Young's modulus (128 GPa), and Poisson's ratio (0.3) which are know at best to 10%.

5.6 Mesh Specification

This section explains the importance of mesh refinement for a finite element analysis and how the element type and mesh density were selected for the innershell and outershell components of the cavity.

Mesh refinement is essentially the technique of making the approximations incorporated into the element interpolation functions become closer to the exact solution as the mesh is refined. Or rather as the mesh density is made finer the structural displacements should converge towards the true value. Therefore, mesh refinement means to repeat the meshing procedure using smaller element sizes until a mesh is obtained that yields structural displacement results that have converged to a suitable level of accuracy, whilst having only a modest running time.

As mentioned previously the element used in the analysis was the 3-D solid element, SOLID 92, which is of tetrahedral form and consists of ten nodes. However, when

conducting a mesh analysis it is good practice to check the suitability of element choice by conducting the analysis with another element type and comparing the results. A comparison of results was carried out using the 3-D solid element, SOLID 72, which is similar to the SOLID 92 element except it has fewer nodes thus making it less accurate than the SOLID 92. The comparison of results obtained from both element types showed there to be a negligible difference in structural displacements. Therefore, since the SOLID 92 element has more nodes than SOLID 72 element it should have a greater accuracy and was therefore used in the finite element model.

The process of mesh refinement was carried out on both the innershell and the outershell. The element size was varied from the extremes of the minimum number needed to represent the structural continuum to the maximum number allowed by the software. The finite element model's sensitivity to mesh density is illustrated in graph (5.1) by observing the structural displacement of the dimension Z_4 over the range of element sizes with an applied pressure of 10 MPa.

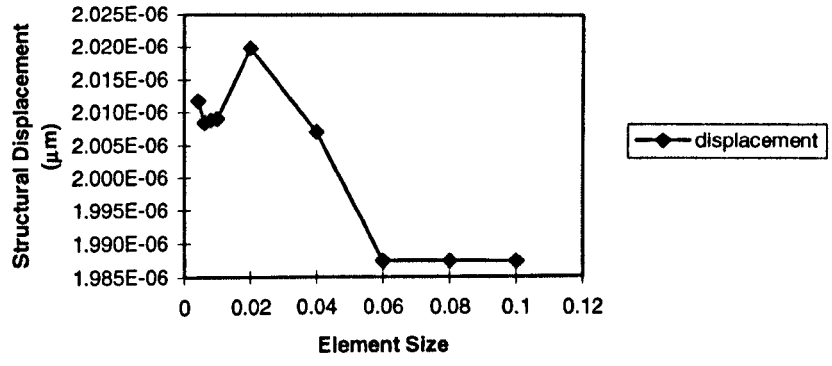

Graph 5.1 Sensitivity of structural displacement to changes in element size. The changes to the dimension Z_4 data were taken from the innershell model at a pressure of 10 MPa.

It can be seen from graph (5.1) that the finite element model is not especially sensitive to mesh density, since the displacements are all in agreement to within approximately

$0.04\mu m$ (similar results are obtained for all other dimensions under consideration). There is also no real convergence of structural displacements with increasing mesh density to a true value as predicted. This result is due to the fact that ANSYS is known to predict accurate results for simple static analysis of this type and that the initial, coarse, mesh is likely to produce results of sufficient accuracy without the need for refinement. It was also pointed out previously that convergence may not be necessary if the user is confident that the finite element model does represent the essential features of the real structure behaviour. However, since it is known that the accuracy of a model improves with increasing mesh density and the finest mesh possible in this case has a short running time, the smallest element size was used to carry out the finite element analysis.

Analysis of the results of the electrical model of the cavity (see Chapter 4) showed that the uncertainty in the changes to the cavity dimensions, $\Delta\bar{x}$, have to be less than $0.1\mu m$ in order to maintain an accuracy in frequency of 0.5 ppm. It was found that this accuracy was easily achievable and from graph (5.1) the differences in structural displacements between a coarse mesh and a fine mesh may be considered negligible.

5.7 Assessment of Results

The results obtained for the finite element analysis on the innershell and outershell have been checked using an appropriated hand calculation to make sure they are of the correct magnitude. The results and method of the finite element analysis have also been verified by conducting a separate analysis on an infinitely long cylinder which acts in a similar fashion to the capacitive section of the resonator. The results of which were in agreement with the analytical expression of the same. The innershell and outershell models were both found to be insensitive to mesh refinement. The reason for this was that ANSYS is known to be accurate for small structural displacements and therefore the results obtained from a coarse mesh may be just as accurate as those from a fine mesh.

The comparison of results of analysis using SOLID 72 and SOLID 92 elements showed there to be a very small difference in structural displacements, therefore, the choice of element type has been justified by the fact that the SOLID 92 element is known to be more accurate than the SOLID 72 element.

The mesh refinement technique that was carried out showed that the models were insensitive to mesh density, therefore, the choice of the smallest element size possible was justified by the fact that meshes with more elements are known to produce greater accuracy and there was no significant increase in running time of the analysis.

References

1. NAFEMS (National Agency for Finite Element Methods and Standards), *A Finite Element Primer,* The Department of Trade and Industry, National Engineering Laboratory, East Kilbride, Glasgow, 1991.
2. ANSYS Element Reference Manual, 1994
3. Department of Mechanical Engineering, University of Strathclyde course notes, *An Introduction to Finite Element Analysis using ANSYS*, 1995.
4. ANSYS Structural Analysis Guide, 1994
5. Ashby, M.F., Jones D.R.H. *Engineering Materials 1, An Introduction to their Properties and Applications;* Pergamon Press, Oxford, 1987.
6. J.F. Harvey, *Pressure Vessel Design: Nuclear and Chemical Applications*, Nuclear Science Series TS-283-H2 (Van Nostrand Company, Princeton, N. J., 1963)

6. Experimental Measurements, Facility and Operation

The theory and method of measuring the relative permittivity of research grade ethylene are described. The measurement principle consists of comparing the resonant frequency of the re-entrant cavity resonator under evacuated and fluid filled conditions at the same temperature over a specified range of conditions.

Modifications to the National Density Standards facility at the National Engineering Laboratory that were required to allow reference-quality measurements of relative permittivity to be undertaken are described.

A technical description of the permittivity cell and associated components is given. Particular emphasis is given to the design, material selection and operation of the re-entrant cavity resonator.

Detailed descriptions of the temperature measurement and control, pressure measurement and frequency measurement apparatus are given along with operational methods and procedures. The experimental procedure and operation is also outlined with specific regard given to the filling circuit.

The measureands recorded at each state point are detailed with specific regard given to the measurement of pressure. The determination of the pressure of the fluid within the permittivity cell is quite complex since it requires correcting for a small head of pressure that exists between the differential pressure transducer mounted on top of the thermostating system and the permittivity cell mounted within the thermostating system.

6.1 Measurement Theory

The density and temperature dependence of the relative permittivity of non-polar fluids, such as natural gases and high value fluids, such as ethylene, can be accurately described by the molar Clausius-Mossotti relation:-

$$\frac{(\varepsilon_r - 1)}{(\varepsilon_r + 2)} \cdot \frac{1}{\rho_m} = A_{\varepsilon_r} + B_{\varepsilon_r}(t)\rho_m + C_{\varepsilon_r}(t)\rho_m^2 + \ldots, \qquad (6.1)$$

where ε_r is the relative permittivity;

ρ_m is the molar density; and

A_{ε_r}, B_{ε_r} and C_{ε_r} are termed dielectric virial coefficients.

In order to determine the density of a fluid from a precise measurement of relative permittivity it is necessary to have an established relationship, such as equation (6.1), between the relative permittivity, temperature and density of the fluid. This fluid *mapping* or *characterisation* can be established from a series of reference quality relative permittivity and density measurements in the laboratory. Regression of these measurements then yields the virial coefficients A_{ε_r}, B_{ε_r} and C_{ε_r} of equation (6.1) and an expression for the density of the fluid in terms of relative permittivity and temperature. These parameters need only be established once for each fluid system.

Reference quality relative permittivity measurements were made on research grade ethylene at temperatures between 0 and 40 °C and at pressures up to 120 bar using the National Density Standards facility at the National Engineering Laboratory (NEL)[1]. Density measurements would normally have been made simultaneously with the UK's primary standard densitometer, however the geometry of the permittivity cell was such that it was not possible to accommodate both of these instruments into the same temperature controlled bath (see figure (6.1)). As a result of this the density had to be

derived separately from the latest reference quality equation of state for this fluid by Smukala, J., Span, R. and Wagner, W.[2]. In order to obtain accurate density data from the equation of state it is necessary to measure the fluid temperature and pressure to a high degree of accuracy.

The reference quality relative permittivity measurements together with the derived density from the equation of state enables the relationship between the relative permittivity, temperature and density of the fluid to be determined very accurately.

The target total uncertainty in density is 0.03% over the entire operational range.

6.2 Experimental Apparatus

Reference quality relative permittivity measurements were made using the National Density Standards facility at NEL. The measurement techniques employed are fully traceable to the fundamental physical standards of measurement maintained by the National Physical Laboratory.

Certain modifications were made to the facility in order to allow reference-quality measurements to be undertaken on ethylene, these were:-

- the use of an alternative method of pressure measurement;
- the design and construction of a new lid for the temperature controlled bath;
- the design and construction of a new piece of support apparatus to accommodate the permittivity cell in the temperature controlled bath; and
- the design and construction of various sections of pipework.

The accuracy of pressure measurement required for measurements of this kind necessitated the incorporation of a Yokogawa EJA130A differential pressure transducer (DPT) into the existing pressure measurement system. However, due to the fact that it

was not possible to accommodate the DPT into the temperature controlled bath alongside the permittivity cell, it was decided to design a new lid for the temperature controlled bath that would allow the DPT and associated pipework to be mounted on it and therefore as close to the cell as possible.

The apparatus is illustrated in figure (6.1) below:-

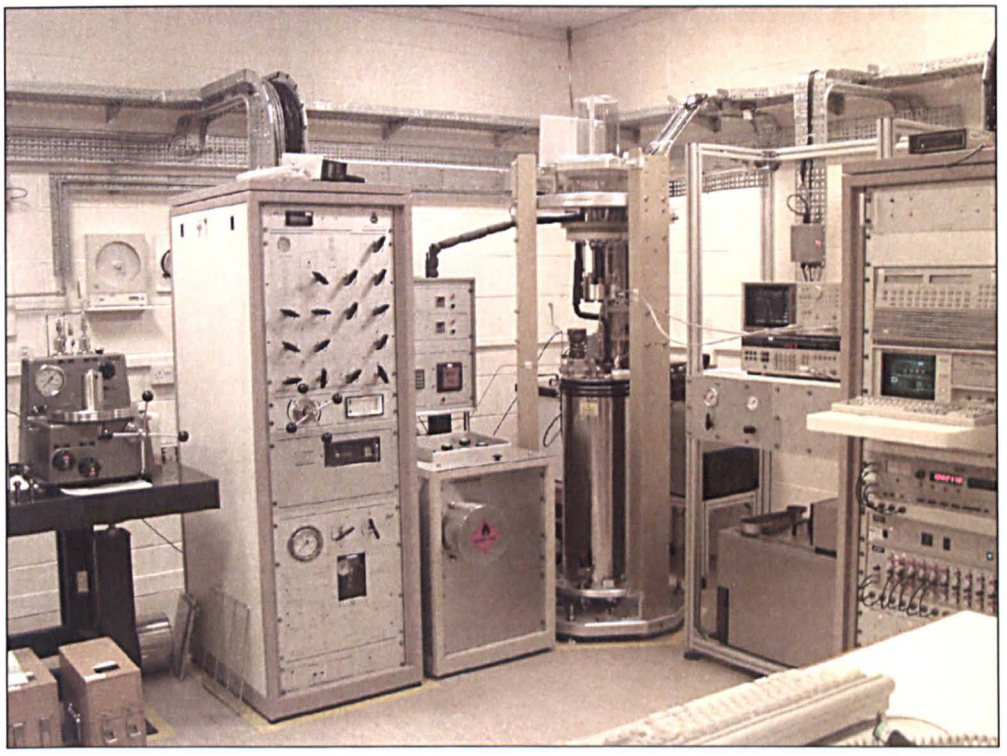

Figure 6.1 Experimental apparatus.

A schematic diagram of the apparatus is given in figure (6.2). The central element in the apparatus is the permittivity cell which is mounted within the temperature controlled bath on a support rig that also accommodates three standards grade platinum resistance thermometers (PRT's) that are used as part of the temperature measurement and control system. The cell is filled from the filling circuit which is housed in a temperature-stabilised enclosure. The pressure in the cylinder may be raised by increasing the ambient temperature of the enclosure. A Paroscientific pressure transducer (PT) type

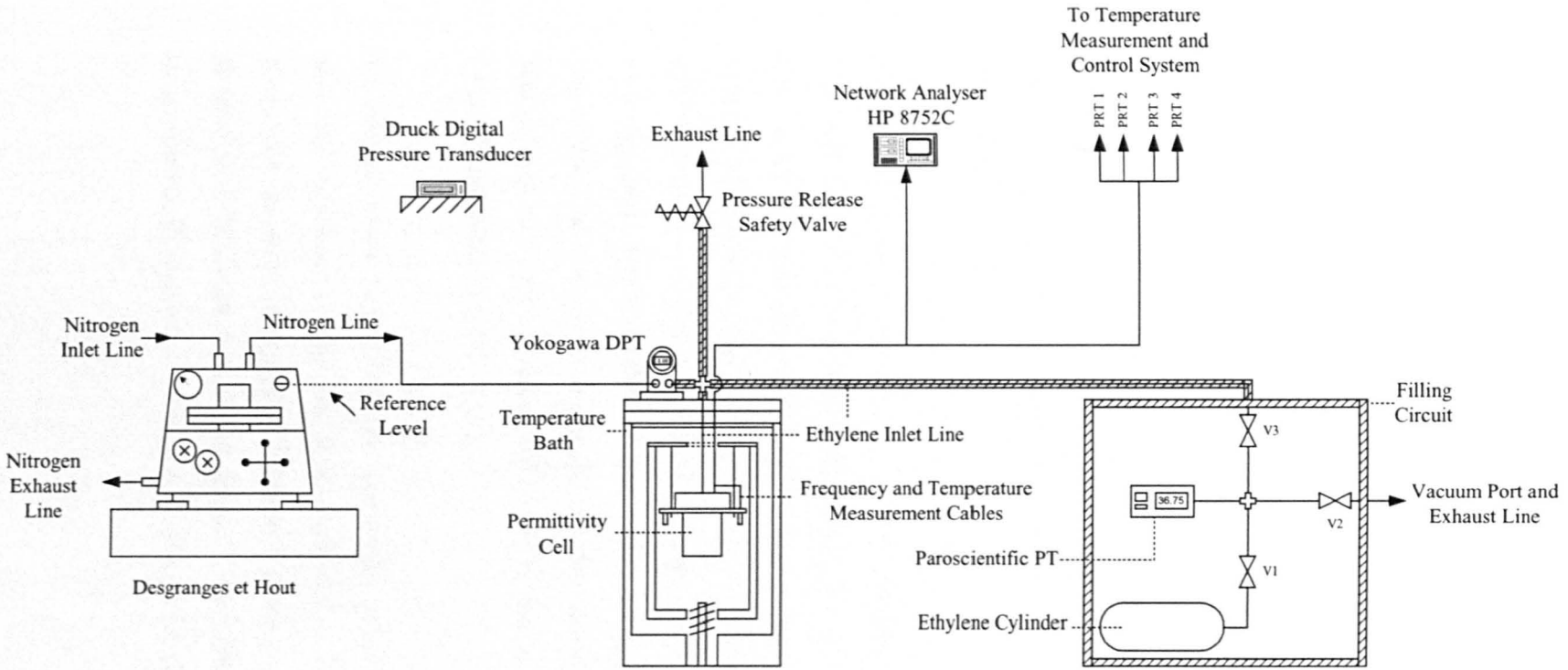

Figure 6.2 Experimental apparatus.

43K-101, also housed within the filling circuit, was used to give an indication of the cylinder, or permittivity cell, pressure. Pressure measurement is achieved through a Desgranges et Huot (D&H), metrology class S2, gas-operated pressure balance together with the Yokogawa DPT and two Druck digital pressure transducers (PT's). The resonant frequency of the cavity was measured with a Hewlett Packard 8752C Network Analyser.

6.3 Permittivity Cell - General Description

The following section contains an overview of the technical features of the permittivity cell and associated components. The relative permittivity apparatus consists of the re-entrant cavity resonator housed within a specially designed pressure containment device, or pressure vessel.

The re-entrant cavity resonator is a self-contained vessel, which can be filled with the test fluid. It is fabricated using only metal parts and glass-insulated feed-throughs. Inside the cavity, the test dielectric fluid fills a volume consisting of two separate toroidal sections. The first of these has a relatively large annular gap, which at radio frequencies (RF) behaves as an inductor, and the second, with a much smaller annular gap, behaves as a capacitor. The inductive section of the cavity is provided with two antenna where one of these acts as a transmitter and couples an external RF source to the cavity and the second acts as a receiver and couples the magnetic component of the internal field to an external detection system.

Re-entrant cavity resonators have particular advantages over other resonant devices in that the resonance modes are well separated in frequency, and the fundamental, low frequency, mode is both stable and non-degenerate. For the present design of cavity the fundamental resonant mode is at around 395 MHz and is well separated from higher order modes, the nearest of which is at around 1.8 GHz.

The physical design of the cavity is such that it can be analysed using a relatively simple lumped-element model or a more complex coupled coaxial waveguide model. The internal geometry exhibits a relatively large capacitance element with overall dimensions optimised for the highest attainable electrical quality factor, Q[3]. The resonant frequency of the cavity is inversely proportional to the square root of the relative permittivity of the fluid contained within it. The value of permittivity for a particular fluid may be obtained with reference to resonant frequency measurements made on the evacuated and fluid filled cavity. With precise frequency determination and the application of corrections for temperature, pressure and electromagnetic penetration depth effects (see section 4.5), uncertainties in calculated permittivities down to part per million are readily attainable.

The cavity, consisting of four main components (the metal top-plate and its bulbous co-axial extension, the surrounding metal enclosure, and the two electrical feed-throughs), is relatively simple to manufacture. The resonator has only two metal-insulator joints, which operate as the RF feed-throughs. Neither of these is subject to large mechanical stresses and neither is required to maintain precise dimensional tolerances.

Ideally the cavity should be installed with the bulbous extension pointing downwards and the gas inlet port positioned on the top plate. The sloping faces on the top and bottom surface of the bulbous extension are not essential to its operation as a resonant cavity, however they provide a mechanism for displacing liquid droplets, or dust particles, which in an on-line environment may be carried through on the inlet gas and which might otherwise accumulate on horizontal surfaces.

Previous designs of re-entrant cavity resonators were not ideally suited for high-precision measurement of relative permittivity. The main issues which needed to be addressed were:-

- the low electrical quality-factor, Q, of the cavity at resonance;

- the dilation of the cavity with pressure; and
- the influence of gaseous adsorption.

The dimensions of the cavity have been optimised to provide a high Q whilst ensuring a compact and physically robust design. Silver and gold plating were used to enhance the electrical conductivity of the internal surface layers and improve the Q of the cavity. The dimensions of the annular gap were calculated to minimise the effect of gaseous adsorption on the measurement of permittivity[3]. The material of construction, a beryllium-copper alloy, has a number of advantageous properties which are outlined later.

6.3.1 Re-entrant Cavity Resonator Construction

The cavity comprises of two main components, an inner component with a bulbous shape and an outer component or *shell* into which the inner part is assembled by means of a fine-pitch screw thread. A thin, flat, gold-plated and annealed copper ring or *gasket* is employed to effect a reliable low-resistance electrical conduction path between both parts when mated. Figure (6.3), below, shows the cavity components before assembly with the inner and outer parts on the left and right respectively:-

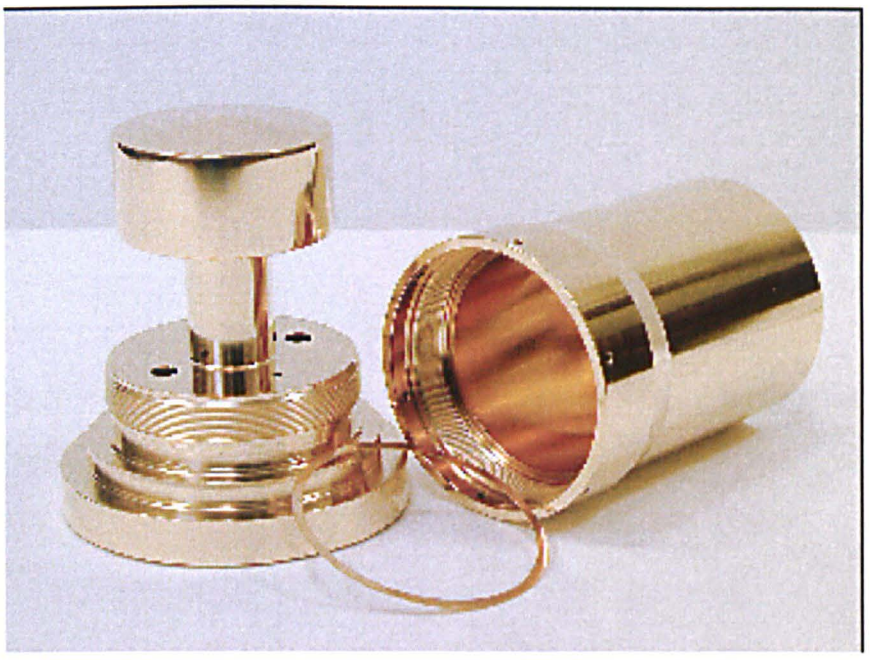

Figure 6.3 Re-entrant cavity resonator.

Entry ports in the *head* of the inner component facilitate the introduction of the test fluid and electromagnetic energy. Each of the main components is machined from solid beryllium-copper alloy bar (Brush Alloy 25, approximately 2% Be) which is purchased from the supplier, Brush Wellman Ltd., in the annealed or *soft* condition initially but specially heat treated prior to machining. After machining the parts are silver plated followed by a protective gold overcoat.

The cavity is assembled by screwing the two major components together and locking them in place. It is important to ensure that all parts are thoroughly clean before assembly. The fully assembled cavity is illustrated in figure (6.4) below:-

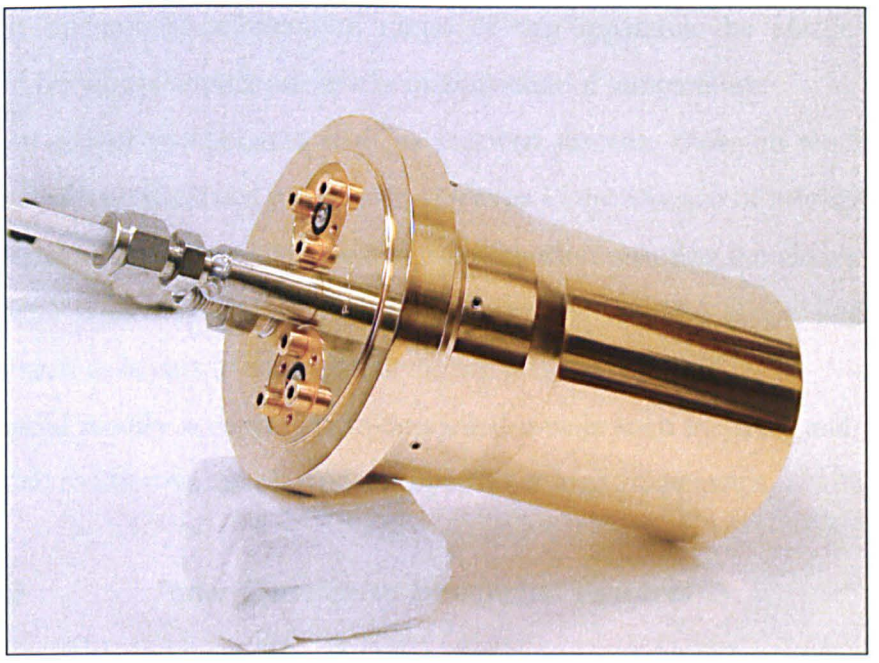

Figure 6.4 Fully assembled re-entrant cavity resonator.

6.3.2 Material Selection

Beryllium-copper was chosen for a number of reasons connected with its good electrical and thermal characteristics as well as suitable mechanical properties, these are:-

- it exhibits extremely low magnetic permeability, significantly less than the best stainless steels;
- it posses relatively high bulk electrical conductivity (up to 28% IACS) and thermal conductivity (105 W/mK) compared with austenitic stainless steel (approximately 10% and 14 W/mK respectively);
- thermal expansion properties are similar to stainless steel thus permitting the combination of parts manufactured from these materials with little or no difficulty;
- the prescribed heat treatment process for annealed beryllium-copper greatly increases the mechanical strength, hardness and durability of the alloy;

- over the operational temperature range of the apparatus the elastic modulii of annealed beryllium-copper are nearly independent of temperature;
- beryllium-copper components such as screwed threads, show no tendency to gall when mated with itself and other materials even in the absence of lubrication;
- the material has excellent stress relaxation properties ensuring the cavity is free from mechanical hysterisis and is able to maintain its original shape under dynamic loading such as occurs to some extent during pressure cycling;
- the material readily accepts electro-deposited metals such as silver and gold, which are needed to improve the electrical properties at high frequencies.

6.3.3 Inner Component Design and Features

As already outlined, the complete re-entrant cavity assembly is designed to be clamped into an external pressure containment vessel in order that the greater part of the cavity structure is completely immersed in the test fluid and not subjected to large dilating forces. Such forces would result if the cavity were also serving as its own pressure containment vessel and would create severe problems arising from complex and partially irreversible geometric deformations with pressure. However for practical reasons, principally concerning accessibility to the cavity, the upper region or *head* of the inner component is very substantial (some 40 mm thick over the greater part of its diameter) and consequently is extremely stiff. This part is subjected to a large axial force arising from the fluid pressure within the containment vessel however the tendency to bend or *dome* upwards is effectively resisted by its considerable stiffness. The complete cavity together with a pressure seal is clamped into the containment vessel by way of an extended flange forming the uppermost end of the inner component. A useful exposed surface area is thus provided on the outside to accommodate various attachments.

The head of the inner component, the uppermost surface of which is accessible with the cavity mounted inside its pressure vessel, is machined to accommodate two RF coupling devices or *coupling loops* used to inject and extract electromagnetic energy into and out

of the cavity respectively. In addition, a coned and threaded recess is provided for the attachment of the test fluid delivery tube and a central blind hole or *well* to accommodate a reference standard PRT. The latter is drilled deep into the bulbous part of the inner cavity component to facilitate accurate temperature measurement within the cavity.

6.3.4 Cavity Component Surface Electroplating

Precise determination of the resonant frequency of the cavity, and hence the relative permittivity of the enclosed fluid, is facilitated by having a high Q factor which, among other things, defines the sharpness of the resonance peak observed when undertaking transmission response measurements. At high frequencies, the magnitude of Q attainable in practice is highly dependent upon the effective electrical resistance associated with the cavity. The *skin effect* in the frequency range of interest here confines the current to a surface layer of less than 10 μm effective thickness. Hence this layer must possess a very high electrical conductivity in order that the associated resistance be kept as low as possible.

The electrical conductivity of the beryllium-copper alloy employed in the construction of the cavity is approximately 28% that of copper. While this material on its own (unplated) has been shown to yield a Q factor in excess of 1000, plating with silver, as traditionally used in RF engineering, more than doubles this value. However silver, and to some extent bare beryllium-copper, can be affected by impurities in the test fluid, particularly sulphides, hence an overcoat of gold is required to protect the silver layer from attack. Strictly speaking, only the surfaces directly in the RF current path need to be plated but for reasons of simplicity of processing and complete chemical protection, the entire surface of each cell component was plated with silver and gold to a thickness of 5-8 μm and 2-3 μm respectively.

6.3.5 RF Coupling Loops

The upper external surface of the inner component of the cavity has two recessed openings, each of which is shaped to receive the specially designed RF coupling devices or *coupling loops*. One of these is employed to excite electromagnetic oscillations in the cavity and the other to detect when the cavity is at resonance. The precision with which the frequency corresponding to the transmission peak can be measured, and hence the relative permittivity of the fluid contained with the cavity, is dependent upon the Q of the cavity under operational conditions. In order to attain the highest precision measurement, the Q factor must be maintained as close to the unloaded or theoretical value as possible and this dictates a low value of coupling to the external measuring circuit. Hence the effective area of coupling loop is made only a small fraction of the total cross-sectional area occupied by the main magnetic field within the cavity and as such it only *links* with a small percentage of the field. In order to exercise a degree of control over the coupling, the orientation of the loops is made adjustable by rotation about their individual axes and the effective loop area is further reduced by the cosine of the angle of rotation from the maximum position. With the overall coupling thus minimised, a typical Q factor in excess of 2000 can be realised over the operating frequency range. A low level of coupling results in the input and output impedances of the cavity being substantially inductive. The RF coupling loop and associated components are illustrated in figure (6.5) below:-

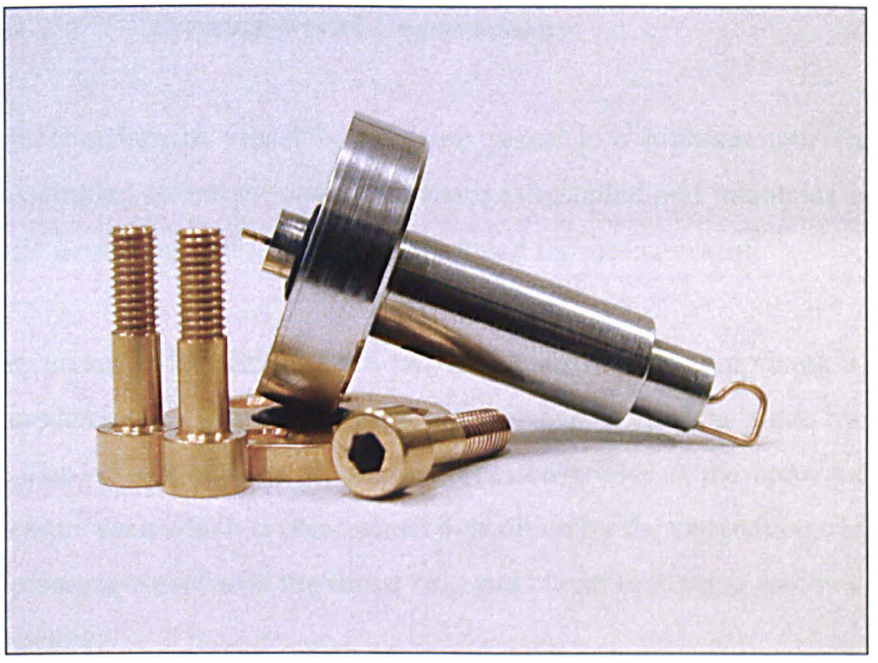

Figure 6.5 RF Coupling loops and associated parts.

The active element of the coupling loop, as illustrated in figure (6.5), is a single turn inductor formed from 0.8 mm diameter, gold plated, nickel-iron alloy wire. This is fused into the stainless steel body using a special glass compound and fired at high temperature to yield a gas-tight seal capable of resisting the large forces resulting from the fluid pressure. The seals are capable of operation at up to 400 bar by virtue of their tapered geometry. The *earthed* or *grounded* end of the wire loop is electrically connected to the body by a brazing process while the other end passes up inside the central hole in the body thereby forming a coaxial structure. This free end, projecting beyond the upper end of the body, is trimmed to a specific length and gold plated to improve its electrical conductivity. By maintaining this in the axial position by silicone and PTFE insulators, the free end forms an effective contact pin which in turn mates with a special coaxial adapter.

6.3.6 Pressure Vessel Construction

The pressure containment vessel or *pressure vessel* is a high-strength structure into which the assembled re-entrant cavity resonator is installed and maintained securely in position while permitting test fluid to be introduced for measurement.

The pressure vessel is fundamentally a two-part construction comprising a main body that accommodates the complete permittivity cell and is held in place by a threaded clamp ring. The vessel body has an internal recessed groove at the open end to receive the main pressure seal, which is constrained in position by the upper flange of the cavity. The empty pressure vessel with the thrust ring and clamp tightening tool is illustrated in figure (6.6) below:-

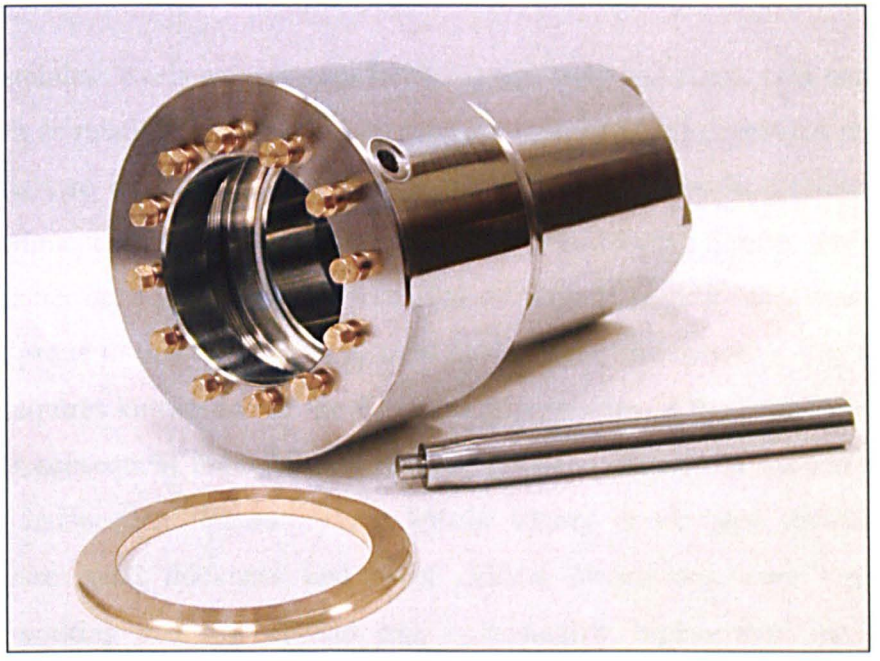

Figure 6.6 Pressure vessel.

The exterior of the body is threaded over part of its length at the open end onto which the clamp ring is attached. The clamp, together with a set of twelve beryllium-copper screws acting upon a thrust ring, serves to compress the seal during final assembly and

resists the axial force acting upon the installed permittivity cell assembly when in use at elevated pressure.

6.3.7 Design Code and Material Selection

The pressure vessel was designed in accordance with the guidelines published in British Standard BS5500[4] with regard to material selection, minimum wall thickness and other geometric features. Although primarily aimed at industrial scale design, this standard is fairly wide in its scope and can be applied to relatively small non-welded structures such as here provided the design geometry can be reduced to simple geometric entities such as cylinders with end caps and so on. As with any pressurised system, the design process focuses on limiting mechanical stress in the materials of construction to a safe value while satisfying the functional requirements.

Austenitic stainless steels were chosen for the vessel body and clamp ring component for reasons such as relatively low cost, moderate strength and high corrosion resistance. In this instance, two different grades of steel were selected from the recommended list. This is recommended practice when combining parts employing threads where there is a risk of seizure or *galling* due to localised frictional heating. Stainless steels are notoriously prone to this due in part to their low thermal conductivity. The design code as applied requires knowledge of the mechanical properties of the actual material batch obtained for subsequent manufacture. In this instance, samples of each material were sent to an independent laboratory for tensile testing at elevated temperature. The pressure vessel wall thickness and other critical dimensions were based upon a maximum working pressure of 350 bar, considerably higher than the operational requirement of 120 bar resulting in an extremely rigid and safe structure with extensible operational capability.

The pressure vessel was designed and manufactured at NEL. Following manufacture, the completed vessels were subjected to non-destructive testing as stipulated by the design

code. Since no welding processes were involved in this design, the testing was limited to thorough visual inspection followed by pressure test at 1.4 times the maximum working pressure equal to 490 bar in this instance. During the pressure test, which involves filling the vessel with hydraulic oil, a beryllium-copper test *plug* with key dimensions similar to the head of the cavity was substituted for the actual cavity. The test procedure, although set up and conducted by NEL staff, was witnessed by a representative of the independent design approval body who issue the final safety certification.

6.3.8 High Pressure Seals

Test gas pressure within the vessel is maintained by the high-pressure seal located in the seal groove at the open end of the vessel body. A PTFE O-ring seal, 81 or 82 mm inside diameter by 2.5 mm section is normally used although a *Viton* fluoro-elastomer seal may also be used. As with all polymer seals, they generally achieve an effective seal on first installation however with some types of fluids (excluding ethylene) absorption effects and gradual deterioration have to be taken into account and these seals may require regular replacement. Metal seals are ideal in that they exhibit negligible absorption effects but with larger sizes, require considerable force to attain perfect seal and can therefore be troublesome. At this time, no satisfactory and easily usable metal seal has been developed.

6.4 Temperature Measurement and Control

Temperature measurement and control was achieved using the National Density Standards high-performance thermostating and measurement system. The temperature stability of the thermostating system is within ± 1 mK and the absolute temperatures of the same can be set by computer-controlled equipment to within a few milli-kelvin of any prescribed temperature over an operating range of –40 to +150 °C. Temperature uncertainty is dependent upon the calibration of the PRT's, which in this case were performed by comparison with an NEL in-house standard reference thermometer itself

traceable to National Standards, and is estimated to be 4 mK over the entire operational temperature range.

Both the measured and reported temperatures are on the International Temperature Scale of 1990 (ITS-90)[5],[6].

6.4.1 Thermostating System

The central element of the thermostating system is the temperature controlled bath which houses the permittivity cell. The bath is illustrated in figure (6.7) below:-

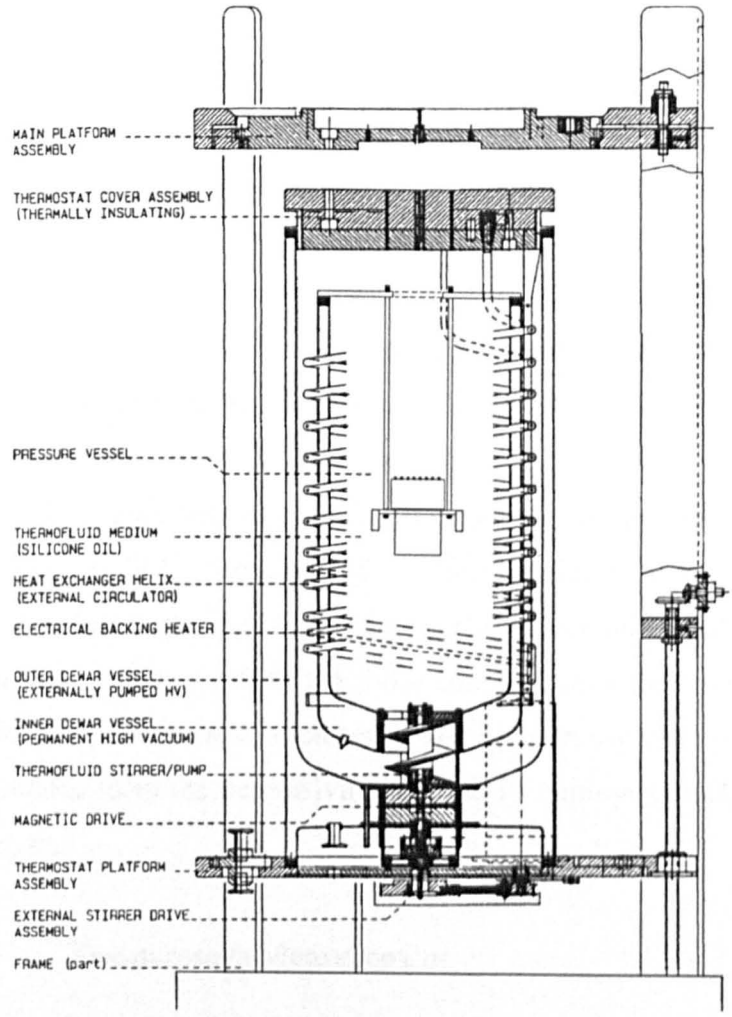

Figure 6.7 Temperature controlled bath.

The bath consists of two Dewar vessels mounted concentrically around the pressure vessel and is filled with some 35 litres of silicon oil which forms the heat transfer medium and the bulk of the thermal mass. Heating and cooling is provided by two separate systems working in parallel with the computer-controlled equipment. The first, or *primary*, control system provides the bulk of the heating and cooling power that is required to get the temperature to within several milli-kelvin of the set-point and the *secondary* control system brings the temperature to within ± 1 mK. The primary control system consists of a heat exchanger coil fashioned in a helix lying between the inner and outer Dewar vessels which is linked to an external Huber HS40 recirculation bath. The

secondary control system consists of an electrical heating element which again lies in a helix between the inner and outer Dewar vessels which is interfaced through the control software to a programmable power supply. Good circulation of the fluid in the bath is achieved by magnetically-driven screw impellers mounted in the base of the outer Dewar vessel. The temperature controlled bath is designed so that the fluid circulates upwards past the pressure vessel through the inner Dewar and then downwards between the inner and outer Dewar thus ensuring that the bath is essentially free from any *dead* regions which may result in temperature gradients being set up within the bath.

The permittivity cell is mounted on a specially designed support rig that also houses three PRT's. Two of the PRT's are mounted in close proximity to the permittivity cell and are accommodated in isothermal blocks to ensure temperature equilibrium between this point and the thermometer well in the inner component of the cavity. These three PRT's are used for temperature measurement of the permittivity cell. The third PRT is mounted some distance from the permittivity cell and is employed solely as part of the thermostating system.

6.4.2 Temperature Measurement

The precise temperature control and measurement that is achieved with the National Density Standards facility is attained through the use of platinum resistance thermometry. The measurements can only be realised through proper selection, calibration and use of PRT sensors and their associated measuring equipment.

PRT's are employed in temperature measurement applications where a higher degree of accuracy, or lower uncertainty, and better repeatability is required than can typically be obtained using other types of temperature measurement devices such as liquid-in-glass thermometers, thermocouples or thermistors. Their principal applications are as reference thermometers and hence they are the specified interpolating instrument employed in the dissemination of the ITS-90. The basic PRT exploits the highly

repeatable electrical resistance versus temperature characteristic of a resistive element formed from specially treated fine platinum wire, suitably mounted and protected to yield a practical thermometer. In addition to the sensor, secondary instrumentation is required to measure the electrical resistance and convert and display this in equivalent temperature units.

Temperature control and measurement is made with the Tinsley model 5187L, 25 Ohm, 50 mm long by 5 mm diameter, thin-walled platinum capsule type PRT. This type of PRT is of *standards* grade and is the most expensive and highly refined meteorological class available. The PRT employs extremely pure platinum in the resistive element and requires meticulous care in fabrication to ensure strain-free mounting as well as the exclusion of all sources of actual or potential contamination especially water. Four electrical connections emerge through a fused glass hermetic seal at the upper end and these are extended using fine PTFE insulated wires. This device, complete with its extension leads, is extremely delicate and as a result the calibration may be adversely effected by mechanical shock.

For temperature measurement it is necessary to realise the high accuracy and resolution capabilities of a typical 25 ohm standard PRT. In order to do this the electrical resistance of the PRT must be measured with a high-performance resistance ratio bridge together with an external reference resistor. The equipment used to do this is an Automatic Systems Laboratories Ltd. (ASL) model F17A autobalancing resistance ratio bridge with a Tinsley model 5685A 25 ohm S-class standard resistor.

The F17A is an alternating current (a.c.) bridge instrument designed to measure the ratio of two four-terminal resistors to a high level of accuracy. In this case the two four-terminal resistors are the specified PRT and the external reference resistor. The resistance measurement of the PRT is therefore a comparative or relative measurement in ratiometric terms and not absolute. In order to measure the PRT resistance the bridge passes a low-frequency a.c. signal through the PRT and reference resistor, which are

connected in series. An a.c. signal of low-frequency has advantages over d.c. techniques in that the thermal emf's due to the various metal junctions of the circuits are cancelled out, however the frequency must be sufficiently low so as to avoid significant quadrature effects that may arise in the external circuitry. It is important to ensure that the current through the PRT when making a resistance measurement is 1 mA, since the PRT's themselves are calibrated with a current of 1 mA and the small increase in resistance due to the heating effect of this current is incorporated into the calibration data. The resulting voltages that are generated across each resistor are measured and the bridge is automatically balanced and quadrature compensated, correcting for the effects of reactive loading of the bridge by the PRT, its extension leads and the reference resistor, and the precise resistance of the PRT is determined.

The resistance of the PRT in the thermostating control circuit is measured using a DATRON 1271 Selfcal Digital Multimeter, which provides high performance in electrical measurements. The multimeter is an enhanced high quality d.c voltmeter which provides four-terminal resistance measurement. The PRT is monitored by the thermostating data acquisition control computers and the power inputs to the heating/cooling systems are adjusted using Proportional-Integral-Derivative (PID) control software.

The measured resistance of a specified PRT is converted to an equivalent temperature by the data acquisition control computers[7]. The software executing the conversion reads the bridge for the PRT resistance and then implements the ITS-90 to calculate the temperature. The software requires the ITS-90 calibration information of a specified PRT, which normally consists of the value of the electrical resistance measured at the triple point of water (0.01°C) and between one and four coefficients of the standard deviation equations for the temperature regions below and above 0.01°C respectively. The number of coefficients required is dependent upon the temperature range over which the PRT has been calibrated, which in the case of the National Density Standards

facility, where the working range is approximately –40 to +150°C, is typically one or two only.

Calibration of the PRT's are performed within the Density Standards Laboratory against the in-house primary standard reference PRT which provides fundamental traceability to the ITS-90. Calibration of the external reference resistor used in the resistance bridge is also done within the Density Standards Laboratory against the in-house primary standard resistor which is the principal source of resistance traceability within the National Density Standards facility.

6.5 Pressure Measurement

The pressure of the fluid contained within the permittivity cell is obtained with reference to the pressure of nitrogen in the Desgranges et Huot (D&H), metrology class S2, gas-operated pressure balance through the Yokogawa EJA130A differential pressure transducer (DPT). Atmospheric pressure is measured by two Druck 140 standard digital pressure transducers (PT).

The total uncertainty in the measurement of pressure is estimated to be 0.01% over the entire operational range of pressures.

Gas-operated pressure balances are primary pressure reference standards and are typically employed in the calibration of secondary pressure measuring devices and applications where a higher degree of accuracy is required than can typically be obtained using other types of pressure measurement devices. The pressure balance is a primary standard because it defines the derived unit of pressure directly from the fundamental units of mass, length and time. The total uncertainty of the D&H metrology class S2 pressure balance is 0.005% of the gauge pressure over the entire operational range.

The pressure balance generates a known pressure from the force resulting from the placement of calibrated masses (or weights) on a very accurately machined piston located in a vertical, close fitting cylinder of known cross-sectional area. A schematic of the measuring principle is illustrated in figure (6.8) below:-

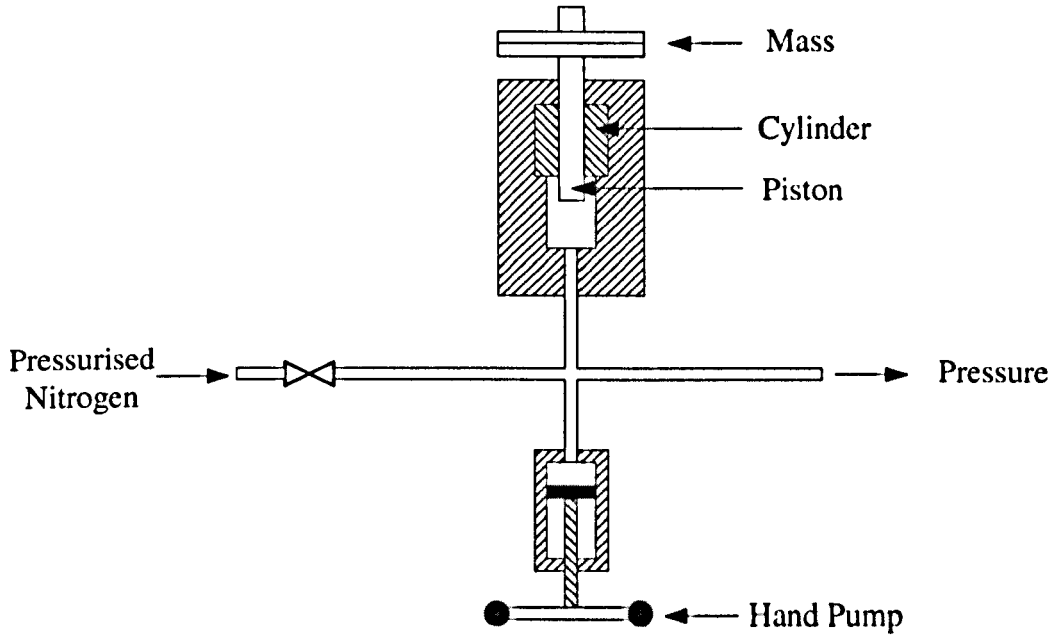

Figure 6.8 Measuring principle.

The hand pump or pressurised gas source is used to slowly increase the pressure in the system until the piston and weights lift. The weights and piston are slowly rotated about their vertical axis to effect proper lubrication between the piston and cylinder reducing frictional drag and consequential errors. When the pressure is finely adjusted, the piston will *float* in an equilibrium position, or reference level, and the resulting system pressure is equal to the gravitational force due to the applied weights and the mass of the piston itself divided by the effective cross-sectional area of the piston.

The accuracy with which a pressure balance can define pressure is a direct function of the accuracy with which the value of the piston-cylinder's cross-sectional area and the

masses that are loaded onto it can be known. To this must be added a number of contributing correction factors that are applied to the basic force/area relationship to compensate for effects such as of air buoyancy and changes in cross-sectional area of the piston-cylinder with temperature and pressure. The average ambient air temperature and relative humidity of the Density Standards Laboratory is measured at each measurement state point and are used to correct for the effects of air buoyancy. The temperature of the piston-cylinder set is measured by a PRT probe which is mounted in close proximity to the same. Local gravity within the Density Standards Laboratory has also been accurately measured.

The primary meteorological components are the pistion-cylinder and mass set, which are both traceable to the fundamental physical standards of measurement through routine calibration at Desgranges et Huot, France.

The Yokogawa EJA130A is a normal resonant silicon sensor differential pressure transducer with an adjustable ± 50 mbar operational range capable of withstanding high positive (300 bar) and negative (<< 1Pa) pressures. The zero offset of the DPT was calibrated by using the D&H to apply static pressures of up to 200 bar to the high and low ports of the transducer. The shift in zero offset is illustrated in graph (6.1) below:-

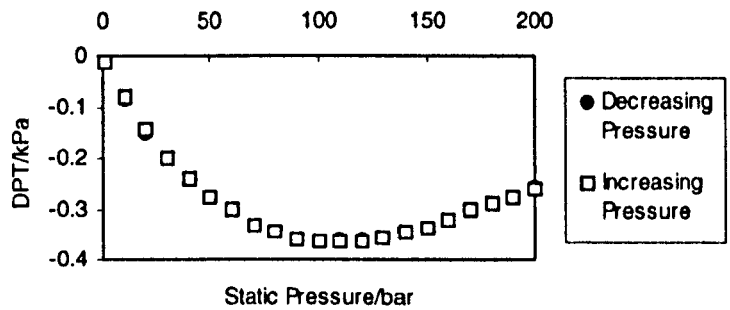

Graph 6.1 Zero offset of DPT.

In order to maintain an uncertainty in density of 0.01% it is has been calculated that the differential pressure reading at certain conditions needs to be known to better than 0.1 kPa. As illustrated in graph (6.1) there is a marked shift in the zero offset of the DPT with static pressure which would result in a significant error in the overall uncertainty in the density measurement. The pressure applied to the DPT was raised to 200 bar from atmosphere and then reduced back to atmospheric conditions. As illustrated there is no significant hysterisis effects in the response. An expression was developed to correct for the zero offset shift in the DPT. The uncertainty associated with this correction was negligible in comparison to the uncertainty associated with the differential pressure measurement and as a result was ignored.

The calibration of the DPT was checked by using an adjustable piston to create a pressure differential of between –60 and 100 mbar between the high and low ports of the DPT. The piston was connected to the high port of the DPT and measured with a Druck PT. The low port of the DPT was set at atmosphere. The difference between the DPT and Druck readings were found to be negligible.

The shift in zero offset of the DPT with overpressure and high vacuum applied at each individual port was checked and found to be negligible over the working range of pressures. The opportunity was also taken to check the integrity of the fittings to the DPT while the zero offset shift was checked.

The total uncertainty of the Yokogawa EJA130A differential pressure transducer is 0.075% of the span of the instrument which equates to 0.12 mbar over the entire operational pressure range.

The Druck 140 is a standard digital pressure transducer with an uncertainty of 0.015%. The uncertainty is estimated from the uncertainties associated with the calibration equipment and measurement limits of the instrument.

6.6 Frequency Measurement

The resonant frequency of the re-entrant cavity resonator is measured with a Hewlett Packard type 8752C RF vector network analyser. The cavity acts as a passive transmission element in the path of a swept RF signal and the resonant frequency is determined by examination of the transmission amplitude response.

The network analyser is a high performance vector network analyser used for laboratory or production measurements of reflection and transmission characteristics of active and passive RF devices and networks. The instrument is essentially a synchronously tuned, low-power radio transmitter and a highly selective measuring receiver coupled with an integral graphics display unit. The high resolution RF source, derived from an external high-stability oven-controlled quartz-crystal oscillator, is digitally synthesised and may be swept continuously between any desired start and stop limits in the range 300 kHz to 6 GHz. The RF signal that is transmitted through the test network, or reflected from its input, is compared with the incident signal. Both signals are then applied to the receiver for measurement, signal processing and display. In transmission mode the graphic display represents the magnitude and phase response of a two-port network, which in this instance is formed by the cavity including its connecting cables, as a function of frequency.

The analyser is inherently complex and possesses a large number of variable operating parameters which must be carefully adjusted to obtain a meaningful display and optimal performance. The basic measuring procedure, under any given test conditions, involves a broadband frequency-sweep initially used to identify approximate frequency of the resonant response. By appropriate manipulation of the instrument controls, the response peak is then expanded using progressively greater amplitude resolution coupled with narrower display bandwidth until the desired overall resolution is obtained.

The capability of the instrument is such that the amplitude and centre frequency resolution corresponding to the maximum of the resonance peak can be readily determined to within 0.001 dB and 200 Hz respectively.

The effects of short-term temperature drift and long-term stability of the instrument are, however, much more important than absolute frequency accuracy since it is the frequency ratios are involved in the permittivity calculation. These aspects of performance are considerably enhanced through the use of the external quartz-crystal oscillator which gives a reference frequency stability of around 1 part in 10^9.

Independently adjustable frequency markers were used to determine the relative half-power (-3 dB) bandwidth of the resonance peak from which the Q of the cavity was calculated.

6.7 Filling Circuit

The filling circuit, illustrated in figure (6.1), accommodates the ethylene sample cylinder, a Paroscientific PT type 43K-101, a Haskel compressor, all the valves and most of the pipework within a temperature-stabilised enclosure. The enclosure is insulated and it's internal ambient temperature maintained at approximately 45 °C by a heat exchange unit fed from an external temperature controlled Haake K circulation bath. At this temperature the initial pressure of the ethylene in the sample cylinder prior to use was approximately 145 bar. It is important ensure that the external bath is held at 70 °C and topped up with water every two days to maintain a constant internal ambient temperature of 45 °C.

The PT associated with the filling circuit was used to give an indication only of the cylinder, or permittivity cell, pressure in order to aid pressure measurement.

The external high pressure line leading to the permittivity cell, DPT and pressure release safety valve was insulated to reduce thermal fluctuations in these components which have a detrimental effect on the stability of the pressure and density of the fluid within the permittivity cell.

Prior to the installation of the ethylene cylinder within the filling circuit a risk assessment was carried out on the possibility of polymerisation of the ethylene sample occurring as a result of using the compressor to intensify the sample pressure. Polymerisation of ethylene under these circumstances is potentially extremely dangerous due to the large exothermic reactions that are involved. Results from research into the polymerisation behaviour of ethylene have shown certain polymerisation to occur at 370 K and 30 MPa[8]. Whilst reaction rates for polymerisation are low at 40 °C and 12 MPa, the use of the compressor was deemed unsafe, as it is recommended to try and avoid rapid increases of pressure[9]. Care was also taken to avoid subjecting the pipework and permittivity cell to mechanical shock. As a result the sample pressure was intensified solely by increasing the ambient temperature of the enclosure.

Due to the extreme flammability hazard diaphragm-sealed valves, guaranteeing leak tightness to 200 bar, Cajon VCR/Swagelok pipe fittings, suitable for both elevated pressure and high vacuum use, and welded joints, where possible, were used to minimise leakage from pipework and fittings. In the unlikely event of a leakage occurring the filling circuit accommodates a gas detection and warning safety system.

6.8 Experimental Operation

The following section contains an overview on the experimental procedures undertaken in the measurement of the relative permittivity of ethylene.

6.8.1 Commissioning of Experimental Facility

Prior to the commencement of the measurement programme on ethylene new metal seals were installed in the VCR valves and the integrity of the pipework and fittings were checked under high vacuum and at high pressure with nitrogen in excess of 200 bar.

The operation of the facility was confirmed by undertaking a small series of relative permittivity measurements on research grade nitrogen. The results were checked against the most recently published values from NIST[10] and the agreement was within the combined uncertainties of the two.

6.8.2 Measurement Programme

The experimental facility was used to make measurements on the relative permittivity of research grade ethylene at temperatures between 0 and 40 °C and at pressures up to 120 bar. It was shown previously that the resonant frequency of the cavity filled with a low-loss, no-conducting fluid is related to that of the evacuated cavity at the same temperature by the expression:-

$$f_{\varepsilon_r}(t,p) \approx \frac{f_0(t)}{\sqrt{\varepsilon_r(t,p)}}, \tag{6.2}$$

where $f_{\varepsilon_r}(t,p)$ is the resonant frequency of the fluid filled cavity at the conditions of measurement;

$f_0(t)$ is the resonant frequency of the cavity under vacuum conditions, $\varepsilon_r = 1$ at temperature t; and

ε_r is the relative permittivity of the fluid at temperature t and absolute pressure p,

and the relative permittivity of the contained dielectric may be obtained from the ratio of the frequencies at the same temperature of measurement:-

$$\varepsilon_r(t,p) \approx \left(\frac{f_0(t)}{f_{\varepsilon_r}(t,p)} \right)^2 \tag{6.3}$$

It can therefore be seen from expression (6.3) that in order to make measurements of relative permittivity it is necessary to characterise the vacuum resonant frequency of the cavity over the range of operating temperatures. Regression of these measurements gives an expression which determines the resonant frequency of the evacuated cavity at a specified temperature.

6.8.3 Vacuum Measurements

The cavity was evacuated using a Lyebold PT 150 two stage vacuum pump connected to the vacuum port/exhaust line of the filling circuit, as illustrated in figure (6.2). In the filling circuit valves V2 and V3 were open and V1 was closed. For safety reasons the ethylene cylinder valve was also closed during evacuation. The system was pumped down until the pressure was << 1Pa, which took approximately 2-3 hours. The level of vacuum was verified with the resonant period output of the PT. Vacuum measurements were made at nine temperatures in the range 0 to 40 °C. The measurements were performed in a random order and repeated for confidence. The repeatability of the resonant frequency measurements were typically to within 100 Hz of the initial measurements.

On completion of the vacuum measurements the system was retained in an evacuated state ready for filling with ethylene. Valve V2 was closed whilst the system was still under high vacuum and the vacuum pump was removed and the port capped.

6.8.4 Ethylene Storage and Handling

The ethylene sample used in the measurement programme was prepared and supplied by Messer (UK) Ltd.. The ethylene is research grade with a purity of 99.995%. The impurities and their concentrations in volume part per million (vpm) are reported to be:-

- Nitrogen ≤ 10;
- Moisture ≤ 10;
- Oxygen ≤ 5;
- Methane ≤ 5;
- Ethane ≤ 5;
- Other Hydrocarbons (C_1 to C_4) ≤ 10; and
- Carbon Dioxide ≤ 5

It is important that the water content of the sample is low, since the relative permittivity of water can be up to 80 times greater than that of the ethylene and even small concentrations of water in the sample could have an undue influence on the relative permittivity measurements.

Following shipment to NEL the cylinder was stored in a specially prepared room within the Density Standards Laboratory, fitted with gas sensors and an emergency evacuation system. Since ethylene is an asyphyxiant and highly flammable extreme diligence and awareness was required at all times during handling and usage.

6.8.5 Ethylene Measurements

It was necessary to evacuate the cavity prior to filling with ethylene in order to maintain the purity of the sample. On filling valves V3 and V2 (see figure (6.2)) are open and closed respectively and, with the sample cylinder valve open, valve V1 was opened

slowly, taking care not to cause a rapid increase in pressure. A pressure release valve, set to ≈ 150 bar, serving as an over-pressure protection safety device, was incorporated into the system. The pressure in the system was monitored by the PT and once the desired pressure had been reached the cylinder valve and valve V1 were both closed. The indicated pressure decreased for some time after filling while the excess heat produced during the compression cycle was removed by the temperature control system (the reverse was true for a pressure decrease). The precise value of the pressure achieved after stabilisation was not important as long as it was within a few bar of the required state point on the measurement schedule. The system pressure could be decreased by slowly venting the ethylene to atmosphere using valves V2 and V3.

An initial measurement programme was prepared containing a set of 72 state points uniformly distributed throughout the measurement range. In order to conserve sample utilisation the normal method of traversing individual isotherms with increasing and decreasing pressure was rejected in favour of the following *isobaric* method. The first state point corresponds to the highest pressure and lowest temperature of measurement. Successive groups of state points correspond to points on seven isobars spanning nine temperatures. Figure (6.9) illustrates the distribution and sequence for the initial measurement schedule. The fundamental process of measurement involves traversing each isobar, alternately increasing and decreasing the temperature. The measurement sequence was as follows:-

1. With the temperature controlled bath set to the first pre-determined temperature set point (0°C), the evacuated cavity was filled with the ethylene sample to the corresponding state point pressure of the first isobar (≈ 120 bar). The ethylene sample cylinder was then isolated from the rest of the system by closing the cylinder valve and valve V1.

2. Relative permittivity measurements were made at the first pre-determined state point.

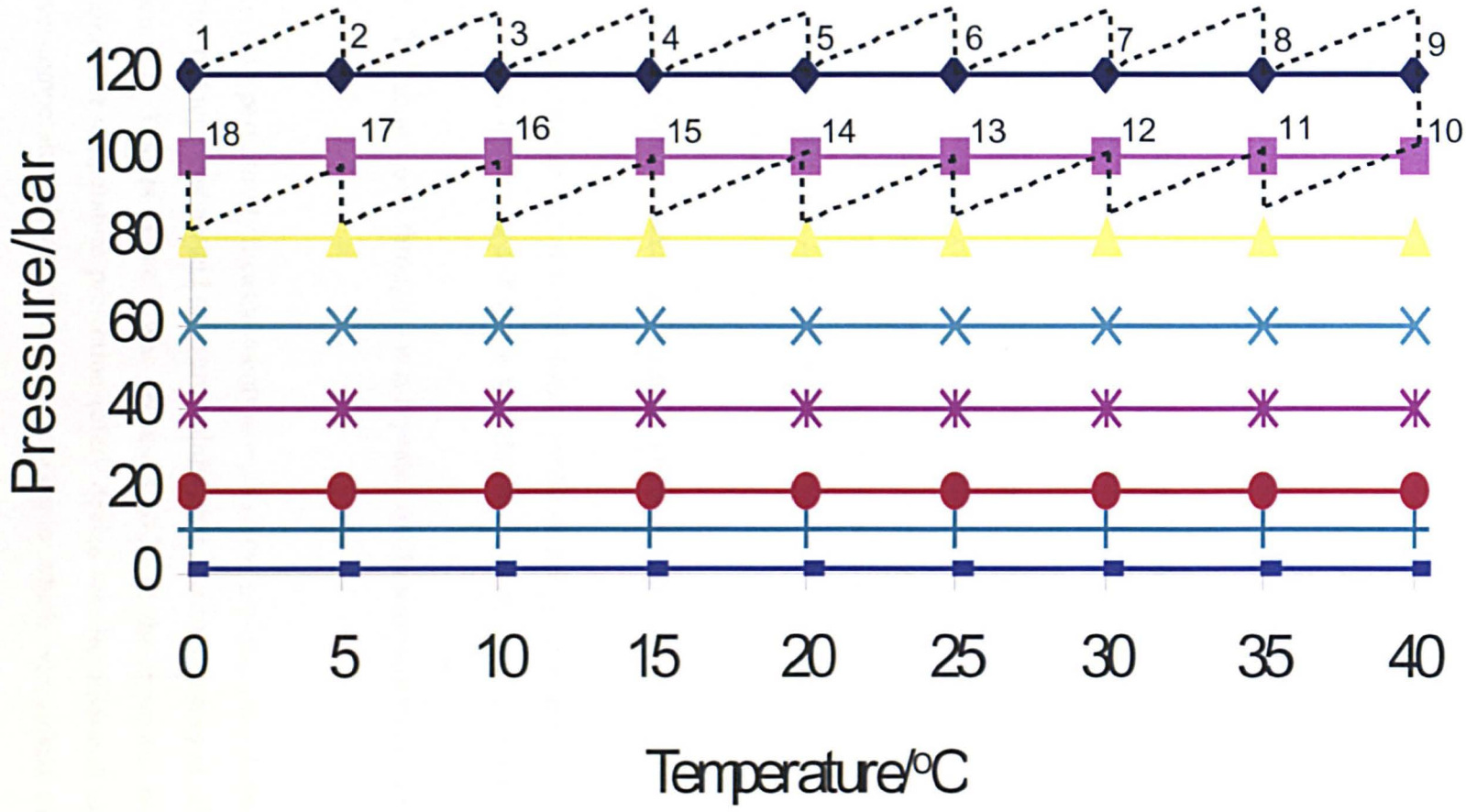

Figure 6.9 Measurement Schedule

3. The temperature of the permittivity cell was raised by 5 °C to the second temperature set point. Once the temperature was stable the pressure was reduced slowly to the state point pressure of the isobar. Following stabilisation a relative permittivity measurement was made.

4. Step 3 was repeated until all measurements had been obtained for the isobar.

5. The pressure was reduced slowly to that of the pre-determined state point on the next isobar. Following stabilisation a relative permittivity measurement was made.

6. The temperature of the permittivity cell was lowered to the next temperature set point. Once the temperature was stable the sample cylinder was re-engaged to the system and the pressure was increased slowly to the state point pressure of the isobar. (Note: After use the ethylene sample cylinder was isolated from the rest of the system for safety reasons.) Following stabilisation a relative permittivity measurement was made.

7. Step 6 was repeated until all measurements had been obtained for the isobar.

8. The pressure was reduced slowly to that of the pre-determined state point on the next isobar. Following stabilisation a relative permittivity measurement was made.

9. The sequence 3 through 8 was repeated until measurements had been obtained for all isobar.

Relative permittivity measurements at each of the pre-determined state points were made after full temperature and pressure stabilisation had been achieved. This normally took a period of 3 hours. Since it was necessary to leave the apparatus running overnight an extra over-temperature protection safety device was incorporated into the facility. The over-temperature device was a thermocouple which was linked to the thermostating

system. If the temperature of the bath should have exceeded 45 °C the power to the primary and secondary heating elements would be cut and the thermostat defaults to a safe temperature of 20 °C.

It should be noted that after the 80 bar isobar was completed (see figure (6.9)) a series of repeat vacuum resonant frequency measurements were performed on the cavity with a view to assessing the repeatability of the values. During these measurements the 81 mm PTFE seal used in the cavity failed resulting in the cavity, associated pipework and vacuum pump being flooded with the silicon oil from the temperature controlled bath. As a result of this the contaminated components of the system were disassembled and thoroughly cleaned before being re-assembled and flushed repeatedly with compressed nitrogen in order to completely eliminate all traces of the silicon oil.

Since the resonant frequency of the cavity is particular to any one individual assembly it was necessary to re-characterise the vacuum resonant frequency of the cavity over the range of operating temperatures. The consequence of the seal failure was that the relative permittivity measurements occur in two *parts*; the first covering isobars 120, 100 and 80, and the second covering all subsequent measurements.

A preliminary analysis of the initial set of measurements identified certain areas within the measurement range with an insufficient number of data points required for accurate mapping of the ethylene surface. As a result of this a further 54 state point measurements were performed throughout the measurement range. Most of these points concentrated around the vapour-pressure curve and the critical and supercritical regions.

6.8.6 State Point Measureands

The following section describes the quantities that constitute a *state point relative permittivity measurement.* In order to map the ethylene surface in terms of relative permittivity and temperature it is necessary to measure the resonant frequency,

temperature and pressure of the cavity at each state point. The resonant frequency and temperature of the cavity can be measured directly, with relative ease from the methods outlined in sections 6.5 and 6.4 above, however the pressure of the permittivity cell cannot be measured directly, and as a result is more difficult to determine, requiring the measurement and application of several specific correction factors.

Associated with these *principal* measurements are a series of *secondary* measurements which are required for correction purposes and for information on the electrical characteristics of the cavity. The complete set of measureands recorded at each state point is given below:-

- Resonant Frequency (MHz), f_{ε_r} :- The frequency associated with the maximum transmission amplitude response of the cavity was recorded for 16 consecutive transmission/response sweeps. The network analyser automatically tracks the maximum transmission amplitude response of the cavity. The resonant frequency of the cavity at each state point was taken as the average of these measurements.

- Temperature (°C), t_{Cell} :- The temperatures of the three measurement PRT's were recorded from the data acquisition control computers. The resistance ratio for each PRT was also recorded from the bridge as a checking measure. The temperature of the cavity at each state point was taken as the average of

these measurements.

- Pressure (MPa), p_{Cell} :- As outlined in section 6.4 the principal measureands are the applied mass to the D&H, the differential pressure from the Yokogawa DPT and the average ambient pressure from the Druck PT's. Associated with these measurements are several measureands which are required for correction factors, these are given below:-

- Ambient Temperature (°C), t_{amb} :- The ambient air temperature was recorded from two digital PT100 units within the Density Standards Laboratory and the average taken.

- Relative Humidity (%), $R.H.$:- The relative humidity of the air was recorded from three hygrometers within the Density Standards Laboratory and the average taken.

- PRT Resistance of D&H (Ω), $R_{D\&H}$:- The resistance of the PRT within the D&H was recorded with an Automatic Systems Laboratories F250 Mk II Precision Thermometer.

- Quality Factor, Q :- The relative half-power (-3 dB) bandwidth of the resonance peak was measured and the Q of the cavity was calculated. The Q of the evacuated

cavity is required as part of the correction for the effective dilation of the cavity due to the change in the penetration depth of the magnetic field into the metal surfaces bounding the cavity. The Q of the fluid filled cavity yields information on the dielectric loss of the ethylene and the electrical characteristics.

- Insertion Phase (°), *IP*:- The insertion phase angle of the cavity at resonance is measured with the network analyser. Information on the insertion phase is important in determining the technical requirements of the *on-line* instrument (see Chapter 9: Development of On-Line Instrument)

- Insertion Loss (dB), *IL*:- The insertion loss of the cavity at resonance is measured with the network analyser. Measurements of the insertion loss yields information on the dielectric loss of the ethylene and the electrical characteristics of the cavity.

6.8.7 Determination of Pressure

The following section describes how the pressure of the contained fluid at the mid-point of the permittivity cell is determined for each state point.

The pressure of the fluid at the mid-point of the permittivity cell could not be measured directly due to the fact that it was not possible to accommodate both the permittivity cell and the DPT into the temperature controlled bath. Therefore, as illustrated in figure (6.10),

below, the physical point of pressure measurement occurs at the DPT on the lid of the temperature controlled bath. (The pressure measured at this point is obtained with reference to the pressure of nitrogen in the D&H and the indicated resulting pressure differential.):-

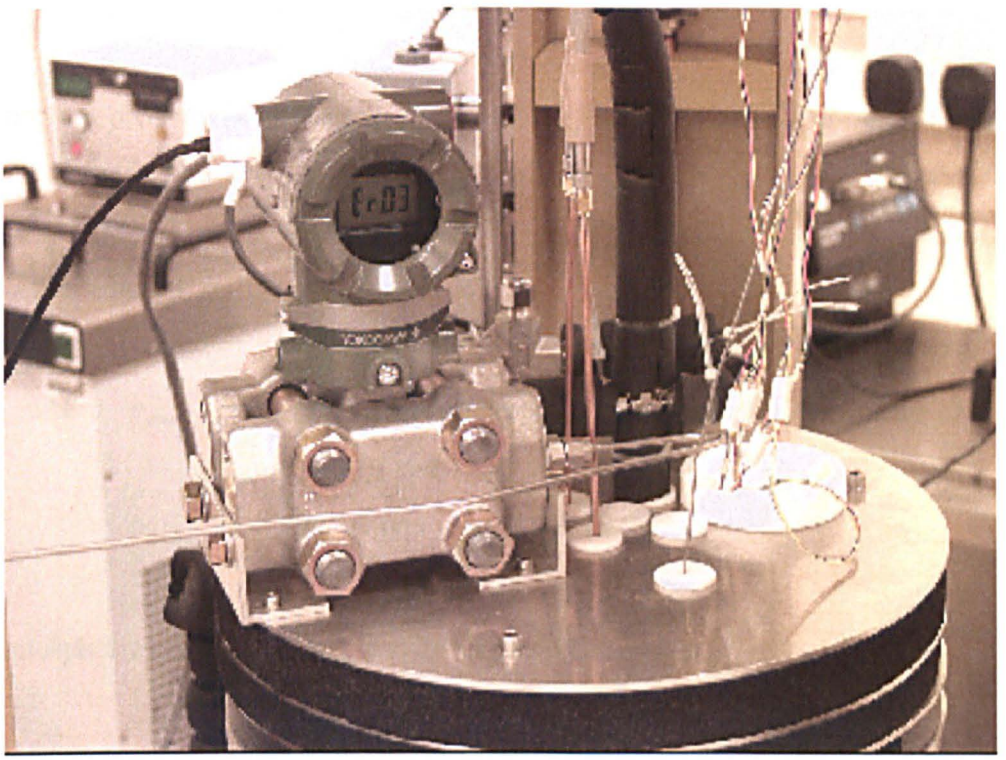

Figure 6.10 Differential pressure transducer mounting.

There therefore exists a small pressure head and temperature gradient in the ethylene pipe between the DPT and the mid-point of the permittivity cell and in order to determine the pressure at the this point it is necessary to apply a correction to the measured pressure which accounts for the head.

The absolute pressure of the contained fluid at the mid-point of the permittivity cell is given by the expression:-

$$p_{Cell} = p_N - p_{DP} + p_{H1}, \tag{6.4}$$

where p_N is the absolute pressure of nitrogen at the mid-point of the DPT;

p_{DP} is the corrected differential pressure; and

p_{H1} is the absolute pressure of the head between the DPT and the mid-point of the permittivity cell.

The absolute pressure of nitrogen, p_N, at the mid-point of the DPT may be expressed as:-

$$p_N = p_{atms} + p_{gauge}, \tag{6.5}$$

where p_{atms} is the atmospheric pressure at the reference level of the D&H (see figure (6.2)); and

p_{gauge} is the gauge pressure of the D&H.

The atmospheric pressure, p_{atms}, may be expressed as:-

$$p_{atms} = p_{PT} + p_{H2}, \tag{6.6}$$

where p_{PT} is the averaged atmospheric pressure as measured by the Druck PT's; and

p_{H2} is the small head of air that exists between the Druck PT's and the reference level of the D&H.

The pressure head between the Druck PT's and the reference level of the D&H may be expressed as:-

$$p_{H2} = g_{loc}.h.\rho_{air}, \tag{6.7}$$

where g_{loc} is the local acceleration due to gravity;

h is the height between the Druck PT's and the reference level of the D&H; and

ρ_{air} is the density of the ambient air.

The density of the ambient air is calculated using the ambient temperature, t_{amb}, the ambient pressure, p_{amb}, and the relative humidity, $R.H.$, with reference to expressions recommended by the Comite International des Poids et Measures (CIPM)[11].

The gauge pressure, p_{gauge}, of the D&H is calculated with reference to the calibration coefficients of the specific piston-cylinder and mass set used, the temperature of the piston-cylinder, the applied mass and the density of the ambient air. Calculation of the gauge pressure involves applying a number of correction factors to the basic force/area relationship to compensate for air buoyancy effects on the applied masses and changes in the cross-sectional area of the piston-cylinder with temperature and pressure. The basic force/area relationship is given by:-

$$P_{gauge} = \frac{m.g_{loc}}{A(t)}, \tag{6.8}$$

where m is the applied mass; and

$A(t)$ is the cross-sectional area of the piston-cylinder assembly at temperature t.

On application of the correction for the effects of air buoyancy on the applied mass equation (6.8) becomes:-

$$P_{gauge} = \frac{m.g_{loc}}{A(t)}.(1+C_B), \tag{6.9}$$

where C_B is the correction factor for the effects of air buoyancy on the applied mass and is equal to $-\left(\rho_{air}/\rho_{mass}\right)$;

where ρ_{mass} is the density of the applied mass set.

The density of the mass set is a constant the value of which is determined upon calibration.

The cross-sectional area of the piston-cylinder is a function of temperature and may be expressed as:-

$$A(t) = A(t_{ref}).(1-\theta).(t_{cyl} - t_{ref}), \tag{6.10}$$

where $A(t_{ref})$ is the effective cross-sectional area of the piston-cylinder at the reference temperature, t_{ref} and zero pressure (obtained on calibration);

t_{ref} is the reference temperature and is taken as 20°C;

θ is the combined thermal expansion coefficients of the piston and cylinder; and

t_{cyl} is the temperature of the piston-cylinder.

The temperature of the piston-cylinder, t_{cyl}, is calculated from resistance value of the PRT probe mounted within the D&H, $R_{D\&H}$. The temperature of the piston-cylinder is obtained from the following expression:-

$$t_{cyl} = \frac{\left(R_{D\&H} - R_o\right)}{\alpha}, \tag{6.11}$$

where $R_{D\&H}$ is the resistance value of the PRT probe mounted within the D&H;

R_o is the resistance value of the PRT probe at 0°C (obtained on calibration); and

α is the conversion coefficient from ohms to degrees C.

On application of the correction for the effects of the changes in the cross-sectional area of the piston-cylinder with pressure equation (6.9) becomes:-

$$P_{gauge} = \frac{\frac{m.g_{loc}}{A(t)}.\left(1 - \rho_{air}/\rho_{mass}\right)}{\left(1 + C_p\right)}, \tag{6.12}$$

where C_p is the correction factor for the effects of the changes in the cross-sectional area of the piston-cylinder with pressure and is equal to $\left(\lambda.p_{gauge}\right)$;

where λ is the pressure distortion coefficient of the piston and cylinder assembly.

It should be noted that there was no pressure head correction required between the reference level of the D&H and the mid-point of the DPT, since both of these points were at the same level and the same ambient temperature.

The corrected differential pressure, p_{DP}, in equation (6.4) is obtained by reading the indicated DPT pressure and applying a correction from graph (6.1).

The pressure head, p_{H1}, which exists between the mid-point of the DPT and the mid-point of the permittivity cell, must be calculated using the equation of state for ethylene. As found by other authors [12], [13], [14], [15] this pressure head must either be eliminated by design or calculated carefully to obtain accurate and unbiased values of the Clausius-Mossotti function for those state points within the near critical region. Though the experimental set-up was not specifically designed for critical region measurements some of the measurements which were undertaken, particularly those on the 10 °C isotherm, lie close to the critical point of ethylene (t_c = 9.2 °C, p_c = 5.0418 MPa)[2] and care is therefore required to calculate the pressure head for the same. Ideally, for near critical region measurements, the mid-point of the DPT and the permittivity cell would have been located in the same thermostatted enclosure at the same level. As explained previously the geometry of the permittivity cell was such that this was not possible.

The pipework which leads from the DPT to the permittivity cell passes vertically down through four separate layers:-

Layer	Thickness/mm	Description
1	50	A layer of insulation above the lid of the thermostatted vessel which is surrounded by air at near ambient temperature.
2	60	The insulated lid of the thermostatted vessel. The heat transfer characteristics of this layer are similar to that of the previous layer.
3	45	A layer of air at near bath temperature between the lower surface of the lid and the surface of the thermostat fluid.
4	311 (from the surface to the mid-point of the cavity)	The thermostat fluid. Beneath the surface of the thermostat fluid the pipe curves horizontally around the cavity to provide a long thermal path between its connection with the cavity vessel and the surface of the fluid.

By far the greatest temperature gradient in the test fluid takes place in the first two layers. Fortunately, they are relatively thin and contribute least to the total pressure correction. However, the temperature profile in these two layers is not known reliably and hence they contribute most to the overall uncertainty in the total pressure correction. The temperature of the test fluid in layer 3, and especially in layer 4, is close to the measured bath temperature.

To help establish the temperature profile within the vertical section of the pipe a series of temperature measurements were taken at the top of the vertical section of pipe for a range of bath temperatures from 0 to 40 °C. The following equation was found to represent the measured temperatures and give a physically realistic profile elsewhere along the pipe:-

$$t_x = t_{bath} + 0.9875.\left(t_{amb} - t_{bath}\right).e^{-\alpha.x}, \tag{6.13}$$

where x is the vertical distance, in m, from the top of the pipe; and

α is a coefficient, here taken to be 34.0 m^{-1}.

An indication of the temperature profile along the pipe for a range of bath temperatures, as generated by equation (6.13) assuming an ambient air temperature of 20 °C, is given in the following table:-

Position	**Depth/m**	**Temperature/°C**					
Top of pipe	0	20.250	20.125	20.063	19.938	19.875	19.750
Junction of layers 2 and 3	0.110	39.531	29.765	24.883	15.117	10.235	0.469
Junction of layers 3 and 4	0.155	39.898	29.949	24.975	15.025	10.051	0.102
Mid-point of cavity	0.466	40.000	30.000	25.000	15.000	10.000	0.000

Table 6.1 Temperature profile along ethylene pipe for a range of bath temperatures.

An additional difficulty exists in that the test fluid becomes progressively more compressible as the critical point is approached, indeed at the critical point the partial derivative $\left(\partial\rho/\partial p\right)_t$ tends to infinity. Thus a small change of pressure can produce a large change in fluid density, the magnitude of which is dependent upon the proximity to the critical point.

The pressure head in a pipe of vertical height l containing a fluid at near critical conditions must therefore be calculated from:-

$$p_{H1} = g.\int_0^l \rho(p_x, t_x).dx, \tag{6.14}$$

where g_{local} is the local acceleration due to gravity;

ρ is the density of the fluid at the specified pressure and temperature;

p_x is the absolute pressure at depth x;

t_x is the absolute temperature at depth x; and

x is the vertical distance from the top of the pipe.

In practice, away from the immediate vicinity of the critical point, the integral in the above expression can be evaluated by sub-dividing the vertical length of pipe, l, into N sub-layers and summing the individual increments in pressure to give:-

$$\begin{aligned}
&\Delta p = \sum_{i=1}^{N} \delta p_i, \\
&\delta p_i = g.\rho(p_{i-1}, t_{i-1}).\delta x, \\
&\delta x = {}^{l}/_{N}, \\
&p_i = p_{i-1} + \delta p_i, \\
&p_o = \text{absolute pressure at the top of the vertical section of pipe,} \\
&x_i = x_{i-1} + \delta x, \\
&t_{i-1} = t_{bath} + 0.9875.(t_{amb} - t_{bath}).e^{-\alpha.x_i}, \text{ and} \\
&x_o = 0.
\end{aligned} \tag{6.15}$$

In the pressure head calculations made using the above set of equations, equation (6.15), the number of increments, N was selected to be 466 making the thickness of each sub-layer, δx, equal to 1 mm. Detailed calculations of the pressure correction were made for a range of both bath temperatures and system pressures. At each state point the calculations were repeated with three different values of the temperature profile

coefficient, α; namely 24.0, 34.0 and 44.0 m^{-1}, respectively. Small percentage differences between the three pressure heads were observed at each state point. For supercritical isotherms these reached a maximum at a pressure corresponding to the critical density, and for sub-critical isotherms the maximum differences in pressure occurred at pressures close to the saturation pressure. The spread of the density values, calculated at the mid-point of the cavity, was negligible in comparison to the uncertainties in the values of density derived from the equation of state.

6.8.8 Uncertainty in Pressure

The main parameters to be determined for a measurement of absolute pressure of the contained fluid at the mid-point of the cavity are:-

- the absolute pressure of nitrogen at the mid-point of the DPT, p_N;
- the corrected differential pressure, p_{DP}; and
- the absolute pressure of the head between the DPT and the mid-point of the cavity, p_{H1}.

The total uncertainty in the measurement of absolute pressure of contained fluid at the mid-point of the cavity may be expressed as:-

$$U^2_{p_{Cell}} = U^2_{p_N} + U^2_{p_{DP}} + U^2_{p_{H1}}, \tag{6.16}$$

where U_{p_N} is the total uncertainty in the absolute value of the reference nitrogen pressure at the mid-point of the DPT;

$U_{p_{DP}}$ is the uncertainty in the indicated differential pressure of the DPT; and

$U_{p_{H1}}$ is the uncertainty in the absolute pressure of the head between the

DPT and the mid-point of the permittivity cell.

The total uncertainty in the absolute value of the reference nitrogen pressure at the mid-point of the DPT, U_{p_N}, may be expressed as:-

$$U_{p_N} = 2.\sqrt{\sigma_{PT}^2 + \sigma_{p_{H2}}^2 + 0.333.\left(\sigma_{p_{Gauge}}^2\right)}, \tag{6.17}$$

where σ_{PT} is the standard deviation of the atmospheric pressure as measured with a Druck PT;

$\sigma_{P_{H2}}$ is the standard deviation of the pressure head of air that exists between the Druck PT and the reference level of the D&H; and

$\sigma_{p_{Gauge}}$ is the total uncertainty in the calculated gauge pressure of the D&H.

The calculated uncertainty in equation (6.17) is the standard deviation multiplied by a factor of two which in the case of a Gaussian distribution implies a confidence level of approximately 95%.

The standard deviation of the atmospheric pressure measurement, σ_{PT}, is estimated from the uncertainty associated with the equipment that was used to calibrate the Drucks and the uncertainty limits in the measurement reading and taken to be 0.015% of the atmospheric pressure.

The standard deviation of the pressure head of air that exists between the Druck PT and the reference level of the D&H, $\sigma_{P_{H2}}$, is estimated from an approximation of the accuracy of the ambient temperature measurement.

The total uncertainty in the calculated gauge pressure of the D&H, as quoted by the

manufacturer, is 0.005% of the gauge pressure.

The uncertainty in the indicated differential pressure of the DPT, $U_{p_{DP}}$, as quoted by the manufacturer, is 0.075% of the span of the instrument. The span of the instrument was set to 160 mbar throughout the measurement programme, therefore the uncertainty in the differential measurement was 0.12 mbar.

The uncertainty in the absolute pressure of the head between the DPT and the mid-point of the cavity, $U_{p_{H1}}$, was estimated to be a maximum of 2.5% of the head value.

The total uncertainty in the measurement of absolute pressure of contained fluid at the mid-point of the cavity is estimated to be 0.01% over the entire operational range of pressures.

References

1. Watson, J. T. R., Ferguson, D. and Ryan, G., *National Standards Facilities for the Density of Liquids and Gases at Elevated Pressures.* Paper presented at the Density Seminar held in the James Watt Conference Centre, National Engineering Laboratory, 24 October, 1994, in conjunction with the North Sea Flow Measurement Workshop, 1994.
2. J. Smukala, R. Span, and W. Wagner, *New Equation of State for Ethylene Covering the Fluid Region for Temperatures From the Melting Line to 450 K at Pressures up to 300 MPa*, J. Phys. Chem. Ref. Data, Vol. 29, No. 5, pp 1053-1121, 2000.
3. Research carried out at the National Engineering Laboratory.
4. British Standards BS5500, *Specification for Unfired Fusion Welded Pressure Vessels.*
5. Comité Consultatif de Thermometrié, *Techniques for approximating the International Temperature Scale of 1990*, published by Bureau International des Poids et Mesures, July 1990.
6. Comité Consultatif de Thermometrié, *Supplementary Information for the International Temperature Scale of 1990*, published Bureau International des Poids et Mesures, December 1990.
7. Ryan, H. G., *Realisation of the ITS-90 using Standard Platinum Resistance Thermometers*, National Engineering Laboratory, 1992.
8. Private correspondence with Prof. Dr. –Ing. W. Wagner, Lehrstuhl fuer Thermodynamik, Ruhr-Universitaet Bochum, Germany.
9. Private correspondence with Jim Ryan, BP Chemicals Limited, Grangemouth, United Kingdom.
10. Buckley, T. J., Hamelin, J. O., and Moldover, M. R., *Toroidal Cross-Capacitor for Measuring the Dielectric Constants of Gases,* Review of Scientific Instruments, 71, 2914-2921, 2000.
11. P. Giacomo, Metrologia, 1982, Vol. 18, pp. 33-45.

12. Barend, J., Thijsse, *The Dielectric Constant of SF_6 Near the Critical Point*, Journal of Chemical Physics, vol 74, pp. 4678-4692, 1981.
13. T. D. Doiron and H. Meyer, *Dielectric Constant of ^3He Near the Liquid-Vapour Critical Point*, Phys. Rev. B 17, 2141, 1979.
14. M. H. W. Chan, *Dielectric Constant of Ne Near its Liquid-Vapour Critical Point*, Phys. Rev. B 21, 1187, 1980.
15. M.W. Pestak and M. H. W. Chan, *Dielectric Constant of CO Near its Liquid-Vapour Critical Point*, Physical Review Letters, Vol. 46, pp. 943-946, (1981).

7. Experimental Results

The results of the fluid *mapping* or *characterisation* of the ethylene surface in terms of relative permittivity and density at temperatures between 0 and 40 °C and at pressures up to 120 bar are presented. It should be noted that only the measurements used in the actual regression analysis are presented here (see section 8.3). The numerical values are reported in Appendix A.

The measureands recorded at each state point of the ethylene measurement programme are plotted as functions of temperature and pressure. The plots illustrate the physical characteristics of the fluid and the associated electrical characteristics of the re-entrant cavity resonator.

7.1 Vapour-Pressure Curve

Interpretation of the measurement results presented here may be facilitated by considering the physical state of the fluid at any one state point of the measurement programme. The vapour-pressure curve of ethylene over the range of temperatures and pressures[1] considered here is plotted in graph (7.1) below:-

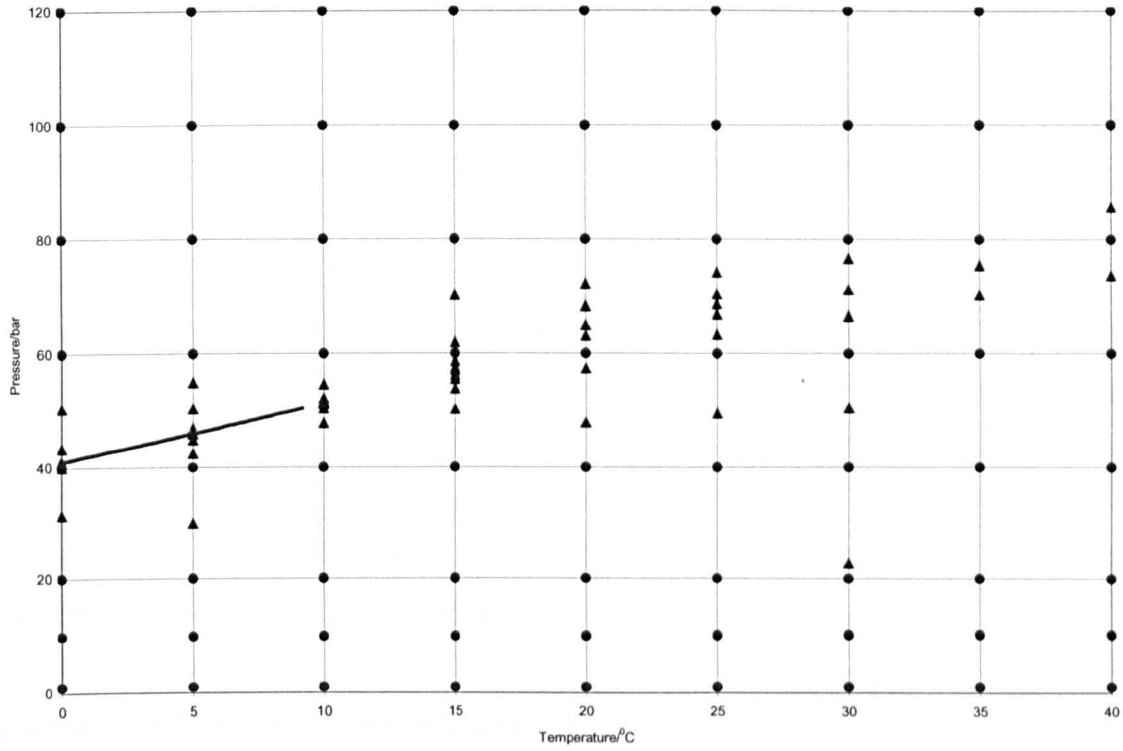

Graph 7.1 State point measurements and the vapour-pressure curve of ethylene.

The areas above and below the saturation curve in graph (7.1) are the respective liquid and vapour regions of the fluid. Each point on the grid represents, approximately, the state points of the measurement programme. The 72 state points of the initial measurement programme, which are distributed uniformly throughout the measurement range, are represented by the symbol ●, and the 54 state points, which concentrate around the vapour-pressure saturation curve and the critical and supercritical regions, are represented by the symbol ▲. The state points that were deemed unsuitable for inclusion in the surface mapping of the ethylene are highlighted in red. It can therefore be seen that an approximately equal number of initial measurement state points in the liquid and vapour regions. It should also be noted that the measurement programme encompasses the critical point of the fluid which occurs at $t_c = 9.2^{\circ}C$ and $p_c = 50.418\,\text{bar}$ [1].

7.2 Density

The density of ethylene calculated from the reference-quality equation of state[1] (see section 8.1) is plotted as a function of temperature and pressure over the range of measurement conditions in graph (7.2).

Graph (7.2) illustrates the characteristics of the fluid over the range of conditions under consideration here. The sub-critical region transition between the vapour and liquid state of the fluid is clearly illustrated by the step-like increase in density. Progressively further into the supercritical region the transition between the two states becomes less distinct. The density takes a maximum value of ≈ 15000 mol/m^{-3} close to 0 °C and 120 bar and a minimum value of ≈ 400 mol/m^{-3} close to 40°C and 10 bar.

It should be noted that for ease of representation all the temperature data for each state point in this section has been approximated to the nearest whole number, as illustrated by the nine isotherms in graph (7.2). The data illustrated in graph (7.2) is reported in table (A.1) in appendix A.

7.3 Resonant Frequency

The resonant frequency of the cavity is plotted as a function of temperature and pressure of the ethylene over the range of measurement conditions in graph (7.3).

Since the resonant frequency of the cavity is an inverse function of the density of the fluid it is to be expected that the characteristics of graph (7.3) are the inverse of the of graph (7.2). The resonant frequency takes a maximum value of ≈ 392 MHz close to 40 °C and 10 bar and a minimum value of ≈ 315 MHz close to 0 °C and 120 bar.

It should be noted that the resonant frequency data reported here represents measurements taken before and after the rebuild of the cavity (see Chapter 6:

Experimental Measurements, Facility and Operation). The first assembly of the cavity covered isobars 120, 100 and 80, and the second covered all subsequent measurements. The vacuum resonant frequency measurements obtained from the re-assembled cavity were found to be within approximately 1ppm of the original set of measurements, therefore the combined data of the two individual assemblies may be represented on one plot without loss of continuity. The data illustrated in graph (7.3) is reported in table (A.2) in appendix A.

7.4 Relative Permittivity

The relative permittivity of the ethylene is obtained from the ratio of the resonant frequencies of the evacuated and fluid filled cavity at the same temperature (see section 4.5). In order to determine the relative permittivity it is therefore necessary to characterise the vacuum resonant frequency of the cavity over the range of operating temperatures.

Since the resonant frequency of the cavity is particular to any one individual assembly data is presented for each assembly used in the measurement programme. The vacuum resonant frequency of the cavity as a function of temperature for assemblies 1 and 2 are presented in graphs (7.4) and (7.5) respectively, below:-

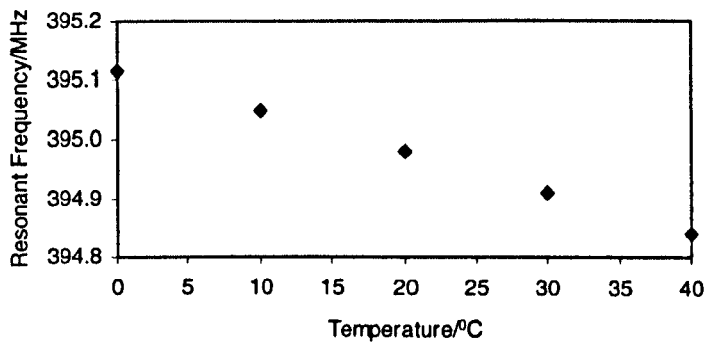

Graph 7.4 Vacuum resonant frequency of assembly 1 as a function of temperature.

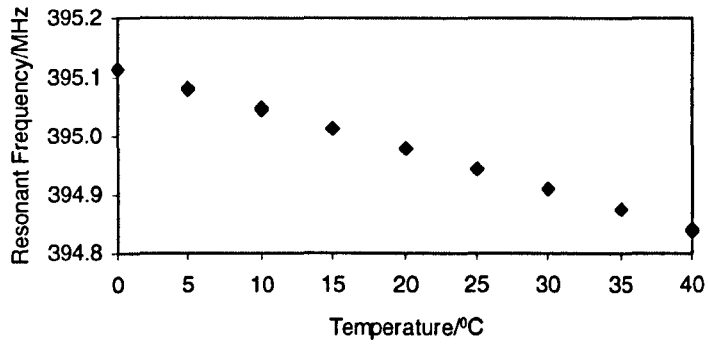

Graph 7.5 Vacuum resonant frequency of assembly 2 as a function of temperature.

It can be seen from graphs (7.4) and (7.5) that the resonant frequency of the evacuated cavity decreases with increasing temperature. As the temperature of the cavity increases the thermal expansion of the inner and outer components of the cavity cause the radial gap between the two to decrease resulting in an increase in the capacitance of the cavity. (The thermal expansion may also result in a small increase in the inductive section of the cavity through the increase in length of the inner component of the cavity, however the effect of this is considered to be small in comparison with the increase in capacitance). Since the resonant frequency is inversely proportional to the square root of the product of the capacitance and inductance (expression (4.3)) its decrease with increasing temperature is expected. The resonant frequency decreases by approximately 0.07% over the temperature range for both assemblies.

Regression of these measurements gives an expression which determines the resonant frequency of the evacuated cavity at a specified temperature. From these data and the resonant frequency data of the fluid filled cavity of section 7.3 the relative permittivity of the ethylene is calculated. The relative permittivity of the ethylene as a function of temperature and pressure over the range of measurement conditions is plotted in graph (7.6).

It can be seen clearly from graph (7.6) that the relative permittivity characteristics are exactly the same as the density characteristics in graph (7.2) and the inverse of the resonant frequency characteristics in graph (7.3). The relative permittivity takes a maximum value of ≈ 1.6 close to 0 °C and 120 bar and a minimum value of ≈ 1.01 close to 40°C and 10 bar. The data illustrated in graph (7.6) is reported in table (A.3) in appendix A.

7.5 Quality Factor

The electrical quality factor of the cavity has been measured as a function of temperature and pressure of the ethylene over the range of conditions, including vacuum conditions. The quality factor of the evacuated cavity is required as part of the correction for the effective dilation of the cavity due to the change in the penetration depth of the magnetic field into the metal surfaces bounding the cavity. The quality factor of the fluid filled cavity also yields information on the dielectric loss of the ethylene and the corresponding electrical characteristics.

Since the quality factor of the evacuated cavity is required for the penetration depth correction factor data is presented for each assembly used in the measurement programme. The quality factor of the cavity is dependent primarily on the electrical resistance of its inner surfaces and as a result is significantly more sensitive to assembly than the resonant frequency. The surface resistance of the inner components of the cavity is mostly effected by the electrical conduction path provided by the electrical gasket between the inner and outer components of the cavity. The quality factor of the cavity as a function of temperature for assemblies 1 and 2 are presented in graph (7.7) below:-

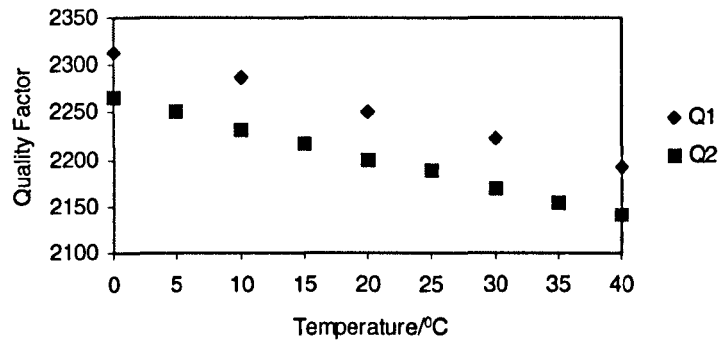

Graph 7.7 Quality factor of evacuated cavity, assemblies 1 and 2.

The sensitivity of the quality factor to assembly is clearly illustrated in graph (7.7). On this particular re-assembly the quality factor of the evacuated cavity drops by approximately 2%. The decrease in quality factor by approximately 5% with temperature for both assemblies is a direct result of the increase in the electrical resistivity of its inner surfaces.

Regression of these measurements gives an expression which determines the quality factor of the evacuated cavity at a specified temperature. From these data and the corresponding resonant frequency data of the evacuated and fluid filled cavity the electromagnetic penetration depth correction factor is calculated.

For a fluid filled cavity the quality factor is dependent primarily on the electrical resistivity of the inner surfaces and the resonant frequency (through the relative permittivity of the contained fluid). The quality factor is also dependent upon the dielectric loss of the fluid contained within the cavity, for ethylene this component is small.

The quality factor of the filled cavity as a function of temperature and pressure over the range of measurement conditions for assemblies 2 and 1 are presented in graphs (7.8) and (7.9) respectively. With reference to the general characteristics illustrated in

previous graphs, the higher quality factor of assembly 1 is clearly evident on comparison of graphs (7.8) and (7.9).

The quality factor does not, however, exhibit exactly the same density dependent characteristic as the resonant frequency. In contrast to the resonant frequency characteristics, the quality factor of the cavity takes it maximum value of ≈ 2250 close to 0 °C and 10 bar and a minimum value of ≈ 2050 close to 40°C and 120 bar, which is completely opposite in terms of temperature. This result illustrates that the effect of temperature on the quality factor of the cavity, through the changes in resistivity of the inner surfaces, is much more influential than the corresponding increase in relative permittivity. The data illustrated in graphs (7.8) and (7.9) is reported in table (A.4) in appendix A.

The most important thing to note is that the quality factor of the cavity, under the measurement conditions considered here, is still well in excess of 1000, which means that the simplified version of Goodwin's theoretical model of the cavity[2] is applicable.

7.6 Insertion Loss

The insertion loss of the cavity has been measured as a function of temperature and pressure of the ethylene over the range of measurement conditions considered here. Measurements of the insertion loss yields information on the total electrical losses of the cavity, which include, the dielectric losses of the fluid, impedance mismatches between the cavity and the network analyser and the electrical resistance. Data on the insertion loss of the cavity is necessary in order to determine the technical requirements of the *on-line* instrument (see Chapter 9).

From the parameters mentioned above it can be seen that insertion loss may also be considered particular to any one assembly. The insertion loss of the cavity as a function of temperature and pressure over the range of measurement conditions for assemblies 2

and 1 are presented in graphs (7.10) and (7.11) respectively.

Again with reference to the general characteristics illustrated in previous graphs, it can be seen that the insertion loss of assembly 1 is greater than that of assembly 2. This result may at first seem to contradict the findings of section (7.5), where an increase in the resistance of the cavity was deemed to be the cause of the decrease in quality factor of the second assembly. However, what these results actually illustrate is that the insertion loss of the cavity is primarily dependent on the impedance mismatch between itself and the network analyser.

The impedance presented to the network analyser is determined by the properties of the coupling antenna itself and the amount of magnetic flux linkage between it and the inductive toroid of the cavity. The degree of coupling is determined by the position of the antenna loop relative to the magnetic flux of the inductive toriod. Therefore each individual assembly of the cavity will have a unique characteristic input impedance and corresponding insertion loss.

The characteristics of the insertion loss of the lower pressure range of measurements (graph (7.10)) are almost exactly the inverse of the quality factor characteristics under the same conditions (graph (7.8)). This result illustrates that, like the quality factor, the effect of temperature on the insertion loss of the cavity, through the changes in resistivity of the inner surfaces, is much more influential than the corresponding increase in relative permittivity and dielectric loss for the lower pressure range of measurements.

This effect, however, is not observed in the characteristics of the insertion loss of the higher pressure range of measurements (graph (7.11)). At higher pressures the insertion loss of the cavity does not appear to display any significant dependence on either temperature or relative permittivity and dielectric loss. Since the insertion loss of the cavity is principally determined by its input impedance, which is a complex quantity dependent on both resistance and reactance, the exact behaviour is hard to predict, but it

would appear in this instance that the effects of the two mechanisms which determine the impedance cancel each other out with no significant change in the insertion loss.

The insertion loss takes a maximum value of ≈ 23 dB for all temperatures at close to 120 bar and a minimum value of ≈ 19 dB close to 0 °C and 10 bar. The data illustrated in graphs (7.10) and (7.11) is reported in table (A.5) in appendix A.

The most important thing to note is that the insertion loss of the cavity is still significantly low enough to enable the unity gain criterion of the oscillator circuit to be easily met with a relatively modest amount of signal amplification (see Chapter 9).

7.7 Insertion Phase

The insertion phase of the cavity has been measured as a function of the temperature and pressure of ethylene over the range of measurement conditions considered here. Data on the insertion phase of the cavity is again necessary to determine the technical requirements of the *on-line* instrument (see Chapter 9).

The insertion phase of the cavity is plotted as a function of temperature and pressure over the range of measurement conditions in graph (7.12).

It should be noted that the insertion phase data reported here represents the measurements taken with cavity assemblies 1 and 2. The change in insertion phase between assemblies was small enough to allow the combined data to be represented on one plot without loss of continuity. It should also be noted that the data has been corrected in terms of 2π to allow the phase changes to be represented in a continuous fashion.

It can be seen clearly from graph (7.12) that the insertion phase has exactly the same characteristics as the relative permittivity in graph (7.6). This is to be expected since the

insertion phase is primarily determined by the capacitive reactance of the cavity. The insertion phase takes a maximum value of ≈ +295° close to 0 °C and 120 bar and a minimum value of ≈ -165° close to 40°C and 10 bar. The total change in insertion phase of the cavity is, however, more important than the above values. The data illustrated in graph (7.12) is reported in table (A.6) in appendix A.

The total change in insertion phase of the cavity is approximately 460° over the range of measurement conditions considered here. This result is extremely significant for the technical specification of the phase shifter component of the *on-line* instrument. If an *on-line* instrument is to be used to perform measurements on ethylene over the range of conditions under consideration here then it must be capable of operating with sufficient accuracy over a full 360°. With reference to Chapter 9: Development of On-Line Instrument, it can be seen that this phase swing is much larger than was achievable with any of the phase shifters that were constructed.

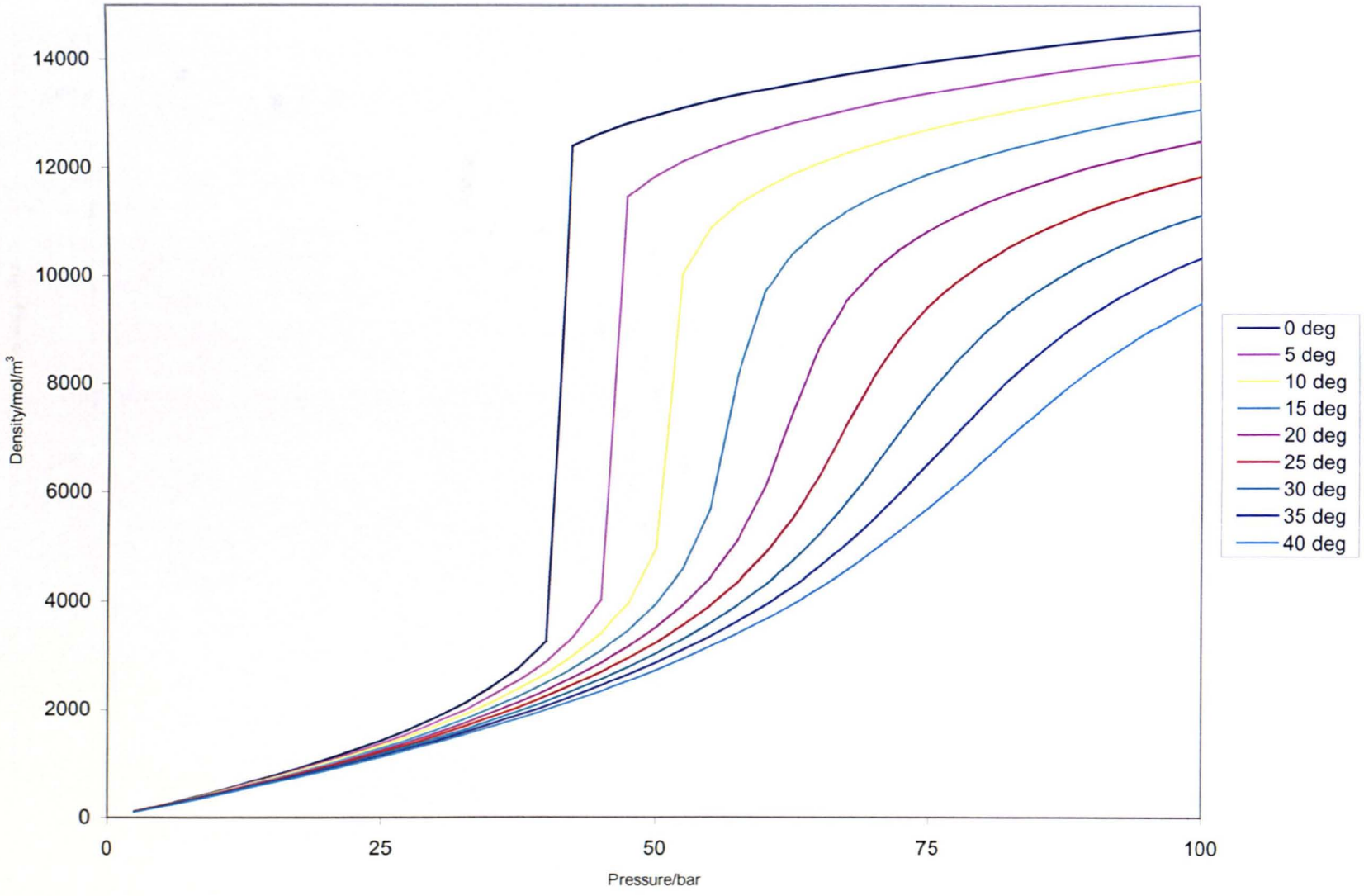

Graph 7.2 Density of ethylene as a function of temperature and pressure.

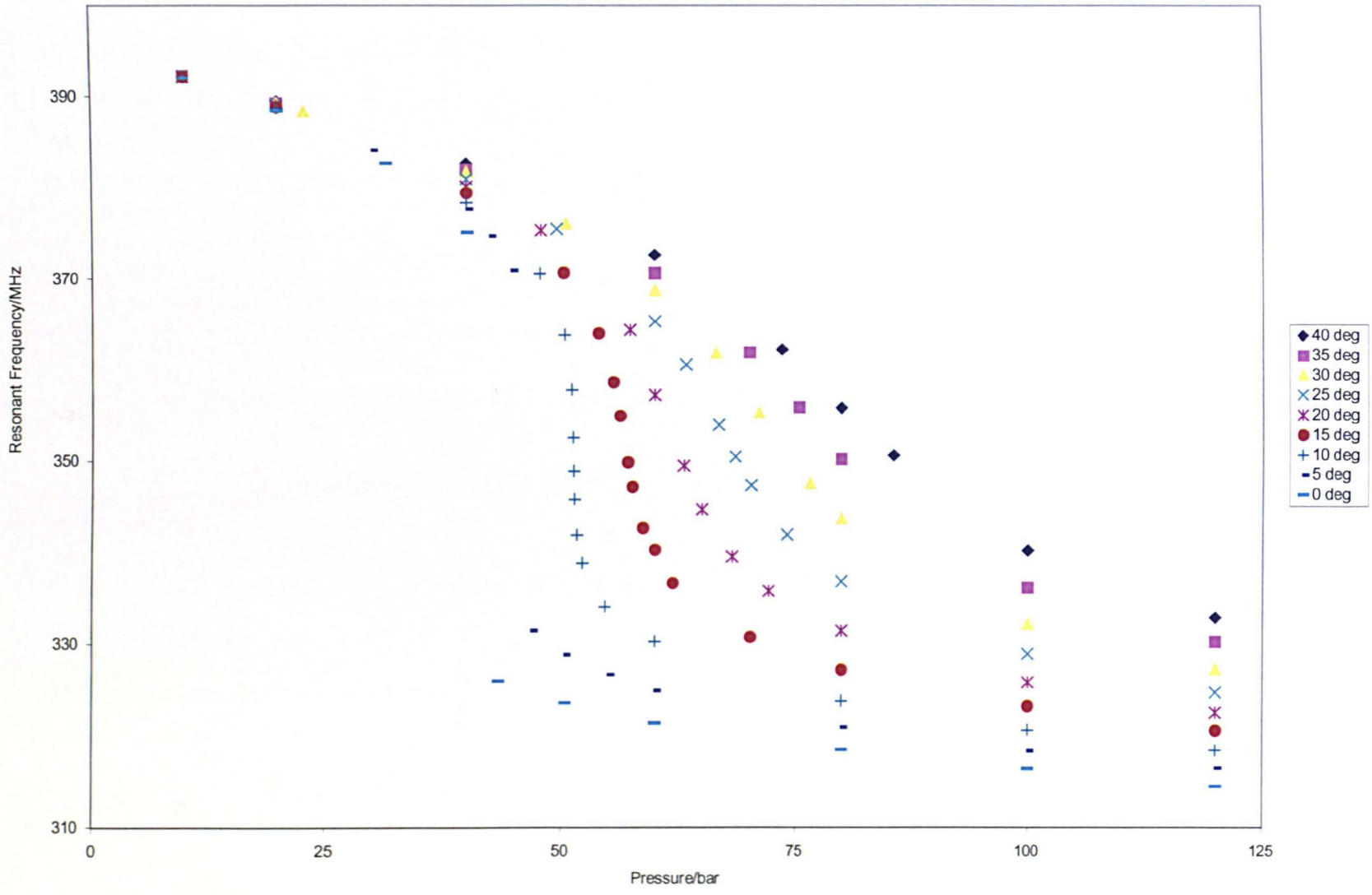

Graph 7.3 Resonant frequency of the cavity as a function of temperature and pressure.

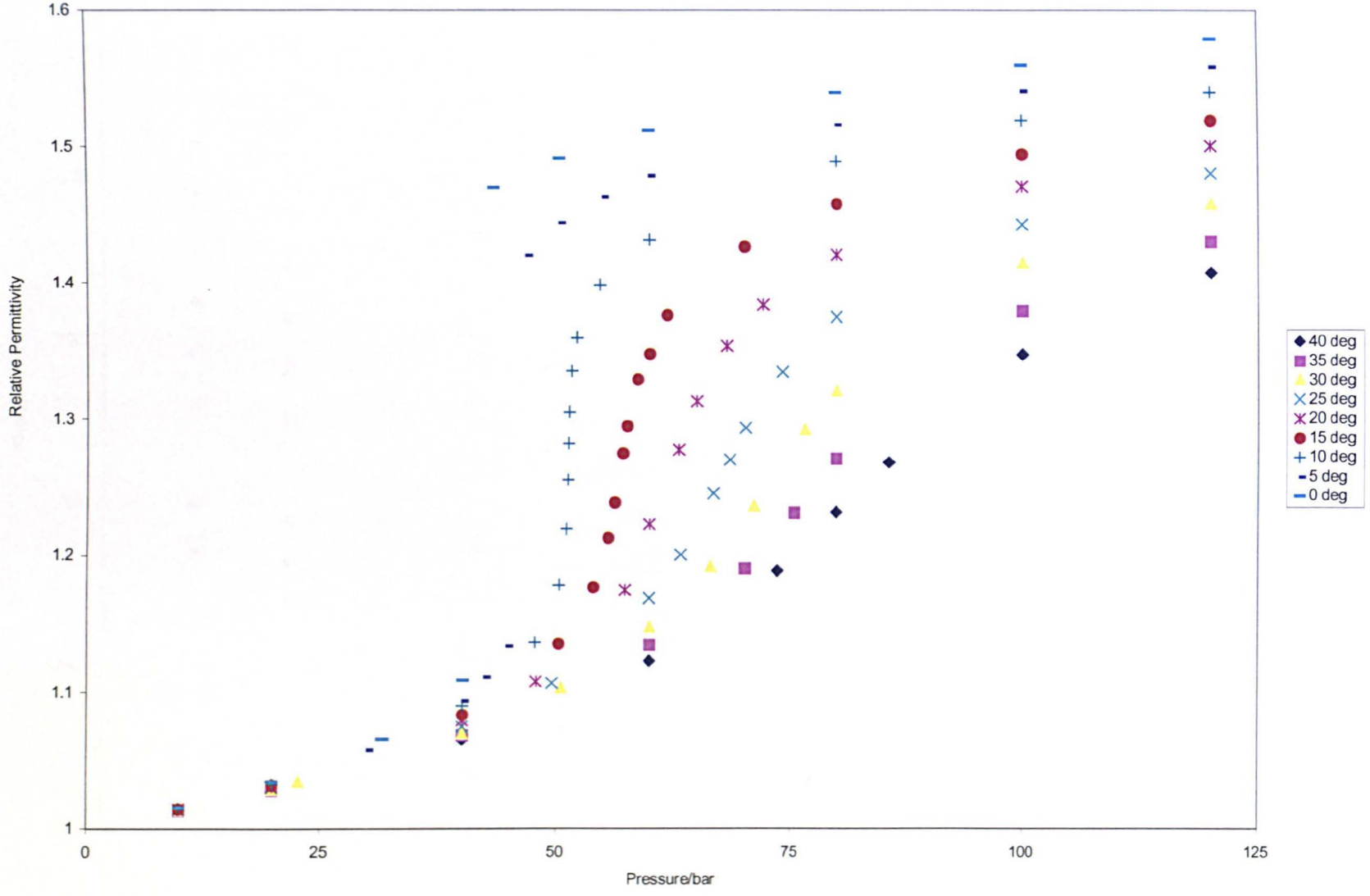

Graph 7.6 Relative permittivity of ethylene as a function of temperature and pressure.

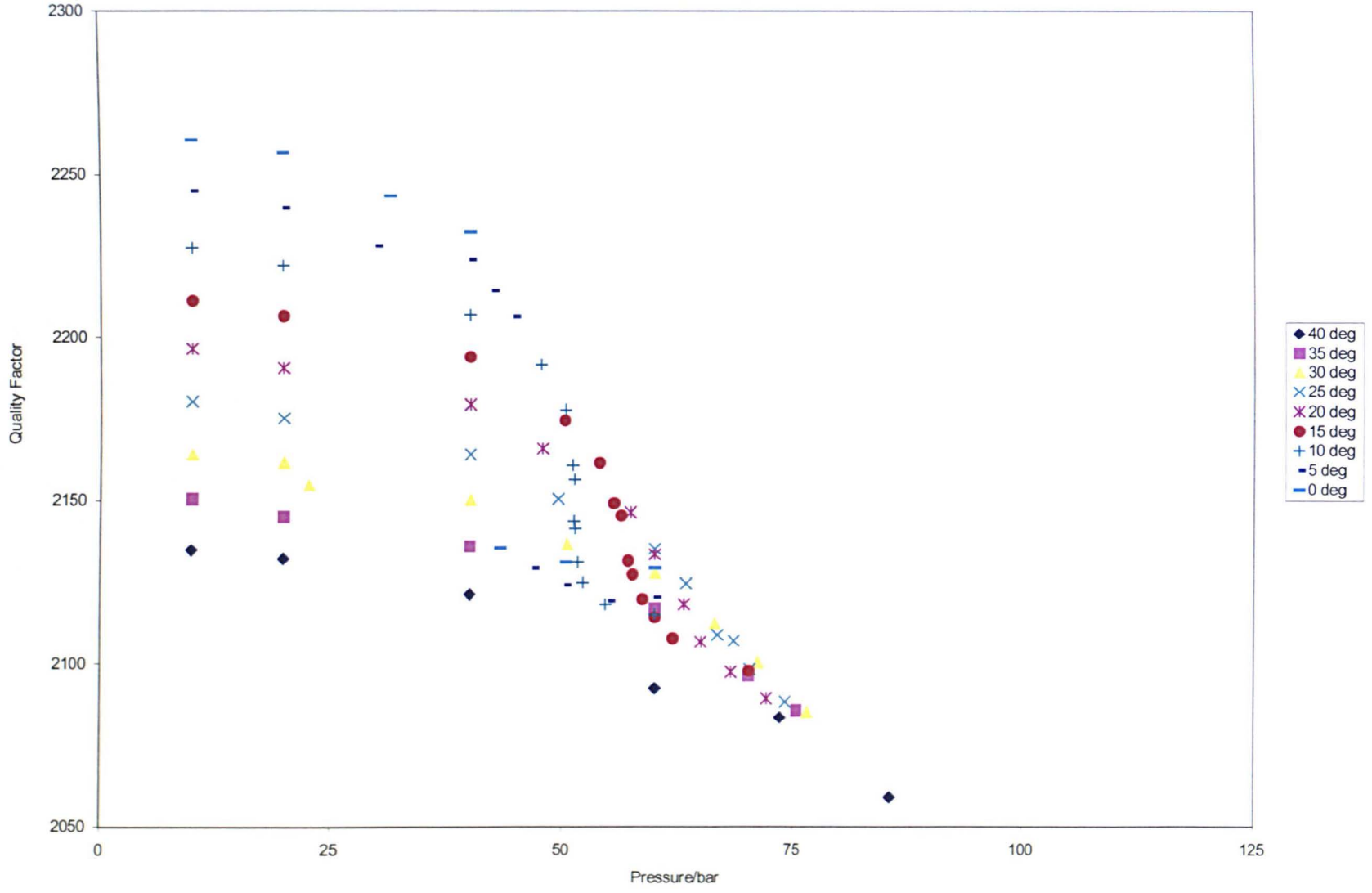

Graph 7.8 Quality factor of the cavity (assembly 2) as a function of temperature and pressure.

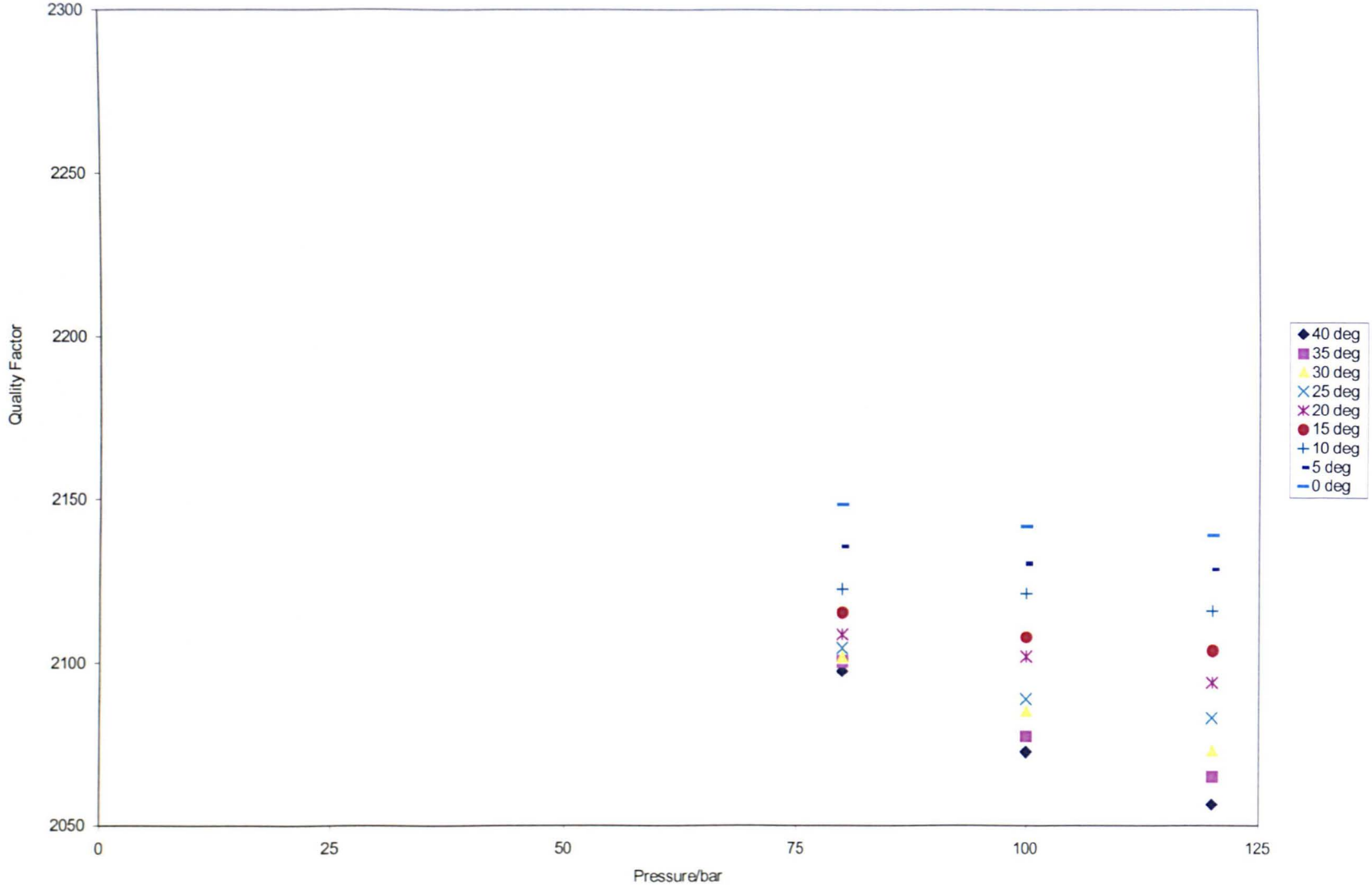

Graph 7.9 Quality factor of the cavity (assembly 1) as a function of temperature and pressure.

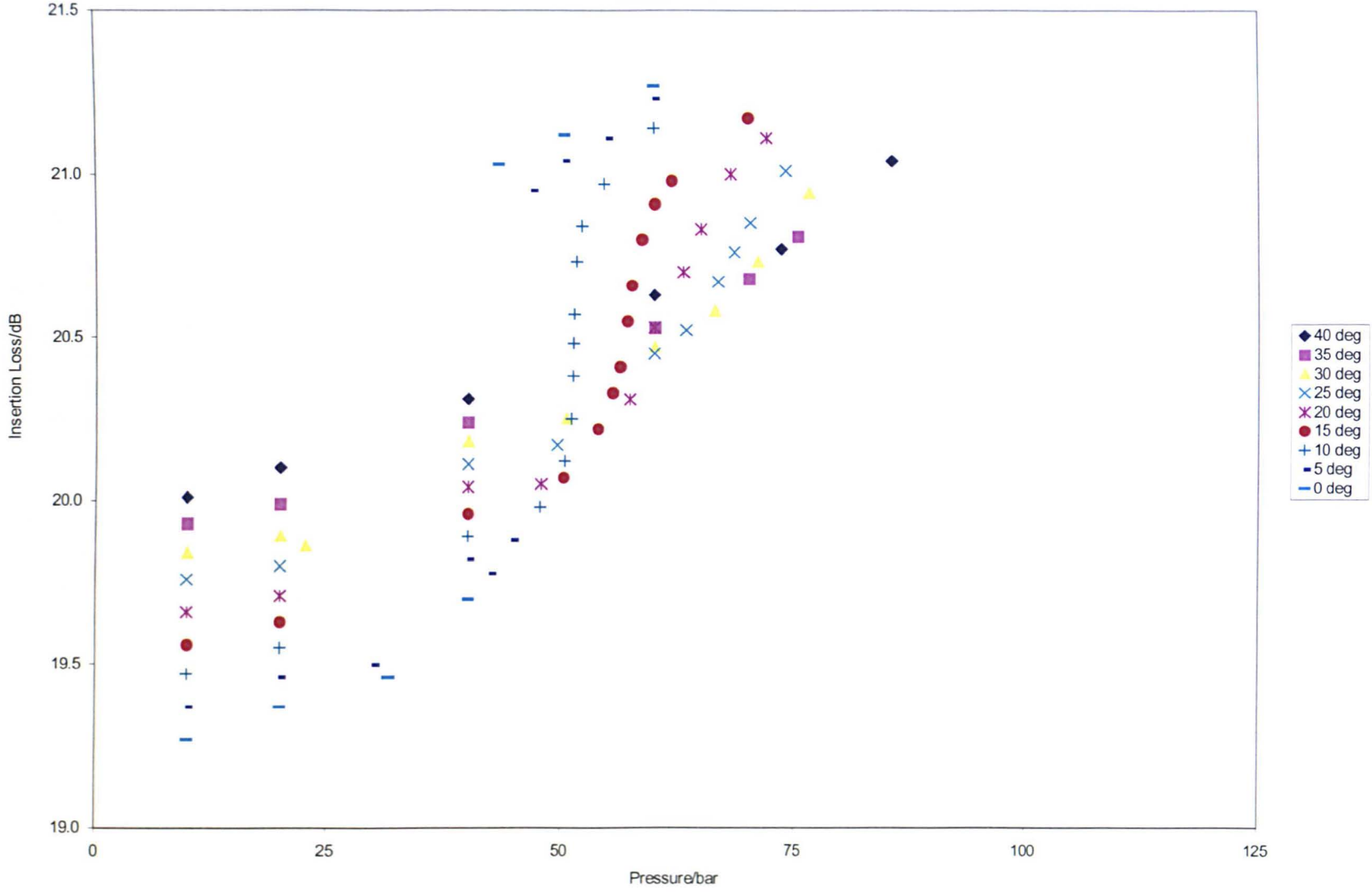

Graph 7.10 Insertion loss of the cavity (assembly 2) as a function of temperature and pressure.

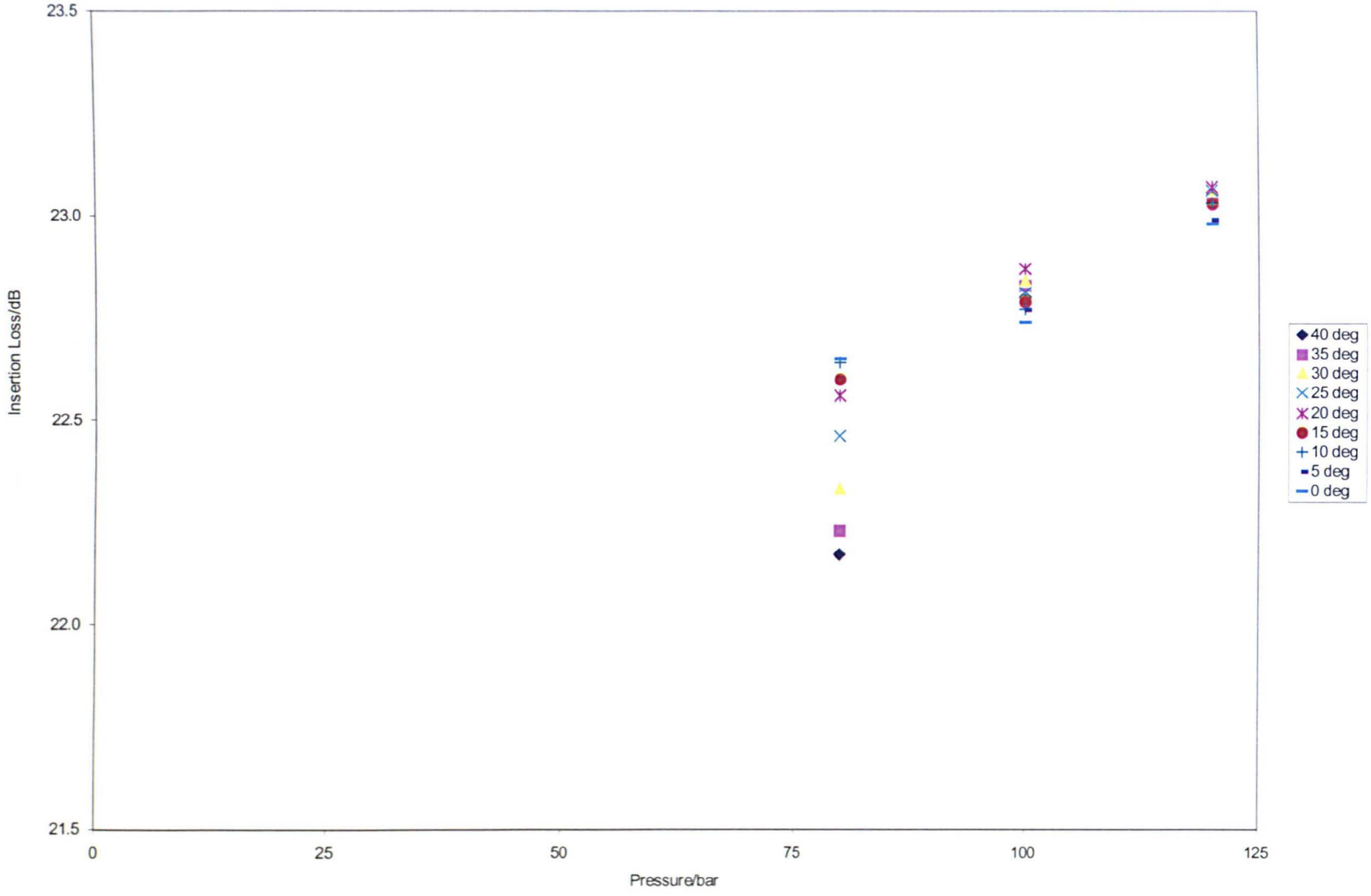

Graph 7.11 Insertion loss of the cavity (assembly 1) as a function of temperature and pressure.

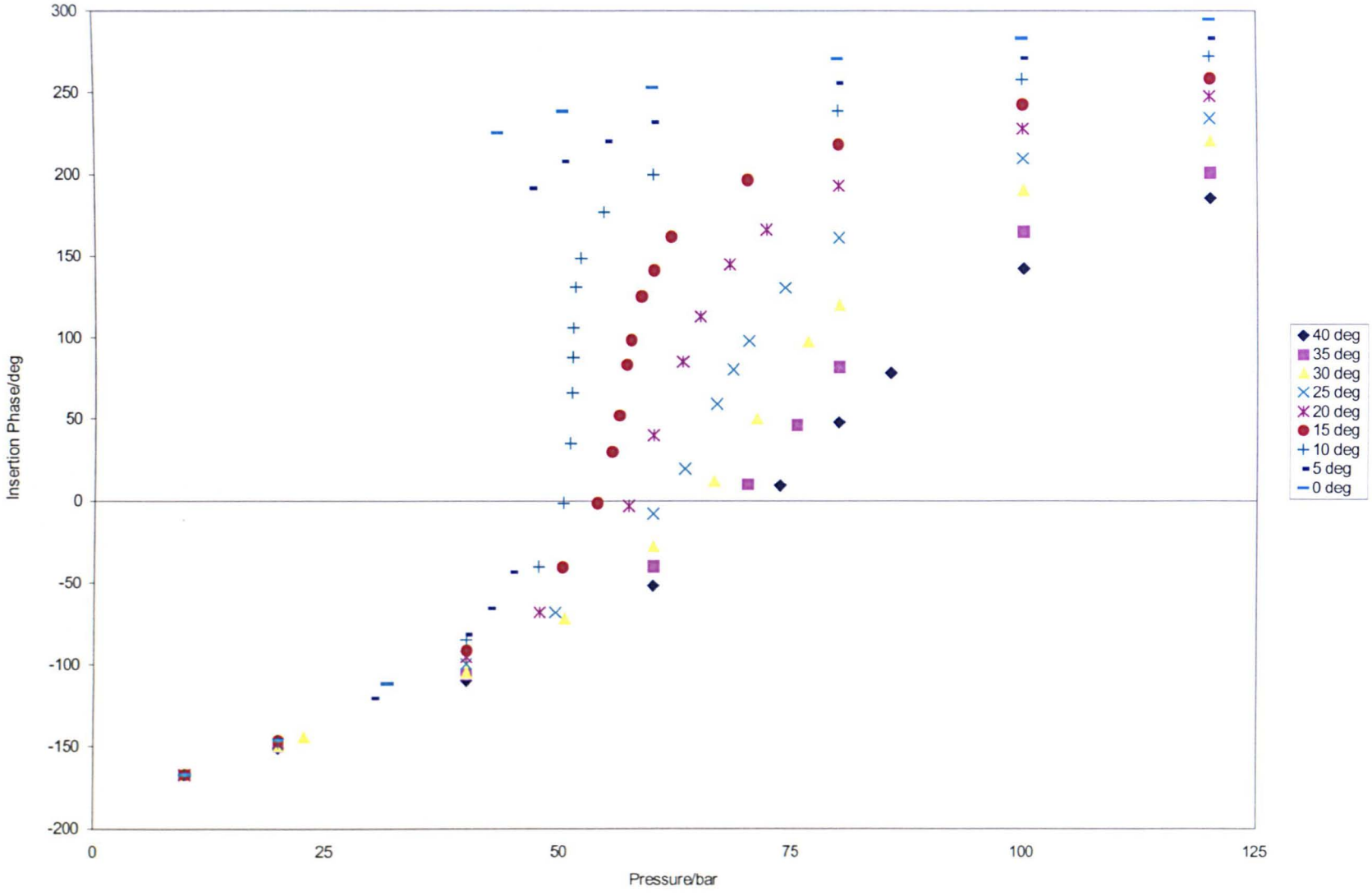

Graph 7.12 Insertion phase of the cavity as a function of temperature and pressure.

References

1. J. Smukala, R. Span, and W. Wagner, *New Equation of State for Ethylene Covering the Fluid Region for Temperatures From the Melting Line to 450 K at Pressures up to 300 MPa*, J. Phys. Chem. Ref. Data, Vol. 29, No. 5, pp 1053-1121, 2000.
2. Goodwin, A.R.H., Mehl, J.B. and Moldover, M.R. *Re-entrant radio-frequency resonator for automated phase-equilibria and dielectric measurements in fluids;* Rev. Sci. Instruments, 1996, 67(12), 4294-4303.

8. Data Analysis

Expressions for the density of ethylene in terms of relative permittivity and temperature are presented along with a detailed description of the techniques used in their development and methods of solution. An expression is presented which is specific to the range of conditions that are normally met with industrial metering applications ($0 \leq t \leq 30^0$C and $5 \leq p \leq 10$MPa).

An intercomparison of values of the molar Clausius-Mossotti function obtained with this work and independent experimenters is also presented.

8.1 Equation of State

The density of ethylene may be determined from a precise measurement of relative permittivity provided that there exists an established relationship, such as the molar Clausius-Mossotti (C_M) function, between the relative permittivity, temperature and density of the fluid. This fluid *mapping* or *characterisation* would normally be established from a series of reference-quality measurements of both relative permittivity and density. However, as explained in Chapter 6: Experimental Measurements, Facility and Operation, the experimental apparatus was such that it was not possible to make simultaneous relative permittivity and density measurements and as a result the density had to be derived separately from a reference-quality equation of state.

The latest reference-quality equation of state of Smukala, J., Span, R. and Wagner, W. for the thermodynamic properties of ethylene[1] was used to calculate the density of ethylene. The new equation of state is an empirical description of the Helmholtz free energy, a, with the independent variables density, ρ, and absolute temperature, T. The dimensionless Helmholtz energy:-

$$\alpha = {}^{a}/_{R.T}, \tag{8.1}$$

where R is the specific gas constant; and

T is the thermodynamic temperature as measured on the the International Temperature Scale of 1990 (ITS-90),

is commonly split into a part α^o, which represents the properties of the ideal gas at given T and ρ, and a part α^r, which takes into account the residual behaviour of the real fluid. The dimensionless Helmholtz energy can be expressed as:-

$$\alpha(\rho_r, T_r) = \alpha^o(\rho_r, T_r) + \alpha^r(\rho_r, T_r), \tag{8.2}$$

where ρ_r is the reduced density and is equal to ρ/ρ_c ; and

T_r is the inverse reduced temperature and is equal to T_c/T,

where both the density and the temperature have been reduced with their critical values ρ_c and T_c respectively.

Since the Helmholtz energy as a function of density and temperature is one of four fundamental forms of an equation of state, all thermodynamic properties of a pure substance can be obtained by combining derivatives of equation (8.2).

The ideal-gas part of the Helmholtz energy, α^o, was calculated from statistical thermodynamics and expressed[1] as:-

$$\alpha^o = \ln(\rho_r) + a_1^o + a_2^o \tau + a_3^o \ln(T_r) + \sum_{i=4}^{7} a_i^o \ln\left[1 - e^{(-\theta_i^o T_r)}\right], \tag{8.3}$$

where a_i^o, θ_i^o are coefficients of the correlation equation.

Since no physically founded equation is known which accurately describes the real thermodynamic behaviour of fluids in the whole fluid region, the residual part of the Helmholtz energy, α^r, was determined in an empirical way and expressed[1] as:-

$$\alpha^r = \sum_{i=1}^{6} n_i \rho_r^{d_i} T_r^{t_i} + \sum_{i=7}^{30} n_i \rho_r^{d_i} T_r^{t_i} e^{-\rho_r^{c_i}} + \sum_{i=31}^{35} n_i \rho_r^{d_i} T_r^{t_i} e^{-\eta_i(\rho_r-\varepsilon_i)^2-\beta_i(t_r-\gamma_i)^2}, \qquad (8.4)$$

where n_i are the coefficients of the correlation equation;

and

$d_i, t_i, c_i, \eta_i, \varepsilon_i, \beta_i, \gamma_i$ are the exponents of the correlation equation.

The equation of state for ethylene, equation (8.2), is the combination of the formulation for α^o given in equation (8.3) and the formulation for α^r given in equation (8.4). The implementation of this thermodynamic equation of state has been validated in the following range of conditions:-

104	$\leq T/\mathrm{K} \leq$	450
10^{-6}	$\leq p/\mathrm{MPa} \leq$	300
10^{-6}	$\leq \rho/(\mathrm{kg/m^3}) \leq$	690

The uncertainty of density values calculated from the equation of state is defined as 0.02% of density, in the temperature range from 104 to 340 K and for pressures up to 12 MPa with exception of the critical region. However, in the supercritical region the uncertainty in the equation of state is expressed as 0.02% of the absolute pressure.

8.2 Analysis Software

The expression for the density of ethylene in terms of relative permittivity and temperature was established by regression of the derived values of the molar Clausius-Mossotti function, derived density and temperature data. The advanced regression software package of Setzmann, U., Span, R. and Wagner, W.[2] was used

to determine the mathematical correlation for the physical dependence between the data.

The regression software utilises the individual uncertainties in the values of the molar C_M function and the uncertainties in density and temperature.

The uncertainty in C_M is given by:-

$$U^2 c_M = \left(3.\frac{U_{\varepsilon_r}}{\varepsilon_r^2}.\frac{1}{\rho_m}\right)^2 + \left(\frac{(\varepsilon_r - 1)}{(\varepsilon_r + 2)}.\frac{U_{\rho_m}}{\rho_m^2}\right)^2, \tag{8.5}$$

where U_{ε_r} is the uncertainty in the measurement of relative permittivity, as detailed in expression (4.39);

U_{ρ_m} is the uncertainty in the molar density as calculated by the equation of state (see below).

The uncertainty in the molar density is calculated from the equation of state as:-

$$U^2_{\rho_m} = \left(1\times10^{-4}.\rho_m\right)^2 + \left(1\times10^{-2}.U_{EOS}.\rho_m\right)^2 + \left(\frac{\partial\rho_m}{\partial T}.U_T\right)^2 + \left(\frac{\partial\rho_m}{\partial p}.U_p\right)^2, \tag{8.6}$$

where U_{EOS} is the percentage uncertainty resulting from the equation of state at temperature t and pressure p (as above);

U_T is the uncertainty in the measurement of temperature (4 mK); and

U_p is the uncertainty in measured pressure, as detailed in expression (6.16) as 0.01%.

A weighted fit was applied to the regression taking into account the individual uncertainties in molar C_M function and density data. The uncertainties in measured

temperature were omitted from the regression due to the weak dependence of the C_M function with temperature.

8.3 Full Range Equation

Of the 126 state point measurements that were obtained throughout the measurement range 15 were deemed unsuitable for inclusion in the surface mapping of the fluid.

Six of the data points omitted from the surface mapping were points that lay essentially on the saturation line. Under these conditions the ethylene contained within the permittivity cell is most probably in the two-phase region, and thus leads to nonsensical measurements. Nine of the points omitted from the surface mapping were points that were measured at atmospheric pressure conditions. Under these conditions the uncertainty associated with the differential pressure reading from the differential pressure transducer (DPT) is large in comparison to the absolute pressure and this significantly increases the uncertainty in the calculated molar C_M values. The error associated with the DPT is quoted as a percentage of the range of the instrument. For the atmospheric pressure measurements the range of the instrument should have been reduced to produce the same uncertainty as the higher pressure measurements.

Of the 126 data points recorded only one point displayed unusual results. The calculated molar C_M value of the point was significantly lower than expected and as a result produced a large percentage deviation in the correlation. Although no explanation, other than human error, can be given for the discrepancy, the point was retained in the regression but its associated uncertainty in molar C_M was increased by a factor of 5 in order to reduce the weight associated with the point. This significantly decreased the percentage deviation in the correlation.

Using the regression technique, discussed in section 8.2, the molar C_M, derived density and temperature data was regressed, to a bank of 141 terms of the form:-

$$\rho_r^i . T_r^j , \tag{8.7}$$

where ρ_r is the reduced density, $\rho_r = \rho_m / \rho_{m,c} = \rho_m / 7636.93$;

ρ_m is the molar density in mol/m^3;

$\rho_{m,c}$ is the critical density in mol/m^3;

T_r is the reduced temperature, $T_r = T / T_c = T / 282.35$;

t_c is the critical temperature in kelvin;

i is an exponent from the set { 0(1),5 }; and

j is an exponent from the set { 0(0.25)4, 4.5, 5(1)10, 12.5(2.5)20 }.

The following equation was found to give an excellent representation of the molar C_M function over the full range of conditions:-

$$CM = a_0 + \rho_r\left(a_1 T_r^{0.25} + a_2 T_r^{0.5}\right) + \rho_r^2\left(a_3 T_r^{0.5} + a_4 T_r^{1.5}\right) + \rho_r^3 a_5 T_r^{0.25} , \tag{8.8}$$

where $a_n \ (n = 0,1,..,5)$ are the coefficients of the equation.

All six coefficients were fully significant at a 95% confidence level. The values of the coefficients obtained from the regression analysis are given in table (8.1), below:-

n	a_n x 10^6
0	10.733529014
1	2.349744605
2	-1.910222459
3	-0.573993986
4	0.299708404
5	0.045247638

Table 8.1 Coefficients of equation (8.8) obtained from regression.

The percentage standard deviation obtained for the fit was 0.0182. Maximum and minimum percentage deviations of 0.1133 and –0.4594 occurred at the 61st and 98th points, respectively. The 111 measurements of reduced density, reduced temperature and molar C_M function are reported in table (8.2), below, together with values of the molar C_M function calculated from equation (8.8) and the percentage agreement between the two.

Table 8.2 Comparison between the measured and calculated values of the molar C_M function for the full range data set.

Pt.	ρ_r	T_r	$10^6.C_{Mmeas}/m^3/mol$	$10^6.C_{Mcalc}/m^3/mol$	%
1	1.432663	1.109115	10.92022	10.92041	0.002
2	1.502903	1.091401	10.91802	10.91823	0.002
3	1.586818	1.073712	10.91378	10.91415	0.003
4	1.655015	1.056006	10.90966	10.91010	0.004
5	1.715546	1.038282	10.90529	10.90591	0.006
6	1.771166	1.020576	10.90118	10.90159	0.004
7	1.832459	1.002865	10.89555	10.89617	0.006
8	1.886781	0.985150	10.89062	10.89102	0.004
9	1.945673	0.967441	10.88496	10.88492	0.000
10	1.243813	1.109114	10.92679	10.92634	-0.004
11	1.345977	1.091388	10.92604	10.92560	-0.004
12	1.453697	1.073721	10.92335	10.92247	-0.008
13	1.541601	1.055993	10.91887	10.91863	-0.002
14	1.626212	1.038287	10.91409	10.91367	-0.004
15	1.697130	1.020575	10.90906	10.90878	-0.003
16	1.771055	1.002859	10.90288	10.90275	-0.001
17	1.834414	0.985145	10.89711	10.89711	0.000
18	1.890666	0.967449	10.89202	10.89179	-0.002
19	0.859663	1.109116	10.91801	10.91856	0.005
20	0.993683	1.091411	10.92699	10.92774	0.007

21	1.155906	1.073699	10.93220	10.93235	0.001
22	1.330201	1.055991	10.92983	10.93062	0.007
23	1.472986	1.038291	10.92525	10.92519	-0.001
24	1.586966	1.020577	10.91914	10.91865	-0.005
25	1.682101	1.002870	10.91249	10.91183	-0.006
26	1.761406	0.985145	10.90578	10.90533	-0.004
27	1.831648	0.967442	10.89977	10.89899	-0.007
28	0.473729	1.109114	10.87272	10.87069	-0.019
29	0.518010	1.091410	10.88217	10.88110	-0.010
30	0.564031	1.073692	10.89172	10.89134	-0.004
31	0.640337	1.055996	10.90638	10.90537	-0.009
32	0.828215	1.038288	10.93181	10.92817	-0.033
33	1.243729	1.020582	10.94149	10.93928	-0.020
34	1.506243	1.002866	10.92685	10.92748	0.006
35	1.650399	0.985158	10.91743	10.91701	-0.004
36	1.748968	0.967448	10.90942	10.90869	-0.007
37	0.257638	1.109114	10.82032	10.82040	0.001
38	0.270499	1.091415	10.82507	10.82541	0.003
39	0.276721	1.073711	10.82690	10.82865	0.016
40	0.293948	1.055997	10.83320	10.83499	0.017
41	0.311720	1.038286	10.84042	10.84152	0.010
42	0.327946	1.020582	10.85694	10.84766	-0.086
43	0.352072	1.002862	10.85388	10.85594	0.019
44	0.366306	0.985152	10.86038	10.86162	0.012
45	0.112687	1.109114	10.77563	10.77540	-0.002
46	0.115364	1.091409	10.77679	10.77701	0.002
47	0.117413	1.073703	10.77756	10.77844	0.008
48	0.121218	1.055994	10.78018	10.78051	0.003
49	0.123732	1.038287	10.78153	10.78216	0.006
50	0.128952	1.020579	10.78429	10.78482	0.005
51	0.131213	1.002865	10.78533	10.78645	0.010
52	0.134852	0.985163	10.78722	10.78862	0.013

53	0.137992	0.967446	10.78985	10.79063	0.007
54	0.053621	1.109114	10.75754	10.75423	-0.031
55	0.054518	1.091414	10.75670	10.75491	-0.017
56	0.055951	1.073704	10.75757	10.75580	-0.016
57	0.056509	1.055998	10.75735	10.75637	-0.009
58	0.058159	1.038289	10.75862	10.75738	-0.012
59	0.058798	1.020573	10.75868	10.75800	-0.006
60	0.059959	1.002869	10.75876	10.75884	0.001
61	0.061824	0.985163	10.74782	10.75999	0.113
62	0.062871	0.967446	10.75897	10.76082	0.017
63	0.423281	0.967444	10.87808	10.87799	-0.001
64	1.623331	0.967446	10.92115	10.92222	0.010
65	1.688245	0.967449	10.91539	10.91543	0.000
66	1.603384	0.985158	10.92145	10.92158	0.001
67	1.544913	0.985157	10.92608	10.92690	0.007
68	1.472488	0.985154	10.93092	10.93283	0.018
69	1.403671	1.002865	10.93332	10.93472	0.013
70	1.281877	1.002863	10.94092	10.94103	0.001
71	1.203313	1.002863	10.94081	10.94356	0.025
72	1.183440	1.020579	10.94347	10.94076	-0.025
73	1.070911	1.020575	10.94070	10.94134	0.006
74	1.335764	1.020577	10.93480	10.93563	0.008
75	1.490884	1.020577	10.92586	10.92619	0.003
76	1.357617	1.038285	10.93768	10.93187	-0.053
77	1.262149	1.038286	10.93462	10.93577	0.011
78	1.131183	1.038282	10.93690	10.93827	0.013
79	1.013860	1.038287	10.93605	10.93723	0.011
80	0.989579	1.055994	10.93146	10.93348	0.019
81	1.066240	1.055993	10.93270	10.93505	0.022
82	1.201183	1.055993	10.93325	10.93452	0.012
83	0.905521	1.055994	10.93050	10.93002	-0.004
84	0.749848	1.055992	10.91905	10.91826	-0.007

85	0.413684	1.055993	10.86443	10.86482	0.004
86	0.417062	1.038288	10.86724	10.86771	0.004
87	0.660873	1.038286	10.91015	10.91094	0.007
88	0.669472	1.020577	10.91502	10.91496	-0.001
89	0.882432	1.020573	10.93567	10.93504	-0.006
90	0.794598	1.020577	10.92779	10.92856	0.007
91	1.005038	1.020575	10.93667	10.94024	0.033
92	0.519220	1.020574	10.88912	10.89116	0.019
93	0.523182	1.002869	10.89601	10.89446	-0.014
94	0.674426	1.002866	10.91820	10.91859	0.004
95	0.815336	1.002868	10.93698	10.93354	-0.031
96	1.026302	1.002866	10.97457	10.94407	-0.278
97	1.105823	1.002866	10.93876	10.94479	0.055
98	0.934383	1.002864	10.99160	10.94110	-0.459
99	0.431236	0.985151	10.87664	10.87759	0.009
100	0.513604	0.985160	10.90402	10.89520	-0.081
101	0.228870	0.985156	10.82013	10.82142	0.012
102	0.259769	0.967452	10.83196	10.83275	0.007
103	0.136793	1.073702	10.78455	10.78519	0.006
104	0.400534	1.073702	10.85800	10.85980	0.017
105	0.720449	1.073700	10.91104	10.91232	0.012
106	1.062446	1.073702	10.93018	10.93207	0.017
107	0.873897	1.073703	10.92447	10.92520	0.007
108	0.857461	1.091407	10.92164	10.92124	-0.004
109	0.716431	1.091407	10.90891	10.90907	0.002
110	0.709943	1.109110	10.90498	10.90563	0.006
111	0.983994	1.109115	10.92460	10.92466	0.001

The measured molar C_M function and the deviation plot between the measured molar C_M function and the calculated molar C_M function are plotted as a function of density in graphs (8.1) and (8.2) respectively.

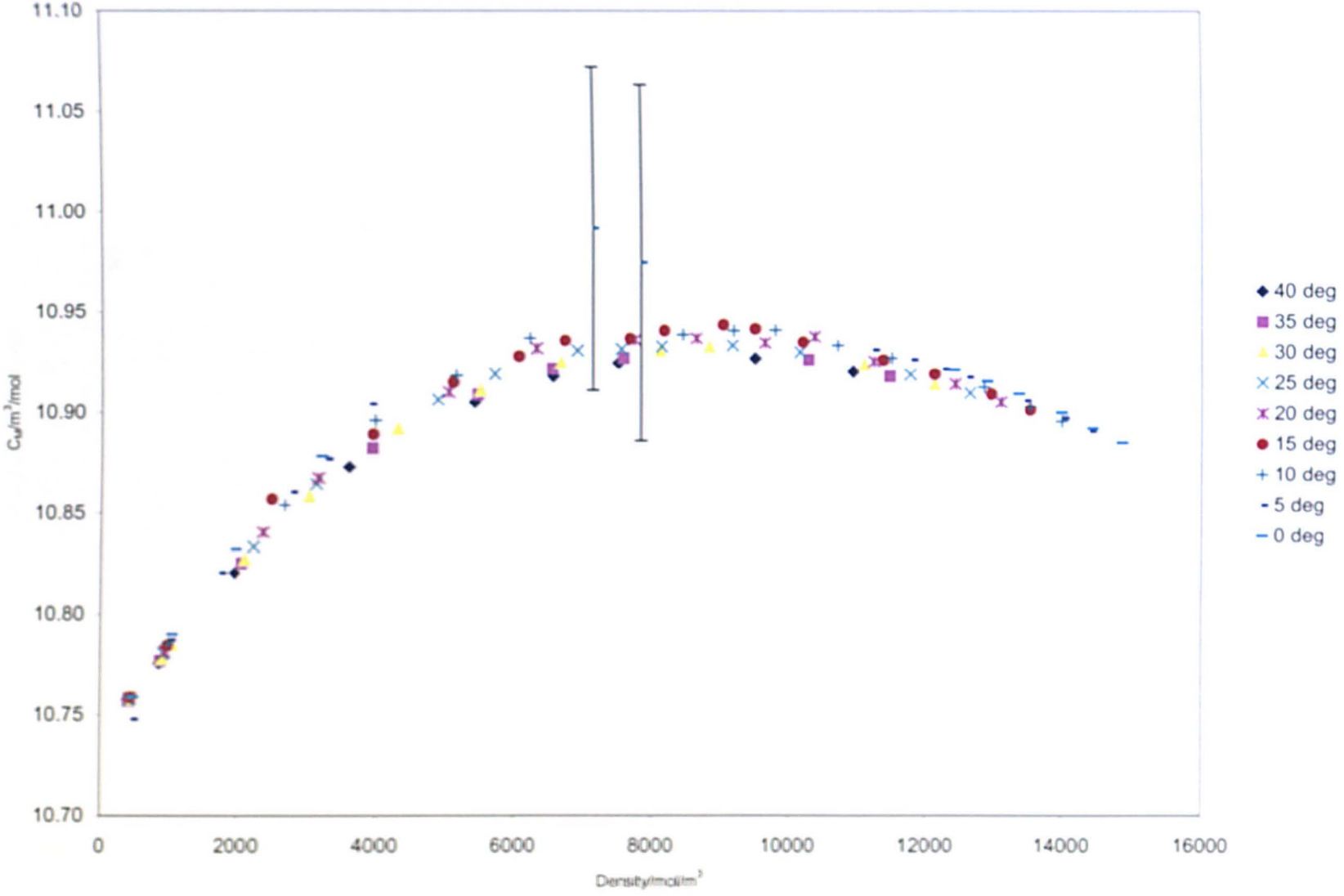

Graph 8.1 Measured values of the molar Clausius-Mossotti function as a function of density.

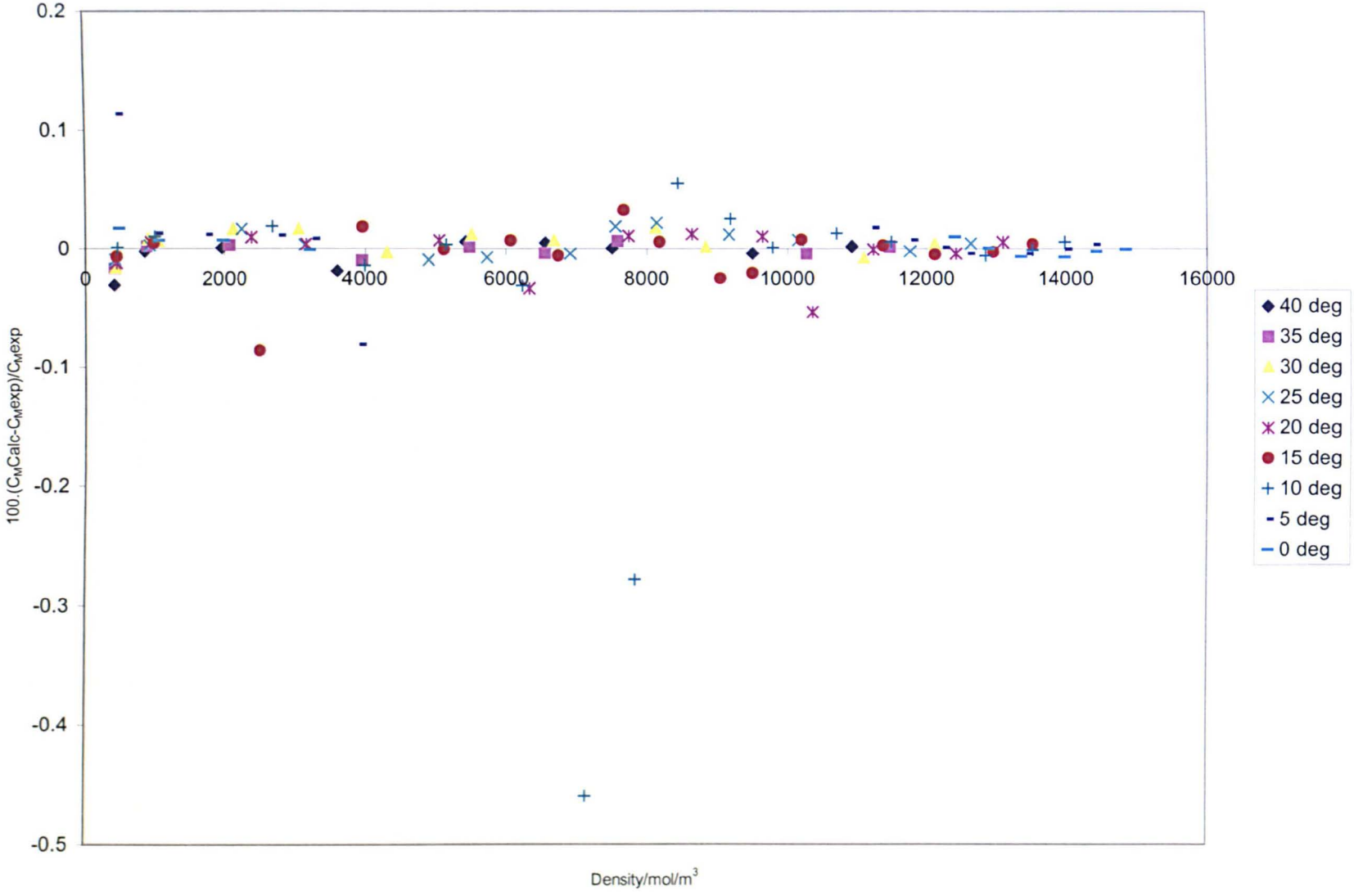

Graph 8.2 Deviation plot of experimental molar Clausius-Mossotti function compared with calculated values from expression 8.8.

Equation (8.8) therefore provides an accurate representation of the molar C_M function for the full range of conditions. In this range the uncertainty in the representation of the molar C_M function is assessed as 0.03%, at a 95% confidence level, and is only marginally greater than the corresponding density values obtained from the equation of state.

8.4 Solution of the Full Range Equation for Density

Given a measurement of the relative permittivity and temperature of the fluid it is possible to solve equation (8.8) for density by a simple iterative technique.

Re-arranging the molar C_M relation we obtain the following expression for reduced density:-

$$\rho_r = \frac{1}{\rho_{m,c}} \left(\frac{\varepsilon_r - 1}{\varepsilon_r + 2} \right) \frac{1}{C_M(\rho_r, T_r)}, \tag{8.9}$$

where $C_M(\rho_r, T_r)$ is a function of reduced density and temperature defined by the right-hand side of equation (8.8).

Since the molar C_M function is only a relatively weak function of reduced density, given an initial estimate of reduced density, $\rho_r^{(0)}$, we can substitute this into the right-hand side of the above equation to obtain an improved estimate for reduced density. The n^{th} estimate of reduced density is given by:-

$$\rho_r^{(n)} = \frac{1}{\rho_{m,c}} \left(\frac{\varepsilon_r - 1}{\varepsilon_r + 2} \right) \frac{1}{C_M(\rho_r^{(n-1)}, T_r)}. \tag{8.10}$$

An accurate solution for reduced density is normally achieved within two or three iterations. The specific, or molar, density of ethylene can then be obtained from:-

$$\rho = 214.24.\rho_r^{(n)} \text{ kg/m}^3 \text{, or } \rho_m = 7636.93.\rho_r^{(n)} \text{ mol/m}^3 .$$

For the full range equation a good initial estimate of reduced density is:-

$$\rho_r^{(0)} = \frac{\varepsilon_r - 1}{0.3}. \tag{8.11}$$

From graph (8.1) it can be seen that the molar C_M function displays only a weak dependence on temperature over the range of conditions considered here. As a result of this it has been calculated that the measurement of temperature of the fluid need only be performed to within several degrees in order to obtain an accurate solution of density from the iterative process. However, it should be noted that the calculation of the vacuum resonant frequency of the cavity requires the temperature to be known much more accurately (some 25 mK).

As detailed in Chapters 4 and 5, the correction for the dilation of the cavity with applied pressure ensures that the relationship between relative permittivity and the resonant frequencies is known to better than 1 ppm at ambient conditions and some 15 ppm at 12 MPa. However, now that we have an established relationship (expression (8.9)) between relative permittivity and density, it is possible to comment on the requirement for the pressure correction.

A rudimentary sensitivity analysis was performed between the uncertainty in permittivity and the resultant uncertainty in density to determine to what extent the uncertainty in permittivity effects the uncertainty in density. An uncertainty in relative permittivity of 100 ppm (corresponding to the magnitude of correction at a pressure of approximately 15 MPa) the corresponding uncertainty in density varies from approximately 0.01% at molar densities of 14500 mol m^{-3}, 0.1% at molar densities of 8100 mol m^{-3} and 0.7% at molar densities of 430 mol m^{-3}. These results show that, as expected, the uncertainty in density is heavily dependent upon the uncertainty of relative permittivity at lower densities and is less dependent at higher densities. For smaller uncertainties in relative permittivity the uncertainties are

reduced, however, the general trend between uncertainties at high and low densities remains constant.

The above analysis demonstrates that the need for pressure correction is valid, and that its omission would lead to a bias in the uncertainty of density. However, under certain operating conditions, namely above critical densities, it may be possible to apply a pressure correction based on a mean pipeline pressure and thereby reduce the bias in the uncertainty in density. If the sensitivity of the density to uncertainties in pressure is sufficiently small, it may be possible to eliminate the need for the pressure correction, and thus eliminate the need to make a physical measurement of pressure.

8.5 Limited Range Equation

The relationship between the density and permittivity of ethylene that was established in the previous section covered a much wider range of conditions than is normally met within metering applications. Metering for custody transfer purposes is usually only undertaken in the temperature range 0 to 30 °C for pressures in the range 5 to 10 MPa.

To obtain as accurate a representation for the molar C_M function in the custody transfer region as possible a subset of data was selected for further analysis. The subset comprised those data points for which:-

$$t \leq 30^0\text{C} \text{ and } \rho_m > 1.2.\rho_{m,c},$$

where ρ_m is the molar density in mol/m^3.

In this region the molar C_M function monotonically decreases with increasing molar density. However, the change with both density and temperature is small; the molar C_M function having an upper bound of 10.94×10^{-6} and a lower bound of

10.88×10^{-6}. The representative equation required terms in both reduced density and temperature in order to define the fine structure of the molar C_M function in this range and to represent the data to within its uncertainties.

Using a technique similar to that previously described the molar C_M values, derived density and temperature of the subset of data was regressed , to a bank of 225 terms of the form:-

$$\rho_r^i . T_r^j , \tag{8.12}$$

where ρ_r is the reduced density, $\rho_r = \rho_m / \rho_{m,c} = \rho_m / 7636.93$;

ρ_m is the molar density in mol/m^3;

$\rho_{m,c}$ is the critical density in mol/m^3;

T_r is the reduced temperature, $T_r = T / T_c = T / 282.35$;

T_c is the critical temperature in kelvin;

i is an exponent from the set { 0(0.5),4 }; and

j is an exponent from the set { 0(0.25)5, 5(1)10 }.

The following equation was found to give an excellent representation of the molar C_M function in the limited range of conditions:-

$$C_M = a_0 + a_1 . \rho_r^{0.5} . T_r^{4.25} + a_2 . \rho_r . T_r^4 + a_3 . \rho_r^3 . T_r^{1.5} , \tag{8.13}$$

where $a_n \ (n = 0,1,..,5)$ are the coefficients of the equation.

All four coefficients were fully significant at a 95% confidence level. The values of the coefficients obtained from the regression analysis are given in table (8.3), below:-

n	$a_n \times 10^6$
0	10.98049917
1	-0.10352428
2	0.08819040
3	-0.01721399

Table 8.3 Coefficients of equation (8.13) obtained from regression.

The percentage standard deviation obtained for the fit was 0.0061. Maximum and minimum percentage deviations of 0.033 and –0.047 occurred at the 37th and 35th points, respectively. The 37 measurements of reduced density, reduced temperature and molar C_M function are reported in Table (8.4), below, together with values of the molar C_M function calculated from equation (8.13) and the percentage agreement between the two.

Table 8.4 Comparison between the measured and calculated values of the molar C_M function for the limited range data set.

Pt.	ρ_r	T_r	$10^6.C_{Mmeas}/m^3/mol$	$10^6.C_{Mcalc}/m^3/mol$	%
1	1.586818	1.073712	10.91378	10.91354	-0.002
2	1.655015	1.056006	10.90966	10.90943	-0.002
3	1.715546	1.038282	10.90529	10.90531	0.000
4	1.771166	1.020576	10.90118	10.90111	-0.001
5	1.832459	1.002865	10.89555	10.89573	0.002
6	1.886781	0.985150	10.89062	10.89073	0.001
7	1.945673	0.967441	10.88496	10.88471	-0.002
8	1.453697	1.073721	10.92335	10.92318	-0.002
9	1.541601	1.055993	10.91887	10.91909	0.002
10	1.626212	1.038287	10.91409	10.91398	-0.001
11	1.697130	1.020575	10.90906	10.90906	0.000
12	1.771055	1.002859	10.90288	10.90299	0.001
13	1.834414	0.985145	10.89711	10.89740	0.003
14	1.890666	0.967449	10.89202	10.89219	0.002

15	1.330201	1.055991	10.92983	10.93190	0.019
16	1.472986	1.038291	10.92525	10.92587	0.006
17	1.586966	1.020577	10.91914	10.91919	0.001
18	1.682101	1.002870	10.91249	10.91236	-0.001
19	1.761406	0.985145	10.90578	10.90590	0.001
20	1.831648	0.967442	10.89977	10.89962	-0.001
21	1.243729	1.020582	10.94149	10.93946	-0.019
22	1.506243	1.002866	10.92685	10.92718	0.003
23	1.650399	0.985158	10.91743	10.91712	-0.003
24	1.748968	0.967448	10.90942	10.90904	-0.004
25	1.623331	0.967446	10.92115	10.92125	0.001
26	1.688245	0.967449	10.91539	10.91524	-0.001
27	1.603384	0.985158	10.92145	10.92129	-0.001
28	1.544913	0.985157	10.92608	10.92602	-0.001
29	1.472488	0.985154	10.93092	10.93119	0.003
30	1.403671	1.002865	10.93332	10.93375	0.004
31	1.281877	1.002863	10.94092	10.93979	-0.010
32	1.203313	1.002863	10.94081	10.94277	0.018
33	1.335764	1.020577	10.93480	10.93553	0.007
34	1.490884	1.020577	10.92586	10.92649	0.006
35	1.357617	1.038285	10.93768	10.93257	-0.047
36	1.262149	1.038286	10.93462	10.93680	0.020
37	1.201183	1.055993	10.93325	10.93683	0.033

Equation (8.13) therefore provides an accurate representation of the molar C_M function for the limited range of conditions relevant to most industrial metering applications. In this limited range, the uncertainty in the representation of the molar C_M function is assessed as 0.03%, at a 95% confidence level, and is only marginally greater than that in the corresponding density values obtained from the equation of state.

8.6 Uncertainty in Values of Density Derived from the Limited Range Equation

Equation (8.13) provides the essential mapping between the relative permittivity and density of ethylene. Given a measurement of relative permittivity and temperature it is possible to solve equation (8.11) for density by the same iterative technique discussed in section 8.4 for the full range equation. In this instance, however, a better initial estimate of reduced density can be obtained from:-

$$\rho_r^{(0)} = \left(\frac{\varepsilon_r - 1}{\varepsilon_r + 2}\right).\frac{10^6}{10.91.\rho_{m,c}} \approx 12.0.\left(\frac{\varepsilon_r - 1}{\varepsilon_r + 2}\right). \tag{8.14}$$

On substitution of equation (8.14) into equation (8.9) an accurate solution for reduced density is normally achieved within two or three iterations.

As discussed in section 8.4, the molar C_M function displays only a weak dependence on temperature over the full range of conditions, including the metering region, therefore the measurement of the temperature of the fluid need again only be performed to within several degrees in order to obtain an accurate solution of density from the iterative process.

Calculation of the uncertainty in molar density from this equation is complicated by the iterative nature of the equation. However, the molar C_M function is only weakly dependent upon reduced density and temperature and, provided the temperature of the fluid is measured to within several degrees, a reliable approximation to the uncertainty in molar density can be obtained from:-

$$U_{\rho_m}^2 \approx \left(\frac{\partial \rho_m}{\partial \varepsilon_r}\right)^2 .U_{\varepsilon_r}^2 + \left(\frac{\partial \rho_m}{\partial C_M}\right)^2 .U_{C_M}^2 , \tag{8.15}$$

which yields:-

$$\left(\frac{U_{\rho_m}}{\rho_m}\right)^2 \approx \left(\frac{2\varepsilon_r + 1}{(\varepsilon_r - 1)(\varepsilon_r + 2)}\right)^2 .U_{\varepsilon_r}^2 + \left(\frac{U_{C_M}}{C_M}\right)^2 . \tag{8.16}$$

For the range of conditions considered here, the first term in brackets on the right-hand side of the equation is approximately equal to 2. On making this approximation and substituting for the uncertainty in the molar C_M function obtained from the previous section we obtain:-

$$\left(\frac{U_{\rho_m}}{\rho_m}\right)^2 \approx 4.U_{\varepsilon_r}^2 + (0.0003)^2 . \tag{8.17}$$

Since the uncertainty in relative permittivity in this region is some 10 ppm, it can be seen that the uncertainty in values of density calculated from the mapping relationship, equation (8.14), is close to 0.03% in density at a 95% confidence level.

8.7 Intercomparison of Clausius-Mossotti Data

As illustrated in graph (8.1), the molar C_M function increases slightly with increasing density, reaching a maximum in the vicinity of the critical density, before decreasing continuously with further increasing density. The existence of a maximum in the molar C_M function is typical for many non-polar fluids and is indeed predicted from the theory developed by Kirkwood[3] and Yvon[4]. The two values of the molar C_M function in graph (8.1) that are significantly higher than expected are points that were measured in the vicinity of the critical region. These points were retained in the regression since the large uncertainty in the molar C_M value of each point reduces the weight associated with it and therefore does not adversely affect the percentage deviation of the correlation.

Values of the molar C_M function, as calculated from expression (8.8), have been compared with independent experimental data. Table (8.5) summarises the available

Reference	Temperature/°C	Density Range/mol/m^3	Measurement Principle	Sample Purity/%	Data
David *et al.* (1951)	25, 50	1000 to 17000	Cylindrical capacitor (0.5-3MHz)	99.7	Dielectric Constant
Johnston and Cole (1962)	25, 31.7, 50, 75	0 to 4000	Parallel plate capacitor (10kHz)/ Burnett expansion method	99.5	Dielectric Virial Coefficient $\left(A_{\varepsilon_r}, B_{\varepsilon_r}\right)$
Orcutt and Cole (1965)	50, 100, 150	0 to 4000	Parallel plate capacitor (10kHz)/ Cyclic expansion method	99.745	Dielectric Virial Coefficient $\left(A_{\varepsilon_r}, B_{\varepsilon_r}, C_{\varepsilon_r}\right)$
Bose and Cole (1971)	50, 100, 150	0 to 4000	Parallel plate capacitor (10kHz)/ Cyclic expansion method	99.9945	Dielectric Virial Coefficient $\left(A_{\varepsilon_r}, B_{\varepsilon_r}, C_{\varepsilon_r}\right)$
Lehmann and Rank (1984)	25.03, 50.13	75 to 5000	Parallel plate capacitor (10kHz)/ Burnett expansion method	99.5	Expression for Dielectric Constant
Haynes (1985)	-3.15 to -73.15	12000 to 18000	Cylindrical capacitor (0.5-3MHz)	99.999	Dielectric Constant

Table 8.5 Summary of the available literature on the dielectric properties of ethylene.

literature on the dielectric properties of ethylene (The author is aware of the optical determination of the mean polarizabilities of ethylene obtained by Häusler and Kerl[5] and St-Arnaud and Bose[6], however due to the uncertainty in the dispersion characteristics of the relative permittivity of ethylene at these frequencies and the subsequent uncertainty in the Maxwell relation $\varepsilon = n^2$, both sets of data have been omitted from the intercomparison presented here).

The observed differences in the molar C_M function are defined in percentage terms as:-

$$100.\frac{(C_{M\,Lit} - C_{M\,\exp})}{C_{M\,\exp}}, \tag{8.18}$$

where $C_{M\,Lit}$ is the value of the molar Clausius-Mossotti function from the literature; and

$C_{M\,\exp}$ is the value of the molar Clausius-Mossotti function as calculated from expression (8.8),

and are illustrated in graphs (8.3) and (8.4). Graph (8.3) represents all the comparable independent experimental data whilst graph (8.4) focuses specifically on the bulk of the data in the range up to 4000 mol/m^3. It should be noted that most of the dielectric measurements made on ethylene were done so in the low density range with a view to obtaining information on the dielectric virial coefficients of the molar C_M function and developing the theories on molecular interactions and molecular polarisability, which is outwith the scope of this thesis.

The intercomparison of molar C_M values is carried out with consideration given to the experimental apparatus, determination of density, sample purity and suitability of use of expression (8.8). To facilitate the comparison it should be noted that, where possible, the equation of state of Smukala, J., Span, R. and Wagner, W. was used to re-calculate any density data from the literature. It should also be noted that for non-

polar gases and vapours, the relative permittivities are constant for all frequencies up to about 10^{16} Hz, the start of the infrared spectrum.

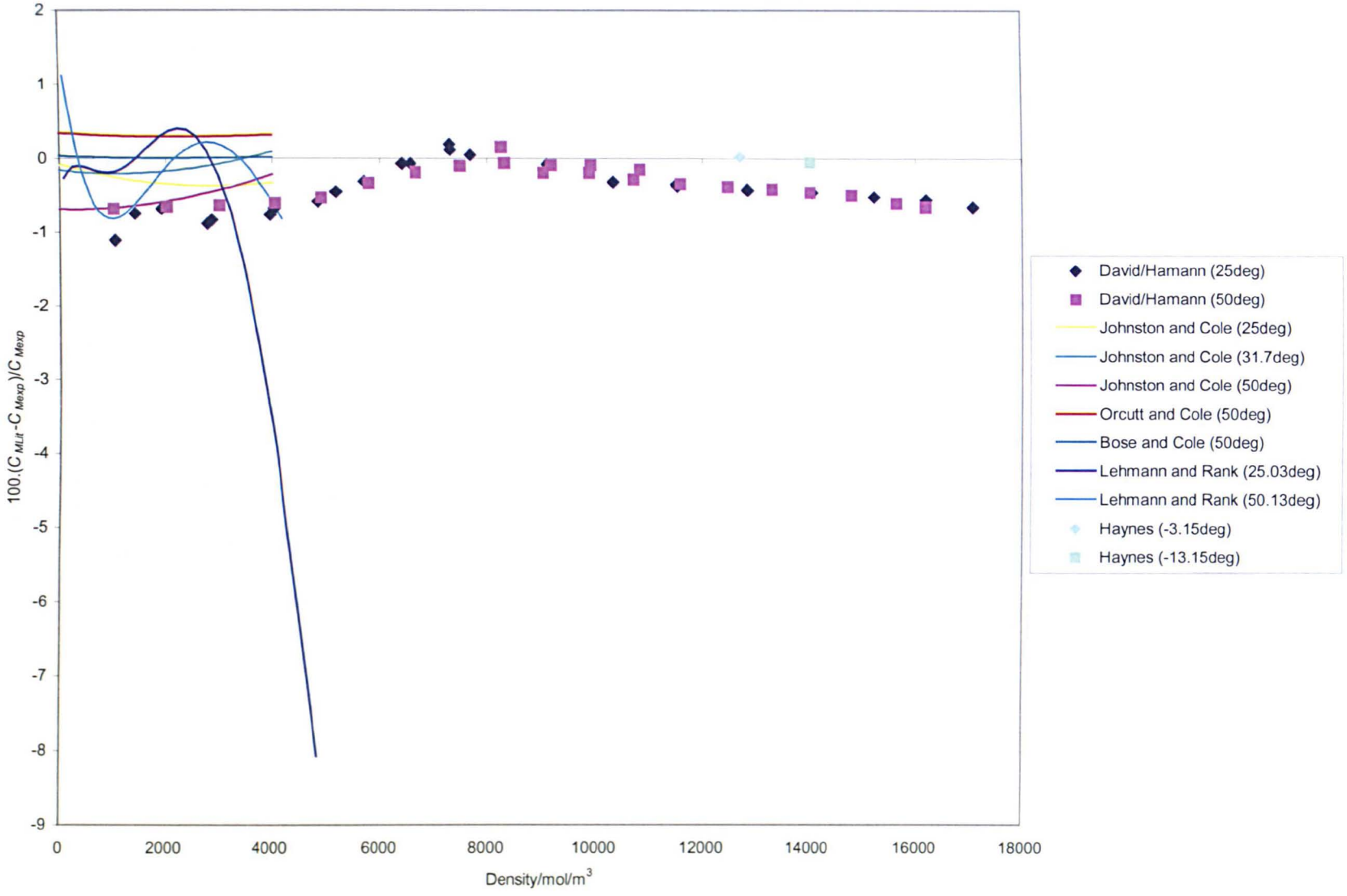

Graph (8.3) Deviation plot of experimental molar Clausius-Mossotti values compared with the corresponding values calculated from expression (8.8).

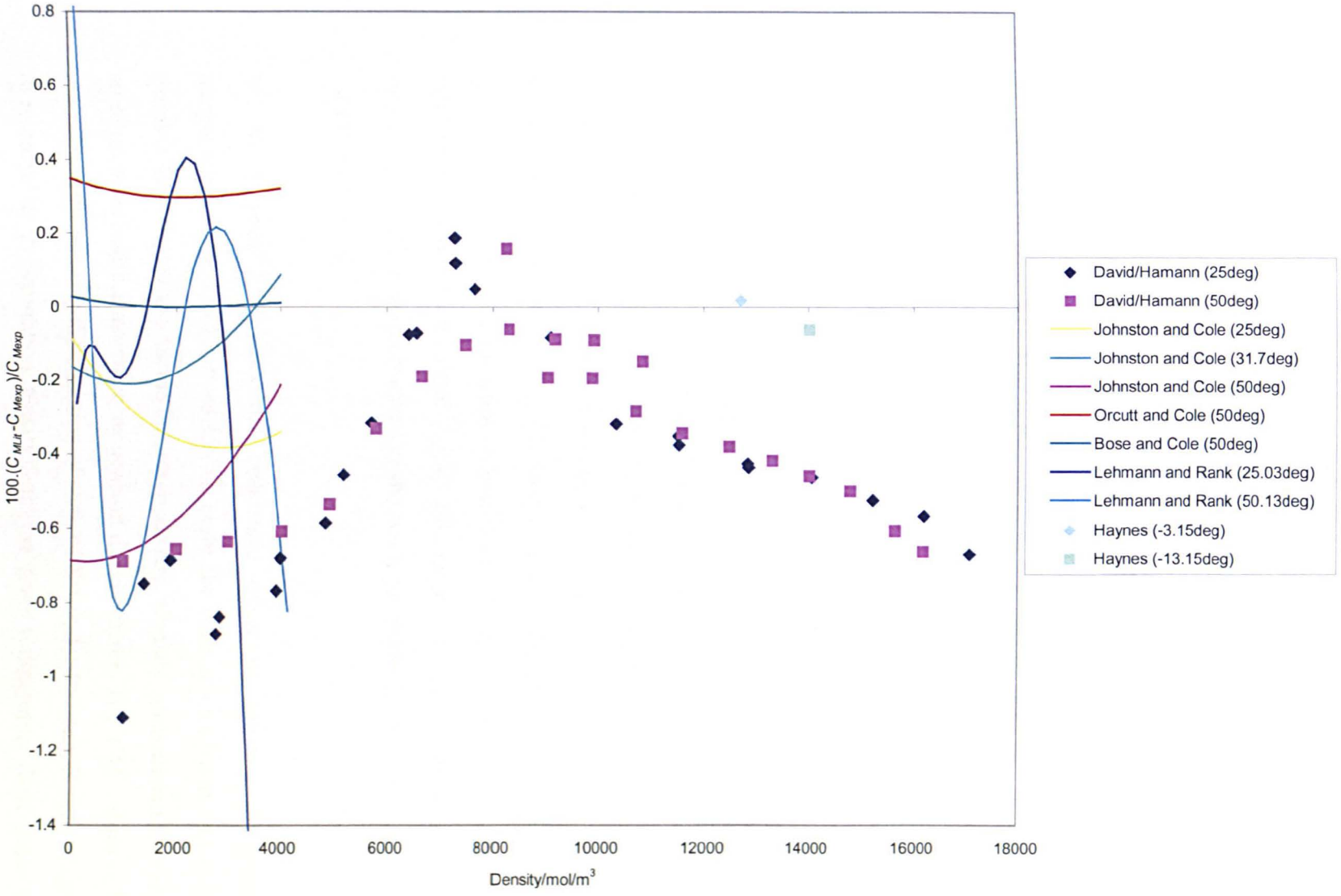

Graph (8.4) Deviation plot of experimental molar Clausius-Mossotti values compared with the corresponding values calculated from expression (8.8).

David *et al.*[7] present the dielectric constant of ethylene at pressures up to approximately 500 bar and at temperatures of 25 and 50 °C. In order to determine densities from the measured pressures they used *pVT* data for ethylene of Michels and Geldermans[8]. The *CM* values of David *et al.* at 25 and 50 °C were determined using the equation of state of Smukala, J., Span, R. and Wagner, W. to re-calculate the density from the given pressure data.

The experimental data of David *et al.* is of particular interest since it covers approximately the same range of densities as the work carried out here. It can be seen from graphs (8.3) and (8.4) that the molar C_M values of both the 25 and 50 °C data generally agree with the results presented to within approximately ± 1%.

Also from graph (8.4) it can be seen that molar C_M functions exhibit a temperature dependent enhancement within the near critical region. The increase in molar C_M function with density is expected to be less than 2% of the low density value over large density and temperature ranges[9], however the increases calculated for the 25 and 50 °C data are 2.6 and 2.2% respectively compared to the corresponding increases over the molar C_M function, as calculated from expression (8.8), of 1.4 and 1.3% respectively. The enhancement at 25 °C is larger than at 50 °C. This enhancement of the molar C_M function is almost certainly the result of failing to make a correction to the measured pressure to include the contribution of a pressure head in the system (see section 6.8.7). Similar critical region enhancements of the molar C_M function were observed in the work presented here prior to the correction for pressure head.

W. M. Haynes[10] presents the orthobaric dielectric constant of ethylene at temperatures from –73.15 to –3.15 °C. Only the data at –3.15 and –13.15 °C was deemed suitable for use in the intercomparison. Density measurements were made simultaneously with a magnetic suspension densitometer. The *CM* values of Haynes were determined using the equation of state of Smukala, J., Span, R. and Wagner, W. to re-calculate the saturation density from the given temperature data. It can be seen

from graph (8.3) that the molar C_M values of both the –3.15 and –13.15 °C data agree with the results presented to within approximately ± 0.06%.

Lehmann and Rank[11] present an expression for the dielectric constant of ethylene as a function of pressure at 25.03 and 50.13 °C. The expression for 25.03 °C is valid up to 60 bar and the expression for 50.13 °C is valid up to 70 bar. The molar C_M values of Lehmann and Rank were determined using the equation of state of Smukala, J., Span, R. and Wagner, W. to re-calculate the density over the range of pressures under consideration. It can be seen from graphs (8.3) and (8.4) that the percentage deviations of the molar C_M values of both the 25.03 and 50.13 °C display an oscillatory behaviour with density. The molar C_M values of the 50.13 °C data agree to within approximately 1% of the results presented here. The molar C_M values of the 25.03 °C diverge greatly from the results presented here at the upper end of its density range.

Johnston and Cole[12] present the first and second dielectric virial coefficients of ethylene at densities up to 4000 mol/m^3 for four temperatures; 25, 31.7, 50 and 75 °C. The 75 °C data was deemed unsuitable for comparison with expression (8.8) and was omitted from the intercomparison. In order to determine densities from measured pressure they used *pVT* data for ethylene of F. Din[13]. The molar C_M values of Johnston and Cole were determined using nominal densities in the range up to 4000 mol/m^3. It can be seen from graphs (8.3) and (8.4) that the molar C_M values of the 25, 31.7, and 50 °C data agree with the results presented here to within approximately ± 0.8%.

Orcutt and Cole[14] present the first three dielectric virial coefficients of ethylene at densities up to 4000 mol/m^3 for three temperatures; 50, 100 and 150 °C. Only the 50 °C data was deemed suitable for use in the intercomparison. In order to determine densities from measured pressure they used *pVT* data for ethylene of Michels and Geldermans[8]. The molar C_M values of Orcutt and Cole were determined using

nominal densities in the range up to 4000 mol/m^3. It can be seen from graphs (8.3) and (8.4) that the molar C_M values of Orcutt and Cole agree with the results presented here to within approximately ± 0.3%.

Bose and Cole[15] also present the first three dielectric virial coefficients of ethylene at densities up to 4000 mol/m^3 for three temperatures; 50, 100 and 150 °C, and again only the 50 °C data was deemed suitable for use in the intercomparison. The molar C_M values of Bose and Cole were determined using nominal densities in the range up to 4000 mol/m^3. It can be seen from graph (8.4) that there is excellent agreement of approximately ± 0.03% between the molar C_M values of Bose and Cole and the results presented here. The results of Bose and Cole lie within the experimental uncertainty of the molar C_M values calculated with expression (8.8).

8.8 Application to Industrial Ethylene

Equations (8.8) and (8.13) are precise relations between the relative permittivity and density of research grade ethylene of 99.995% purity. In practice, however, industrially produced ethylene is a mixture containing one or two percent mole fraction of other components. That produced by BP's Grangemouth plant from North Sea crude and transported by pipeline to plastic producers in the UK typically has the following percentage mole fraction composition[16]:-

Ethylene	99.9 (min)
Methane + Ethane	0.001 (max)
Ethane	0.0005 (max)
Nitrogen	0.0001 (max)
Hydrogen	0.00001 (max)
Propylene	0.00001 (max)
Water	0.00001 (max)
Solvents	0.00001 (max)
Acetylene	0.000005 (max)

Oxygen	0.000005 (max)
Carbon Dioxide	0.000005 (max)
Carbon Monoxide	0.000002 (max)
Sulphur	0.000002 (max)
Ammonia	0.000001 (max)

Provided the dielectric virial coefficients of each of the additional components are known, the density of industrial ethylene can be obtained from a measurement of permittivity of the same.

The molar Clausius-Mossotti function for a multi-component mixture is:-

$$C_{M\,mix} = \frac{(\varepsilon_{r_{mix}} - 1)}{(\varepsilon_{r_{mix}} + 2)} \cdot \frac{1}{\rho_{m_{mix}}} = A_{\varepsilon_{r_{mix}}} + B_{\varepsilon_{r_{mix}}}(T)\rho_{m_{mix}} + C_{\varepsilon_{r_{mix}}}(T)\rho^2_{m_{mix}} + \ldots, \qquad (8.19)$$

where $\varepsilon_{r_{mix}}$ is the relative permittivity of the mixture;

$\rho_{m_{mix}}$ is the molar density of the mixture; and

$A_{\varepsilon_{r_{mix}}}$, $B_{\varepsilon_{r_{mix}}}$ and $C_{\varepsilon_{r_{mix}}}$ are the dielectric virial coefficients of the mixture.

The dielectric virial coefficients of an *N*-component non-polar mixture are related to those of the pure components by the following equations[17]:-

$$A_{\varepsilon_r,mix} = \sum_{i=1}^{N} x_i . A_{\varepsilon_r,i},$$

$$B_{\varepsilon_r,mix} = \sum_{i=1}^{N}\sum_{j=1}^{N} x_i . x_j . \left(B_{\varepsilon_r,i} . B_{\varepsilon_r,j}\right)^{1/2}, \qquad (8.20)$$

where x_i, x_j is the mole fraction of component i, j etc.

The additional components found in industrial ethylene mixtures are basically the components of natural gas mixtures. Drs Manfred Jaeschke and Peter Schley of Rhurgas, Dorsten, using an experimental facility developed by NEL, have undertaken a large programme of work to determine the dielectric virial coefficients of the major constituents of natural gas[18].

Thus given the composition of the mixture, the dielectric virial coefficients of each of the *N*-components and an accurate measurement of the relative permittivity of the mixture, it is possible to solve the above equations, using the technique given in section 8.4, and obtain an accurate and reliable value for its molar and specific density. Since industrial ethylene is a relatively pure mixture $\left(x_{C_2H_4} \approx 0.99\right)$ and the permittivities of the additional components are relatively similar, the composition of the mixture need not be known precisely. An approximate knowledge of the composition will suffice to establish the density to within an uncertainty of 0.05% at a 95% confidence level.

References

1. J. Smukala, R. Span, and W. Wagner, *New Equation of State for Ethylene Covering the Fluid Region for Temperatures From the Melting Line to 450 K at Pressures up to 300 MPa*, J. Phys. Chem. Ref. Data, Vol. 29, No. 5, pp 1053-1121, (2000).
2. U. Setzmann, R. Span, and W. Wagner, *Two Methods for Optimising Structure and Length of Correlation Equations*, Rhur-Universtät Report, Bochum, April (1990).
3. J. G. Kirkwood, J. Chem. Phys. Vol. 4, pp 592, (1936).
4. J. Yvon, Act. Sci. Ind. (1935).
5. H. Häusler and K. Kerl, *Mean Polarzabilities and Second and Third Virial Coefficients of the Gases C_2H_4, C_2H_6 and SF_6*, International Journal of Thermodynamics, Vol. 9, No. 1, pp 117, (1988).
6. J. M. St-Arnaud and T. K. Bose, J. Chem. Phys. Vol. 68, pp 2129, (1978).
7. H. G. David, S. D. Hamann and J. F. Pearse, *The Dielectric Constant of Ethylene at High Pressures*, The Journal of Chemical Physics, Volume 19, Number 12, pp 1491, (1951).
8. A. Michels and M. Geldermanns, Physica Vol. 9, pp 967, (1942).
9. D. E. Diller, *The Clausius-Mossotti Functions (Molar Polarizabilities) of Pure Compressed Gaseous and Liquid Methane, Ethane, Propane, Butanes, and Nitrogen*, Cryogenics, pp 215, April (1974).
10. W. M. Haynes, *Othobaric Liquid Densities and Dielectric Constants of Ethylene*, Cryogenics, Vol 25, pp 68, February (1985).
11. J. K. Lehmann and V. Rank, *Eine Apparatur zur Bestimmung der dielektrischen Virialkoeffizienten von Gasen-Die Ermittlung des ersten, zweiten und dritten dielektrischen Virialkoeffizienten von Ethen bei 298 K und 323 K*, Wissenschaftliche Zeitschriftt der Wilhelm-Pieck-Universität Rostock, 33, Jahrgang pp 22, (1984).
12. D. R. Johnston and R. H. Cole, *Dielectric Constants of Imperfect Gases. II. Carbon Dioxide and Ethylene*, The Journal of Chemical Physics, Volume 36, Number 2, PP 318, January (1962).

13. F. Din, *Thermodynamic Properties of Gases* (Butterworth's Scientific Pulications, Ltd., London, (1956).

14. R. H. Orcutt and R. H. Cole, *Dielectric Constants and Pair Interactions in Argon, Carbon Dioxide and Ethylene*, Physica, Volume 31, pp 1779, (1965).

15. T. K. Bose and R. H. Cole, *Dielectric and Pressure Virial Coefficients of Imperfect Gases. IV C_2H_4 and C_2H_4-Ar Mixtures*, The Journal of Chemical Physics, Volume 54, Number 9, pp 3829, (1971).

16. Jim Ryan, BP Chemicals Limited, Grangemouth, United Kingdom – Private Communication.

17. Dr Peter Schley, Rhurgas AG, Betriebsstelle Dorsten, Germany – Private Communication.

18. Drs Mjaeschke and P Schley, Rhurgas AG, Betriebsstelle Dorsten, Germany – Private Communication.

9. Development of On-Line Instrument

One of the objectives of this doctoral submission was to develop a prototype on-line instrument for the accurate metering of the density of high-value fluids and fluid mixtures over an industrially relevant range of temperatures and pressures based on the measurement of relative permittivity.

As previously discussed, two arrangements of the permittivity cell are possible:-

- a laboratory version with high-quality electrical instrumentation suitable for precise measurements on fluids and for mapping relative permittivity as a function of both density and temperature; and
- a robust on-line version with built-in electronics and low-cost instrumentation suitable for the precise measurements on fluids as a function of both density and temperature.

The laboratory facility was based around a high-performance RF network analyser as the principle measuring instrument. This approach would easily meet the measurement criteria, however, it is completely inappropriate for use in the field as an on-line measurement instrument.

An on-line instrument must be simple to operate, relatively compact, robust and considerably less expensive; particularly if it is to be widely deployed.

The aimed accuracy in the measurement of relative permittivity of the on-line instrument was 5 ppm; a factor of five lower than the laboratory instrument.

In order to satisfy the above requirements it was decided to incorporate the re-entrant cavity resonator into a feedback oscillator circuit as the frequency determining element. The on-line instrument would be maintained in continuous oscillation about its natural

resonant frequency with relatively in-expensive modular electronic components and measured with a frequency counter.

9.1 Essential Elements of the On-Line Instrument

The essential elements of the on-line instrument are[1],[2]:-

- a re-entrant cavity resonator;
- an amplifier; and
- a phase shifter.

The re-entrant cavity resonator and the phase shifter are arranged in a feedback loop with the amplifier to create a classical feedback oscillator circuit.

In this arrangement the cavity acts as an extremely narrow bandwidth filter. The high Q factor of the cavity means that it is highly selective in the range of frequencies about its natural resonant frequency that are transmitted with little or no attenuation.

The amplifier, as in any oscillator, is the oscillation provoking device which compensates for the dissipative losses of the system and maintains the total loop gain of the system in excess of one, thus satisfying the unity gain criterion for oscillation to occur.

The phase shifter controls the total phase of the system and enables the oscillator to oscillate at the natural resonant frequency of the cavity by allowing the total phase of the system to be passed through 0°.

In order to completely understand the operation of the on-line instrument, and to assess its performance, it is essential to understand the operation and characteristics of each of the above elements of the oscillator circuit.

A major challenge in the development of the on-line instrument was obtaining a *constant insertion loss phase swing* from the phase shifter element. This characteristic was paramount to the accuracy obtainable from the on-line instrument and, therefore, its industrial applicability. Several phase shifters were constructed as part of the development of the on-line instrument, however, only the more suitable ones are described in any depth here.

The following is a detailed analysis of the characteristics of the on-line instrument and each of its constituent elements.

9.2 Electrical Properties of Re-entrant Cavity Resonator

The electrical properties of the re-entrant cavity resonator were characterised with a HP8752C Vector Network Analyser.

9.2.1 Coupling Antenna

The impedance properties of the coupling antenna of the cavity were measured with the network analyser. The antenna section, illustrated in figure (9.1) below, consists of the antenna loop and its cavity fittings.

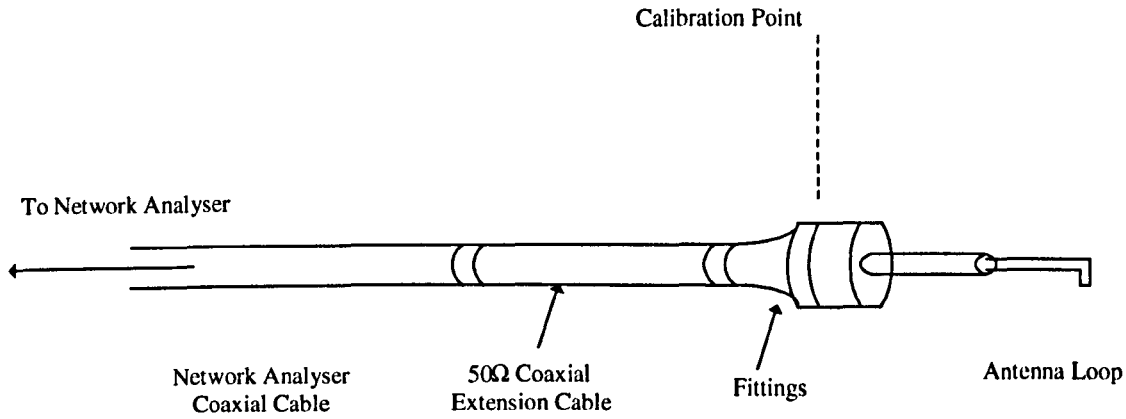

Figure 9.1 Impedance measurements on coupling antenna section.

The network analyser was calibrated to take into account its own lead and the coaxial extension connected to the antenna. This ensures that the impedance measured is only that of the antenna section. The network analyser's lead was calibrated for by using a calibration standard kit. The coaxial extension from the lead to the antenna section was calibrated for by using the network analyser to measure and account for the electrical length of the extension.

The impedance of the coupling antenna section was measured as a function of frequency over the operating range of the cavity. The results are given in table 9.1 below:-

Frequency/MHz	Resistance/Ω	Reactance/Ω	Inductance/nH
375	10.8	52.1	22.1
380	10.9	53.1	22.1
385	11.1	54.1	22.4
390	11.1	55.2	22.5
395	11.3	56.2	22.6
400	11.5	57.3	22.8

Table 9.1 Impedance of coupling antenna section as a function of frequency.

Also given in table (9.1) is the inductance value of the reactance at each frequency. The impedance of the coupling antenna is plotted in graph (9.1) below:-

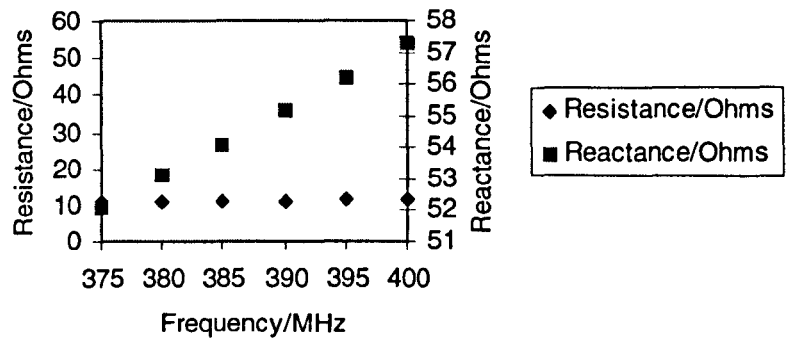

Graph 9.1 Impedance of coupling antenna section.

As expected, the results illustrated above show the coupling antenna section behaves like an inductor. The result that the resistance and reactance both increase with increasing frequency is also to be expected since the resistance is inversely proportional to skin depth, which decreases with increasing frequency, and the reactance is directly proportional to frequency.

9.2.2 Re-entrant Cavity and Single Coupling Antenna

The impedance properties of the re-entrant cavity under atmospheric conditions with a single coupling antenna in the minimum coupling position have been measured. The set up is illustrated in figure (9.2) below:-

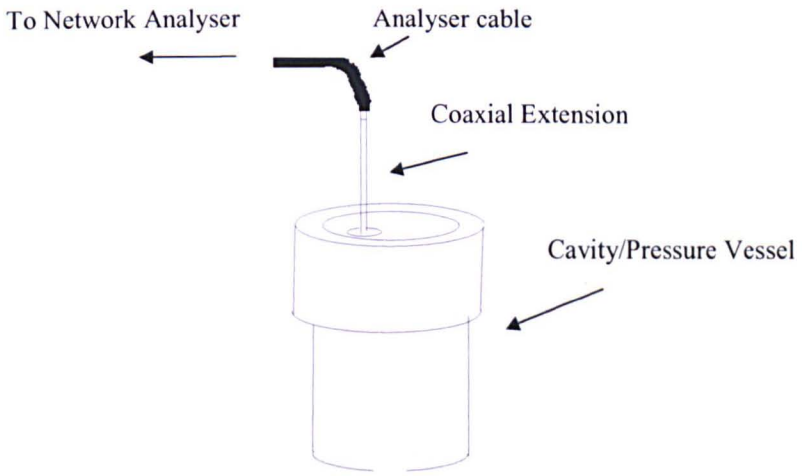

Figure 9.2 Impedance measurements on cavity with single antenna in the minimum coupling position.

The network analyser was set up and calibrated the same way as in section 9.2.1, with the calibration point at the end of the coaxial extension. The impedance of the cavity is plotted in graph (9.2) below:-

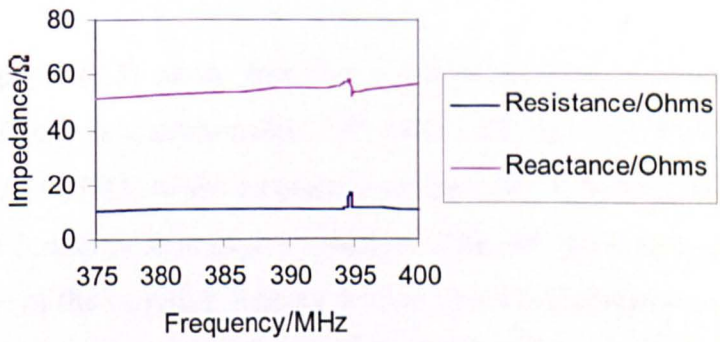

Graph 9.2 Impedance measurements on cavity with single coupling antenna.

Graph (9.2) illustrates the resonance of the cavity. The resonant frequency of the cavity under these conditions can be seen to occur around 395 MHz. These results can be compared to those obtained in section 9.2.1 and plotted on graph (9.3) below:-

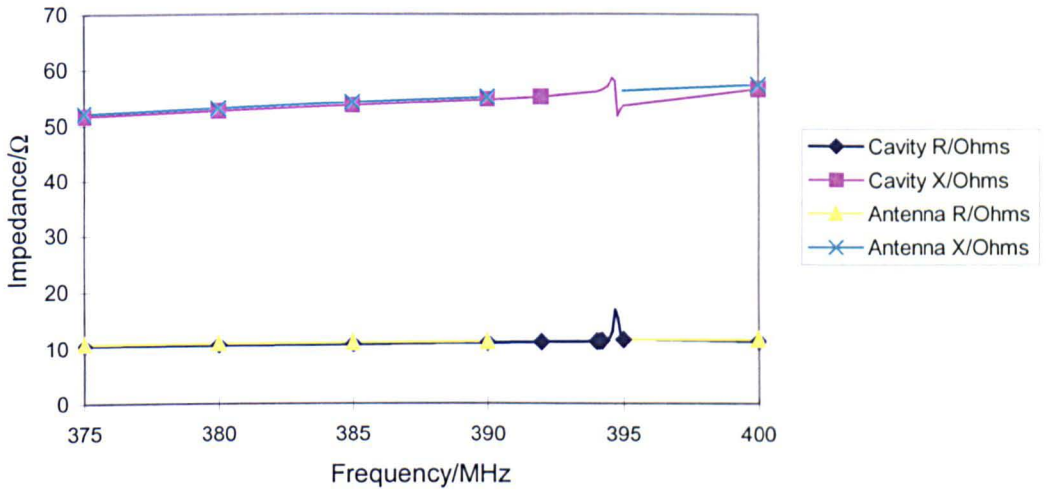

Graph 9.3 Comparison of impedance measurements on antenna and re-entrant cavity and single antenna.

These results show that, with exception of the resonance, the impedance properties of the cavity and single coupling antenna are almost identical to the impedance properties of the coupling antenna. This demonstrates that the coupling between the antenna and the cavity is very small.

The results in graph (9.3) show that the resonant frequency of the cavity under atmospheric conditions is approximately 395 MHz and the impedance at this point is approximately 17Ω + j52Ω. At the resonant frequency the impedance of the cavity is at its maximum and furthermore is purely resistive. This resistance then appears in series with the resistance of the coupling antenna section thus explaining the resistance peak in graph (9.2). The reactance of the cavity is discontinuous at the resonant frequency. This is due to the fact that at frequencies above or below the resonant frequency the cavity appears inductive or capacitive respectively. Therefore at frequencies below resonance the inductive reactance increases as resonance is approached. At resonance the inductive and capacitive reactances are equal and opposite and therefore cancel. As the frequency is increased away from resonance the inductive reactance decreases due to the increase in the capacitive reactance. As the frequency increases further this capacitive reactance

decreases and the curve starts to approach the inductive reactance curve of the coupling antenna section, as in graph (9.1). It is shown in graphs (9.2) and (9.3) that the coupling antenna section dominates the impedance measurements. This is due to the fact that the coupling factor between the antenna and the cavity is very small.

9.2.3 Re-entrant Cavity with Coaxial Extensions

The re-entrant cavity with both its coupling antennas (both set in the minimum coupling position) and the coaxial extensions was characterised with the network analyser under various pressures of nitrogen. The cavity set up is illustrated in figure (9.3) below:-

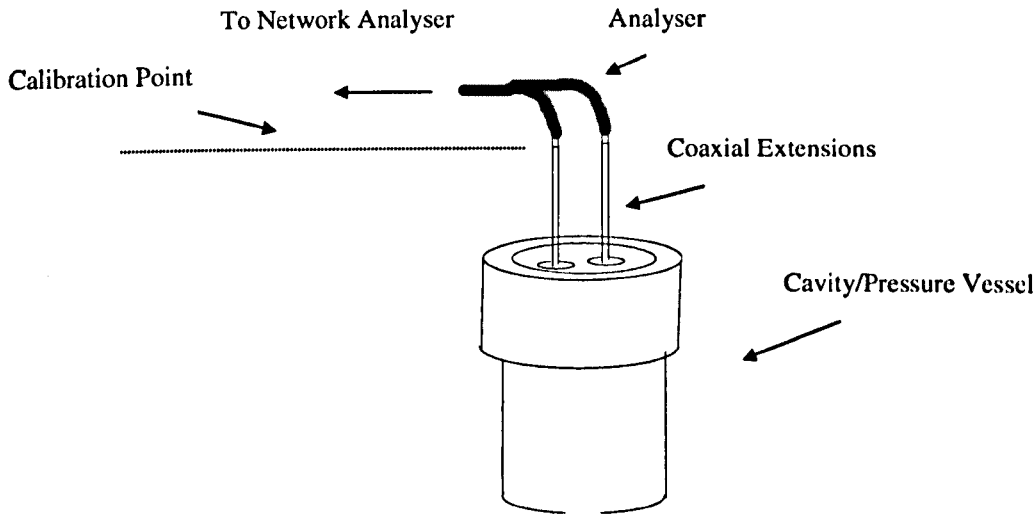

Figure 9.3 Cavity with both antennas in the minimum coupling position.

The calibration point in this set up is the end of the network analysers leads since it is the cavity with both its coupling antennas plus the coaxial extensions that is being characterised.

The network analyser was set up to measure the transmission response of the cavity. This is a swept frequency method that enables the electrical characteristics of the cavity, such as resonant frequency, insertion loss and quality factor to be determined.

Measurements on the cavity were performed at atmospheric, 50 bar nitrogen and 100 bar nitrogen conditions. The transmission response data for the three conditions is plotted in graph (9.4) below:-

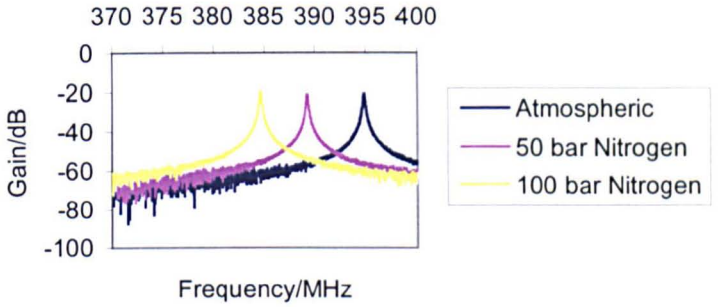

Graph 9.4 Transmission response of cavity for atmospheric, 50 bar nitrogen and 100 bar nitrogen conditions.

It can be seen from graph (9.4) that the resonant frequency of the cavity is approximately 395 MHz at atmospheric conditions, 389 MHz at 50 bar nitrogen conditions and 385 MHz at 100 bar nitrogen conditions. The resonant frequency of the cavity is inversely proportional to the square of the relative permittivity of the fluid under test. Thus it can be seen that the relative permittivity of nitrogen increases with pressure. The insertion loss of the cavity at resonance is fairly constant, approximately 20 dB. The magnitude of the insertion loss of the cavity is partly associated with the impedance mismatch between the network analyser and the cavity. Because the coupling between the cavity and the external RF source is so small, most of the injected power from the network analyser is reflected back and dissipated at the source. The quality factor of the cavity at each condition has been measured and was found to be 2224 at atmospheric conditions, 2201 at 50 bar nitrogen conditions and 2176 at 100 bar nitrogen conditions. The quality factor is inversely proportional to any loss mechanisms incurred within the cavity.

The above measurements were performed at room temperature. The electrical properties of the cavity are, of course, temperature dependent. For example, given a change in ambient temperature of approximately + 1.5°C, the resonant frequency of the cavity at atmospheric conditions decreases by approximately 5 kHz. This is to be expected since the thermal expansion of the cavity walls results in the capacitive section of the cavity increasing which reduces the resonant frequency.

Impedance measurements were carried out on the cavity with the network analyser, set up again with the calibration point at the end of the network analyser's leads. The input impedance at the atmospheric resonant frequency is approximately $8\Omega + j2\Omega$. Obviously when the coaxial extensions are not included in the calibration the impedance measured is different. However this is the input impedance that any external circuit connected to the cavity will *see*. (From this point on *the cavity* will mean cavity, coupling antennae and coaxial extensions.)

Impedance measurements were carried out on the cavity as it was pressurised with nitrogen. The purpose of making these measurements was to observe the change in the input impedance of the cavity with pressurised fluid. The resonant frequency and input impedance at each pressure were recorded and are given in table (9.2) below:-

Resonant Frequency/MHz	Resistance/Ω	Reactance/Ω	Pressure/bar	Relative Permittivity (nitrogen)
394.9688			Vacuum	1
394.8750	8.02	1.38	Atmospheric	1.000474890
391.7750	7.44	1.48	20	1.016370456
390.7850	7.94	0.14	40	1.021526648
388.4650	7.96	-1.07	60	1.033764656
386.7750	7.93	-1.73	80	1.042818390
384.6900	7.89	-2.21	100	1.054153068
382.5025	7.90	-3.20	120	1.066244773
381.0500	7.85	-4.08	140	1.074388965
379.8790	7.82	-4.15	150	1.081022912

Table 9.2 Input impedance of cavity as a function of relative permittivity.

Also shown in table (9.2) is a rough calculation of the relative permittivity of nitrogen at the various conditions. (Note: No corrections were applied to the relative permittivity calculation). Graph (9.5) below illustrates the relationship between the input impedance of the cavity and the relative permittivity of nitrogen.

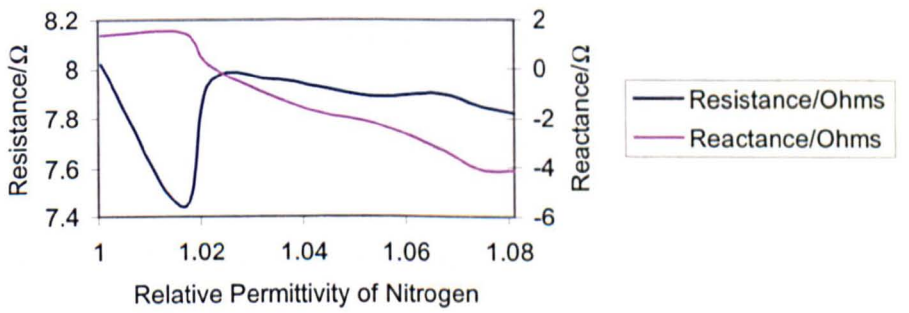

Graph 9.5 Input impedance of the cavity as a function of relative permittivity of nitrogen.

From graph (9.5) it can be seen that the reactance of the cavity varies quite considerably with relative permittivity. The reactance changes from being inductive at low relative permittivities to capacitive at higher relative permittivities.

Input impedance measurements were performed on the cavity using both antenna. The network analyser swept over the frequency range of operation and the impedance data was recorded. Comparisons between the two antennae at atmospheric conditions are illustrated in graph (9.6) below:-

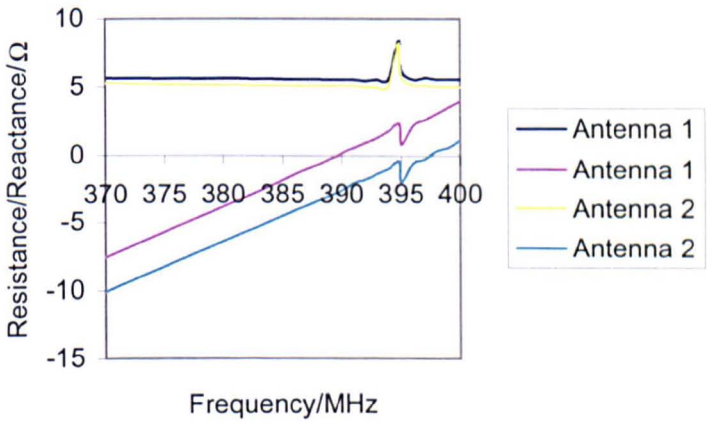

Graph 9.6 Comparison of the two coupling antenna.

It can be seen from graph (9.6) that the two antennae have slightly different electrical properties. This result means that it is important to be consistent with the antennae used over the course of a series of measurements. Similar results have been obtained for measurements taken at 50 and 100 bar nitrogen conditions.

9.2.4 Loading of Re-entrant Cavity

The resonant frequency of the re-entrant cavity at atmospheric conditions was measured with the network analyser as it was loaded with various components of the oscillator

circuit. The purpose of doing this was to observe any change in resonant frequency that the components of the oscillator circuit may cause. The network analyser injects a -22 dBm signal over the frequency range of interest.

The cavity was set up with two ZFL1000GH (section 9.3) amplifiers connected to its input and output ports, as illustrated in figure (9.4) below:-

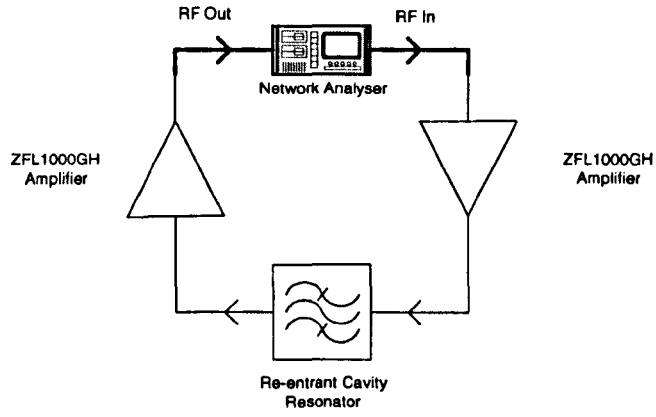

Figure 9.4 Schematic diagram of the ZFL1000GH amplifier loading of the cavity.

It was found that the two amplifiers had no effect on the resonant frequency of the cavity. This result is to be expected since the input and output ports of the of the ZFL1000GH amplifier approximately match that of the network analyser (50Ω) and the frequency response of the amplifier is flat over the range of operating frequencies. Therefore the loading of the cavity has effectively not changed.

One of the test phase shifters (the two stage electronic EMS (electromagnetically shielded) phase shifter) was added to the set-up to complete all the components of the oscillator circuit, as illustrated in figure (9.5) below:-

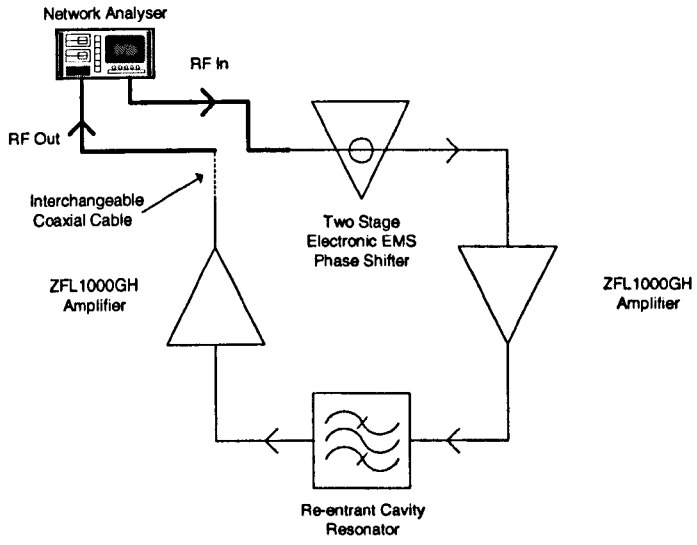

Figure 9.5 Schematic diagram of the two stage electronic EMS phase shifter oscillator circuit.

It was found that the addition of the phase shifter to the circuit made no difference to the resonant frequency of the cavity. This result is to be expected since the cavity is buffered from the phase shifter by both the amplifiers and the frequency response of the phase shifter is relatively flat over its range of bias voltages.

The cavity was set up with the two stage electronic EMS phase shifter connected directly to its input port, as illustrated in figure (9.6) below:-

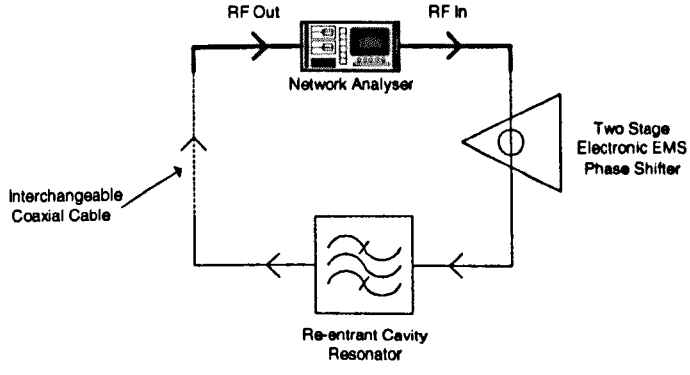

Figure 9.6 Schematic diagram of the two stage electronic EMS phase shifter loading of the cavity.

The resonant frequency was measured over the range of bias voltages to the phase shifter. It was found that for a bias of 10 V there was no difference in frequency. However at bias voltages of 5 and 10 V the frequency increased by 1.4 and 4.6 kHz respectively. The differences in frequency may be explained by considering the fact that the cavity now *looks* directly into the phase shifter which has a variable, non-50Ω, output impedance. Although the coupling between the re-entrant cavity and the antenna is small it is possible that the connection of the phase shifter has caused the electrical properties of the cavity, and consequently, the resonant frequency to change. It is also possible that the frequency response of the phase shifter is no longer flat, and thus the resonant frequency is *pushed* or *pulled.*

It has been shown that the resonant frequency of the cavity is not affected by the external electronics of the oscillator circuit, provided the cavity is buffered from the phase shifter.

9.3 Electrical Properties of Mini-Circuits Broadband Linear ZFL1000GH Amplifier

The Mini-Circuits Broadband Linear Variable Gain ZFL1000GH Amplifier was characterised using the network analyser. Plot (9.1), below, illustrates the bandwidth and gain of the amplifier when the analogue gain control (AGC) bias voltage is 0 V (maximum gain conditions).

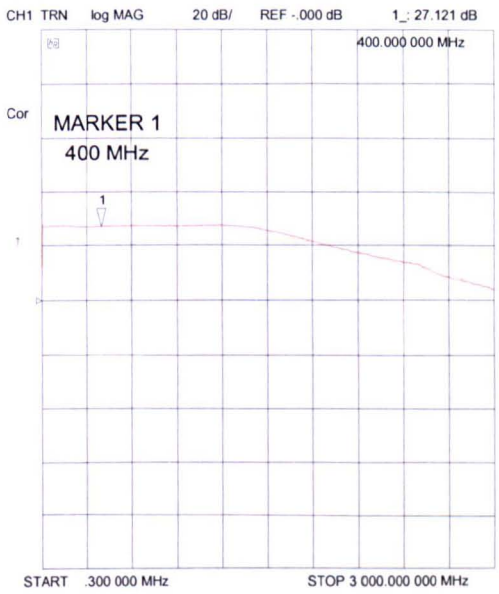

Plot 9.1 Transmission response of ZFL1000GH amplifier with AGC set to 0V.

Plot (9.1) shows the gain of the amplifier over the frequency range 0.3 MHz to 3 GHz. The gain is shown to be constant at approximately 27 dB over the 1200 MHz bandwidth.

9.3.1 Gain Characteristics

The gain characteristics of the amplifier were measured with the network analyser over the frequency range of interest (370 to 400 MHz) as a function of AGC bias. The RF signal injected into the amplifier was -22 dBm. This relatively low RF level was used because the maximum RF into the network analyser is +5 dBm. The frequency response of the amplifier as a function of AGC bias is illustrated in graph (9.7) below:-

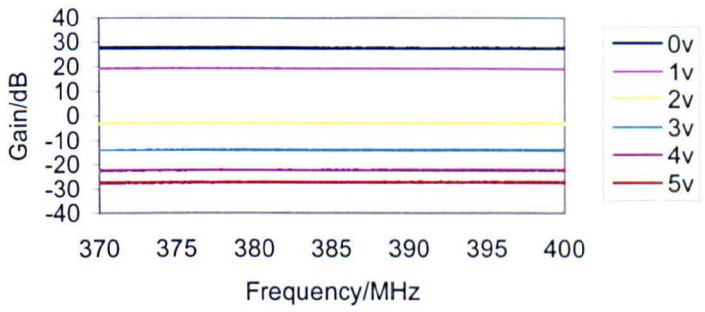

Graph 9.7 Frequency response of gain of ZFL1000GH amplifier as a function of AGC bias.

It can be seen from graph (9.7) that the AGC bias has quite a pronounced effect on the gain of the amplifier. The AGC bias applied to the amplifier can be from 0 to 5 V with 0 V producing maximum gain conditions. More importantly it should be noted that the response of the amplifier over the range of operating frequencies is flat. It is important that the frequency response of the amplifier is flat in order to ensure that when the amplifier is within the oscillator it does not *push* or *pull* the re-entrant cavity resonance in any way.

The ZFL1000GH needs to have an AGC bias voltage of less than 2 V in order for it to amplify any signals. However since the insertion loss of the cavity is of the order of 20 dB the gain provided by the amplifier needs to be at least 20 dB in order compensate for this and other losses caused by components of the oscillator circuit (e.g. phase shifter, cables etc.). Therefore the only region of interest in graph (9.7) is for AGC biases of between 0 and 1 V. The frequency response of the amplifier at these bias voltages is illustrated in graph (9.8) below:-

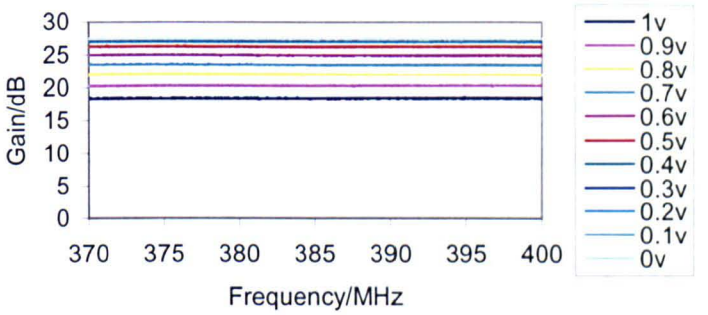

Graph 9.8 Frequency response of gain of ZFL1000GH amplifier for AGC bias of 0 to 1 V.

Graph (9.8) illustrates the frequency response of the amplifier over the selected range of AGC bias voltages. Again it can be seen that the response is flat over the operating frequencies. (Any differences in graphs (9.7) and (9.8) are due to the fact that for graph (9.7) the AGC bias was set with the reading from the bench power supply and for graph (9.8) the AGC bias was set by using a hand-held multimeter.) Graph (9.9), below, is a summary of graph (9.8) taken at a point frequency of 394.86 MHz. (The selected frequency is of no importance since the response is flat across the frequency range of interest.)

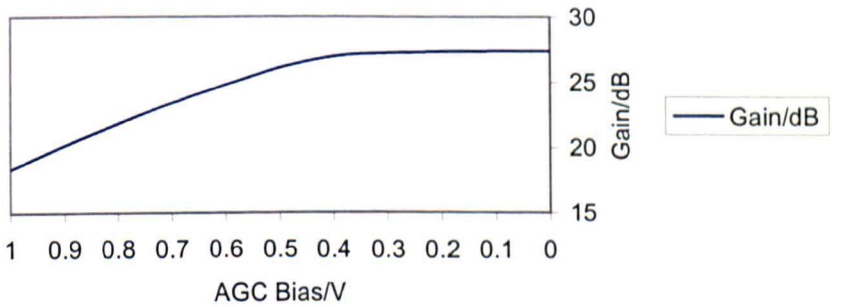

Graph 9.9 Gain of ZFL1000GH as a function of AGC bias.

Graph (9.9) shows that as the AGC bias is reduced from 1 V the gain of the amplifier starts to level off to its maximum value of approximately 27 dB at 0.4 V bias.

9.3.2 Phase Characteristics

The phase characteristics of the amplifier were measured with the network analyser as a function of AGC bias. Again the RF signal injected into the amplifier was kept to -22 dBm. The frequency response of the amplifier as a function of AGC bias is illustrated in graph (9.10) below:-

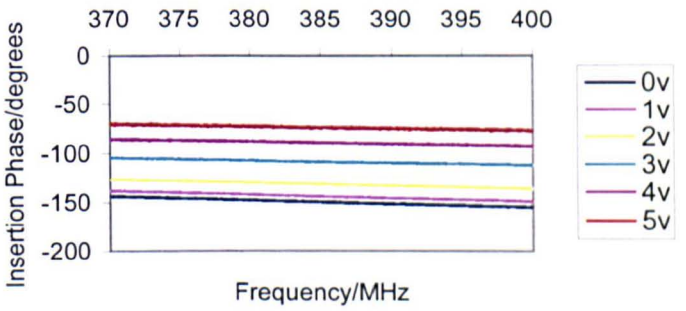

Graph 9.10 Frequency response of insertion phase of ZFL1000GH as a function of AGC bias.

Graph (9.10) shows that once again that the AGC bias has quite a pronounced effect on the insertion phase of the amplifier. Again the region where the AGC bias is set to between 1 and 0 V is the only one of interest. It can be seen that the insertion phase of the amplifier increases with frequency, ranging from approximately -138° to -150° at 0 V, and from approximately -144° to -155° at 1 V as the frequency is swept from 370 MHz to 400 MHz.

9.3.3 Impedance Characteristics

The impedance properties of the ZFL1000GH amplifier were measured with the network analyser. The network analyser's lead was calibrated for using a calibration standard kit. The input and output impedances of the amplifier were measured as a function of

frequency over the frequency range of interest and AGC bias voltage. The input impedance of the amplifier varies very little over the frequency range but is slightly dependent on AGC bias. It varies from 46Ω + j2.4Ω at a AGC bias of 0 V to 42Ω + j4.2Ω at 1 V. The output impedance again has only a slight dependence on AGC bias only varying from 50Ω - j16Ω at 0 V AGC bias to from 55Ω - j11Ω at 1 V. Thus the amplifier has reasonably good 50Ω input and output impedances.

The impedance properties are not affected by how the ports are terminated. This was verified by using the HP calibration kit to terminate the relevant port in open, short and 50Ω standards. This shows that the amplifier has a high directivity.

9.3.4 Loading Characteristics

The ZFL1000GH amplifier was loaded with non-50Ω loads to observe any effects this may have on the gain and gain flatness. The network analyser was used to measure the transmission response of each set up thus determining both gain and gain flatness.

The first set up consisted of the amplifier with the two stage electronic EMS phase shifter connected to its input. The network analyser drives the input to the phase shifter over the frequency range of interest (370 MHz to 400 MHz) at an RF signal level of -22 dBm and the output from the amplifier is observed. The bias voltage of the phase shifter is set to 10 V, at this condition its output impedance varies from approximately 64Ω - j25Ω at 370 MHz to 65Ω - j30Ω at 400 MHz (see section 9.4.4). (Obviously the output impedance of the phase shifter is dependent on the bias voltage applied to it but the purpose of this measurement was to determine the immediate effect of changing the loads on the amplifier to other than 50Ω). The AGC bias to the amplifier was varied from 1 to 0 V. There was no observable change in the flatness of the transmission response from that of graph (9.8) as the AGC bias was varied from 1 to 0 V. Graph (9.11), below, is a summary of the results observed from these measurements.

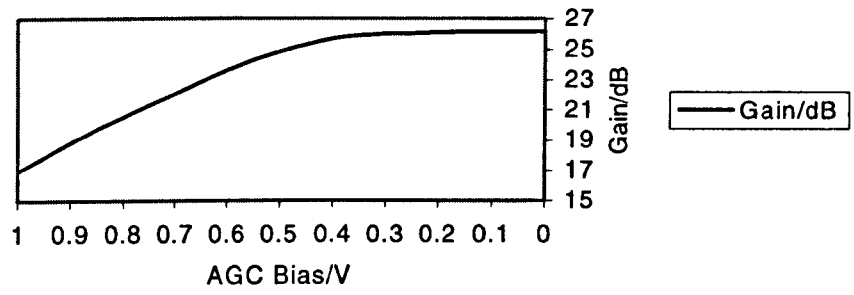

Graph 9.11 Gain of ZFL1000GH and two stage electronic EMS phase shifter as a function of AGC bias.

Graph (9.11) shows that the only effect that the phase shifter has on the response of the amplifier is that it reduces the gain of the response curve by a value that corresponds to its own insertion loss. The gain of the set up is approximately 26 dB at an AGC bias of 0 V. This is approximately 1 dB less than the corresponding condition in graph (9.9). This 1 dB difference is accounted for by the phase shifters insertion loss when it is biased at 10 V (see section 9.4.2).

The second set up was the same as the first but included a single stage electronic phase shifter connected to the output of the amplifier. The network analyser again drives the input to the two stage phase shifter over the frequency range of interest at an RF signal level of -22 dBm and the output is observed from the output of the single stage phase shifter. The bias voltage of the two stage phase shifter is kept at 10 V and the bias voltage to the single stage phase shifter is 0 V. At a bias voltage of 0 V the input impedance of the single stage phase shifter is approximately 20Ω + j40Ω over the frequency range of interest. Again the AGC bias voltage was varied from 1 to 0 V. There was again no observable change in the flatness of the transmission response from that of graph (9.8) as the AGC bias was varied from 1 to 0 V. Graph (9.12), below, is a summary of the results observed from these measurements.

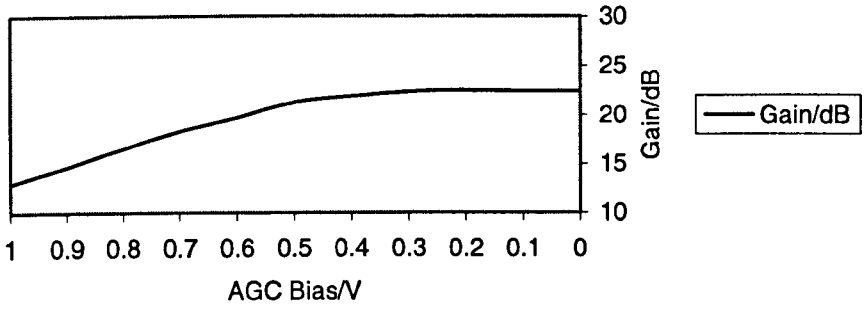

Graph 9.12 Gain of ZFL1000GH, two stage electronic EMS phase shifter and single stage electronic phase shifter as a function of AGC bias.

Graph (9.12) shows that the only effect that loading the amplifier with non-50Ω loads is that the gain of the response curve is reduced by a value that corresponds to the sum of the insertion loss of each phase shifter. The gain of this set up is approximately 22 dB at an AGC bias of 0 V. This is approximately 5 dB less than the corresponding condition in graph (9.9). This 5 dB difference can be accredited to the 1 dB insertion loss of the two stage electronic EMS phase shifter and 4 dB insertion loss of the single stage electronic phase shifter at these conditions.

These results show that the ZFL1000GH amplifier is unaffected in terms of gain and gain flatness when it is terminated with non-50Ω loads.

9.3.5 RF Signal Level Characteristics

The ZFL1000GH amplifier was also characterised for different levels of RF signals. The previous measurements used an RF signal level of -22 dBm but in order to characterise the amplifier fully it is important to know its behaviour over all usable RF signal levels.

In order to characterise the amplifier in terms of output power and gain a 1 GHz signal generator was used to inject RF signals into the amplifier and a 500 MHz oscilloscope was used to observe the amplified signals. The signal generator was used to inject a 400

MHz signal of between -50 and +5 dBm into the amplifier. The amplified signal is then observed on the oscilloscope in V_{rms}.

The bandwidth of the oscilloscope is 500 MHz, which means that at 400 MHz it only reads approximately 80% of the input signal. Therefore all the readings taken on the oscilloscope were corrected to account for this bandwidth drop-off. The RF level was swept from -50 to +5 dBm for AGC bias voltages between 1 and 0 V and the output V_{rms} is observed on the oscilloscope. The V_{rms} signal as taken from the oscilloscope is then equated to its corresponding signal level in dBm. This conversion assumed that the system impedance is 50Ω, which was satisfactory since the signal generator and the oscilloscope have 50Ω inputs and the amplifier has an approximate input/output impedance of 50Ω.

The results may be interpreted in terms of output RF signal level or in terms of amplifier gain. Both interpretations are illustrated in graphs (9.13) and (9.14) below:-

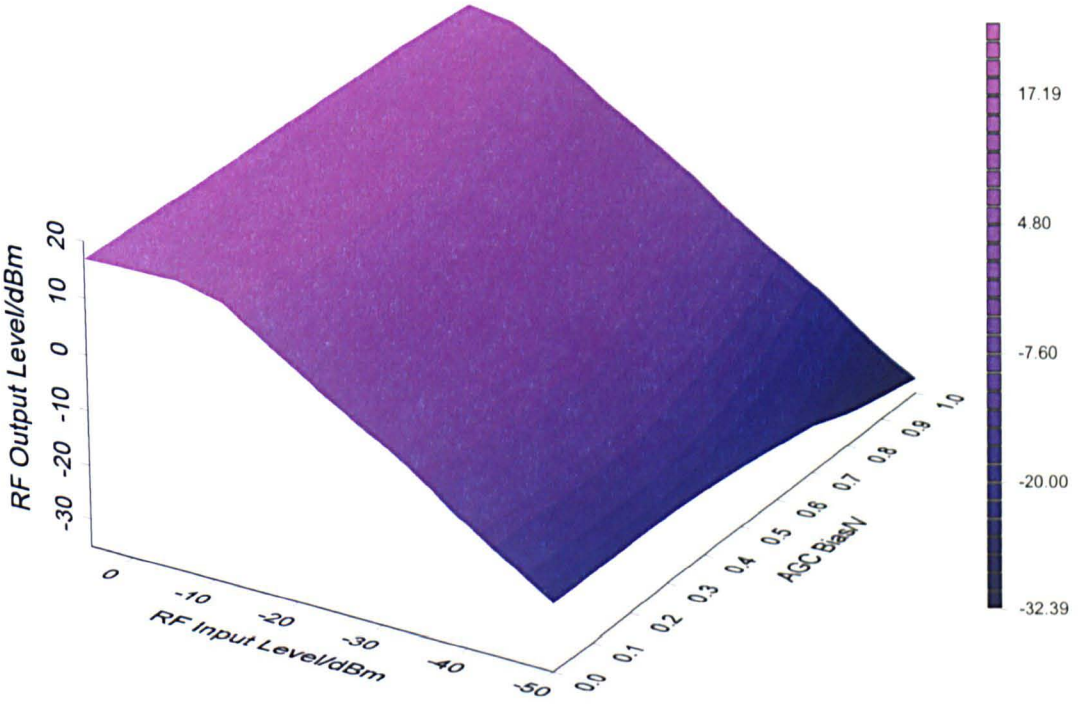

Graph 9.13 Output RF signal level as a function of input RF signal level and AGC bias.

Graph (9.13) illustrates the RF output level of the amplifier as a function of RF input and AGC bias. It can be seen from graph (9.13) that the output of the amplifier saturates at approximately +17 dBm. The saturation of the amplifier obviously occurs at different RF input levels for different AGC biases. At an AGC bias of 1 V the amplifier saturates at an RF input of -5 dBm and at an AGC bias of 0 V the amplifier saturates at an RF input of -10dBm.

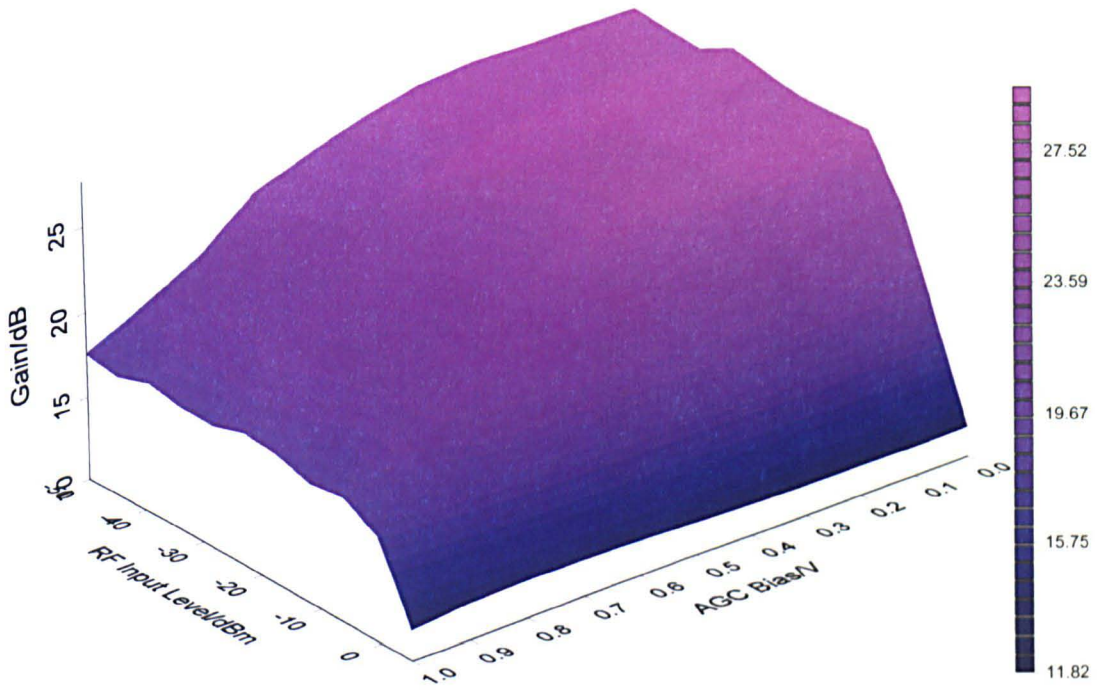

Graph 9.14 Gain as a function of input RF signal level and AGC bias.

Graph (9.14) illustrates the gain of the amplifier as a function of RF input and AGC bias. It can be seen from graph (9.14) that for low RF input signals (-50 to -15 dBm) the gain of the amplifier increases in the same fashion as that of graph (9.9) with a maximum gain of approximately 27 dB at an AGC bias of 0 V. As the RF input signal increases beyond -15 dBm the amplifier starts to saturate and subsequently the gain is reduced.

In order to characterise the amplifier in terms of insertion phase the network analyser was used to inject an RF signal of between -20 and +5 dBm into the amplifier and the insertion phase of the amplifier was recorded. The RF level was swept from -20 to +5 dBm for AGC bias voltages between 1 and 0 V. In order to limit the RF signal level entering the network analyser 30 dB of attenuation was connected to the output of the amplifier (this attenuation has been corrected for in the illustrated data).

The results are illustrated in graph (9.15) below:-

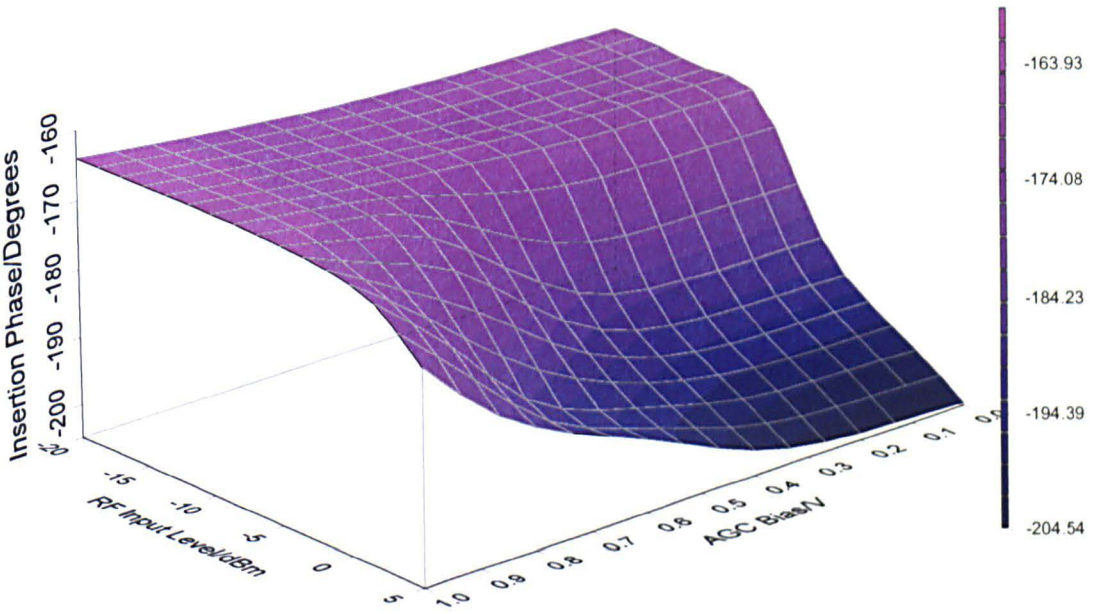

Graph 9.15 Insertion phase as a function of input RF signal level and AGC bias.

Graph (9.15) illustrates the insertion phase of the amplifier as a function of RF input signal and AGC bias. It can be seen from graph (9.15) that as the amplifier saturates the insertion phase of the amplifier increases sharply. At low RF input signals (-20 to -10 dBm) the insertion phase increases from approximately -164° to -170° as the AGC bias is swept from 1 to 0 V. However for higher RF input signals the amplifier starts to saturate as the AGC bias is increased and as a result the insertion phase increases from around -170° towards -205°.

9.4 Electrical Properties of Phase Shifter Elements

In order to satisfy the requirement for an easily operable, compact and inexpensive on-line instrument, it was decided to try and develop a phase shifter device that was simple

to operate with minimal number of readily available commercial components. In accordance with the above the development of a phase shifter device was approached from a transmission line theory view point; that is, the phase shifter was developed comprising two (or more) complementary reactive components connected in parallel, namely an inductor and a capacitor.

As previously mentioned, only those phase shifters considered suitable for this application are described in any depth here.

9.4.1 Two Stage Electronic Phase Shifter

The two stage electronic phase shifter is illustrated in figure (9.7) below:-

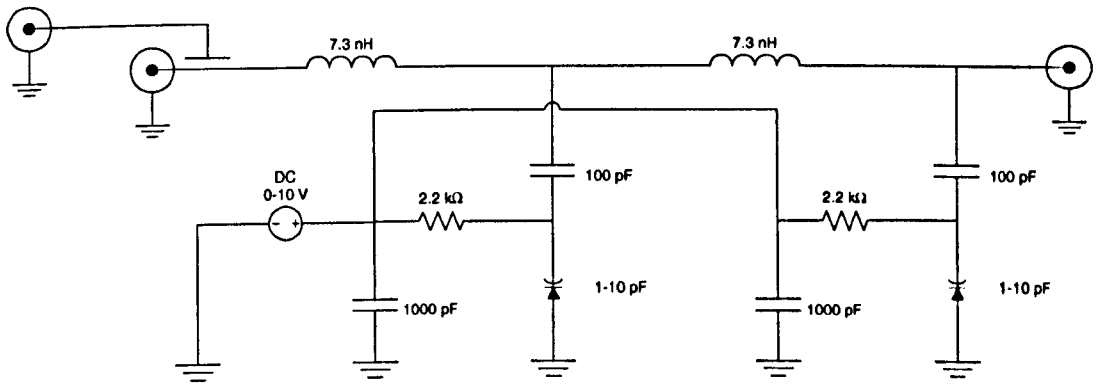

Figure 9.7 Circuit diagram of the two stage electronic phase shifter.

The two stage electronic phase shifter consists of a 7.3 nH inductor in parallel with a variable (1-10 pF) capacitance. The inductor is fabricated from a section of tinned copper wire 3.8 cm in length and 1 mm in diameter. The variable capacitance consists of a varactor diode which enables the phase to be varied with a dc bias voltage. The varactor diode is a Siemens BB 833 Silicon Tuning Diode. The diode has an extended operating frequency range of 2.5 GHz and the typical diode capacitance as a function of bias reverse bias voltage is illustrated in graph (9.16) below:-

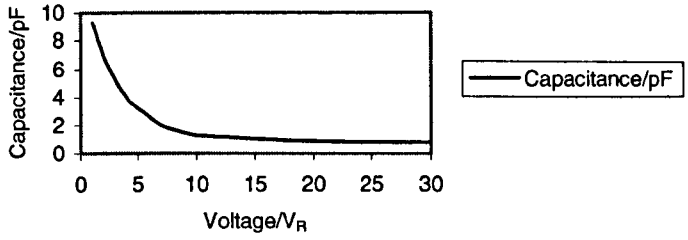

Graph 9.16 Typical capacitance of BB 833 tuning diode as a function of bias voltage.

In figure (9.7) the 100 pF capacitors are Murata UHF surface mount capacitors which serve as a dc block, isolating the rest of the circuit from the dc bias voltage applied to the varactor. Its value was chosen to be ten times the maximum capacitance of the varactor so that the total capacitance was relatively unaffected. The 2.2 kΩ resistor acts as an RF choke, isolating the dc voltage supply. A resistor was chosen due to the fact that its leads present a large inductive reactance and thus contributes to the resistors impedance. The 1000 pF capacitor is a Murata UHF surface mount capacitor which serves as an RF sink for any signals that pass through the resistor. Any RF signals that superimpose onto the dc voltage biasing the varactor may be considered of negligible magnitude in comparison.

The capacitive coupling to the phase shifter is shown at the RF input point of the circuit (see section 9.6). The capacitive coupling was a coaxial jack stub in close proximity to the RF input coaxial jack stub.

9.4.2 Insertion Loss Characteristics

The insertion loss characteristics of the two stage electronic phase shifter were measured with the network analyser over the frequency range of interest as a function of bias voltage. The insertion loss frequency response of the phase shifter as a function of bias voltage is illustrated in graph (9.17) below:-

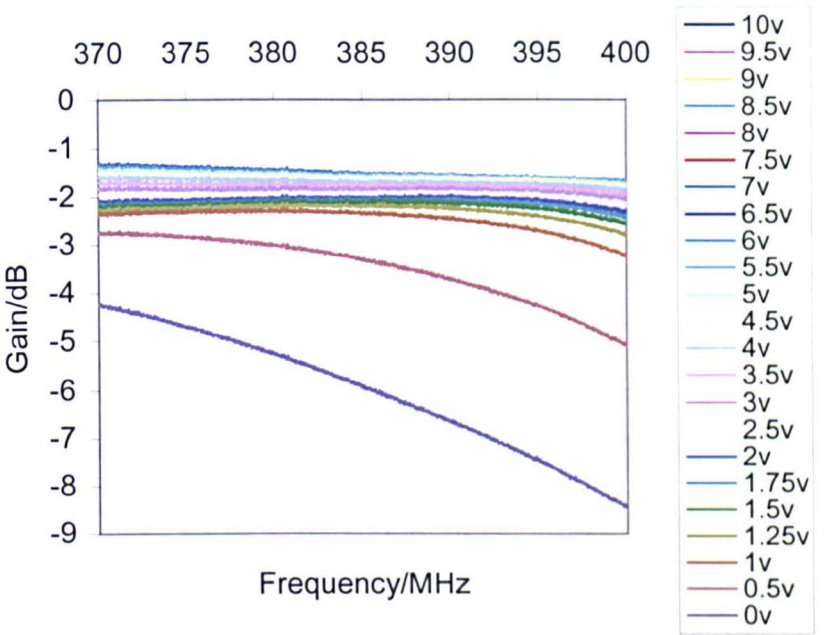

Graph 9.17 Insertion loss frequency response of two stage electronic phase shifter as a function of bias voltage.

It can be seen from graph (9.17) that the insertion loss of the phase shifter is relatively flat with frequency at voltages between 10 and 3 V. However as the bias voltage is reduced the insertion loss starts to increases sharply.

The magnitude of the insertion loss at 0 V is approximately double that of the single stage electronic phase shifter. The variation of insertion loss with frequency and voltage is illustrated further in graph (9.18) below:-

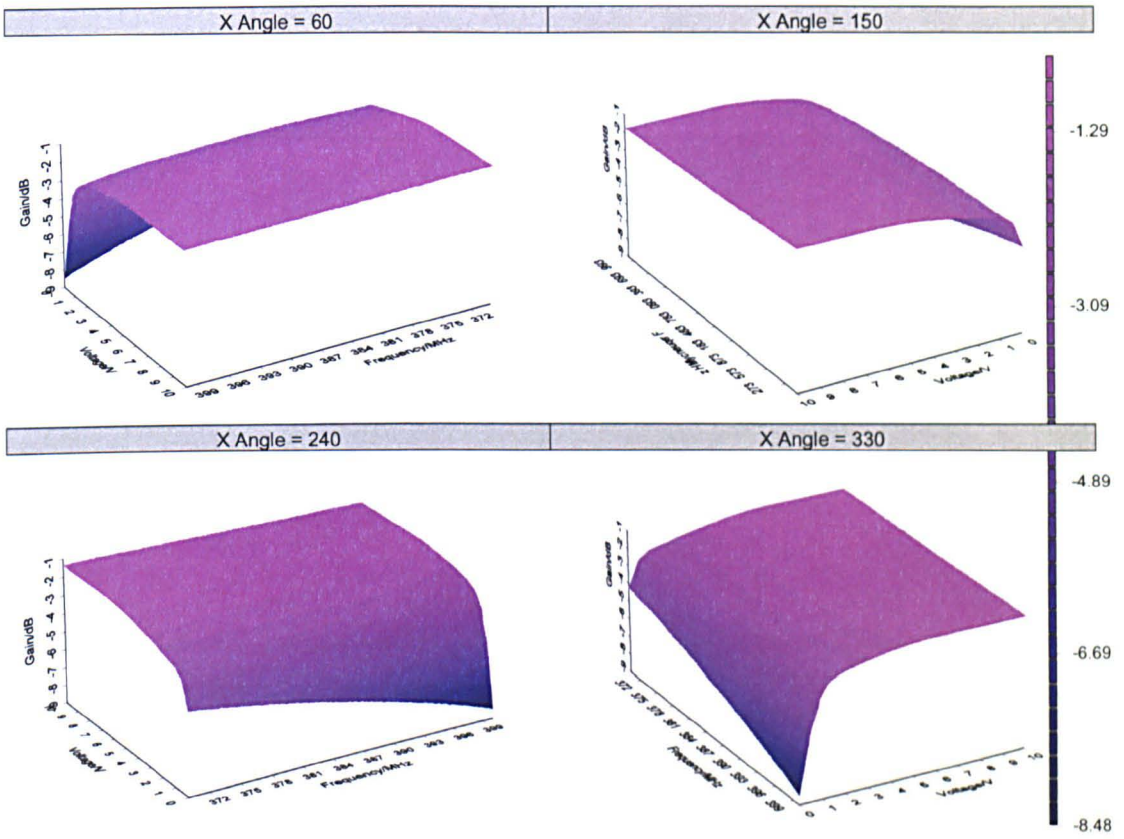

Graph 9.18 Insertion loss frequency response of two stage electronic phase shifter as a function of bias voltage.

It can be seen from graph (9.18) that the insertion loss of the phase shifter appears constant with frequency as the voltage is varied from 10 to approximately 5.5 V. Again as the voltage is reduced below this value the insertion loss increases sharply. The flatness of the insertion loss is illustrated further in graph (9.19) below:-

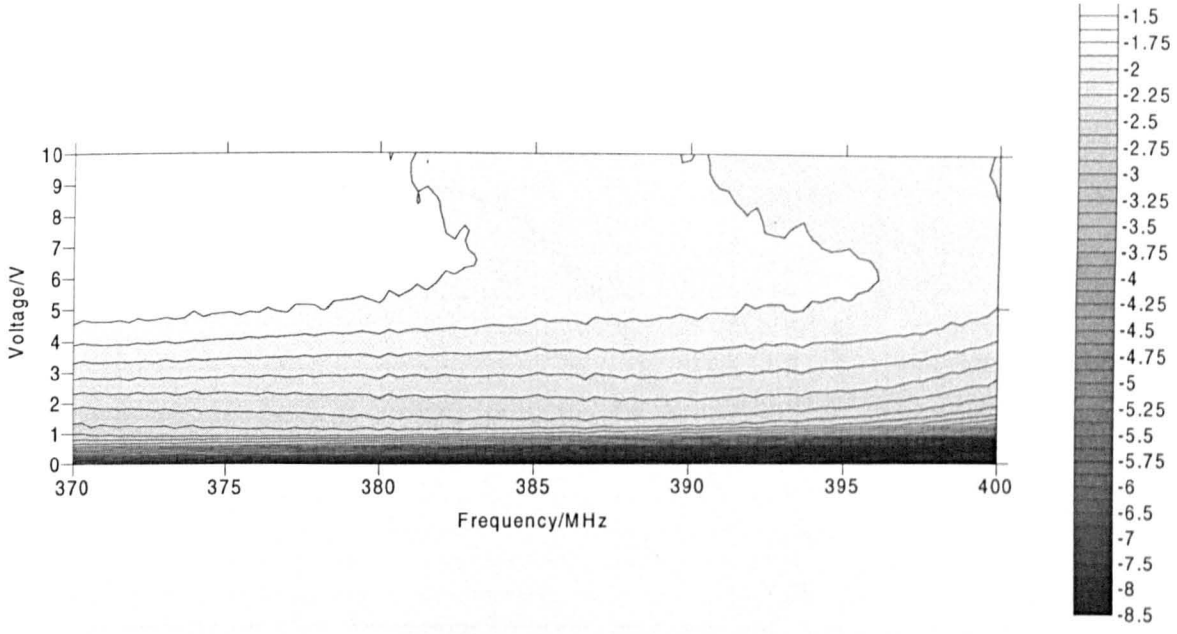

Graph 9.19 Insertion loss contour plot of frequency response of two stage electronic phase shifter as a function of bias voltage.

Graph (9.19) is a contour plot of the frequency response of the two stage electronic phase shifter as a function of bias voltage. It can be seen from graph (9.19) that the insertion loss varies slightly with frequency and voltage in the region of 10 to approximately 5.5 V. A cross section of graph (9.18) at selected frequencies is illustrated in graph (9.20) below:-

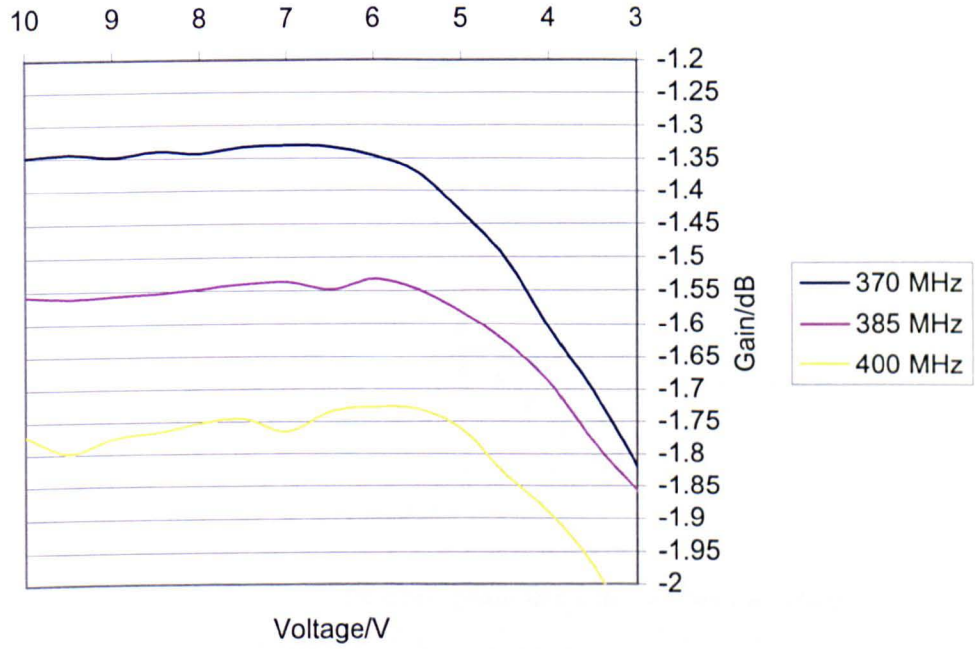

Graph 9.20 Insertion loss of two stage electronic phase shifter as a function of bias voltage.

It can be seen from graph (9.20) that at 370 MHz the insertion loss decreases from approximately 1.35 dB at 10 V to 1.33 dB at 7 V and then increases to 1.35 dB again before dropping off sharply. Therefore the insertion loss over this section is approximately 1.34 ± 0.01 dB. The insertion loss at 385 MHz behaves in a similar fashion with a general decrease in insertion loss from approximately 1.56 dB at 10 V to 1.53 dB at 6 V. The flat section of the insertion loss at 385 MHz is slightly greater than that of 370 MHz with the insertion loss starting to drop off at approximately 5.5 V. The insertion loss over this section is approximately 1.545 ± 0.015 dB. At 400 MHz the insertion loss fluctuates more than the other plots but stills follows the general trend of an initial decrease in insertion loss followed by a sharp increase as the voltage is reduced. The insertion loss over this section is approximately 1.7625 ± 0.0375 dB.

It should be noted that this particular two stage phase shifter was not mounted in any electromagnetically shielded casing therefore the characteristics of the phase shifter are effected by any objects in its proximity. One of the main factors affecting the

characteristics were the voltage leads which were free to move around the phase shifter. The consistency of measurements is illustrated in graph (9.21), below, at 400 MHz for three separate measurements.

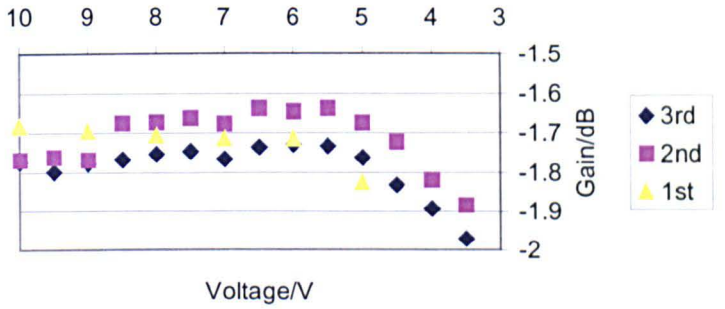

Graph 9.21 Insertion loss of two stage electronic phase shifter as a function of voltage for three separate measurements at 400MHz.

It can be seen from graph (9.21) that the repeated measurements differ slightly from one another. The measurements follow the general trend of having relatively flat insertion loss at higher voltages before starting to increase rapidly in the region of 5.5 V. The first measurement displays a different characteristic from the second and third in that the insertion loss gradually increases as the voltage is reduced from 10 V.

To show that these characteristics are not merely fluctuations of noise a more detailed insertion loss frequency response graph for the third measurement is illustrated in graph (9.22) below:-

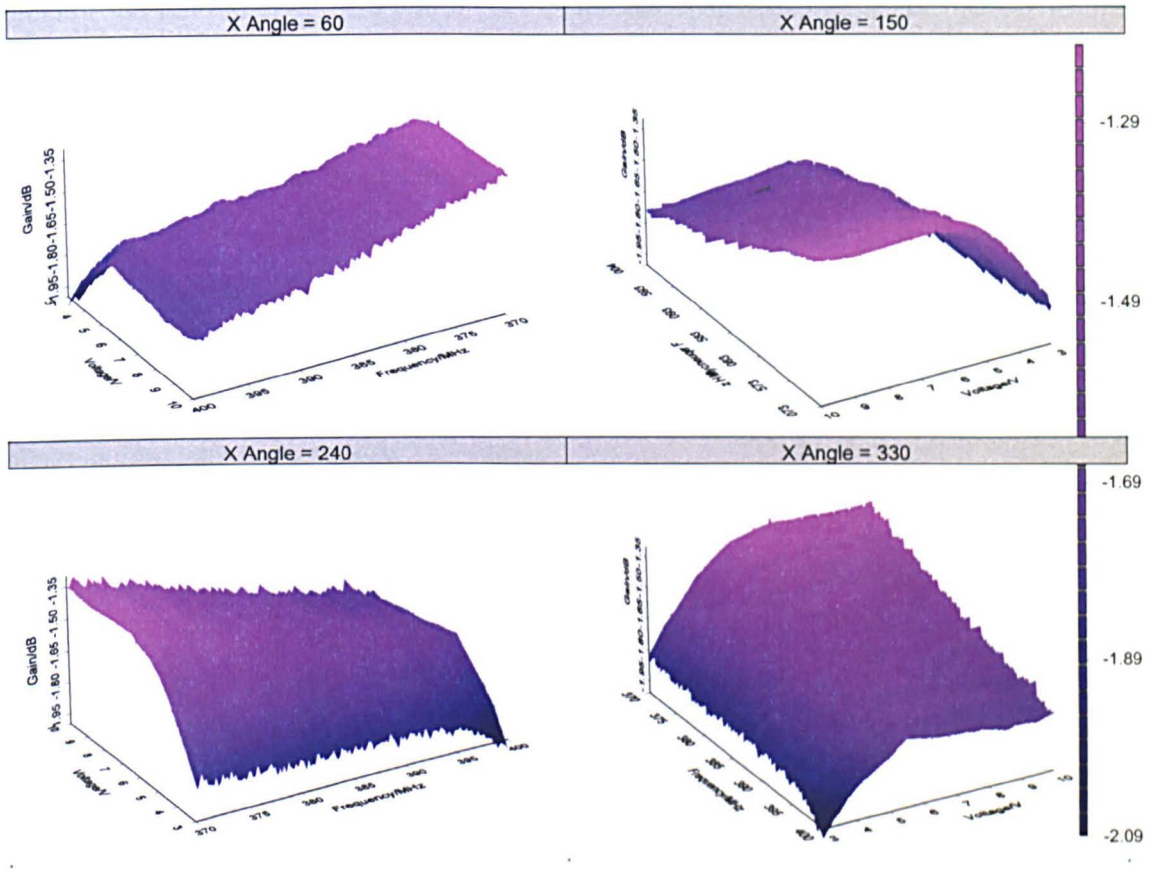

Graph 9.22 Insertion loss frequency response of two stage electronic phase shifter as a function of bias voltage.

It can be seen from graph (9.22) that the general characteristics are the same over the frequency range of interest. The small differences in the characteristics are more difficult to account for since any comparisons made from graph (9.20) must be done so by taking into consideration that the phase shifter is subject to temperature effects, noise and obviously a different frequency of measurement, therefore it is difficult to distinguish one effect from an other. The dependence of the characteristics of the phase shifter on frequency are evident not only in the general increase of insertion loss with frequency but also with constant frequency *ridges* that occur throughout the range. This suggests that superimposed noise does not have a large influence on the characteristics of the phase shifter. The effects of noise have been minimised in the third measurement by

reducing the intermediate bandwidth (IF) of the network analyser from 3000Hz to 300 Hz.

9.4.3 Insertion Phase Characteristics

The insertion phase characteristics of the two stage electronic phase shifter were measured with the network analyser over the frequency range of interest as a function of bias voltage. The insertion phase frequency response of the phase shifter as a function of voltage is illustrated in graph (9.23) below:-

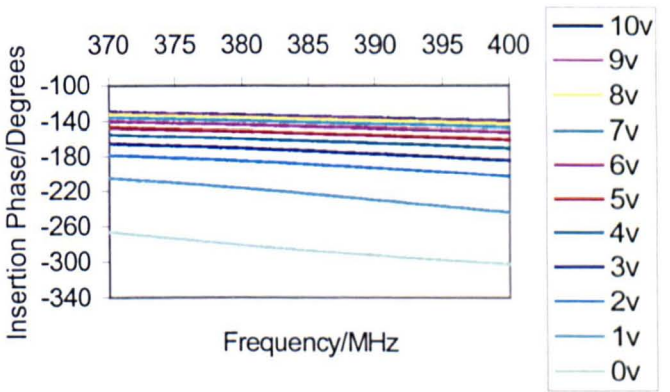

Graph 9.23 Insertion phase frequency response of two stage electronic phase shifter as a function of bias voltage.

The insertion phase frequency response characteristics of the two stage electronic phase shifter are similar to those of the single stage versions, the main differences being the magnitude of both the initial insertion phase and the phase swing. The insertion phase of the phase shifter at 10 V and 370 MHz is approximately -129°, this is almost exactly double that of the single stage phase shifter at the same conditions. This is to be expected since the two stage phase shifter is equivalent to connecting two single stages together.

At a frequency of 370 MHz the insertion phase at 10 and 0 V is approximately -129° and -266° respectively. Therefore an approximate phase swing of 136° is achievable with a 10 to 0 V dc voltage bias. (At higher frequencies the phase swing is slightly greater due parasitic inductances). Again it can also be seen from graph (9.23) that the insertion phase of the phase shifter increases by a small amount over the frequency range for a constant voltage. This increase in insertion phase with frequency may again be accredited to parasitic inductances. The non-linear increase in insertion phase with decreasing voltage is a direct result of the junction capacitance Vs reverse bias voltage of the diode, as illustrated in graph (9.16).

It was observed in section 9.4.2 that the insertion loss of the phase shifter was relatively constant over the voltage range 10 to 5.5 V. The corresponding change in insertion phase of the phase shifter over the same range is approximately 15°. Thus the two stage electronic phase shifter provides a relatively constant insertion loss phase swing of 15°.

9.4.4 Impedance Characteristics

The input impedance of the two stage electronic phase shifter was measured with the network analyser over the frequency range of interest as a function of bias voltage. The phase shifter was terminated at its output with a ZFL1000GH amplifier, which has an approximate 50Ω input. This termination is appropriate since the same amplifier is connected to the output of the phase shifter in the oscillator circuit. The impedance measurements of the phase shifter are independent of the terminating amplifiers AGC bias voltage or how its output is terminated. The input impedance characteristics as a function of frequency and voltage are illustrated in graphs (9.24) and (9.25) below:-

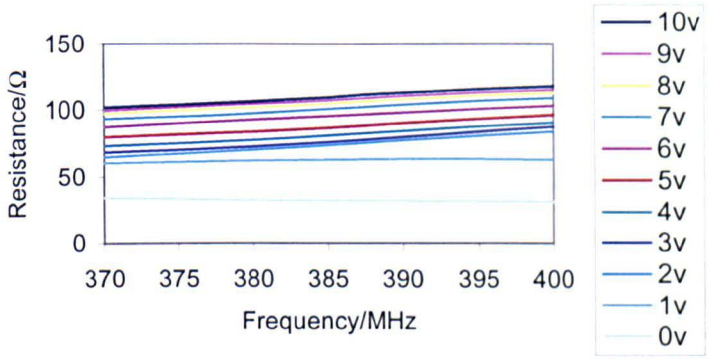

Graph 9.24 Input resistance of two stage electronic phase shifter as a function of frequency and bias voltage.

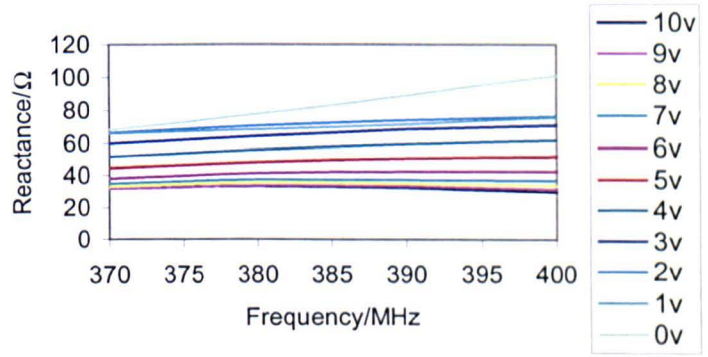

Graph 9.25 Input reactance of two stage electronic phase shifter as a function of frequency and bias voltage.

It can be seen from graphs (9.24) and (9.25) that the input impedance of the phase shifter varies both with bias voltage and frequency. The resistance shows a general increase with frequency at all voltages above 1 V and a decrease with decreasing voltage. The reactance is inductive and increases with decreasing voltage. There is also a slight variation with frequency.

9.4.5 Loading Characteristics

The insertion loss characteristics of the two stage electronic phase shifter terminated at its input and output ports with ZFL1000GH amplifiers were measured with the network analyser over the frequency range of interest as a function of voltage. The purpose of

characterising the phase shifter with this set up was to determine the effects of loading the phase shifter at its input and output ports with the actual components used in the oscillator circuit. The insertion loss frequency response of the amplifier loaded phase shifter as a function of bias voltage is illustrated in graph (9.26) below:-

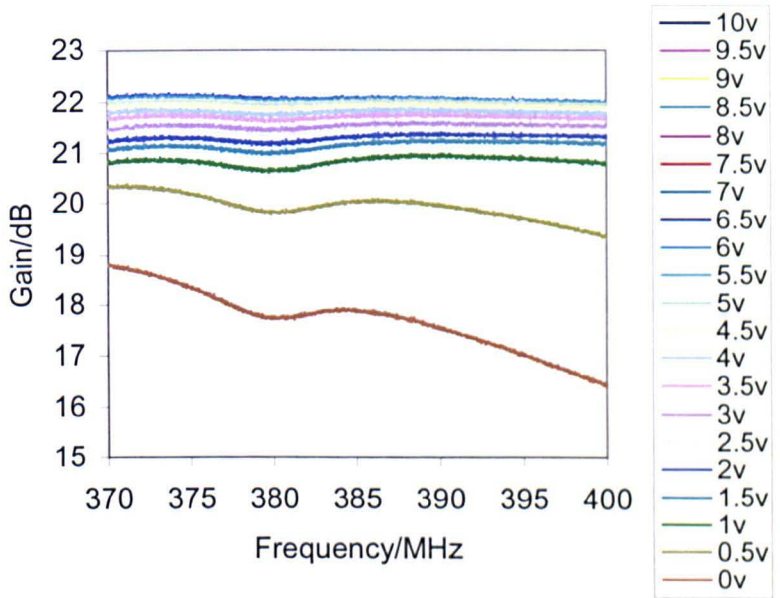

Graph 9.26 Insertion loss frequency response of amplifier loaded two stage electronic phase shifter as a function of bias voltage.

It can be seen from graph (9.26) that the insertion loss frequency response characteristics of the amplifier loaded two stage electronic phase shifter are similar to those of the isolated two stage phase shifter. This result is to be expected since the input and output impedances of the ZFL1000GH amplifier have been shown to be close to 50Ω (see section 9.3.3), which is, of course, the terminating impedance of the network analyser. The main difference is the gain of the frequency response. The amplifier connected to the input of the phase shifter is set with an AGC bias voltage of 1.47 V which means that the gain is approximately unity. The amplifier connected to the output of the phase shifter is set with an AGC bias voltage of just under 1 V which means that the gain is approximately 23 dB (see section 9.3.1). The variation of insertion loss with voltage at selected frequencies is illustrated in graph (9.27) below:-

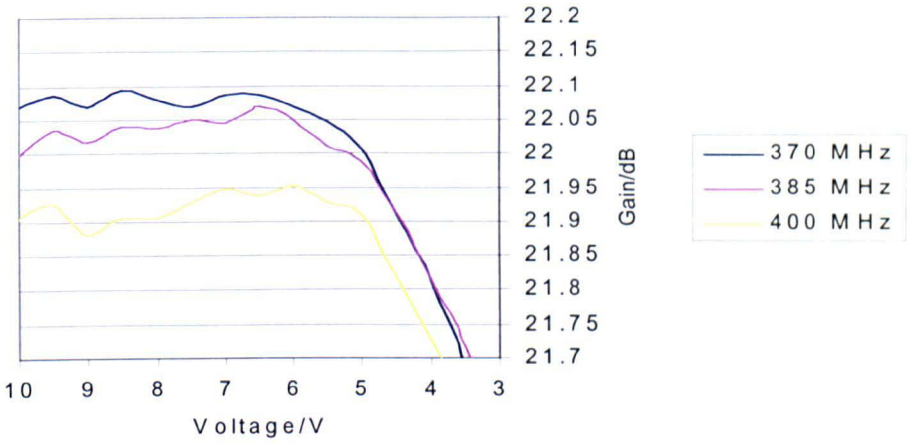

Graph 9.27 Insertion loss of amplifier loaded two stage electronic phase shifter as a function of bias voltage.

It can be seen from graph (9.27) that the variation of insertion loss with voltage is again similar to those of the isolated phase shifter. The only noticeable difference is that the insertion loss varies less over the frequency range. This can be observed in graph (9.26) by the flatness of the frequency response at higher voltages and in graph (9.27) by the smaller spread in insertion loss over the frequency range. The differences in the characteristics may also be partially effected by the uncertainty in the consistency of the measurements made on the phase shifter due to the presence of the voltage leads. The small differences may be explained by remembering that the phase shifter is subject to temperature effects and noise.

It has been shown that the general characteristics of the two stage electronic phase shifter are unaltered when it is loaded at its input and output ports with ZFL1000GH amplifiers. However, any comparisons made between the two set ups must be done so by remembering to take into account the effects that the voltage leads have on the consistency of measurements.

9.5 Electrical Properties of Oscillator Circuits

The previous sections focused on the characteristics of the individual elements of the on-line instrument, however, it is more important to determine the characteristics of the feedback oscillator circuit as a complete instrument. The following is a detailed analysis of the characteristics of the feedback oscillator circuit with the two stage electronic phase shifter.

9.5.1 Two Stage Electronic Phase Shifter Oscillator Circuit

The oscillator circuit consists of the ZFL1000GH amplifier, re-entrant cavity resonator and the two stage electronic phase shifter. The re-entrant cavity resonator is the frequency determining element of the feedback oscillator. The oscillator circuit is illustrated in figure (9.8) below:-

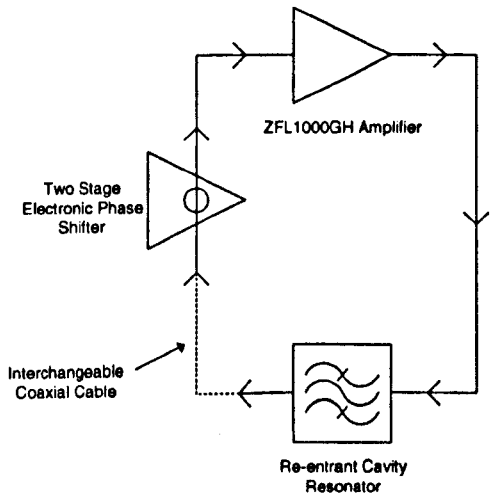

Figure 9.8 Schematic diagram of the two stage electronic phase shifter oscillator circuit.

The oscillator circuit was characterised with the network analyser in terms of loop gain and phase as functions of both the AGC bias voltage of the amplifier and bias voltage of the phase shifter. The loop gain and phase characteristics of the oscillator circuit were

measured with the network analyser by injecting an RF signal into the oscillator loop and measuring its response.

9.5.2 Varying AGC Bias Voltage of ZFL1000GH Amplifier

The oscillator circuit was characterised in terms of loop gain and phase as a function of the AGC bias voltage of the amplifier. The network analyser was inserted between the input to the phase shifter and the output of the interchangeable coaxial cable, as illustrated in figure (9.9) below:-

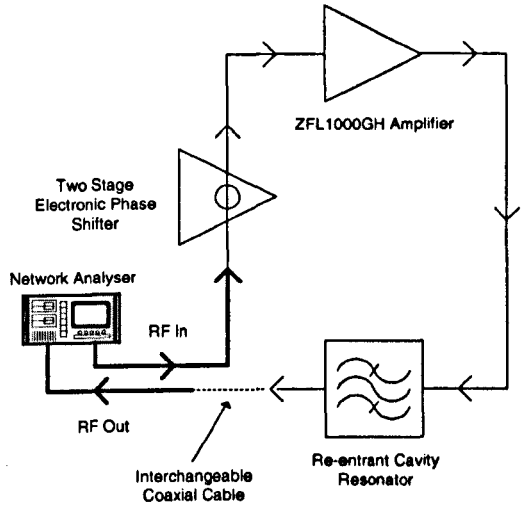

Figure 9.9 Schematic diagram of the two stage electronic phase shifter oscillator circuit.

The oscillator circuit was characterised under atmospheric conditions at room temperature. The resonance frequency of the cavity under these conditions lies between 394 and 395 MHz. The network analyser injects an RF signal level of -22dBm over the frequency range of interest. The length of the interchangeable coaxial cable was selected to make the total phase of the oscillator loop close to zero for an AGC bias voltage of 0 V to the amplifier and 10 V bias to the phase shifter.

The response of the oscillator circuit was measured as the AGC bias voltage to the amplifier was increased from 0 to 5 V. The voltage applied to the phase shifter was held at 10 V throughout the measurement. The gain response of the oscillator circuit is illustrated in graph (9.28) below:-

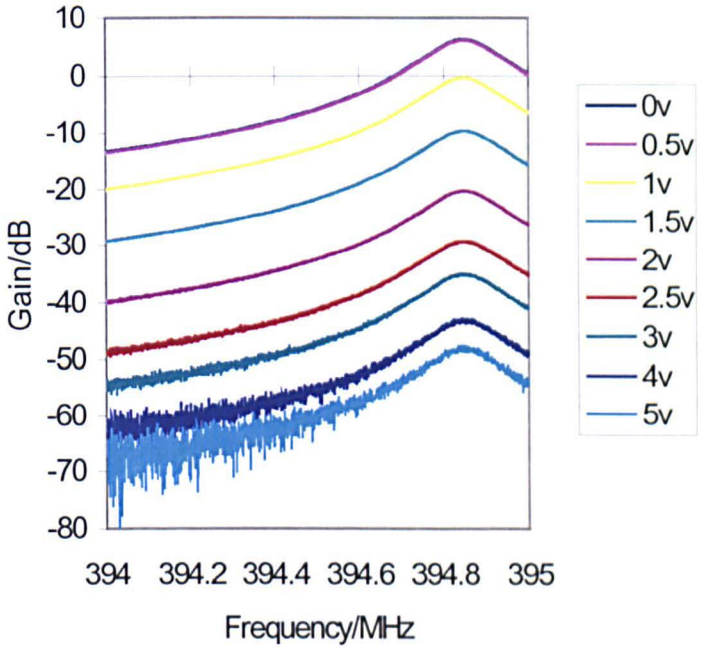

Graph 9.28 Gain response of the two stage electronic phase shifter oscillator circuit as a function of AGC bias voltage.

It can be seen from graph (9.28) that the resonant frequency of the cavity occurs at approximately 394.8 MHz. More importantly it can also be seen that only over the voltage range 0 to just under 1 V is the gain criterion for oscillation satisfied, that is, the gain of the loop is at least unity. Therefore the only region of interest in graph (9.28) is for AGC biases of between 0 and just under 1 V. The gain budget of the oscillator at AGC bias of 0V is approximately 6 dB.

The phase response of the oscillator circuit is illustrated in the form of a polar plot (magnitude and phase) in graph (9.29) below:-

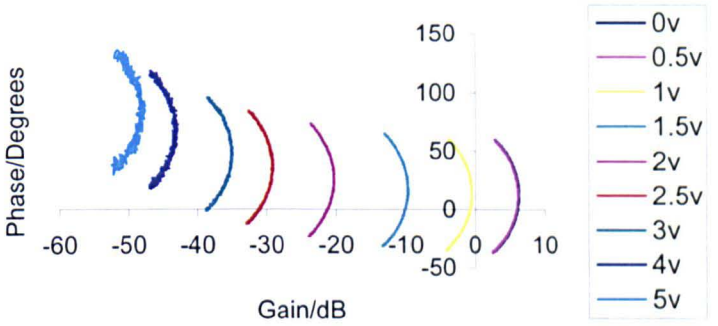

Graph 9.29 Polar plot of the two stage electronic phase shifter oscillator circuit as a function of AGC bias voltage.

The data plotted in the polar plot is taken over the frequency range 394.75 to 394.95 MHz. The frequency increases in the clockwise direction with the resonant frequency again occurring at the maximum gain point. It can be seen from graph (9.29) that as the AGC bias voltage to the amplifier is increased from 0 to 5 V the total phase of the oscillator loop moves away from the 0° point. This result is in agreement with the measurements made on the amplifier in section (9.3.2) where the insertion phase of the amplifier decreases with increasing AGC bias voltage. It should be noted that the total phase of the oscillator loop is approximately constant over the AGC bias voltage range of interest. These results are to be expected since each phase shifter is held at a bias of 10 V throughout the measurements.

9.5.3 Varying Bias Voltage of Two Stage Electronic Phase Shifter

The oscillator circuit was characterised in terms of loop gain and phase as a function of bias voltage of the two stage electronic phase shifter. The oscillator set up and measurement was the same as that illustrated in figure (9.9).

The response of the oscillator circuit was measured as the bias voltage to the phase shifter was reduced from 10 to 0 V. The AGC bias voltage applied to the amplifier was

held at 0 V throughout the measurement. The loop gain and phase response of the oscillator circuit is illustrated in the form of a polar plot in graph (9.30) below:-

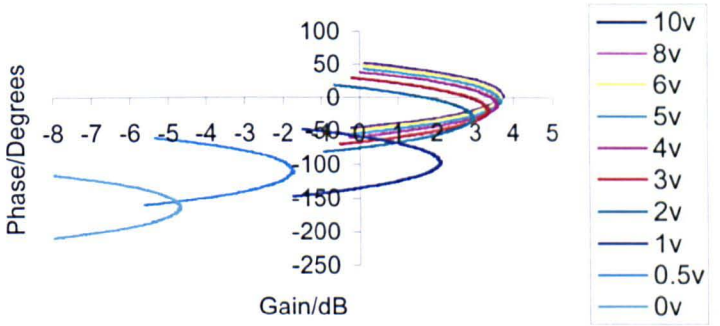

Graph 9.30 Polar plot of the two stage electronic phase shifter oscillator circuit as a function of phase shifter bias voltage.

The data plotted in the polar plot is again taken over the frequency range 394.75 to 394.95 MHz. It can be seen from graph (9.30) that as the bias voltage to the phase shifter is reduced from 10 to 0 V the total phase of the oscillator loop increases as expected with the resonant frequency passing through the 0° point. The total phase swing over this range is approximately 160°. This is in agreement with the measurements made on the two stage electronic phase shifter in section (9.4.3).

It can also be seen from graph (9.30) that the loop gain of the oscillator is fairly constant as the voltage is reduced to approximately 5 V. Below this the gain starts to decrease rapidly. This is also in agreement with the measurements made on the two stage electronic phase shifter in section (9.4.3). The oscillator loop gain response at resonance is compared to the insertion loss response of the two stage electronic phase shifter at the same frequency in graph (9.31) below:-

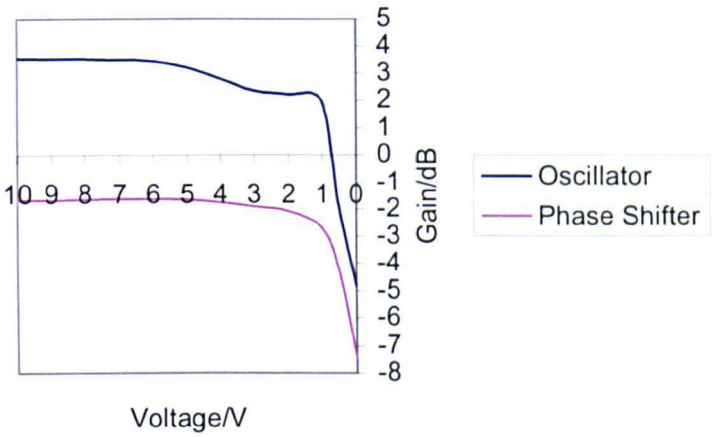

Graph 9.31 Comparison of oscillator loop gain response and insertion loss of two stage electronic phase shifter as a function of phase shifter bias voltage.

It can be seen from graph (9.31) that the loop gain response characteristics of the oscillator circuit are quite similar to those of the two stage electronic phase shifter. The small differences in the characteristics may be explained by considering that the input impedance of the amplifier is not quite 50Ω, any temperature differences when each measurement was made and also by objects in its proximity since it is not enclosed in an electromagnetically shielded case.

The reason the loop gain and phase characteristics of the oscillator circuit are similar to those of the two stage electronic phase shifter can be explained by considering the measurement set up, illustrated in figure (9.9). As illustrated the network analyser was inserted between the input to the phase shifter and the output of the interchangeable coaxial cable. With this set up the input to the phase shifter is connected to the network analyser and its output is connected to the input of the ZFL1000GH amplifier. The input impedance to the amplifier has been shown to be close to 50Ω, therefore the phase shifter is operating approximately as it would if it were being characterised in isolation.

The measurements made with this set-up are, however, frivolous due to the fact that when the network analyser is removed and the oscillator circuit is reconnected the input

to the phase shifter is once again connected directly (through the interchangeable coaxial cable) to the output coupling antenna of the cavity which will therefore cause the loop gain and phase characteristics of the oscillator circuit to differ from those presented above.

In order for the oscillator circuit's loop gain and phase characteristics to be the same as those of the phase shifter that is being used it is essential to isolate the phase shifter from the cavity. In order to achieve this a second ZFL1000GH amplifier, acting as a unity gain buffer, was added to the oscillator circuit. It is also essential that when characterising the oscillator circuit the network analyser be inserted at a point that will not effect the characteristics of the components it is connected to.

9.5.4 Two Stage Electronic Phase Shifter and Buffer ZFL1000GH Amplifier Oscillator Circuit

The oscillator circuit was set-up again with a second ZFL1000GH amplifier placed between the input to the phase shifter and the output of the re-entrant cavity. This second amplifier serves two purposes, the first is that with this set-up both the cavity and the phase shifter now *look into* 50Ω and the second is that it acts as a unity gain buffer between the cavity and the phase shifter.

The AGC bias to the amplifier was set to approximately 1.47 V in order to achieve unity gain. The oscillator circuit was set-up again with the second ZFL1000GH amplifier as illustrated in figure (9.10) below:-

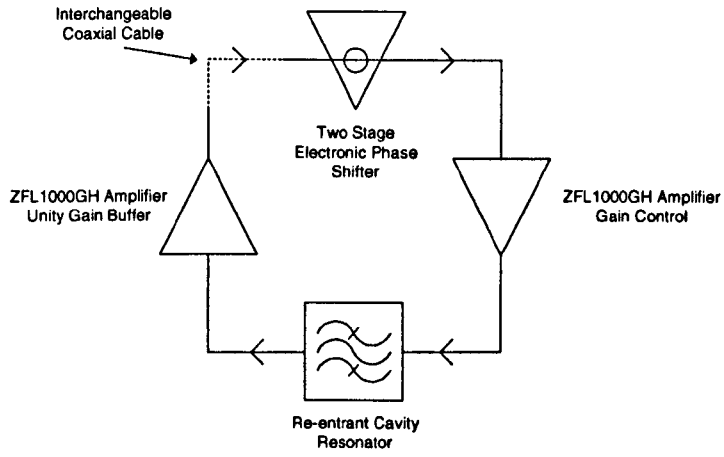

Figure 9.10 Schematic diagram of the two stage electronic phase shifter and second ZFL1000GH amplifier oscillator circuit.

The oscillator circuit was characterised in terms of loop gain and phase as a function of the bias voltage of the phase shifter. The loop gain and phase characteristics of the oscillator circuit were measured with the network analyser by injecting an RF signal into the oscillator loop and measuring its response.

9.5.5 Varying Bias Voltage of Two Stage Electronic Phase Shifter

The oscillator circuit was characterised in terms of loop gain and phase as a function of the bias voltage of the phase shifter. The network analyser was inserted between the input to the phase shifter and the output of the interchangeable coaxial cable, as illustrated in figure (9.11) below:-

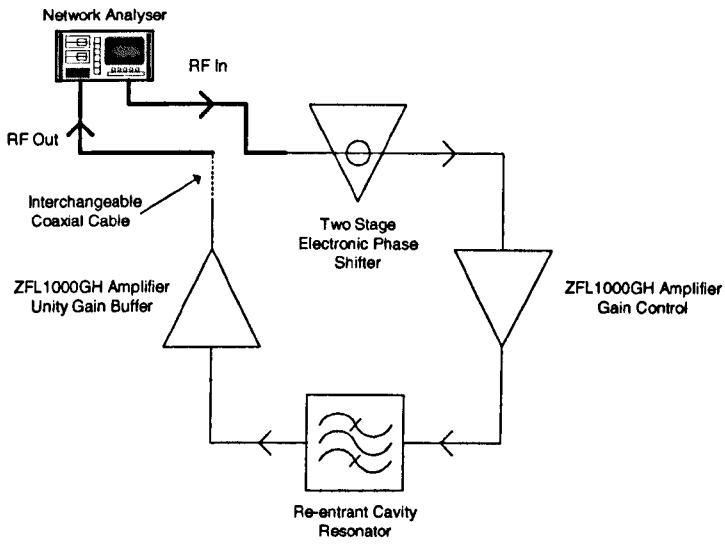

Figure 9.11 Schematic diagram of the two stage electronic phase shifter and second ZFL1000GH amplifier oscillator circuit.

The position of the network analyser within the circuit ensures that the input of the phase shifter *sees* 50Ω (the output impedance of the network analyser), the same as it would if the oscillator loop were closed.

The oscillator circuit was characterised under atmospheric conditions at room temperature. The resonance frequency of the cavity under these conditions lies between 394 and 395 MHz. The network analyser injects an RF signal level of -22dBm over the frequency range of interest. The response of the oscillator circuit was measured as the bias voltage to the phase shifter was reduced from 10 to 0 V. The AGC bias voltage applied to the gain control amplifier was held approximately 0.7 V throughout the measurement. The lengths of the interchangeable coaxial cable used were selected to make the total phase of the oscillator loop close to zero for an AGC bias voltage of approximately 0.7 V to the gain control amplifier and 1.5 V to the phase shifter. The loop gain and phase response of the oscillator circuit is illustrated in the form of a polar plot in graph (9.32) below:-

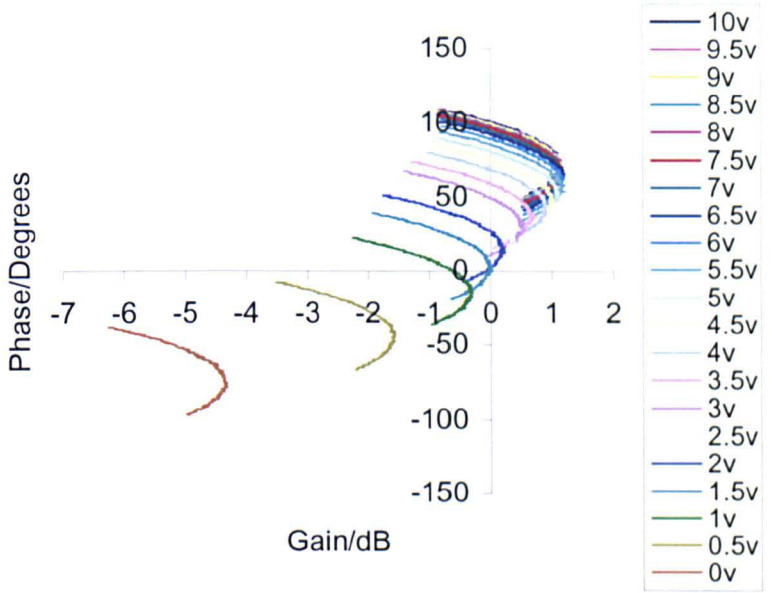

Graph 9.32 Polar plot of the two stage electronic phase shifter and second ZFL1000GH amplifier oscillator circuit as a function of phase shifter bias voltage.

The data plotted in the polar plot is taken over the frequency range 394.8 to 394.9 MHz. It can be seen from graph (9.32) that as the bias voltage to the phase shifter is reduced from 10 to 0 V the total phase of the oscillator loop increases as expected with the resonant frequency passing through the 0° point. The total phase swing over this range is approximately 155°. This is again in agreement with the measurements made on the two stage electronic phase shifter in section (9.4.3).

It can again be seen from graph (9.32) that the loop gain of the oscillator is fairly constant as the voltage is reduced to approximately 5.5 V. This is also in agreement with the measurements made on the two stage electronic phase shifter in section (9.4.3). The oscillator loop gain response at resonance is compared to the insertion loss response of the two stage electronic phase shifter at the same frequency in graph (9.33) below:-

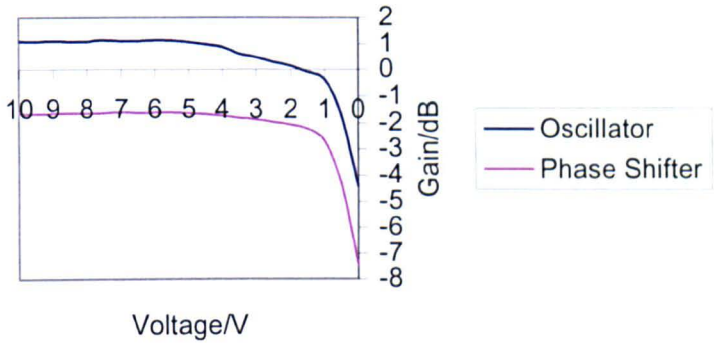

Graph 9.33 Comparison of oscillator loop gain response and insertion loss of two stage electronic phase shifter as a function of phase shifter bias voltage.

It can be seen from graph (9.33) that the loop gain response characteristics of the oscillator circuit are, as expected, similar to those of the two stage electronic phase shifter. The small differences in the characteristics may again be explained by the input impedance of the gain control amplifier not being quite 50Ω, any temperature differences between measurements and electromagnetic interference from objects in the phase shifters proximity.

With the buffer amplifier in the oscillator circuit the phase shifter is completely isolated from the cavity and the closed loop gain and phase characteristics should be the same as those measured with network analyser. (There may be a slight difference in the characteristics due to the positioning of the network analyser. Although the input of the phase shifter *sees* 50Ω, as required, it should do so through the interchangeable coaxial cable. When the oscillator loop is closed the interchangeable coaxial cable connects to the phase shifter and thus loads the phase shifter in a different manor to that of the network analyser resulting in a possible change in characteristics. This effect has been shown to be small when the unity gain buffer is used in the oscillator circuit.)

It has been shown that the oscillator circuit is capable of oscillating at the same resonant frequency as (or close to) the re-entrant cavity by virtue of the fact that the gain of the

system can be made at least unity and the total phase of the system can be made to pass through 0°.

9.6 Comparison of Oscillator and Re-entrant Cavity Frequency Measurements

The resonant frequency of the re-entrant cavity is compared with measurements made with two stage phase shifter oscillator circuit. The resonant frequency of the cavity was measured with the network analyser.

9.6.1 Two Stage Electronic Phase Shifter Oscillator Circuit

The resonant frequency of the cavity is compared with measurements made with two stage electronic phase shifter oscillator circuit. The comparisons are made with the cavity at three different conditions; atmospheric, 50 and 100 bar nitrogen. At each condition comparisons are made with the resonant frequency occurring at various phase angles i.e. for various total phase conditions of the oscillator loop.

The purpose of making comparisons at different cavity conditions and phase angles was to determine the effect that the phase shifter has on the accuracy of the oscillator circuit. The three cavity conditions ensure that the phase shifter operates between approximately 394.8 MHz (atmospheric) and 384.5 MHz (100 bar nitrogen). The various total phase conditions simulate a change in insertion phase of the cavity and ensure that the phase shifter operates over its operating range i.e. finding the resonance of the cavity at different bias voltages.

The oscillator circuit again consists of the gain control ZFL1000GH amplifier, the unity gain buffer ZFL1000GH amplifier, the re-entrant cavity resonator and the two stage electronic phase shifter. The oscillator circuit is illustrated in figure (9.12) below:-

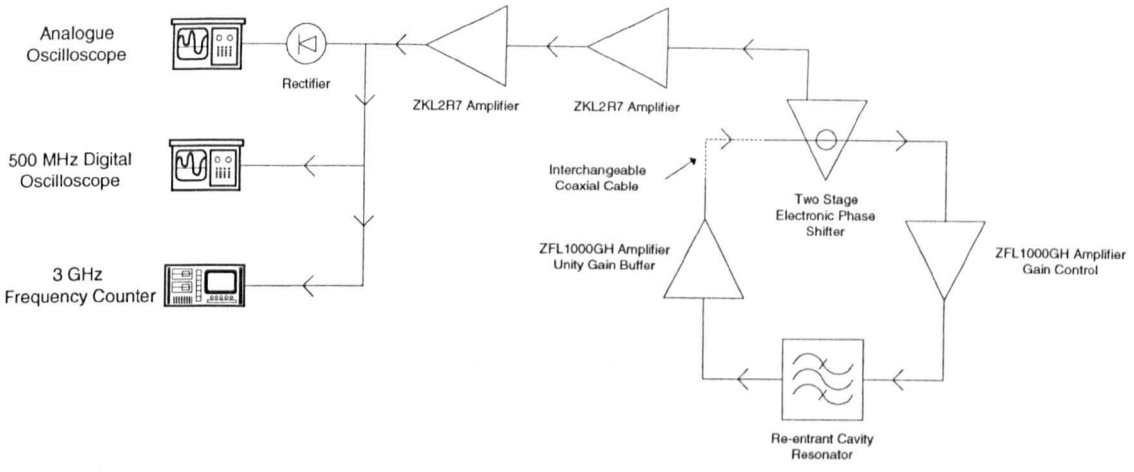

Figure 9.12 Schematic diagram of the two stage electronic phase shifter oscillator circuit.

In order to ensure the frequency of the oscillator is the same as that of the resonant frequency of the cavity it is necessary to know when the total phase of the oscillator loop is 0°. To accomplish this a small portion of the oscillator signal is sampled and rectified to dc. As the total phase of the loop passes through 0° the signal level within the loop reaches a maximum, this 0° total phase condition is therefore indicated by a maximum in the rectified dc.

The RF signal sampled from the oscillator is amplified by two ZKL2R7 amplifiers before being rectified and observed on an analogue oscilloscope. (The ZKL2R7 is a Mini-Circuits broadband linear gain amplifier that delivers approximately 24 dB of gain over a bandwidth of 2.7 GHz). The sampled RF signal is also observed on a 500 MHz digital oscilloscope and a 3 GHz frequency counter. The buffer ZFL1000GH amplifier is set to an AGC bias of 1.47 V throughout the measurements.

The measurement procedure for the oscillator circuit is as follows:

1. Set phase shifter bias to 10 V and gain control amplifier AGC bias to 5 V.
2. Reduce AGC bias voltage of gain control amplifier until a signal appears on the 500 MHz digital oscilloscope.

3. Reduce phase shifter bias voltage until a maximum signal is observed on the analogue oscilloscope.
4. Vary the AGC bias voltage of gain control amplifier until the smallest possible signal is observed on the 500 MHz oscilloscope.
5. Vary the phase shifter bias voltage until a maximum signal is observed on the analogue oscilloscope.
6. Read the oscillation frequency from the frequency counter.

9.6.2 Results

The results of the comparisons between the resonant frequency of the cavity and the two stage electronic phase shifter oscillator circuit at various cavity conditions and phase conditions are presented in table (9.3) below:-

Atmospheric					
Phase Shifter Bias/V	8	7.1	5.3	3	1.5
Frequency Error/kHz	+ 0.6	+ 1.8	+ 8.7	+ 9	+ 2.4
50 bar nitrogen					
Phase Shifter Bias/V	7.6	6.1	4.7	3.3	1.5
Frequency Error /kHz	+ 1.1	+ 5.9	+ 12.6	+ 14.2	+ 6.5
100 bar nitrogen					
Phase Shifter Bias/V	9.8	5.6	4	2.6	0.6
Frequency Error /kHz	+ 0.5	+ 8.3	+ 14.6	+ 12.7	+ 18.3

Table 9.3 Results of comparisons between the resonant frequency of the cavity and the two stage electronic phase shifter oscillator circuit.

The results obtained at various total phase conditions, or rather, phase shifter bias voltages, were done so by adjusting the lengths of the interchangeable coaxial cable used in the oscillator circuit. Various lengths of 50Ω coaxial cable were constructed for this

purpose. The results presented are the average of ten repeated measurements taken at room temperature.

The frequency error data in table (9.3) is the difference between the oscillator and the cavity frequencies. The positive values indicate that the oscillator readings were consistently higher than the cavity. It can seen from the data that the frequency error is better than 2 kHz when the oscillator operates with a phase shifter bias voltage of greater than 7 V. As the oscillator operates at lower phase shifter bias voltages the frequency error varies by large amounts.

The results can be explained by considering the loop gain characteristics of the oscillator circuit as a function of the phase shifter bias voltage (see section (9.5.3)). The loop gain characteristics of the oscillator circuit were shown to be similar to the insertion loss characteristics of the phase shifter, that is the insertion loss is fairly constant with bias voltage from 10 to approximately 5.5 V but increases rapidly as the voltage is reduced towards 0 V. It can be shown that it is the shape of the response of the insertion loss Vs phase shifter bias voltage curve that determines the magnitude and sign of the error in the oscillator measurements.

This can be demonstrated by considering the magnitude of the detected dc signal of the oscillator as the measurement procedure is followed. If the insertion loss of the phase shifter is absolutely constant with bias voltage then the detected dc signal will have exactly the same response characteristics as the cavity, with the maximum dc occurring at the true resonance peak of the cavity. The response of such a system is illustrated in figure (9.13) below:-

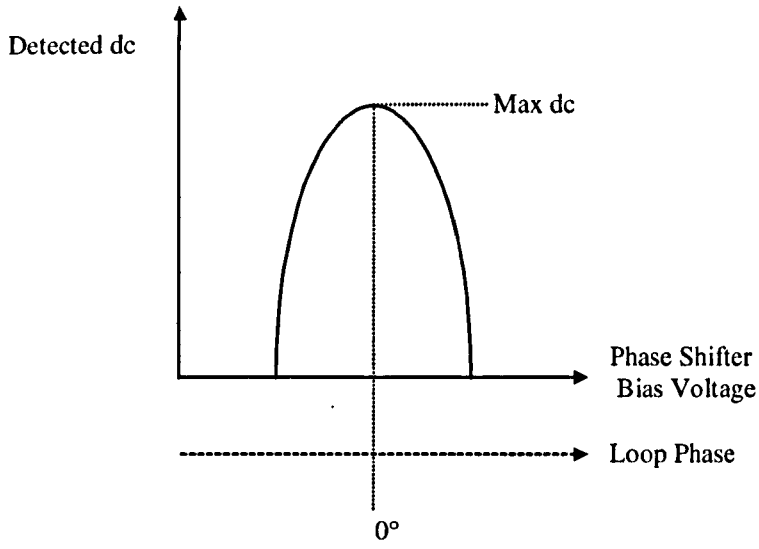

Figure 9.13 Ideal response of detected dc signal in oscillator circuit.

However if the insertion loss of the phase shifter increases say, with decreasing phase shifter bias voltage then the detected dc signal will have a different response characteristic to that of the cavity. This is illustrated in figure (9.14) below:-

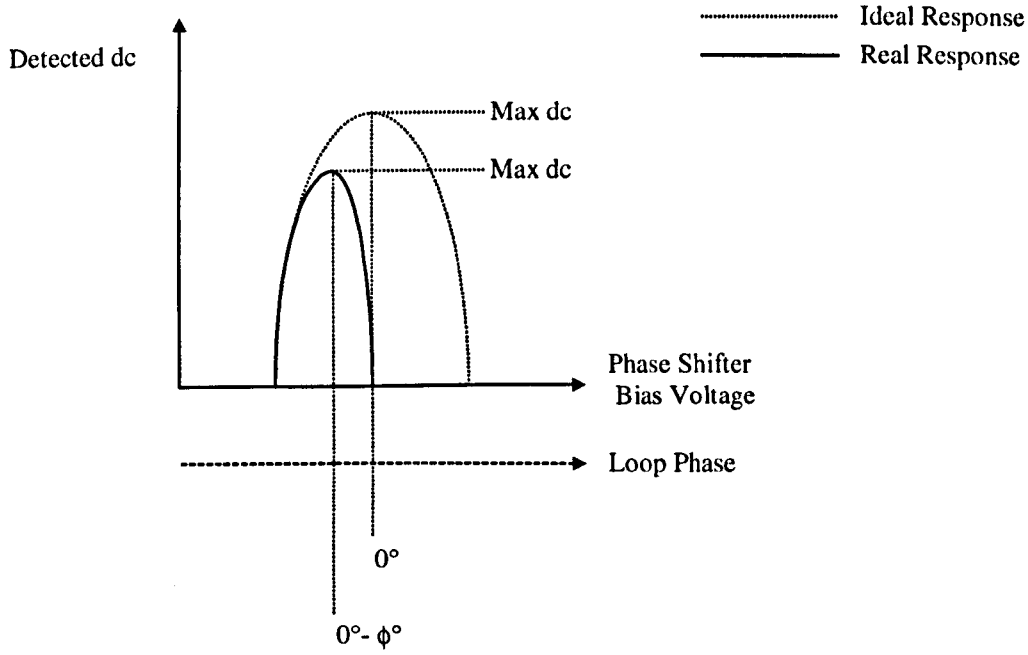

Figure 9.14 Ideal and real response of detected dc signal in oscillator circuit.

It can be seen from figure (9.14) that if the insertion loss of the phase shifter increases with decreasing voltage then the effect is that the detected dc maximum is pulled in such a way that the peak occurs before that of an ideal response system (the opposite of this is true for a phase shifter with decreasing insertion loss with decreasing bias voltage). The amount that the detected dc maximum is pulled is dependent on the shape of the response of the insertion loss Vs phase shifter bias voltage curve. As a result of this the oscillator will oscillate at a frequency that is $\phi°$ away from the true resonant frequency of cavity, as illustrated in figure (9.15) below:-

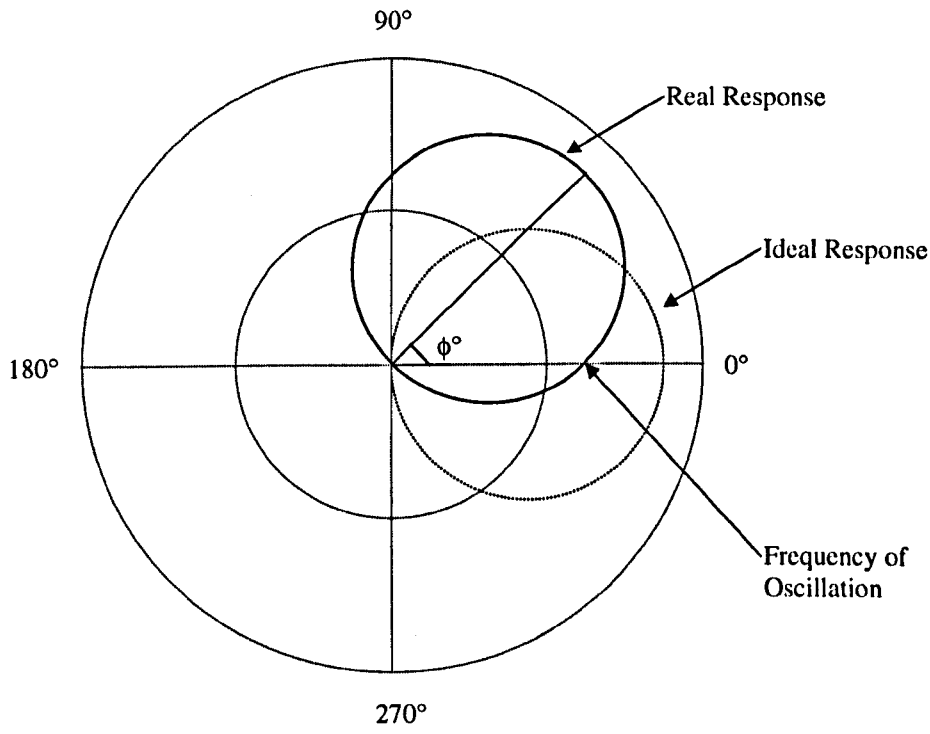

Figure 9.15 Polar Chart of ideal and real response of oscillator circuit.

It can be seen from figure (9.15) that the oscillator circuit will oscillate at a frequency that is $\phi°$ short of 0°. In this case where it has been assumed that the insertion loss of the phase shifter increases with decreasing bias voltage the frequency of the oscillator circuit will be higher than the true resonant frequency of the cavity. The angle ϕ, and

consequently, the frequency error is dependent on the shape of the response of the insertion loss Vs phase shifter bias curve. If the insertion loss of the phase shifter varies linearly with decreasing bias voltage then the angle ϕ and the frequency error will be directly proportional to the gradient of the insertion loss Vs phase shifter bias curve. If, however, the insertion loss is a more complicated function then the frequency error will be a function of the combination of the phase shifter response and the cavity response.

The results in table (9.3) may now be interpreted by observing the loop gain characteristics of the oscillator circuit as a function of the phase shifter bias voltage. The oscillator circuit was characterised at atmospheric (approximately 394.8 MHz) conditions with the network analyser in terms of loop gain as a function of the bias voltage of the phase shifter. The network analyser injects an RF signal level of -22dBm over the frequency range of interest. The loop gain characteristics are illustrated with the atmospheric frequency errors from table (9.3) in graph (9.34) below:-

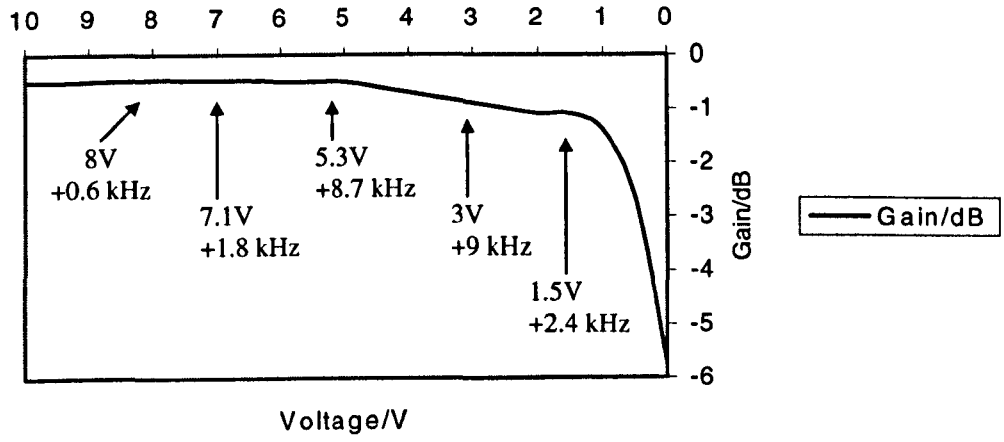

Graph 9.34 Loop gain response of the two stage electronic phase shifter oscillator circuit as a function of phase shifter bias voltage.

It can be seen from graph (9.34) that the magnitude and sign of the atmospheric condition frequency errors are in good agreement with the shape of the response of the loop gain Vs phase shifter bias curve of the oscillator circuit. The magnitude and sign of

the 50 and 100 bar nitrogen condition frequency errors are also in good agreement with the atmospheric measurements. This is to be expected since the characteristics of the phase shifter are similar over the frequency range of operation (see section (9.4.2)).

It should be noted that any comparisons made between the accuracy of the oscillator circuit and the shape of the response of the loop gain vs phase shifter bias voltage curve must be made bearing in mind that there may be small differences between the measured loop gain response and the actual loop gain response characteristics due to the positioning of the network analyser within the oscillator circuit (this effect has been shown to be small when the unity gain buffer is used in the oscillator circuit). The characteristics of the phase shifter may also vary with each set-up due to temperature effects and also due to the fact that it is not enclosed in an electromagnetically shielded case. As a result it is difficult to quantify the effect of the shape of the response of the loop gain curve on the frequency errors with graph (9.34), however, it illustrates the typical relationship between frequency error and shape of the response of the loop gain curve.

It has been shown that the oscillator circuit with the two stage electronic phase shifter is capable of oscillating to within approximately 0.5 kHz ($\approx$ 1.25 ppm) of the true resonant frequency of the re-entrant cavity. This is greater than the aimed accuracy of 1 kHz ($\approx$ 2.5 ppm). However this accuracy is only achievable over a limited range of operating conditions of the phase shifter, approximately 10 to 8 V. The phase swing of the phase shifter over this voltage range is approximately 3°, which is far less than the required phase swing of 20° (20° is the approximate insertion phase change of the cavity as it is pressurised from atmospheric conditions to 100 bar nitrogen). It has been shown that it is the shape of the response of the insertion loss vs phase shifter bias curve that determines the magnitude and sign of the error in the oscillator measurements.

The oscillator measurements were verified at each phase set-up by measuring the response of the oscillator circuit with the network analyser. At each phase set up the

oscillator frequency was measured, then the network analyser was used to measure the loop gain and phase characteristics. The network analyser injects an RF signal level of -22dBm over the frequency range of interest. An illustration of a typical network analyser plot is presented with the frequency measurements below, plot (a) indicates the resonant frequency position and plot (b) indicates the oscillator frequency (or 0° phase position).

3 V

Resonant Frequency/MHz = 394.857,15
Oscillator Frequency/MHz = 394.866,15
Difference/kHz = + 9

Oscillator Polar Plots:

(a) Resonant Frequency

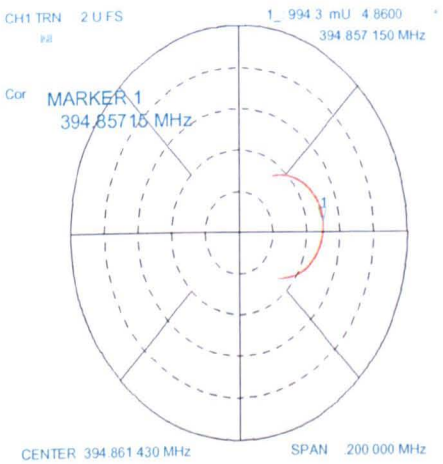

(b) 0° Phase Position

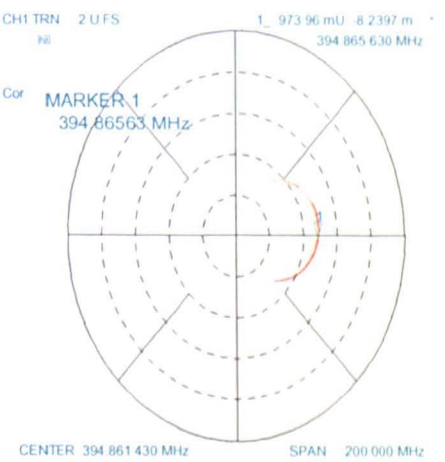

It can be seen from plot (a) that the resonant frequency occurs at approximately 4.9° before the 0° phase position. Plot (b) illustrates the approximate 0° phase frequency that the oscillator circuit should oscillate at. It can be seen that the marker frequency is in

good agreement with the measured oscillator frequency. The ratio of the phase angle to frequency error is approximately 0.54°/kHz.

The above results verify the oscillator measurements and demonstrate that it is the shape of the response of the insertion loss vs phase shifter bias curve that determines the magnitude and sign of the error in the oscillator measurements.

9.6.3 Effect of Insertion Loss Phase Shifter Response on Frequency Errors

In order to establish the exact relationship between the frequency error and the shape of the response of the loop gain vs phase shifter bias voltage curve of graph (9.34) it would be necessary to measure the loop gain characteristics of the oscillator circuit with the network analyser connected between the input to the interchangeable coaxial cable and the output of the buffer amplifier and fit a function to its response and then combine this with the cavity response function. However, it is possible to obtain an approximate idea of what the relationship between frequency error and gradient of the loop gain curve would be for a linear insertion loss response by considering one of the phase set up conditions. This determines the required flatness of insertion loss of a phase shifter for a 1 kHz aimed oscillator accuracy. At a particular phase set up condition with one of the phase shifters the loop gain response of the oscillator circuit was considered linear from 10 to 9 V with a gradient of -0.09 and a corresponding frequency error of -9.2 kHz. Therefore in order to obtain a 1 kHz oscillator accuracy the flatness of the response of the phase shifter should be ± 0.005 dB. This result is in reasonable agreement with the insertion loss characteristics of the two stage electronic phase shifter (see section (9.4.2)) and the comparisons of the two stage electronic phase shifter oscillator and re-entrant cavity frequency measurements (see section (9.6.1)).

If a function could be fitted to the three dimensional data of any of the phase shifters over the operating temperature range then it would be possible to make corrections for

the non-ideal behaviour of the phase shifter and thus, obtain the required accuracy of frequency measurements.

It has been demonstrated that it is the shape of the response of the insertion loss vs phase shifter bias curve that determines the magnitude and sign of the error in the oscillator measurements. The oscillator measurements have also been verified with network analyser plots on the oscillator circuit set-up at each phase.

It was also found that the loop gain characteristics of the oscillator circuit without the buffer amplifier differs from those of the two stage electronic phase shifter and are dependent on the length of coaxial cable between the output of the cavity and the input to the phase shifter. Therefore, in order for the oscillator circuit's loop gain and phase characteristics to be the same as those of the phase shifter it is essential to isolate the phase shifter from the cavity. It is also necessary to characterise the oscillator circuit at a point where the insertion of the network analyser will not effect the characteristics of the components it is connected to. More importantly, with this set-up it is possible that the electrical properties of the cavity, and consequently the resonant frequency, have been changed as it loaded with the interchangeable coaxial cable and the phase shifter. Thus any comparisons between the oscillator frequency and the resonant frequency are subject to error.

9.7 Electrical Characteristics of Rectifier Circuit

The characteristics of the rectifier circuit used in the oscillator circuits were measured with a 1GHz Marconi signal generator and a 500 MHz oscilloscope. The rectifier circuit is illustrated in figure (9.16) below:-

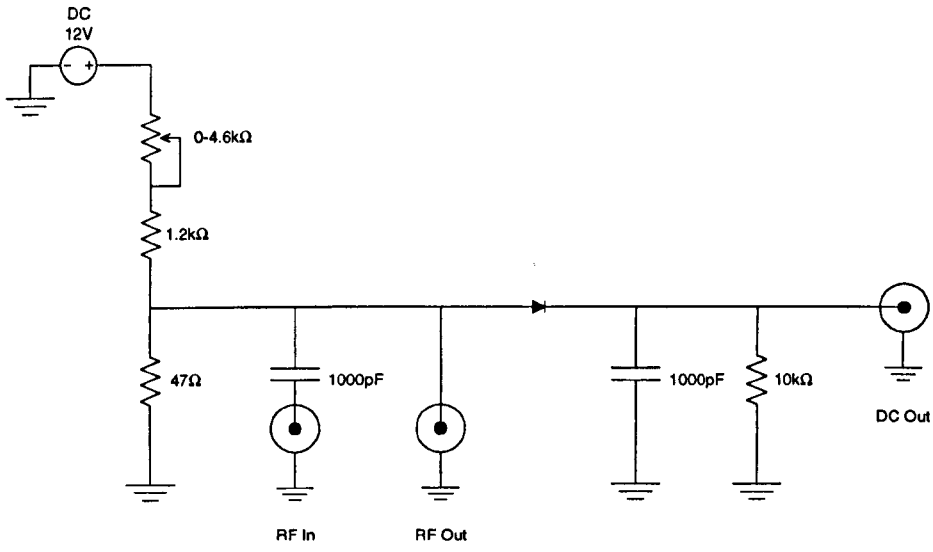

Figure 9.16 Circuit diagram of rectifier.

The rectifier was constructed and mounted in an electromagnetically shielded case. The diode used was a Siemens BAT 15-099 Silicon Dual Schottky Diode, which has a low reverse voltage, (320 mV), and a operational frequency of up to 12 GHz. The diode is forward biased to reduce the reverse voltage so that it will conduct at small signal levels. The amount of bias can be varied from approximately 0.09 to 0.45 V with the potentiometer. The 1000 pF capacitors are Murata UHF surface mount capacitors. The capacitor at the RF input acts as a dc block for the biasing voltage. The RF output port is connected to the 500 MHz oscilloscope and the 3 GHz frequency counter in the oscillator circuit.

9.7.1 Characteristics of the Rectifier Circuit

The rectifier circuit was characterised with a 1 GHz Marconi frequency generator and the precision multimeter. The frequency generator injects an RF signal into the rectifier and the rectified signal is observed on the precision multimeter (the RF output port was not connected to any instrument). The results for various RF signal levels at minimum

and maximum bias conditions are illustrated in graph (9.35) below (the superimposed bias voltage has been corrected for in the graph):-

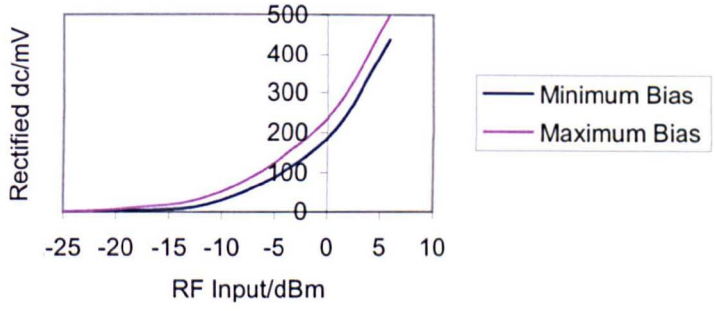

Graph 9.35 Rectified dc for minimum and maximum bias as a function of RF input.

It can be seen from graph (9.35) that by increasing the forward bias the diode starts to conduct at lower signal levels. It can also be seen that at maximum bias conditions the rectified dc output for a 6 dBm RF input is approximately 500 mV. Since the input to the rectifier is approximately 50Ω the input levels in dBm can be easily converted to V_{rms}, or V_{p-p} and it can be seen that the output dc is approximately 80% of the peak input signal. (This figure will obviously drop with lower signals used). The output of the rectifier will, obviously be lower if the oscilloscope and frequency counter are connected to the RF output port.

9.7.2 Characteristics of the Two Stage Electronic EMS phase shifter and Rectifier Circuits

In order to determine the signal level within the oscillator loop the two stage electronic EMS phase shifter and the rectifier circuit were characterised in terms of RF input to the phase shifter and dc output from the rectifier. The set-up is illustrated in figure (9.17) below:-

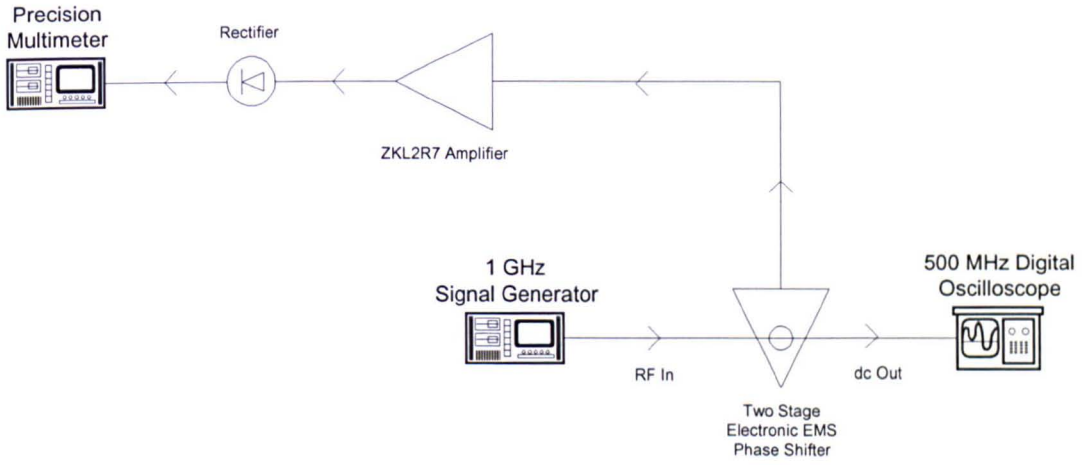

Figure 9.17 Schematic diagram of the two stage electronic EMS phase shifter and rectifier circuit.

The set-up illustrated in figure (9.16) was designed to simulate that of the oscillator circuit. The phase shifter is loaded at its input and output ports with 50Ω, as it is in the oscillator circuit. The signal generator injects an RF signal into the phase shifter and the sampled signal is rectified and observed on the precision multimeter. The oscilloscope provides a 50Ω termination to the output signal from the phase shifter. The set-up was characterised over a range of frequencies and signal levels. The results are illustrated in graph (9.36) below:-

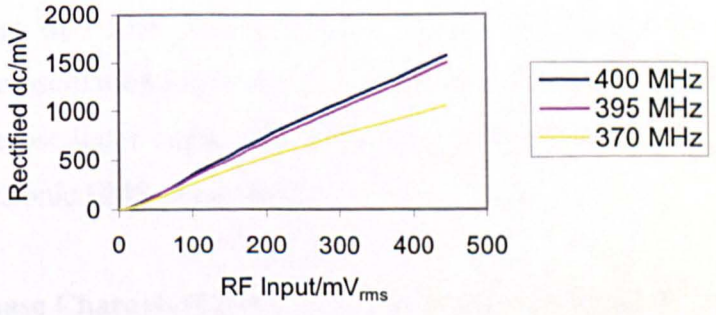

Graph 9.36 Rectified dc as a function of RF input and frequency.

The frequency selectivity of the capacitive coupling to the phase shifter is illustrated in graph (9.36). As the frequency decreases the reactance of the capacitive coupling increases and reduces the sampled signal. The frequency selectivity of the capacitive coupling to the phase shifter does not effect the oscillator circuit since the changes in frequency are of the order of kilohertz. The phase shifter bias voltage was held at 10 V throughout the measurements. The bandwidth of the oscilloscope is 500 MHz, which means that at 400 MHz it only reads approximately 80% of the input signal. Therefore all the readings taken on the oscilloscope were corrected to account for this bandwidth drop-off.

The relationship illustrated in graph (9.36) between RF input to the phase shifter and rectified dc enables the RF signal level within the oscillator circuit to be calculated. Once the RF signal level going into the phase shifter is known it is possible to determine the signal level at any point in the oscillator loop.

9.8 Characteristics of Two Stage Electronic EMS Phase Shifter Oscillator

The two stage electronic EMS phase shifter oscillator was characterised as a function of both the bias voltage of the phase shifter and AGC bias voltage of the gain control amplifier in order to determine the voltage steps required of each control unit to achieve a frequency change of 1 kHz. It is essential to know the relationship between voltage step and change in oscillation frequency of the oscillator if any computer control is to be implemented. The oscillator circuit was the same as that in section (9.6.1) except with the two stage electronic EMS phase shifter.

9.8.1 Phase Characteristics of Two Stage Electronic EMS Phase Shifter Oscillator

In order to determine the relationship between phase and frequency the oscillator circuit was characterised with the network analyser. The AGC bias voltage applied to the gain

control amplifier and the unity gain buffer amplifier was held at approximately 0.5 V and 1.47 V respectively throughout the measurements. The lengths of the coaxial cables used were selected to make the total phase of the oscillator loop close to zero for an AGC bias voltage of approximately 0.5 V to the gain control amplifier and 10 V to the phase shifter. The phase characteristics of the oscillator circuit were measured at atmospheric conditions with the network analyser by injecting an RF signal into the oscillator loop and measuring its response. The network analyser injects an RF signal level of -22dBm over the frequency range of interest. The phase characteristics of the oscillator circuit are illustrated in plot (9.2) below:-

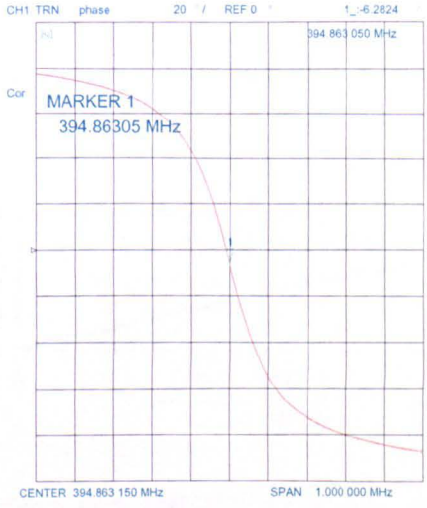

Plot 9.2 Network analyser plot of the phase characteristics of the two stage electronic EMS phase shifter oscillator circuit.

The marker in plot (9.2) indicates the resonant frequency as 394.863,05 MHz. It can be seen that at resonance the total phase of the oscillator loop is approximately -6.2°. This is the expected phase response of the oscillator circuit when the phase shifter bias voltage is 10 V. The relationship between phase and frequency over the linear region of plot (9.2) is illustrated in table (9.4) below:-

Frequency/MHz	Phase/Degrees	Phase Change From Resonance/Degrees
394.863,05 (Resonance)	-6.2	0
394.862,05	-5.56	0.64
394.861,05	-4.85	1.35
394.858,05	-2.98	3.22
394.853,05	0.28	6.48
394.813,05	24.02	30.22

Table 9.4 Relationship between phase and frequency over the linear region of plot (9.2) for the two stage electronic EMS phase shifter oscillator circuit.

The data from table (9.4) is illustrated in graph (9.37) below:-

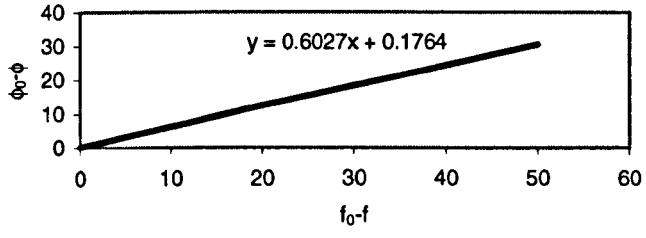

Graph 9.37 Relationship between phase and frequency over the linear region of plot (9.2) for the two stage electronic EMS phase shifter.

It can be seen from graph (9.37) that the phase changes with frequency by approximately 0.6°/kHz. This means that to achieve a 1 kHz accuracy in frequency the phase must be known to within 0.6°.

9.8.2 Sensitivity of Two Stage Electronic EMS Phase Shifter Oscillator to Phase Shifter Bias Voltage

In order to determine the phase shifter bias voltage step required to achieve a 0.6° change in phase the phase characteristics of the oscillator circuit were measured at atmospheric conditions with the network analyser as the bias voltage to the phase shifter was reduced from 10 to 0 V.

The relationship between phase shifter bias voltage and total phase of the oscillator loop is illustrated in graph (9.38) below:-

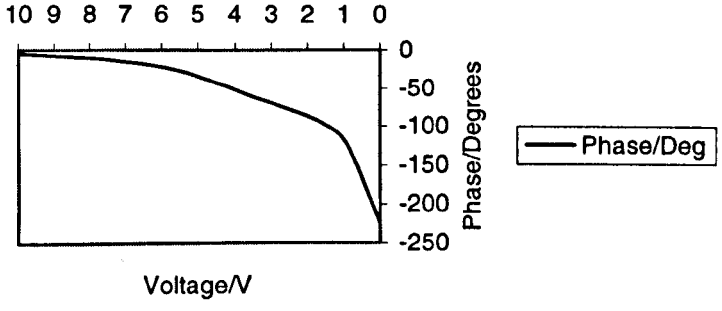

Graph 9.38 Relationship between phase shifter bias voltage and total phase of the oscillator loop.

It can be seen from graph (9.38) that, as expected, the total phase of the oscillator loop increases as the voltage to the phase shifter is reduced. The exponential increase in phase is in agreement with the diode capacitance curve (see section (9.4.1)). It was shown that the capacitance of the diode increased exponentially with decreasing voltage bias, therefore it should be expected that the insertion phase of the phase shifter should behave similarly.

The total phase of the oscillator loop was recorded at 0.5 V intervals as the voltage was decreased. The required voltage step of the phase shifter in order to achieve a 0.6° change in phase is illustrated in graph (9.39) below:-

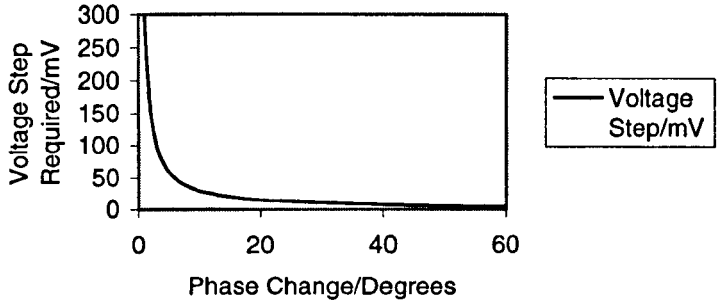

Graph 9.39 Phase shifter voltage step required for a 0.6° change in frequency.

The 'Phase Change' axis of graph (9.39) corresponds to the voltage bias of the phase shifter i.e. a low phase change corresponds to a high voltage bias. It can be seen from graph (9.39) that the voltage step required to achieve a 0.6° change in frequency varies in accordance with the phase change (phase shifter voltage bias). If the phase shifter is operated at around 10 V then the required voltage step of the phase shifter must be less than approximately 300 mV. The required voltage step decreases exponentially with increasing phase change (phase shifter voltage bias) and must be less than approximately 5 mV around a bias voltage of 0 V. These voltage steps are easily achievable with computer controlled hardware.

In order to confirm these results the relationship between the phase shifter bias voltage and oscillator frequency was determined. The voltage step required to achieve a 1 kHz change in frequency was determined with the oscillator circuit was set up in the same way as section (9.6.3) at atmospheric conditions and the frequency reading was observed as the bias voltage to the phase shifter was reduced from 10 to 1 V. In order to cover the voltage range of the phase shifter bias two oscillator phase set-ups were studied. The

first set-up was the 9.5 V set-up which operated between 10 and 4 V and the second was the 3.5 V set-up which operated between 4 and 1 V.

The relationship between phase shifter bias voltage and oscillator frequency for the 9.5 V and 3.5 V set-ups are illustrated in graphs (9.40) and (9.41) below:-

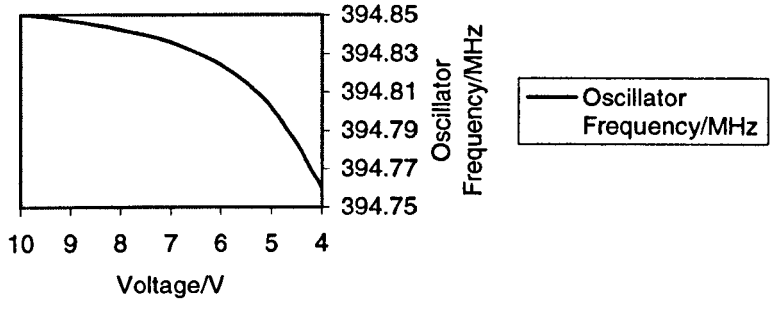

Graph 9.40 Relationship between phase shifter bias voltage and oscillator frequency for 9.5 V phase set-up.

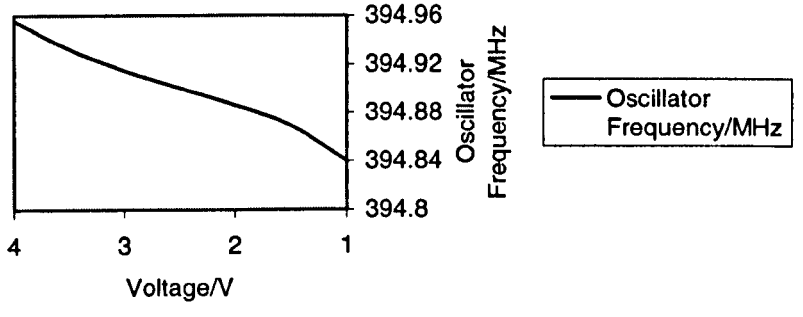

Graph 9.41 Relationship between phase shifter bias voltage and oscillator frequency for 3.5 V phase set-up.

It can be seen from graph (9.40) that, as expected, the frequency reading of the oscillator decreases as the voltage to the phase shifter is reduced. This exponential decrease in frequency is a direct result of the relationship between phase shifter bias voltage and total phase of the oscillator loop. Graph (9.41) represents the continuing trend of the oscillator frequency over the lower range of voltages. (The measurements for the 3.5 V

set-up were performed at a different room temperature to those of the 9.5 V set-up, hence the different frequency values).

The required voltage step to the phase shifter in order to achieve a 1 kHz change in frequency was calculated using the data from the 9.5 V and 3.5 V phase set-ups. The oscillator frequency was recorded at 0.5 V intervals as the voltage was decreased. The results are illustrated in graph (9.42) below:-

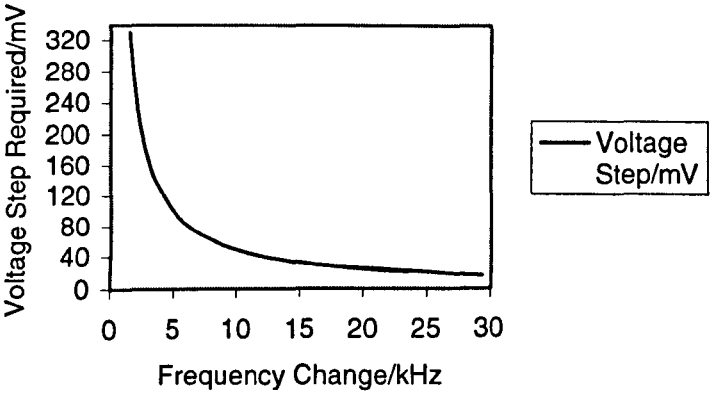

Graph 9.42 Phase shifter voltage step required for a 1 kHz change in frequency.

The 'Frequency Change' axis of graph (9.42) corresponds to the voltage bias of the phase shifter i.e. a low frequency change corresponds to a high voltage bias. It can be seen from graph (9.42) that the voltage step required to achieve a 1 kHz change in frequency varies in accordance with the frequency change (phase shifter voltage bias). If the phase shifter is operated at around 10 V then the required voltage step of the phase shifter must be less than approximately 330 mV. The required voltage step decreases exponentially with increasing frequency change (phase shifter voltage bias) and must be less than approximately 17 mV around a bias voltage of 1 V. These voltage steps are again easily achievable with computer controlled hardware.

The detected dc of the oscillator circuit was of the order of 50 to 100 mV and was easily measured to within 0.1mV with the precision multimeter.

9.8.3 Sensitivity of Two Stage Electronic EMS Phase Shifter Oscillator to AGC Bias Voltage of the Gain Control Amplifier

In order to determine the relationship between AGC bias voltage of the gain control amplifier and oscillator frequency the oscillator circuit was set in the same way as section (9.6.3) at atmospheric conditions and the frequency reading was observed as the AGC bias voltage was reduced towards 0 V. The relationship between AGC bias voltage and oscillator frequency is illustrated in graph (9.43) below:-

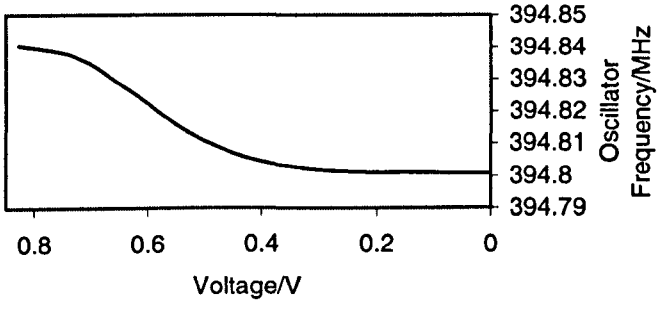

Graph 9.43 Relationship between AGC bias voltage and oscillator frequency.

The oscillator was set with the AGC bias at the minimum condition for oscillation and then it was decreased in 0.1 V steps. It can be seen from graph (9.43) that the oscillator frequency decreases by approximately 40 kHz as the AGC bias is reduced from 0.8 V to 0.4 V then remains constant.

In practice the AGC bias voltage of the gain control amplifier is always approximately 0.7 V, since this setting provides enough gain to satisfy the gain oscillation criterion. Therefore in order to determine the AGC bias voltage step required to achieve a 1 kHz change in frequency it is only the section of the graph (9.43) around 0.7 V that is of

interest. Over this region it has been calculated that a AGC bias voltage step of approximately 28 mV would be required to obtain a 1 kHz change in frequency.

The decrease in oscillator frequency with decreasing AGC bias is due to the phase characteristics of the amplifier as it goes into saturation (see section (9.3.5)). As the AGC bias is reduced the signal level within the oscillator increases and eventually the amplifier saturates. The saturation of the amplifier can be verified by observing the detected dc of the oscillator as the AGC bias is reduced. This is illustrated in graph (9.44) below:-

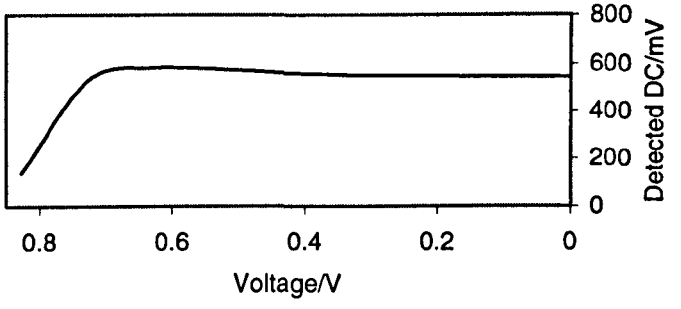

Graph 9.44 Relationship between AGC bias voltage and detected dc signal.

It can be seen from graph (9.44) that the detected dc initially increases as the AGC bias is reduced. This shows that the amplifier is operating linearly at this point. However as the AGC bias is reduced further the signal within the oscillator increases to a level whereby the amplifier becomes saturated. At this point the gain of the amplifier and subsequently the detected dc cannot increase further and indeed decrease with subsequent decrease in AGC bias. Reducing the AGC bias below approximately 0.4 V produces no further effects. This is in agreement with characteristics of the amplifier, as observed section (9.3.1).

The phase characteristics of the amplifier as a function of RF input and AGC bias were illustrated in graph (9.15) in section (9.3.5). It was shown that as the amplifier became

saturated the insertion phase increased dramatically. Therefore as the AGC bias is reduced and the amplifier starts to saturate, the total phase of the oscillator increases and as a result the frequency of the oscillator decreases. The decrease in frequency of approximately 40 kHz is in agreement with the increase of the insertion phase of 25° of the amplifier. The measurements were repeated with similar results at various phase set-ups of the oscillator loop.

9.8.4 RF Signal Level Analysis of Two Stage Electronic EMS Phase Shifter Oscillator

In order to determine the signal level within the oscillator loop the oscillator circuit was set up in the same way as section (9.6.3) at atmospheric conditions (approximately 394.8 MHz), except without the digital oscilloscope and the frequency counter, and the detected dc reading was observed as the AGC bias voltage of the gain control amplifier was reduced towards 0 V for each phase set-up. The results are illustrated in graph (9.45) below:-

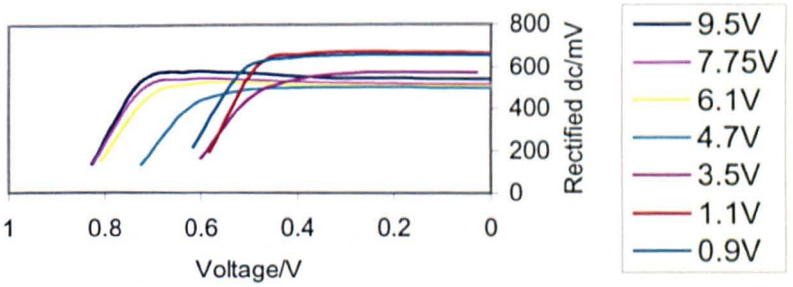

Graph 9.45 Relationship between AGC bias voltage and detected dc signal at each phase set-up.

It can be seen from graph (9.45) that, as expected, the detected dc varies in the same way with AGC bias voltage at each phase set-up. The signal level within the oscillator can be determined by using the relationship developed in section (9.8.1) between the RF input

to the phase shifter and the rectified dc. The results for the 9.5 V phase set-up are illustrated in table (9.5) below:-

Detected dc/mV	Signal Level at Phase Shifter/mV_{rms}	Output of Amplifier/dBm
139	45.7	6.2
525.6	159.4	17.0
577.0	174.6	17.8
571.3	172.9	17.7
556.3	168.5	17.5
547.4	165.9	17.4
544.7	165.1	17.3
542.5	164.4	17.3
542.4	164.4	17.3
542.7	164.5	17.3

Table 9.5 Signal level within oscillator for 9.5 V phase set-up as a function of AGC bias voltage.

Table (9.5) shows the detected dc of the oscillator circuit as the AGC bias voltage is increased. The relationship developed between RF input and rectified dc was used to calculate the signal level at the phase shifter. This value was then used to calculate the output signal level from the gain control amplifier. It can be seen from table (9.5) that as the AGC bias is reduced the amplifier, as already observed, saturates. The maximum specified output of the ZFL1000GH amplifier is + 17 dBm. It can also be seen that at the lowest AGC bias voltage (near unity loop gain and oscillator frequency measurement point) the output of the amplifier is only + 6 dBm therefore the amplifier is working in it's linear region and will not distort the signal within the oscillator.

9.8.5 Stability of Two Stage Electronic EMS Phase Shifter Oscillator

It was seen above that the oscillator measurements were performed with the ZFL1000GH gain control amplifier operating in its linear region. This means that the signal level within the oscillator loop is constant at a level that is not high enough to cause the amplifier to saturate. Therefore the oscillator can be said to have a stable signal amplitude. Normally in an oscillator without amplitude control the intended sinusoidal output can become highly distorted due to the fact that once the critical gain of the loop has been attained the amplitude of oscillation increases until the linear region of the amplifier has been exceeded and non-linear operation results.

The reason the oscillator circuit achieves internal balance and maintains a linear output can be explained by considering the operation of the ZFL1000GH amplifier as a function of temperature. It was found that the gain of the amplifier is inversely proportional to temperature. Therefore as the amplitude of oscillation starts to increase the temperature of the amplifier also increases producing a drop in gain, and ultimately preventing the signal level from reaching a level that causes the amplifier to saturate. Thus the amplitude of oscillation is self-limiting. This stability is relatively short term in comparison to the effects caused by ambient temperature change.

The long term and, to a certain degree, short term stabilities of the oscillator circuit are, however, irrelevant to the proposed computer controlled measurement procedure. The computer controlled measurement incorporates an *active* technique where the 0° total phase frequency is periodically measured by continuously sweeping the loop gain and phase of the system and monitoring the detected dc.

9.9 Uncertainty in Measured Oscillator Frequency

The measured oscillator frequency is influenced by:-

- phase shifter bias voltage;
- gain control amplifier AGC bias voltage;
- unity gain buffer amplifier AGC bias voltage;
- detected dc voltage;
- relative permittivity;
- re-entrant cavity temperature;
- gain control amplifier temperature;
- unity gain buffer amplifier temperature;
- passive component temperature.

The total uncertainty in measured oscillator frequency can be approximated by:-

$$U^2_{f,total} = \left[\left(\frac{\partial f}{\partial V_{PS}}\right).U_{V_{PS}}\right]^2 + \left[\left(\frac{\partial f}{\partial V_{GA}}\right).U_{V_{GA}}\right]^2 + \left[\left(\frac{\partial f}{\partial V_{BA}}\right).U_{V_{BA}}\right]^2 + \left[\left(\frac{\partial f}{\partial V_{D}}\right).U_{V_{D}}\right]^2 + \left[\left(\frac{\partial f}{\partial T_{GA}}\right).U_{T_{GA}}\right]^2 + \left[\left(\frac{\partial f}{\partial T_{BA}}\right).U_{T_{BA}}\right]^2 + \left[\left(\frac{\partial f}{\partial T_{PC}}\right).U_{T_{PC}}\right]^2 , \quad (9.1)$$

where $U_{V_{PS}}$ is the uncertainty in the setting of the bias voltage to the phase shifter (inclusive of superimposed noise);

$U_{V_{GA}}$ is the uncertainty in the setting of the gain control amplifier AGC bias voltage (inclusive of superimposed noise);

$U_{V_{BA}}$ is the uncertainty in the setting of the unity gain buffer amplifier AGC bias voltage (inclusive of superimposed noise);

U_{V_D} is the uncertainty in the measurement of detected dc (inclusive of superimposed noise);

$U_{T_{GA}}$ is the uncertainty in the temperature of the gain control amplifier;

$U_{T_{BA}}$ is the uncertainty in the temperature of the unity gain buffer amplifier;

$U_{T_{PC}}$ is the uncertainty in the temperature of the passive components of the oscillator.

- ***Relative Permittivity:-*** The relative permittivity influences the resonant frequency, insertion phase and quality factor, Q, of the cavity. If the relative permittivity was such that the Q of the cavity was significantly reduced then the resonance peak would be broader and harder to define with the oscillator circuit and as a result there would be a greater uncertainty in the measured oscillator frequency. It has been shown (see section (9.2.3)) that the Q of a 100 bar nitrogen filled cavity ($\varepsilon_r \approx 1.054$) is only 2.2% lower than at atmospheric conditions. The insertion phase of the cavity contributes to the total phase of the oscillator loop, which should be ideally 0° in order to measure the same frequency as the resonant frequency of the cavity. Therefore, if the insertion phase of the cavity is subject to change due to fluctuations in the relative permittivity then there will again be an uncertainty in the phase and gain control bias voltages. As previously mentioned, the insertion phase of the cavity decreased by approximately 20° as the cavity was filled with nitrogen to 100 bar. This corresponds to a change in relative permittivity of approximately 5% (see table (9.2)). Thus the uncertainty in relative permittivity would only have to be 0.15% to achieve a 0.6° phase accuracy, or rather a 1 kHz oscillator frequency accuracy. It can be seen that the uncertainty, or fluctuation, of relative permittivity influences the measured oscillator frequency by influencing the sensitivities of the phase and gain control bias voltages of equation (9.1). These effects have been shown to be minor, and as a result the influence of relative permittivity may be considered as having a negligible effect on the measured oscillator frequency.

- ***Re-entrant Cavity Temperature:-*** The resonant frequency and, as a direct result, the insertion phase of the cavity are influenced by the dimension of the cavity and the thermal properties of the cavity walls. If the insertion phase of the cavity is subject to change due to fluctuations in the cavity temperature then there will be an uncertainty in the phase and gain control bias voltages. It has been found that the change in insertion phase associated with a temperature related decrease in the resonant frequency of the cavity of approximately 15.3 kHz is only 0.4°. Therefore, since an ambient temperature increase of 1.5°C produces a decrease in resonant frequency of approximately 5 kHz, it can be seen that the uncertainty in cavity temperature need only be approximately 7°C in order to achieve a 0.6° phase accuracy, or rather a 1 kHz oscillator frequency accuracy. It can be seen that the uncertainty of the cavity temperature influences the measured oscillator frequency by influencing the sensitivities of the phase and gain control bias voltages. These effects have been shown to be minor, and as a result the uncertainty of cavity temperature may be considered as having a negligible effect on the measured oscillator frequency.

- ***Gain Control and Buffer Amplifier Temperature:-*** The gain and insertion phase of the gain control and buffer amplifiers are influenced by their operating temperatures. If the gain and insertion phase of either amplifier is subject to change due to fluctuations in the operating temperature then there will be an uncertainty in the phase and gain control bias voltages. If either amplifier is subjected to large fluctuations in temperature then there is a possibility that the critical loop gain will not be satisfied and oscillations will cease, or the loop gain will become so great that the amplifiers become saturated resulting in large shifts in insertion phase (see section (9.3.5)). It has been found that the change in measured oscillator frequency as the amplifier is subjected to temperature gradients of 2-3°C is of the order of 500 Hz. Therefore, since the stability of the oscillator frequency at each measurement condition is of the order of tens of hertz, it can be estimated that the shift in either amplifier temperature would have to be 10% in order to change the oscillator frequency by 1 kHz. Any temperature related fluctuations in loop gain obviously have a direct effect on the

detected dc, however, since these measurements were performed at a relatively stable room temperature the variation of detected dc over the course of each measurement was negligible. It can be seen that the stability of either the gain control or buffer amplifiers temperature influences the measured oscillator frequency by influencing the sensitivities of the phase and gain control bias voltages. These effects have been shown to be minor, and as a result amplifier temperature may be considered as having a negligible effect on the measured oscillator frequency.

- ***Passive Component Temperature:-*** The total loop gain and phase characteristics of the oscillator circuit are influenced by the temperature of the passive components (including cables, connectors etc.). If the insertion loss and phase characteristics of the passive components are subject to change due to fluctuations in the operating temperature then there will be an uncertainty in the phase and gain control bias voltages. In practice the effects of temperature fluctuations in the passive components are small and are masked by the effects of the gain control and buffer amplifier. It can be seen that the uncertainty of the temperature of the passive components may be considered as having a negligible effect on the measured oscillator frequency.

- ***Phase Shifter Bias Voltage:-*** The total loop phase of the oscillator is controlled by the bias voltage to the phase shifter. If the insertion phase of the phase shifter is subject to error due to uncertainties in bias voltage or superimposed noise on the bias then there will be an uncertainty in the loop phase of the oscillator and, consequently, the measured oscillator frequency. The uncertainty in measured oscillator frequency due to the uncertainty in the phase shifter bias voltage is:-

$$U_f = \left| \left(\frac{\partial f}{\partial V_{PS}} \right) . U_{V_{PS}} \right| \approx 25Hz \qquad (9.2)$$

where $\left(\frac{\partial f}{\partial V_{PS}}\right)$ has been approximated from section (9.8.2) at a phase shifter bias voltage of 8 V (mean operating voltage of phase shifter) where a 1 kHz change in measured oscillator frequency corresponds to a 200 mV change in phase shifter bias voltage;

and $U_{V_{PS}}$ has been estimated to be less than 5 mV.

- ***Gain Control and Buffer Amplifier AGC Bias Voltages:-*** The loop gain of the oscillator is controlled by the AGC bias to the gain control and buffer amplifier. (The buffer amplifier requires a constant AGC bias to maintain unity gain conditions). If the gain of either amplifier is subject to error due to uncertainties in setting the AGC bias voltage or superimposed noise on the bias then there will be an uncertainty in the total loop gain and phase of the oscillator and, consequently, the measured oscillator frequency. The uncertainty in measured oscillator frequency due to the uncertainty in the AGC bias voltage to the gain control amplifier, for example, is:-

$$U_f = \left|\left(\frac{\partial f}{\partial V_{GA}}\right).U_{V_{GA}}\right| \approx 178Hz \qquad (9.3)$$

where $\left(\frac{\partial f}{\partial V_{GA}}\right)$ has been approximated from section (9.8.3), where a 1 kHz change in measured oscillator frequency corresponds to a 28 mV change in AGC bias voltage;

and $U_{V_{GA}}$ has been estimated to be less than 5 mV.

The uncertainty in the buffer amplifier AGC bias voltage is the same.

- ***Detected dc:-*** The magnitude of the detected dc indicates the signal level within the oscillator and, consequently, determines the measured frequency. If the measurement

of the detected dc is subject to error due to fluctuations in oscillator signal and superimposed noise then there will be an uncertainty in the measured oscillator frequency. The uncertainty in measured oscillator frequency due to the uncertainty in the detected is:-

$$U_f = \left| \left(\frac{\partial f}{\partial V_D} \right) . U_{V_D} \right| \approx 37 Hz \qquad (9.4)$$

where $\left(\frac{\partial f}{\partial V_D} \right)$ has been approximated from section (9.8.2) at a phase shifter bias of 8 V where a 1 kHz change in measured oscillator frequency corresponds to a 3 mV change in detected dc;

and U_{V_D} from measurement is 0.1 mV.

Table (9.6), below, details the uncertainty budget for the measured oscillator frequency:-

Symbol	Source of Uncertainty	Uncertainty in Measured Oscillator Frequency/kHz
V_{PS}	Phase shifter bias voltage	0.025
V_{GA}	Gain control amplifier AGC bias voltage	0.178
V_{BA}	Buffer amplifier AGC bias voltage	0.178
V_D	Detected dc	0.037
T_{GA}	Gain control amplifier temperature	-
T_{BA}	Buffer amplifier temperature	-
T_{PC}	Passive component temperature	-
U_f	**Combined Uncertainty**	**0.255**

Table 9.6 Uncertainty of measured oscillator frequency (at mid-point of phase shifter operating region).

Table (9.6) gives the total, or combined, uncertainty in the measured oscillator frequency. It can be seen that the total uncertainty is well within the 1 kHz target uncertainty. It should be noted, however, that the total uncertainty was calculated for the phase shifter operating around 8 V, which corresponds to the *flat* region of its insertion loss. If the phase shifter were to operate at low bias voltages (below 5 V) then the uncertainty in measured oscillator frequency would be significantly higher. The calculated total uncertainty of the 0.225 kHz is commensurate with the measured differences in frequency of section (9.6.1).

9.10 Conclusions

The aim of this part of the work was to develop a prototype on-line instrument that was suitable for the making of accurate relative permittivity measurements on high-value fluids over an industrially relevant range of temperatures and pressures.

A requirement of the on-line instrument was that it should be simple to operate, relatively compact, robust and considerably less expensive than the associated laboratory instrument. In order to satisfy these requirements it was decided to develop a feedback oscillator circuit around the re-entrant cavity comprising relatively in-expensive modular electronic components.

It has been shown that the on-line instrument is capable of oscillating to within approximately 0.5 kHz of the true resonant frequency of the re-entrant cavity (see section 9.6.1). This accuracy of frequency measurement equates to an uncertainty in relative permittivity of approximately 2.5 ppm; a factor of two greater than the aimed uncertainty for the on-line instrument of 5ppm. This accuracy of frequency measurement is, however, only achievable over a relatively narrow range of operating conditions.

An extensive analysis of the characteristics of the on-line instrument, and each of its constituent components, revealed that the insertion loss characteristics of the phase shifter component is the limiting factor which ultimately obviates adoption of this method for the measurement of the relative permittivity of high value fluids under consideration here.

This feedback oscillator type arrangement, although not suitable for the extremely high precision required here, may, of course, be applied to other industrial or research sectors where such a high level of precision is not required.

References

1. P. L. D. Abrie, *Design of RF and microwave amplifiers and oscillators*; Boston, Artech House, 1999.
2. F. Nibler. *et al.*, *High Frequency Circuits*, IEEE Circuits and Systems Inspec, 1993.

10. Conclusions

The programme of work which forms the object of this doctoral submission centered around the development and validation of a novel method for the accurate and traceable determination of fluid density. The impetus for this work stemmed from the requirements of the oil and gas industry for more accurate and cost effective methods for determining mass and energy flow rates; particularly for on-line metering purposes.

It was considered unlikely that this objective could be achieved through the direct measurement of density and, consequently, it was the indirect method that was chosen for advancement. The alternative measurement parameter considered was relative permittivity. The well known Clausius-Mossotti relationship between relative permittivity and density allows for an alternative indirect route to determining the density of gases and liquids both in the laboratory and in on-line situations.

The refinement of measurement techniques for relative permittivity in recent years has allowed for precise measurements of relative permittivity over the industrially relevant pressure and temperature range in the laboratory and in on-line situations to within an uncertainty of a few parts per million using relatively simple and robust instrumentation. The prototype permittivity cell developed by The National Engineering Laboratory is capable of the precise determination of the relative permittivity of gases and hydrocarbon liquids over a wide range of both pressures and temperatures.

The selection of the re-entrant cavity technique as the most appropriate experimental technique for making precise measurements of the relative permittivity of high value fluids over an industrially relevant range of temperatures and pressures was explained in Chapter 3: Choice of Experimental Technique.

The prototype permittivity cell, comprising the re-entrant cavity, is capable of making relative permittivity measurements on gases and hydrocarbon liquids over a wide range

of both pressures and temperatures to within an accuracy of 1 ppm provided that the cavity has a high electrical quality factor at resonance; and the dimensions of the dielectric filled cavity are the same as those of the evacuated cavity at the same temperature of measurement. Excluding temperature effects, which may be easily quantified, the dimensional stability of the cavity is influenced by the dilation of the dielectric filled cavity with applied pressure; and the effective dilation of the dielectric filled cavity due to a change in the penetration depth of the electromagnetic field into the metal surfaces of the cavity.

One of the objectives of the work presented here was therefore to investigate the dimensional stability of the re-entrant cavity resonator both in terms of the applied physical pressure of the contained dielectric fluid and the spatial distribution of the electromagnetic field between evacuated and filled conditions.

In order to quantify and correct for the effects of changes in pressure and penetration depth of the electromagnetic field a mathematical model of the cavity was developed around an established theoretical model of the same. The theoretical model, developed as part of Chapter 4: Theory of Operation, establishes accurate relationships between the dielectric constant of the fluid, the geometry of the cavity, the resonance frequency and the quality factor, and allows the effects of change in pressure and penetration depth to be accounted for.

Reliable estimates of the dimensional changes in the cavity dimensions with applied pressure were obtained from a detailed finite element analysis study of the re-entrant cavity using ANSYS (a finite-element analysis package produced by SAS IP Inc.) (See Chapter 5: Pressure Effect Corrections). The dimensional data results presented in Chapter 5 were used in the theoretical model to correct for the effects of pressure on the resonant frequency of the cavity.

The frequency dependent spatial distribution of the electric and magnetic fields within the re-entrant cavity was calculated using the mathematical model and the changes in effective dimensions were used to correct for the effects on resonant frequency of the cavity.

Two arrangements of the permittivity cell are possible; a laboratory version with high-quality electrical instrumentation suitable for precise measurements on fluids and for mapping relative permittivity as a function of both density and temperature; and a robust, yet precise, on-line version with built-in electronics and low-cost instrumentation suitable for the precise measurements on fluids as a function of both density and temperature.

It was an object of the work presented here to develop and commission the laboratory facility for making precise measurements of the relative permittivity of high value fluids over an industrially relevant range of temperatures and pressures.

The National Density Standards facility at NEL was employed in the development and commissioning of the above laboratory facility. However, certain modifications to the National Density Standards facility were required to allow reference-quality measurements to be undertaken on high value fluids. The main modifications to the facility were the use of an alternative method of pressure measurement and the accommodation of the permittivity cell apparatus into the thermostating system. Chapter 6: Experimental Measurements, Facility and Operation describes, *inter alia,* the necessary modifications that were made to the National Density Standards facility to facilitate reference-quality measurements, the operation of the facility and the commissioning of the facility.

In order to determine the density of a fluid from a precise measurement of relative permittivity it is necessary to have an established relationship, such as the Clausius-Mossotti relation, between the relative permittivity, temperature and density of the fluid.

Consequently a further objective was to employ the laboratory facility in the mapping of the relative permittivity of ethylene over the relevant range of temperatures and pressures with a view to establishing an accurate expression for the density of ethylene in terms of relative permittivity and temperature. Chapter 6: Experimental Measurements, Facility and Operation also describes the mapping measurements made with the laboratory facility on the relative permittivity of research grade ethylene at temperatures between 0 and 40 °C and at pressures up to 120 bar. The results of this fluid mapping of the ethylene surface are presented in Chapter 7: Experimental Results.

Expressions for the density of ethylene in terms of relative permittivity and temperature are presented in Chapter 8: Data Analysis, along with a detailed description of the regression techniques used in their development and methods of solution.

These new expressions presented in Chapter 8: Data Analysis were found to give excellent representations of the Clausius-Mossotti relation over the full range of measurement conditions. Over the range of conditions under consideration here, the uncertainty in the representation of the Clausius-Mossotti relation is assessed as 0.03%, at a 95% confidence level. The author, therefore, believes that these expressions are the most accurate available at the present time.

Most on-line commercial densitometers are normally calibrated with pure fluids but are used with fluid mixtures, which may be a significant source of error. The permittivity cell can, however, be used for the determination of the density of fluid mixtures.

It has been demonstrated in Chapter 8: Data Analysis that, with the work carried out on the determination of the density of research grade ethylene (99.995% purity), it is also possible to determine accurately the density of industrial grade ethylene (typically 99% purity) of known approximate composition solely through a measurement of it's relative permittivity.

The ability to determine accurately the density of important industrial/technical fluid mixtures simply from an approximate knowledge of the composition of the mixture, it's temperature and relative permittivity is of considerable interest to producers, transporters and distributors of high value fluids. Although this topic is not covered in any length in this doctoral submission the industrial potential is such that it forms part of the recommendation for further work.

The laboratory facility was based around the high-performance RF network analyser as the principle measuring instrument. This approach meets the measurement criteria, however, is completely inappropriate for use as an on-line instrument. The criterion for the on-line instrument was that it must be simple to operate, relatively compact, robust and considerably less expensive; particularly if it is to be widely deployed.

Consequently another objective of the work was to develop a robust, on-line instrument, with low-cost electronics for making precise measurements of the relative permittivity of high value fluids over an industrially relevant range of temperatures and pressures.

In order to satisfy these requirements a feedback oscillator circuit was developed in Chapter 9: Development of On-Line Instrument, around the re-entrant cavity comprising relatively in-expensive modular electronic components.

It has been shown that the on-line instrument is capable of oscillating to within approximately 0.5 kHz of the true resonant frequency of the re-entrant cavity. This accuracy of frequency measurement equates to an uncertainty in relative permittivity of approximately 2.5 ppm; a factor of two greater than the aimed uncertainty for the on-line instrument of 5ppm. This accuracy of frequency measurement is, however, only achievable over a relatively narrow range of operating conditions.

An extensive analysis of the characteristics of the on-line instrument, and each of its constituent components, revealed that the insertion loss characteristics of the phase

shifter component are the limiting factor which ultimately obviate adoption of this method for the measurement of the relative permittivity of high value fluids under consideration here.

This feedback oscillator type arrangement, although not suitable for the extremely high precision required here, may, of course, be applied to other industrial or research sectors where such a high level of precision is not required.

To summarise, the work presented in this doctoral submission provides the underpinning traceability framework for the application and development of a novel method for the accurate and traceable determination of the density of fluids and fluid mixtures over an industrially relevant range of temperatures and pressures both in the laboratory and in on-line situations.

10.1 Recommendations for Further Work

As suggested above, perhaps the most pertinent work that should now follow on from the work presented here should be the development and validation of this new technology for the accurate and traceable determination of the density of fluid mixtures.

The next obvious step would be to employ the laboratory facility in the characterisation of the relative permittivity of industrial grade ethylene, with a view to confirming that, given a measurement solely of the relative permittivity and temperature of the mixture, together with an approximate knowledge of it's composition, it is possible to determine it's density.

Another area that requires further investigation is the phase shifting component of the on-line instrument. It was shown in Chapter: 9 Development of On-line Instrument that the on-line instrument is capable of satisfying the relative permittivity measurement criterion only over a relatively narrow range of operating conditions. It was revealed that

the insertion loss characteristics of the phase shifting component were the result of the limited performance of the on-line instrument.

It is therefore recommended that further work should be carried out in the development of the phase shifting component with a view to increasing the *constant insertion loss phase swing* to meet the requirements predetermined by the electrical characteristics of the re-entrant cavity.

In view of the findings of Chapter 9: Development of On-Line Instrument, where it was discovered that, in order to satisfy the phase requirements of the fluid filled cavity, the phase shifter component must be capable of providing 360° of constant insertion loss phase swing, the author believes that work should be carried out to develop a low-cost vector modulator component that is suitable for incorporation into the feedback oscillator circuit.

Appendix A

Numerical Values of Experimental Results

Table A.1 Density of ethylene as calculated from the equation of state.

Pt.	Temperature/°C	Pressure/bar	Density/(mol/m^3)
1	40.009	120.44	10941
2	35.007	119.32	11478
3	30.013	121.20	12118
4	25.013	121.17	12639
5	20.009	120.17	13102
6	15.010	118.57	13526
7	10.009	119.73	13994
8	5.007	119.75	14409
9	0.007	123.26	14859
10	40.008	100.64	9498.9
11	35.003	100.13	10279
12	30.015	100.78	11102
13	25.010	100.17	11773
14	20.010	100.32	12419
15	15.009	99.290	12961
16	10.007	100.47	13525
17	5.006	100.56	14009
18	0.009	99.752	14439
19	40.009	80.243	6565.2
20	35.010	80.274	7588.7
21	30.009	79.903	8827.6
22	25.009	79.981	10159
23	20.011	80.062	11249
24	15.010	80.143	12120
25	10.010	80.403	12846
26	5.006	80.198	13452
27	0.007	80.001	13988
28	40.008	59.864	3617.8
29	35.010	60.425	3956.0
30	30.007	60.233	4307.5
31	25.010	60.216	4890.2
32	20.011	60.545	6325.0
33	15.011	59.632	9498.3
34	10.009	59.647	11503
35	5.009	60.358	12604
36	0.009	60.215	13357
37	40.008	39.901	1967.6
38	35.011	40.269	2065.8
39	30.012	39.792	2113.3
40	25.011	40.262	2244.9
41	20.010	40.511	2380.6

42	15.011	40.365	2504.5
43	10.008	40.444	2688.7
44	5.008	39.581	2797.5
45	40.008	20.090	860.59
46	35.009	20.101	881.02
47	30.010	19.994	896.67
48	25.010	20.121	925.74
49	20.010	20.031	944.93
50	15.010	20.277	984.79
51	10.009	20.092	1002.1
52	5.011	20.052	1029.9
53	0.008	19.915	1053.8
54	40.008	10.124	409.50
55	35.011	10.101	416.35
56	30.010	10.163	427.29
57	25.011	10.067	431.56
58	20.011	10.145	444.15
59	15.009	10.049	449.04
60	10.010	10.029	457.90
61	5.011	10.105	472.15
62	0.008	10.046	480.14
63	0.008	40.017	3232.6
64	0.008	43.325	12397
65	0.009	50.384	12893
66	5.009	55.034	12245
67	5.009	50.341	11798
68	5.008	46.820	11245
69	10.009	54.682	10720
70	10.008	52.239	9789.6
71	10.008	51.675	9189.6
72	15.010	58.704	9037.8
73	15.009	57.591	8178.5
74	15.010	61.886	10201
75	15.010	70.106	11386
76	20.010	72.077	10368
77	20.010	68.170	9638.9
78	20.009	64.958	8638.8
79	20.010	63.093	7742.8
80	25.010	68.524	7557.3
81	25.010	70.236	8142.8
82	25.010	74.106	9173.3
83	25.010	66.787	6915.4
84	25.009	63.341	5726.5
85	25.010	49.577	3159.3
86	20.011	47.856	3185.1

87	20.010	57.380	5047.0
88	15.010	53.987	5112.7
89	15.009	56.309	6739.1
90	15.010	55.589	6068.3
91	15.009	57.124	7675.4
92	15.009	50.269	3965.2
93	10.010	47.730	3995.5
94	10.009	50.358	5150.5
95	10.010	51.129	6226.7
96	10.009	51.356	7837.8
97	10.009	51.428	8445.1
98	10.009	51.295	7135.8
99	5.007	42.424	3293.3
100	5.010	44.791	3922.4
101	5.009	29.992	1747.9
102	0.010	31.511	1983.8
103	30.010	22.822	1044.7
104	30.010	50.532	3058.8
105	30.009	66.434	5502.0
106	30.010	76.542	8113.8
107	30.010	71.050	6673.9
108	35.009	75.372	6548.4
109	35.009	70.095	5471.3
110	40.007	73.561	5421.8
111	40.009	85.682	7514.7

Table A.2 Resonant frequency of the ethylene filled cavity.

Pt.	Temperature/°C	Pressure/bar	Resonant Frequency/MHz
1	40.009	120.44	332.9181
2	35.007	119.32	330.2934
3	30.013	121.20	327.1986
4	25.013	121.17	324.7222
5	20.009	120.17	322.5532
6	15.010	118.57	320.5809
7	10.009	119.73	318.4310
8	5.007	119.75	316.5453
9	0.007	123.26	314.5187
10	40.008	100.64	340.1977
11	35.003	100.13	336.2465
12	30.015	100.78	332.1569
13	25.010	100.17	328.8878
14	20.010	100.32	325.7877
15	15.009	99.290	323.2309
16	10.007	100.47	320.6004
17	5.006	100.56	318.3765
18	0.009	99.752	316.4230
19	40.009	80.243	355.8161
20	35.010	80.274	350.2628
21	30.009	79.903	343.7131
22	25.009	79.981	336.8957
23	20.011	80.062	331.4696
24	15.010	80.143	327.2441
25	10.010	80.403	323.7885
26	5.006	80.198	320.9585
27	0.007	80.001	318.4846
28	40.008	59.864	372.6407
29	35.010	60.425	370.6796
30	30.007	60.233	368.6543
31	25.010	60.216	365.3080
32	20.011	60.545	357.2155
33	15.011	59.632	340.2786
34	10.009	59.647	330.2580
35	5.009	60.358	324.9547
36	0.009	60.215	321.4150
37	40.008	39.901	382.5690
38	35.011	40.269	382.0005
39	30.012	39.792	381.7435
40	25.011	40.262	380.9727
41	20.010	40.511	380.1771

42	15.011	40.365	379.4411
43	10.008	40.444	378.3717
44	5.008	39.581	377.7436
45	40.008	20.090	389.4170
46	35.009	20.101	389.3232
47	30.010	19.994	389.2594
48	25.010	20.121	389.1111
49	20.010	20.031	389.0248
50	15.010	20.277	388.8090
51	10.009	20.092	388.7346
52	5.011	20.052	388.5940
53	0.008	19.915	388.4765
54	40.008	10.124	392.2483
55	35.011	10.101	392.2398
56	30.010	10.163	392.2051
57	25.011	10.067	392.2126
58	20.011	10.145	392.1673
59	15.009	10.049	392.1706
60	10.010	10.029	392.1487
61	5.011	10.105	392.0957
62	0.008	10.046	392.0757
63	0.008	40.017	375.1571
64	0.008	43.325	325.9613
65	0.009	50.384	323.5989
66	5.009	55.034	326.6742
67	5.009	50.341	328.8334
68	5.008	46.820	331.5417
69	10.009	54.682	334.1287
70	10.008	52.239	338.8120
71	10.008	51.675	341.9065
72	15.010	58.704	342.6554
73	15.009	57.591	347.1828
74	15.010	61.886	336.7132
75	15.010	70.106	330.8165
76	20.010	72.077	335.8256
77	20.010	68.170	339.5572
78	20.009	64.958	344.7407
79	20.010	63.093	349.4927
80	25.010	68.524	350.4745
81	25.010	70.236	347.3451
82	25.010	74.106	341.9381
83	25.010	66.787	353.9508
84	25.009	63.341	360.5508
85	25.010	49.577	375.4547
86	20.011	47.856	375.3294

87	20.010	57.380	364.4371
88	15.010	53.987	364.0824
89	15.009	56.309	354.9563
90	15.010	55.589	358.6806
91	15.009	57.124	349.8807
92	15.009	50.269	370.7389
93	10.010	47.730	370.5798
94	10.009	50.358	363.8902
95	10.010	51.129	357.8037
96	10.009	51.356	348.8960
97	10.009	51.428	345.8097
98	10.009	51.295	352.6260
99	5.007	42.424	374.7686
100	5.010	44.791	371.0205
101	5.009	29.992	384.1413
102	0.010	31.511	382.7214
103	30.010	22.822	388.3354
104	30.010	50.532	376.0285
105	30.009	66.434	361.8018
106	30.010	76.542	347.4793
107	30.010	71.050	355.2602
108	35.009	75.372	355.9273
109	35.009	70.095	361.9492
110	40.007	73.561	362.2077
111	40.009	85.682	350.6395

Table A.3 Relative permittivity of ethylene.

Pt.	Temperature/°C	Pressure/bar	Relative Permittivity
1	40.009	120.44	1.407077
2	35.007	119.32	1.429795
3	30.013	121.20	1.457248
4	25.013	121.17	1.479833
5	20.009	120.17	1.500076
6	15.010	118.57	1.518865
7	10.009	119.73	1.539724
8	5.007	119.75	1.558403
9	0.007	123.26	1.578838
10	40.008	100.64	1.347439
11	35.003	100.13	1.379559
12	30.015	100.78	1.414013
13	25.010	100.17	1.442534
14	20.010	100.32	1.470395
15	15.009	99.290	1.494023
16	10.007	100.47	1.518921
17	5.006	100.56	1.540495
18	0.009	99.752	1.559853
19	40.009	80.243	1.231640
20	35.010	80.274	1.271258
21	30.009	79.903	1.320438
22	25.009	79.981	1.374701
23	20.011	80.062	1.420359
24	15.010	80.143	1.457556
25	10.010	80.403	1.489114
26	5.006	80.198	1.515769
27	0.007	80.001	1.539688
28	40.008	59.864	1.122839
29	35.010	60.425	1.134960
30	30.007	60.233	1.147675
31	25.010	60.216	1.169018
32	20.011	60.545	1.222840
33	15.011	59.632	1.347935
34	10.009	59.647	1.431287
35	5.009	60.358	1.478676
36	0.009	60.215	1.511706
37	40.008	39.901	1.065258
38	35.011	40.269	1.068621
39	30.012	39.792	1.070249
40	25.011	40.262	1.074776
41	20.010	40.511	1.079470

42	15.011	40.365	1.083854
43	10.008	40.444	1.090182
44	5.008	39.581	1.094000
45	40.008	20.090	1.028080
46	35.009	20.101	1.028757
47	30.010	19.994	1.029275
48	25.010	20.121	1.030241
49	20.010	20.031	1.030878
50	15.010	20.277	1.032203
51	10.009	20.092	1.032777
52	5.011	20.052	1.033702
53	0.008	19.915	1.034505
54	40.008	10.124	1.013274
55	35.011	10.101	1.013496
56	30.010	10.163	1.013854
57	25.011	10.067	1.013992
58	20.011	10.145	1.014404
59	15.009	10.049	1.014564
60	10.010	10.029	1.014852
61	5.011	10.105	1.015301
62	0.008	10.046	1.015578
63	0.008	40.017	1.109337
64	0.008	43.325	1.469782
65	0.009	50.384	1.491345
66	5.009	55.034	1.463133
67	5.009	50.341	1.443962
68	5.008	46.820	1.420446
69	10.009	54.682	1.398287
70	10.008	52.239	1.359866
71	10.008	51.675	1.335342
72	15.010	58.704	1.329284
73	15.009	57.591	1.294814
74	15.010	61.886	1.376657
75	15.010	70.106	1.426220
76	20.010	72.077	1.383721
77	20.010	68.170	1.353447
78	20.009	64.958	1.313018
79	20.010	63.093	1.277526
80	25.010	68.524	1.270157
81	25.010	70.236	1.293167
82	25.010	74.106	1.334424
83	25.010	66.787	1.245309
84	25.009	63.341	1.200097
85	25.010	49.577	1.106631
86	20.011	47.856	1.107562

87	20.010	57.380	1.174818
88	15.010	53.987	1.177311
89	15.009	56.309	1.238678
90	15.010	55.589	1.213068
91	15.009	57.124	1.274907
92	15.009	50.269	1.135380
93	10.010	47.730	1.136550
94	10.009	50.358	1.178756
95	10.010	51.129	1.219233
96	10.009	51.356	1.282335
97	10.009	51.428	1.305344
98	10.009	51.295	1.255329
99	5.007	42.424	1.111453
100	5.010	44.791	1.134041
101	5.009	29.992	1.057830
102	0.010	31.511	1.065882
103	30.010	22.822	1.034184
104	30.010	50.532	1.103062
105	30.009	66.434	1.191601
106	30.010	76.542	1.291948
107	30.010	71.050	1.235927
108	35.009	75.372	1.231084
109	35.009	70.095	1.190425
110	40.007	73.561	1.188520
111	40.009	85.682	1.268312

Table A.4 *Quality* factor of ethylene filled cavity.

Pt.	Temperature/°C	Pressure/bar	Quality Factor
1	40.009	120.44	2056
2	35.007	119.32	2065
3	30.013	121.20	2073
4	25.013	121.17	2083
5	20.009	120.17	2094
6	15.010	118.57	2104
7	10.009	119.73	2116
8	5.007	119.75	2129
9	0.007	123.26	2139
10	40.008	100.64	2072
11	35.003	100.13	2078
12	30.015	100.78	2085
13	25.010	100.17	2089
14	20.010	100.32	2102
15	15.009	99.290	2108
16	10.007	100.47	2121
17	5.006	100.56	2130
18	0.009	99.752	2142
19	40.009	80.243	2097
20	35.010	80.274	2101
21	30.009	79.903	2102
22	25.009	79.981	2104
23	20.011	80.062	2109
24	15.010	80.143	2115
25	10.010	80.403	2123
26	5.006	80.198	2135
27	0.007	80.001	2148
28	40.008	59.864	2092
29	35.010	60.425	2117
30	30.007	60.233	2128
31	25.010	60.216	2135
32	20.011	60.545	2133
33	15.011	59.632	2114
34	10.009	59.647	2115
35	5.009	60.358	2120
36	0.009	60.215	2129
37	40.008	39.901	2121
38	35.011	40.269	2136
39	30.012	39.792	2150
40	25.011	40.262	2164
41	20.010	40.511	2179

42	15.011	40.365	2194
43	10.008	40.444	2207
44	5.008	39.581	2224
45	40.008	20.090	2132
46	35.009	20.101	2145
47	30.010	19.994	2161
48	25.010	20.121	2175
49	20.010	20.031	2190
50	15.010	20.277	2207
51	10.009	20.092	2222
52	5.011	20.052	2240
53	0.008	19.915	2257
54	40.008	10.124	2135
55	35.011	10.101	2150
56	30.010	10.163	2164
57	25.011	10.067	2180
58	20.011	10.145	2196
59	15.009	10.049	2211
60	10.010	10.029	2227
61	5.011	10.105	2245
62	0.008	10.046	2260
63	0.008	40.017	2232
64	0.008	43.325	2135
65	0.009	50.384	2131
66	5.009	55.034	2119
67	5.009	50.341	2124
68	5.008	46.820	2129
69	10.009	54.682	2118
70	10.008	52.239	2125
71	10.008	51.675	2131
72	15.010	58.704	2120
73	15.009	57.591	2127
74	15.010	61.886	2108
75	15.010	70.106	2098
76	20.010	72.077	2089
77	20.010	68.170	2097
78	20.009	64.958	2107
79	20.010	63.093	2118
80	25.010	68.524	2107
81	25.010	70.236	2098
82	25.010	74.106	2088
83	25.010	66.787	2109
84	25.009	63.341	2125
85	25.010	49.577	2150
86	20.011	47.856	2166

87	20.010	57.380	2146
88	15.010	53.987	2161
89	15.009	56.309	2145
90	15.010	55.589	2149
91	15.009	57.124	2131
92	15.009	50.269	2174
93	10.010	47.730	2191
94	10.009	50.358	2178
95	10.010	51.129	2161
96	10.009	51.356	2156
97	10.009	51.428	2141
98	10.009	51.295	2144
99	5.007	42.424	2214
100	5.010	44.791	2206
101	5.009	29.992	2228
102	0.010	31.511	2243
103	30.010	22.822	2154
104	30.010	50.532	2137
105	30.009	66.434	2112
106	30.010	76.542	2085
107	30.010	71.050	2100
108	35.009	75.372	2086
109	35.009	70.095	2096
110	40.007	73.561	2083
111	40.009	85.682	2059

Table A.5 Insertion loss of ethylene filled cavity.

Pt.	Temperature/°C	Pressure/bar	Insertion Loss/dB
1	40.009	120.44	23.03
2	35.007	119.32	23.04
3	30.013	121.20	23.06
4	25.013	121.17	23.06
5	20.009	120.17	23.07
6	15.010	118.57	23.03
7	10.009	119.73	23.03
8	5.007	119.75	22.99
9	0.007	123.26	22.98
10	40.008	100.64	22.80
11	35.003	100.13	22.83
12	30.015	100.78	22.84
13	25.010	100.17	22.81
14	20.010	100.32	22.87
15	15.009	99.290	22.79
16	10.007	100.47	22.77
17	5.006	100.56	22.77
18	0.009	99.752	22.74
19	40.009	80.243	22.17
20	35.010	80.274	22.23
21	30.009	79.903	22.33
22	25.009	79.981	22.46
23	20.011	80.062	22.56
24	15.010	80.143	22.60
25	10.010	80.403	22.64
26	5.006	80.198	22.65
27	0.007	80.001	22.65
28	40.008	59.864	20.63
29	35.010	60.425	20.53
30	30.007	60.233	20.47
31	25.010	60.216	20.45
32	20.011	60.545	20.53
33	15.011	59.632	20.91
34	10.009	59.647	21.14
35	5.009	60.358	21.23
36	0.009	60.215	21.27
37	40.008	39.901	20.31
38	35.011	40.269	20.24
39	30.012	39.792	20.18
40	25.011	40.262	20.11
41	20.010	40.511	20.04

42	15.011	40.365	19.96
43	10.008	40.444	19.89
44	5.008	39.581	19.82
45	40.008	20.090	20.10
46	35.009	20.101	19.99
47	30.010	19.994	19.89
48	25.010	20.121	19.80
49	20.010	20.031	19.71
50	15.010	20.277	19.63
51	10.009	20.092	19.55
52	5.011	20.052	19.46
53	0.008	19.915	19.37
54	40.008	10.124	20.01
55	35.011	10.101	19.93
56	30.010	10.163	19.84
57	25.011	10.067	19.76
58	20.011	10.145	19.66
59	15.009	10.049	19.56
60	10.010	10.029	19.47
61	5.011	10.105	19.37
62	0.008	10.046	19.27
63	0.008	40.017	19.70
64	0.008	43.325	21.03
65	0.009	50.384	21.12
66	5.009	55.034	21.11
67	5.009	50.341	21.04
68	5.008	46.820	20.95
69	10.009	54.682	20.97
70	10.008	52.239	20.84
71	10.008	51.675	20.73
72	15.010	58.704	20.80
73	15.009	57.591	20.66
74	15.010	61.886	20.98
75	15.010	70.106	21.17
76	20.010	72.077	21.11
77	20.010	68.170	21.00
78	20.009	64.958	20.83
79	20.010	63.093	20.70
80	25.010	68.524	20.76
81	25.010	70.236	20.85
82	25.010	74.106	21.01
83	25.010	66.787	20.67
84	25.009	63.341	20.52
85	25.010	49.577	20.17
86	20.011	47.856	20.05

87	20.010	57.380	20.31
88	15.010	53.987	20.22
89	15.009	56.309	20.41
90	15.010	55.589	20.33
91	15.009	57.124	20.55
92	15.009	50.269	20.07
93	10.010	47.730	19.98
94	10.009	50.358	20.12
95	10.010	51.129	20.25
96	10.009	51.356	20.48
97	10.009	51.428	20.57
98	10.009	51.295	20.38
99	5.007	42.424	19.78
100	5.010	44.791	19.88
101	5.009	29.992	19.50
102	0.010	31.511	19.46
103	30.010	22.822	19.86
104	30.010	50.532	20.25
105	30.009	66.434	20.58
106	30.010	76.542	20.94
107	30.010	71.050	20.73
108	35.009	75.372	20.81
109	35.009	70.095	20.68
110	40.007	73.561	20.77
111	40.009	85.682	21.04

Table A.6 Insertion phase of ethylene filled cavity.

Pt.	Temperature/°C	Pressure/bar	Insertion Phase/°
1	40.009	120.44	185.3
2	35.007	119.32	201.0
3	30.013	121.20	220.0
4	25.013	121.17	234.1
5	20.009	120.17	247.6
6	15.010	118.57	258.6
7	10.009	119.73	271.8
8	5.007	119.75	282.9
9	0.007	123.26	294.9
10	40.008	100.64	142.1
11	35.003	100.13	165.1
12	30.015	100.78	190.1
13	25.010	100.17	209.5
14	20.010	100.32	227.8
15	15.009	99.290	242.3
16	10.007	100.47	257.8
17	5.006	100.56	271.0
18	0.009	99.752	282.7
19	40.009	80.243	47.8
20	35.010	80.274	82.0
21	30.009	79.903	119.6
22	25.009	79.981	160.9
23	20.011	80.062	193.1
24	15.010	80.143	218.1
25	10.010	80.403	238.5
26	5.006	80.198	255.7
27	0.007	80.001	270.6
28	40.008	59.864	-51.8
29	35.010	60.425	-39.8
30	30.007	60.233	-28.3
31	25.010	60.216	-8.0
32	20.011	60.545	40.0
33	15.011	59.632	141.0
34	10.009	59.647	199.6
35	5.009	60.358	231.7
36	0.009	60.215	253.1
37	40.008	39.901	-110.0
38	35.011	40.269	-105.7
39	30.012	39.792	-105.0
40	25.011	40.262	-99.9
41	20.010	40.511	-95.3

42	15.011	40.365	-91.6
43	10.008	40.444	-84.8
44	5.008	39.581	-81.4
45	40.008	20.090	-151.0
46	35.009	20.101	-149.9
47	30.010	19.994	-149.6
48	25.010	20.121	-148.7
49	20.010	20.031	-148.2
50	15.010	20.277	-146.6
51	10.009	20.092	-146.6
52	5.011	20.052	-145.7
53	0.008	19.915	-146.0
54	40.008	10.124	-167.2
55	35.011	10.101	-167.3
56	30.010	10.163	-167.3
57	25.011	10.067	-167.0
58	20.011	10.145	-167.1
59	15.009	10.049	-167.1
60	10.010	10.029	-167.2
61	5.011	10.105	-167.2
62	0.008	10.046	-166.8
63	0.008	43.325	225.1
64	0.009	50.384	238.6
65	5.009	55.034	220.1
66	5.009	50.341	207.8
67	5.008	46.820	191.7
68	10.009	54.682	176.6
69	10.008	52.239	148.5
70	10.008	51.675	130.6
71	15.010	58.704	125.2
72	15.009	57.591	98.7
73	15.010	61.886	161.7
74	15.010	70.106	196.7
75	20.010	72.077	166.0
76	20.010	68.170	144.9
77	20.009	64.958	113.0
78	20.010	63.093	84.9
79	25.010	68.524	80.1
80	25.010	70.236	97.8
81	25.010	74.106	130.5
82	25.010	66.787	59.2
83	25.009	63.341	19.2
84	25.010	49.577	-68.3
85	20.011	47.856	-68.1
86	20.010	57.380	-3.2

87	15.010	53.987	-1.6
88	15.009	56.309	52.2
89	15.010	55.589	30.0
90	15.009	57.124	83.3
91	15.009	50.269	-40.6
92	10.010	47.730	-40.4
93	10.009	50.358	-1.6
94	10.010	51.129	34.9
95	10.009	51.356	87.6
96	10.009	51.428	105.9
97	10.009	51.295	65.7
98	5.007	42.424	-65.2
99	5.010	44.791	-43.3
100	5.009	29.992	-120.5
101	0.010	31.511	-111.8
102	30.010	22.822	-144.5
103	30.010	50.532	-72.1
104	30.009	66.434	11.6
105	30.010	76.542	97.4
106	30.010	71.050	49.8
107	35.009	75.372	46.5
108	35.009	70.095	10.1
109	40.007	73.561	9.2
110	40.009	85.682	78.3